High Power Uni-Travelling-Carrier Photodiodes for THz Wireless Communications

Xiaoli Lin

A thesis submitted to University College London
for the degree of Doctor of Philosophy

Department of Electronic and Electrical Engineering
University College London

March, 2022

Statement of Originality

I, Xiaoli Lin, confirm that the work presented in this thesis is my own other than where I have clearly indicated that it is the work of others. Where information has been derived from other sources, I confirm that this has been indicated in the thesis.

I confirm that Figure 2.5, Figure 2.10, Figure 2.13 and Figure B.4 were obtained under the help of Dr. Chris Graham, and Figure 2.16, Figure 2.17 and Figure 2.19 were based on the antenna design on UTC-PDs from Dr. Michele Natrella. Test samples (coplanar waveguide UTC-PDs and antenna integrated UTC-PDs) used for CW and pulse measurements in this thesis were designed and fabricated by Ultra-Fast Photonics Group at University College London.

Abstract

The research work in this thesis is concerned with improving the output RF power of Uni-Travelling Carrier Photodiodes (UTC-PDs) by increasing their bias voltage capability and improving their thermal performance, targeting the frequency range of 200 – 300 GHz for ultra-high-speed wireless communications. Antenna integrated UTC-PDs with higher output power will enable sub-THz signals to be transmitted over longer distance and with higher signal to noise ratio (SNR). At the beginning of this thesis, types of continuous wave THz sources are reviewed in the literature to compare their suitability for wireless communications. Photonic techniques, benefiting from signal transmission over optical fibre cables, allow THz modulated optical signals to be distributed over long distances, superior to electronic techniques in this aspect. With respect to frequency bandwidth, tuneability and room temperature operation, UTC-PDs have exhibited advantages over competing photonic devices, and were chosen as the signal source for sub-THz wireless communications to investigate in this thesis.

Following this, the first waveguide coupled phosphide-based UTC-PDs grown by Solid Source Molecular Beam Epitaxy are reported. Coplanar Waveguide (CPW) integrated UTC-PDs and antenna integrated UTC-PDs were fabricated and characterised. Techniques were developed to reduce the leakage current of UTC-PDs from several μA to less than 100 nA (biased at -1V) for different sizes of devices up to 7×15 μm^2, and bias voltage capability was improved to enable UTC-PDs work up to -5V voltage. Limitations due to thermal effects in UTC-PDs are studied in detail. Experiments with pulsed heterodyne input signals were used to separate the thermal effects on the output power of CPW devices. Pulse measurement results indicate that UTC-PD output saturation power can be increased by more than 3 dB by reducing thermal effects. Thermal modelling of UTC-PDs is presented to show the temperature distribution inside devices. The modelling shows the restrictions preventing heat dissipation mainly come from two factors: the small cross-sectional area of the P-type contact and the low thermal conductivity of semiconductor materials. Three solutions are proposed to reduce thermal resistance and improve heat dissipation inside UTC-PDs. In addition, verification experiments were conducted to measure UTC-PD temperature and compare with the simulated results. Good agreement was achieved, demonstrating the validity of the thermal modelling presented in this thesis.

Impact Statement

Wireless communication is developing rapidly both in speed and in quality in recent years. With more and more people using wireless networks to access online multimedia services, especially high-resolution video, the prospective data rate for wireless communications is expected to reach 100 Gb/s by 2026. In order to support such a high mobile data consumption and to enable ultra-high-speed wireless communication, one of the most promising and effective ways is to increase the carrier frequency to sub-THz range (like 200 GHz - 300 GHz). Antenna integrated UTC-PDs, with large bandwidth, tunability, compatible with optical networks, and working at room temperature, are competitive sub-THz sources for high-speed wireless networks and key devices to realise communications beyond 100 Gb/s.

The work in this thesis focuses on the development of high-power antenna integrated UTC-PDs by increasing the bias voltage capability and reducing device thermal resistance. High temperature, caused by high input optical power and large photocurrent, decreases the electron mobility and increases the transit time of electrons. Piled up electrons reduce the electric field inside UTC-PDs and cause the RF output power to saturate. Pulse measurement experiments show the saturated RF output power can be increased by more than 3dB when there is reduced thermal heating inside UTC-PDs. Thermal modelling indicates the maximum temperature inside 4x15 μm^2 antenna integrated UTC-PDs can be reduced by 53% through effective thermal management. Accordingly, the saturated RF output power can be increased by around 2dB. Experiments on bow-tie antenna integrated UTC-PDs demonstrate the saturated RF output power can be improved by 1.2 dB by using thermal conductive adhesives replacing the nitrocellulose bonding layer conventionally used.

With a higher sub-THz radiated power, antenna integrated UTC-PDs can provide larger SNR and extend the signal reaching distance without increasing the sensitivity of receivers, making sub-THz wireless communications more practical in a wider range of applications. In addition, antenna integrated UTC-PDs can be used as millimetre/THz emitters in CW spectroscopy systems. Higher power UTC-PDs can improve the dynamic range and the SNR of the system, enabling more accurate spectroscopic measurements. A higher dynamic range enables the spectroscopy systems to accept more losses in a sample, and a larger SNR benefits the measurement system with a clearer response.

Acknowledgments

PhD journey is challenging and full of frustrations and failures. Luckily, I have my supervisors, colleagues and my family helping me and supporting me. All the backings and encouragements from them make this journey meaningful and fruitful, comprising a very important part of my life.

First of all, I would like to thank my supervisor Prof Alwyn Seeds for his continuous guidance and support throughout the course of my PhD study. I can always gain better understanding of technical questions and get motivated for further research during our regular meetings. Through discussions on the difficulties and problems I met in experiments and fabrications, my supervisor always sparks my inspiration and gives me directions to carry on.

I would also like to thank my second supervisor Prof Cyril Renaud for his input to my work and suggestions on my experiments.

I am really thankful to Dr. Chris Graham for being always happy to share his expertise of fabrication and device measurement, and for his plenty of time on training me fabrication steps of UTC-PDs in clean room. Most of my experiment devices come from Chris' hard work, and without his help my experiments wouldn't carry out smoothly.

I am also grateful to Dr. James Seddon for his help on CST modelling and for technical discussions on UTC-PD structure, designs and characterisations.

I would also express my thanks to Dr. Michele Natrela for his help on understanding optical modelling on UTC-PDs, and to Dr. Lalitha Ponnampalam for her support on my lab works.

Finally, I need to thank my little girl, Yuxuan Wang (11 years old now). Though she has being tried her best to disturb my study at home, her magic words letting me "keep calm and carry on" really give me energy every time when I want to give up.

Table of Contents

List of Figures

List of Tables

List of Acronyms

ASE	Amplified Spontaneous Emission
BWO	Backward Wave Oscillators
CC-MUTC PD	Charge-Compensated MUTC PD
CPW	Coplanar Waveguide
CST	Computer Simulation Technology
CTE	Coefficient of Thermal Expansion
CW	Continuous Wave
DDR-PD	Dual Depletion Region Photodiode
EDFA	Erbium Doped Fibre Amplifier
FEL	Free Electron Lasers
FFT	Fast Fourier Transform
FSPL	Free Space Path Loss
FWHM	Full Width at Half Maximum
GS-MBE	Gas Source Molecular Beam Epitaxy
HiPIMS	High-power impulse magnetron sputtering
HR-UTC-PD	High-Reflectivity UTC-PD
IMPATT	Impact Avalanche Transit Time
ICPCVD	Inductive Coupled Plasma Chemical Vapour Deposition
IDE	Integrated Development Environment
IVB	Intervalence Band
LT-GaAs	Low Temperature grown GaAs
MBE	Molecular Beam Epitaxy
MOCVD	Metal Organic Chemical Vapour Deposition
MOVPE	Metal Organic Vapour Phase Epitaxy

MUTC	Modified UTC-PD
MZ	Mach-Zehnder
NBUTC-PD	Near Ballistic Uni-Traveling Carrier Photodiode
NTP	Normal Temperature and Pressure
N-UTC-PD	Novel design for the collector layer UTC-PD
PDA-PD	Partially-doped absorber photodiode
PD	Photodiode
PECVD	Plasma Enhanced Chemical Vapour Deposition
PIN-PD	Positive-Intrinsic-Negative Photodiode
PM	Polarisation Maintaining
QCL	Quantum Cascade Lasers
RIE	Reactive Ion Etching
RTA	Rapid Thermal Annealing
RTD	Resonant Tunnelling Diode
SBD	Schottky Barrier Diode
SI	Semi Insulation
SNR	Signal to Noise Ratio
SOA	Semiconductor Optical Amplifiers
SOI	Silicon-on-Insulator
SOP	State of Polarisation
SS-MBE	Solid-Source Molecular Beam Epitaxy
TEC	Thermoelectric Cooler
TUNNETT	Tunnel Injection Transit Time
TW-UTC-PD	Traveling-wave UTC-PD
UTC-PD	Uni-Traveling Carrier Photodiode
VOA	Variable Optical Attenuator

Chapter 1
Introduction

1.1 Terahertz Gap

Terahertz (THz) waves refer to the electromagnetic waves at the frequency from 100 GHz to 10 THz (wavelengths between 3 mm and 30 μm), which lie in the frequency region between microwaves and infrared light waves, see Figure 1.1. It had been named as 'THz Gap' as this frequency range had rarely been utilized 20 years ago, except in astronomy and other related fields, because of the lack of devices for generating and detecting them. Currently the THz range is underutilized and the subject of ongoing research, therefore it is not as commercially developed as its adjacent microwave and infrared light wave regions. Therefore, in the literature this frequency range is still referred to as THz gap [1.1].

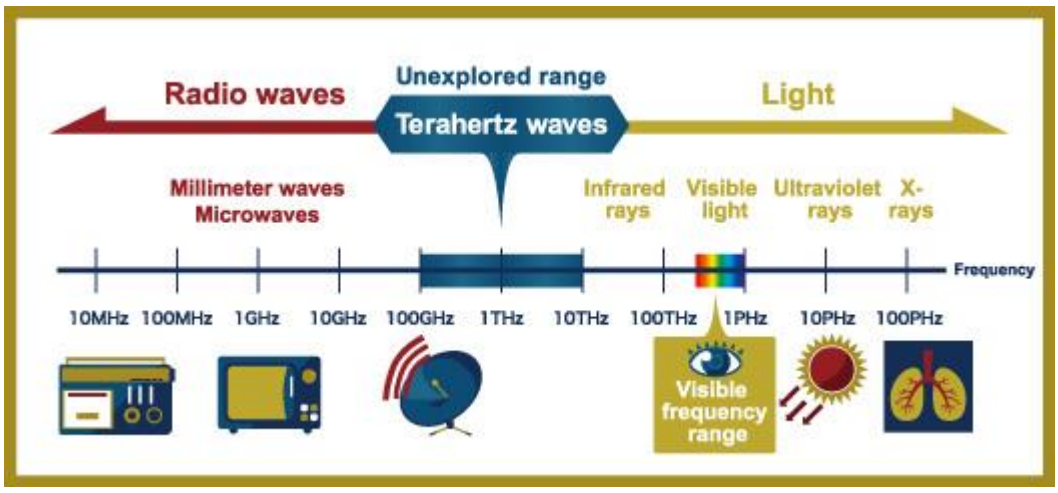

Figure 1.1: THz frequency gap in the electromagnetic spectrum [1.3].

This frequency range is attractive in that its lower end merges into the realm of radio waves, and its upper end into the infrared range, which makes THz wave possess some unique properties and stimulate the development of THz industry [1.1]. One major advantage of THz waves is that many materials, which block visible and IR spectra, appear to be transparent in the THz region. THz can "look

inside" plastics, textiles, paper and cardboard, and is selectively absorbed by water and organic substances. Compared to microwave radiation, the THz frequency is able to achieve a fairly good spatial resolution required for rendering quality imaging. These unique properties make THz much more attractive and informative than X-rays and near infrared radiation. Another unique property of THz emission is its harmlessness for biological entities. As opposed to X-rays, THz waves are non-ionizing, and are non-invasive and safe for humans, animals and plants. Moreover, many biomolecules, proteins, explosives or narcotics reveal their feature characteristic absorption lines, so-called spectral "fingerprints", at frequencies between 0.1 and 5.0 THz, which provides unique information about their structure and allows conducting their chemical analysis. Besides, THz band has much higher frequency, larger available bandwidth (ranges from a few GHz to over 1 THz) and more channels than microwave band. These properties make THz frequency suitable for higher speed wireless communication systems [1.4]. Although optical frequencies have higher frequency and bandwidth than THz, optical signals have power losses two orders of magnitude higher at some weather conditions, for example fogs, compared to THz signals (up to 1 THz) [1.5]. All above these unique properties enable potential applications of THz radiation in spectroscopy [1.6] - [1.11], industrial manufacturing [1.12], material science [1.3], medical science [1.13], security imaging [1.14] - [1.18], high date rate wireless communications [1.19] - [1.23], and so on. For example, identification of molecules (by using their chemical fingerprint), hazardous gas detection, non-contact quality inspection, drugs or explosives detection, detecting diseases at early stages, and etc (see Figure 1.2).

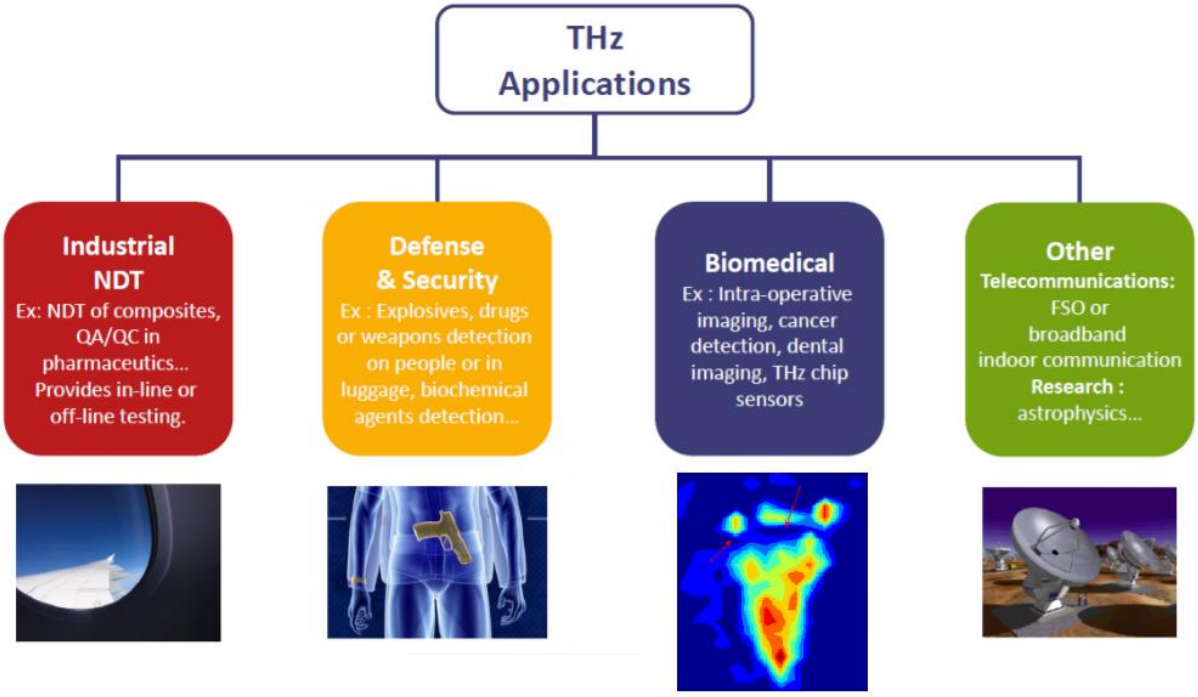

Figure 1.2: THz application fields and examples [1.24].

For high-speed THz wireless transmission, THz sources are expected to be compact, tuneable, power efficient, cost-effective, and operate at room temperature. Photonic techniques, benefiting from signal transmission over optical fibre cables, allow THz modulated optical signals to be distributed over long distances, superior to electronic techniques in this aspect. With respect to bandwidth, tuneability and room temperature operation, UTC-PDs have exhibited advantages over competing photonic devices, and were chosen as the signal source for sub-THz wireless communications to investigate in this thesis. In the following Section 1.2, the demand for high-speed wireless communications is discussed, and in Section 1.3 an overview of continuous wave (CW) THz sources is presented with special attention given to photomixing techniques employing UTC-PDs. Methods having been reported to achieve high power UTC-PDs is covered in Section 1.4, and Section 1.5 gives a summary for CW THz sources. Finally, the structure and organisation of this thesis is outlined in Section 1.6.

1.2 Future Wireless Communications

Wireless communication is developing very rapidly both in speed and in quality in recent years. With more and more people using wireless networks through laptop, smartphone and tablet, especially the data consumption on high resolution videos, the demand for the ultra-fast wireless communication systems is increasing. According to the published Ericsson Mobility Report 2019 [1.25], in 2024 monthly mobile data traffic per active smartphone in North America will reach 39 GB (see Figure 1.3(a)), and total mobile data traffic is predicted to increase, reaching 131 exabytes (EB) per month by the end of 2024 (see Figure 1.3(b)). The total mobile data traffic is expected to rise at a compound annual growth rate (CAGR) of 30%. Among such heavy monthly mobile data traffic, mobile video traffic is forecast to grow by around 34% annually up to 2024 to account for nearly 3 quarters of all mobile data traffic (see Figure 1.4), from approximately 60% in 2018. Extrapolating the evolution of cellular wireless data rates from [1.26] results in a prediction of around 100 Gb/s required by 2030. To date, the demand for increasing wireless communication speed has been accomplished by employing high spectral efficiency modulation formats (e.g. 512-QAM) and signal-processing technologies at microwave frequencies. However, these methods would increase the signal-to-noise level and reduce the communication link length, so it is quite challenging to reach data rates of 10 Gb/s or faster under the fundamental limitations of current technologies - low millimetre wave frequency (less than 100 GHz) and narrow bandwidth (8.6 GHz or less) [1.27]. Therefore, without increasing the carrier frequencies for more spectral resources, it would be quite difficult to keep up with the increasing needs of wireless link users.

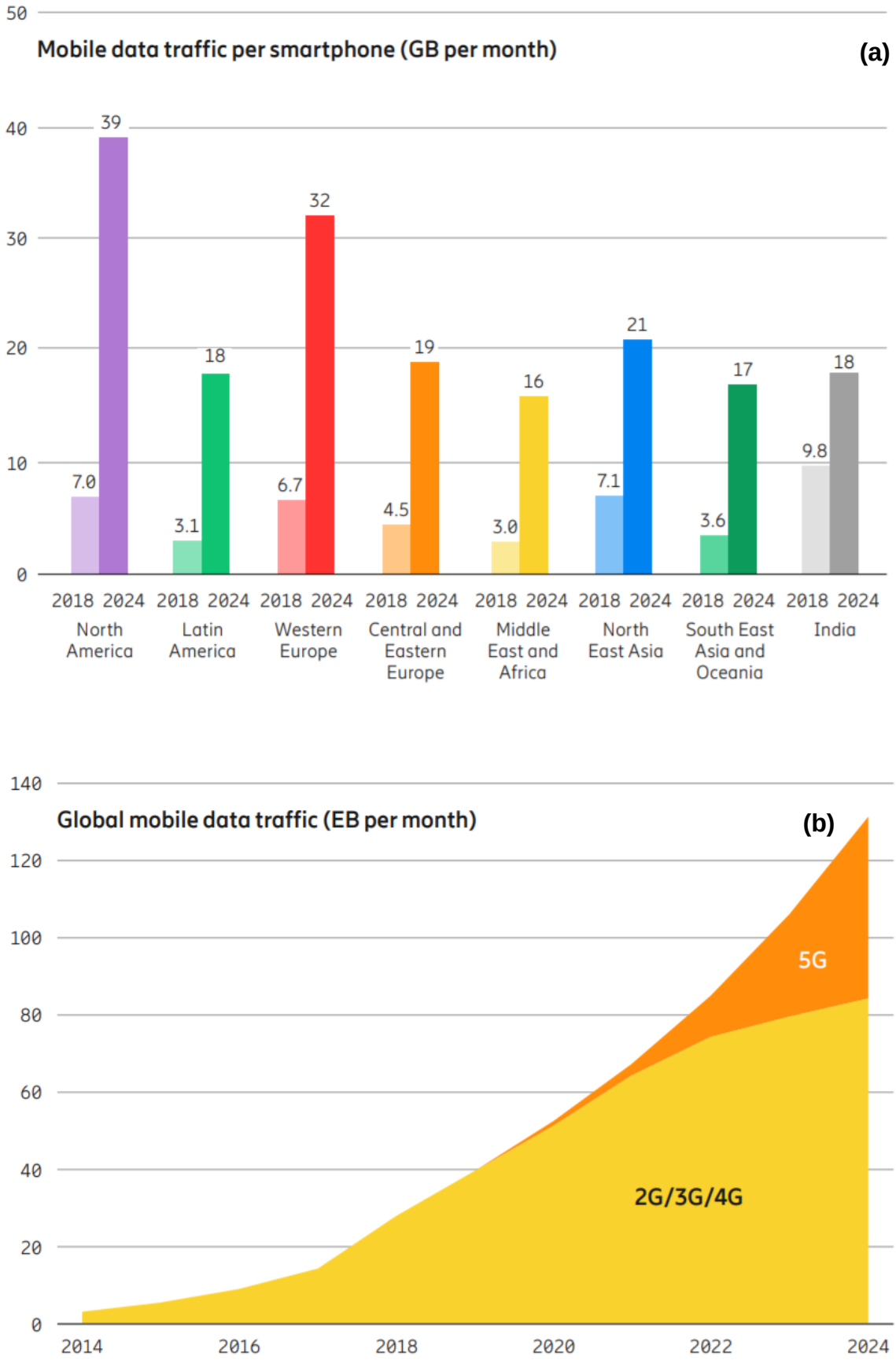

Figure 1.3: (a) Outlook for monthly mobile data traffic per smartphone in 2024, (b) Outlook for global total mobile data traffic by the end of 2024 [1.25].

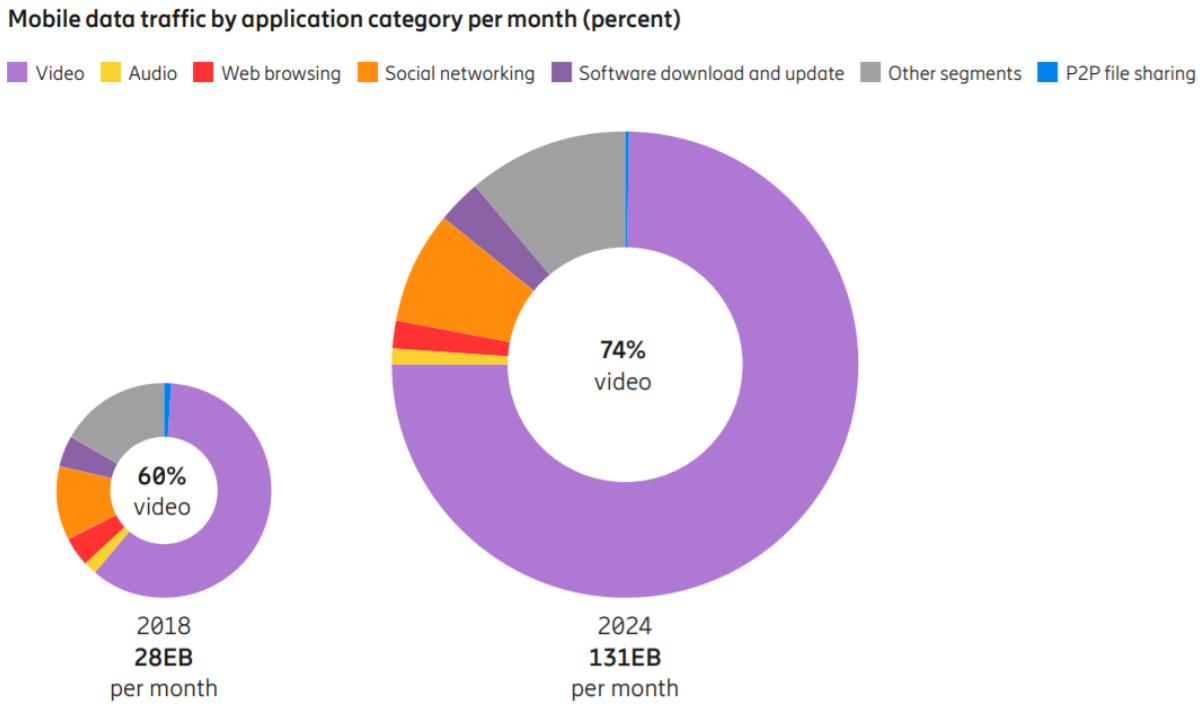

Figure 1.4: Mobile data traffic by application category per month (Exabytes) [1.25].

In order to support such a high mobile data consumption and to enable ultra-high-speed wireless communication, we need to look to higher carrier frequencies to make use of their extreme bandwidth, especially those unallocated frequency regions of the electromagnetic spectrum above 275 GHz (USA) or 300 GHz (Europe). Two obstacles of using THz waves in wireless communications are free space path loss (FSPL) and atmospheric attenuation due to water vapour absorption. The FSPL is governed by $(4\pi df/c)^2$, where d is link distance, f is carrier frequency, and c is the velocity of light, and increases as the square of f and d, see the dotted lines in Figure 1.5 (a) [1.28]. Atmospheric attenuation per kilometre due to water absorption is shown in Figure 1.5 (b) [1.28], up to 3 THz, which also increases with frequency. Below 1 THz, there are several frequency windows where the water vapour absorption is relatively low and has a bandwidth of several tens of GHz, making them suitable for high-speed wireless communications. For the frequencies above 1 THz, atmospheric attenuation becomes much higher (10 dB attenuation at only 10 m distance) and more

fluctuant, therefore no low loss and stable spectral windows are available for wireless communications. To solve the issue of high FSPL and atmospheric attenuation in windows below 1 THz, high-gain, steerable, phased-array antennas can be deployed to build directional, line-of-sight wireless systems [1.29], like the architecture having already be deployed on the 60 GHz band.

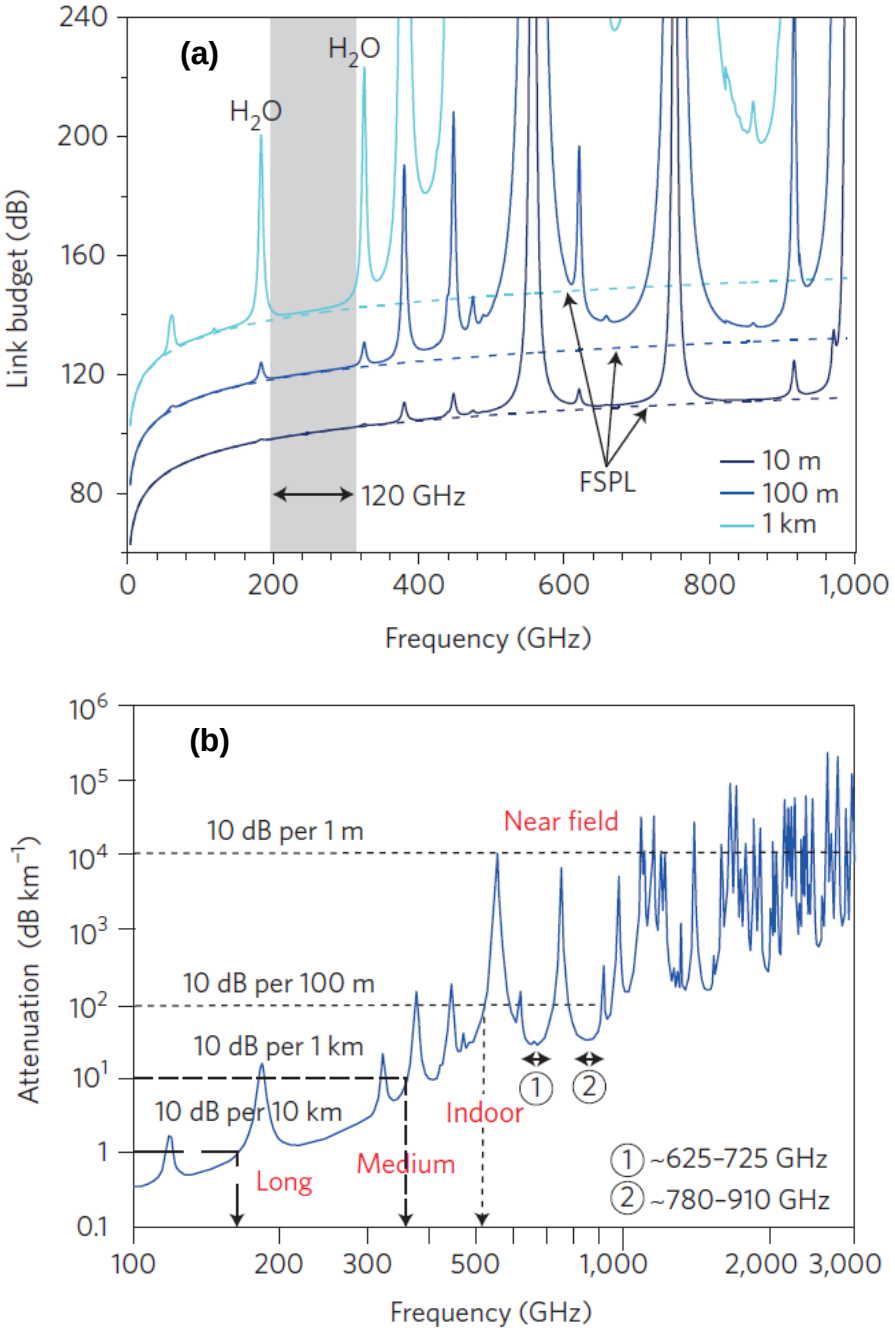

Figure 1.5: (a) Link losses due to atmospheric attenuation and FSPL (dotted lines: without atmospheric attenuation at 10 m, 100 m and 1 km) [1.28], (b) atmospheric attenuation per kilometre from 100 GHz to 3 THz [1.28].

The photonic generation of a multiband signal for sub-THz wireless-over-fibre transmission was experimentally demonstrated in [1.30], with downlink wireless transmission up to 100 Gbit/s (20 Gbit/s per channel at 1.33 bit/s/Hz spectral efficiency) using the full spectrum 220 – 280 GHz and 10 Gbit/s OOK on the uplink optical stream. [1.31] demonstrated 160 Gbit/s wireless transmission with a single THz emitter and modulating 25 GHz spaced 8 channels (20 Gbps per channel) in the 300 - 500 GHz band, by using a single UTC-PD based transmitter and a Schottky mixer-based receiver. In [1.32], a THz photonic wireless transmission with a data rate of 100.8 Gbit/s over 26.8 m distance operating at 350 GHz without any THz amplification was experimentally demonstrated, which was enabled by combining probabilistic shaping and OFDM techniques, a UTC-PD and a pair of high-gain Cassegrain antennas, and Schottky mixer improving the receiver sensitivity. These reported experiments show the feasibility to realise wireless communications beyond 100 Gbit/s data rates at sub-THz range, to meet the growing traffic demand in the near future.

The important component for THz wireless transmission is the THz source, which needs to be broadband, high power and have high directivity. The bulky, expensive, power-hungry THz sources are not suitable for public wireless networks. Besides wide bandwidth and high output power, we also desire compact, tuneable, cost-effective, power efficient, room temperature operating, and CW running THz sources for future communications. These figures of merit will be used as the criteria to judge whether the approaches realising THz emission discussed in Section 1.3 are acceptable as practical THz sources for high-speed wireless communications.

1.3 Continuous Wave Terahertz Sources

The unique properties of THz radiation (non-ionizing, high chemical sensitivity, less scattering, wideband, etc.) make its technologies bear great potential applications in spectroscopy, material science, medical science, security imaging, and high-speed wireless communication, etc. To make these applications possible, efficient THz wave generation and detection are required, with the former being the most challenging technology issue. THz technology is at the

junction between two families of technology: electronic family and photonic family, which indicates that THz sources can base on electronics principles but used at higher frequencies, and also can base on photonic sources working at decreased frequencies [1.33] (see Figure 1.6). Therefore, electronic techniques and photonic techniques are the two major approaches for THz generation.

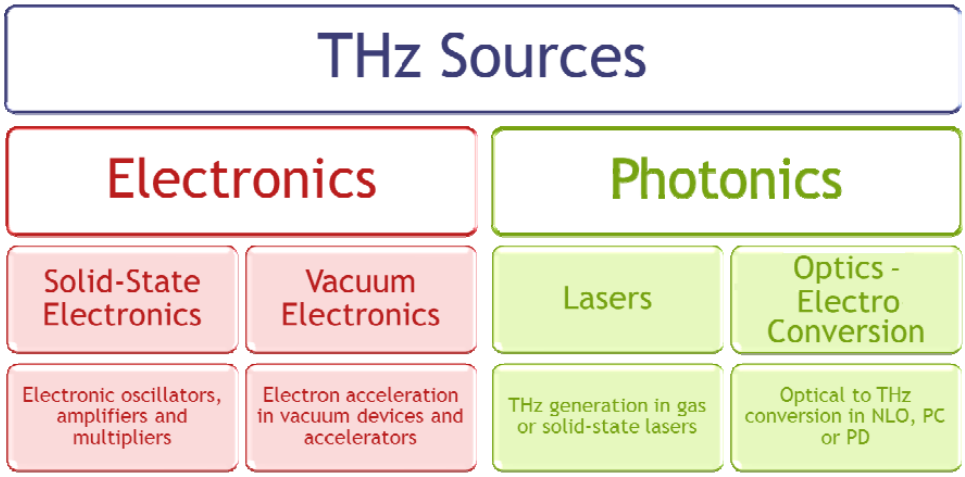

Figure 1.6: Classification of THz sources [1.33].

1.3.1 THz generation with electronic techniques

For the conventional electronic techniques, vacuum electronics and solid-state electronics are the major approaches for THz generation, which are already well established at low frequencies. In the past more than 100 years, the vacuum tube has evolved from kHz to THz and from mW to MW [1.34]. Vacuum electronic devices convert electrical stored energy into kinetic energy of an accelerated electron beam, which is then converted into electromagnetic field energy with the aid of electromagnetic waveguides or cavities [1.35]. Vacuum electronic sources are the practical solution for high power THz sources covering 0.1 THz to several THz radiation [1.34] - [1.38]. Vacuum electronic source includes backward wave oscillators (BWOs) [1.39], free electron lasers (FELs) [1.40] and Gyrotrons [1.41]. Gyrotron is the most powerful source in the THz region and can produce average power up to 600 kW under CW operation at the frequency of 170 GHz [1.42]. With the magnetic field intensity of 9.2 T, Gyrotron can emit 200 W at 203 GHz

and 50 W at 395 GHz, reported in [1.43]. Increasing the magnetic field intensity to 20 T, Gyrotron achieved more than 10 W output power at 1.014 THz by using second harmonics in CW operation mode [1.44]. BWOs are tuneable and relatively low cost due to no need to use either a high magnetic field or a large accelerator facility, and its output power are lower than Gyrotron and FEL. A wide frequency range can be tuned by adjusting the electron beam voltage to alter the synchronous frequency. In [1.45], a BWO generated a maximum power of 20 W over a frequency range of 186 GHz - 202 GHz, with an average power of around 30 mW. BWOs can produce the level of several mW power at the frequency of 1 THz, reported in [1.46]. A novel BWO was reported with output power of 1 W range at 346 GHz in [1.47], by adopting two different topologies of slow-wave structures, the double-staggered grating and the double-corrugated waveguide. The FEL produces coherent radiation from a beam of free electrons with wider frequency tuning range at high operating frequencies. CW FEL based on an accelerator-recuperator is capable of produce max average power of 400 W at the frequency of 1.28 - 2.73 THz [1.48]. In [1.49], a CW tuneable FEL was reported providing the max output power of 580 W at 469 GHz and 1.09 kW at 1.29 THz, with the complete system occupying an area less than 4 x 7 m^2.

Although vacuum electronic sources are tuneable and can provide high power CW THz beams up to several THz, they are power-hungry, large, heavy and expensive. They are mainly used for fundamental science and laboratory applications. Even for the compact sub-THz Gyrotron (FU CW CI), developed for application to the 600 MHz DNP-NMR spectroscopy (with the output power of 31 W at 394 GHz), its height was reported 1.3 m and the total floor area was about 1 × 3 m^2, with the accelerating voltage of 15 kV [1.50]. The novel design of THz BWO in [1.47] was reported have compact dimensions of 200 - 300 cm^3 and weight of around 4.5 kg, obtaining a beam voltage of 17.4 kV and a current of 14 mA. The compact advanced FEL source from ENEA-Frascati for the spectroscopic measurement, working between 0.3 and 0.7 THz frequency, is an example of compact FEL. It is a laboratory scale device which can fit into a space of 2 m^3 [1.51]. Obviously, even for these compact vacuum electronic sources, they are high power consumption (more than hundreds of Watts) and too big for practical wireless communications. Below Table 1.1 gives a quick indication to

show vacuum electronic sources comparing with figures of merit desired in high-speed wireless communications.

Table 1.1: Vacuum electronic sources compare with figures of merit desired in high-speed wireless communications (the values in the table are examples)

Technology	Compact	Tuneable	Room temperature	Power consumption	Output Power	Power efficiency	Frequecy range	Solid state	Ref
Gyrotrons	1 x 3 x 1.3 m^3	●	●	3300 W	31 W	0.93% @ 394 GHz	0 - 1 THz	●	[1.50]
BWO	200 - 300 cm^3 4.5 kg	tens of GHz	●	243.6 W	1 W	0.41% @ 346 GHz	0 - 1 THz	●	[1.47]
FEL	area: 4 x 7 m^2	0.4 - 1.2 THz	●	180 kW	CW: 580 W	0.32% @ 469 GHz	0 - 3 THz	●	[1.49]
	area: 1 x 2 m^2	0.5 - 1.5 THz	●	4 MV	pulse: 1 W (average)	NA		●	[1.51]

Solid-state sources have already well established at low THz frequencies, including InP-based tunnel injection transit time (TUNNETT) diodes, impact avalanche transit time (IMPATT) diodes, Gunn diodes, and resonant tunnelling diodes (RTDs). TUNNETT, IMPATT and Gunn diodes can work up to 500 GHz, and RTDs have exhibited the highest oscillation frequency up to 2 THz. All of the four types oscillators are differential negative resistance devices, and their difference is at how the negative differential resistance is achieved. TUNNETT diodes on diamond heatsink have achieved 140 µW at 350 GHz [1.135]. IMPATT diodes have shown high CW powers up to 361 GHz: 78 mW at 185 GHz, 7.5 mW at 285 GHz, and 200 µW at 361 GHz [1.52]. Due to the avalanche process, IMPATT diodes are noisy and their efficiency decreases quickly at higher frequencies. InP-based third-harmonic mode Gunn diodes with output power of 85 µW at 479 GHz (with a power consumption of up to 1 W) [1.53] and RTDs with 7 µW output power at 1.04 THz [1.54] have been fabricated.

Besides the fundamental oscillators, another useful type of solid-state sources to bridge the THz gap is frequency multipliers, which utilize the reactive and/or resistive nonlinearity of the diode and translate a signal of lower frequency to a higher harmonic frequency while suppressing undesired ones. By providing appropriate embedding impedances at each integer multiple of the input frequency, it is possible to design frequency doublers, triplers, or even quintuplers.

The GaAs Schottky barrier diode (SBD) is the dominant technology for terahertz frequency multipliers [1.136]. In [1.55], a 190 GHz Schottky-diode high power input frequency doubler was presented. High thermal conductivity AlN was adopted as the circuit substrate, and the 6-anode Schottky diode doubler was reported to handle up to 260 mW input power. The maximum output power was measured to be 20 mW at 193 GHz with the peak efficiency of 8%. Based on a novel patented circuit topology [1.56] and precise optimization for high power operation [1.57], Jet Propulsion Laboratory reported high output power of all-solid-state frequency multiplied THz sources in the 160 GHz - 1.6 THz range. The measured output power levels at room temperature were 500 mW at 180 GHz (30% peak efficiency), 110 mW at 220 GHz (21% peak efficiency), 35 mW at 330 GHz (14% peak efficiency), 30 mW at 530 GHz (9% peak efficiency), 2 mW at 1.03 THz (5% peak efficiency), and 0.7 mW at 1.64 THz (3.5% peak efficiency) [1.137].

Though RTD, IMPATT, Gunn and TUNNETT are compact and room temperature operation, they have limited frequency tuneability. RTD has 70 GHz tuning range at 655 GHz [1.58], IMPATT has 86 GHz tuning range at 500 GHz [1.59] and Gunn has no tuneable effect when DC bias is less than 8V [1.60]. Gunn and TUNNETT have very lower power efficiency: 0.92 W DC power generating 85 μW power at 479 GHz (0.01% power efficiency) [1.61] and 0.65 W DC power producing 140 μW power at 355 GHz (0.022% power efficiency) [1.135], respectively. RTD and IMPATT have better power efficiency, but lower than UTC-PDs, see Figure 1.7. It is better to use $\eta_{THz} = \frac{P_{THz}}{P_{opt}^2}$ for UTC-PD's power efficiency. As there is no optical power input for solid-state sources, $\frac{P_{THz}}{P_{ele}}$ is used to calculate power efficiency in Figure 1.7 in order to making comparison between UTC-PDs and solid-state sources. Among them, only RTD had been reported used as transmitter in THz wireless communications: 11 Gb/s data rate at 344 GHz frequency was reported in [1.62] and 2.5 Gb/s at 300 GHz frequency was reported in [1.63]. For frequency multipliers, considering the minimum sizes of waveguide blocks and the need for complex biasing circuits, they are not ideal for wireless communications which prefer compact transmitters less than cm^3.

Below Table 1.2 gives a quick indication to show solid-state sources comparing with figures of merit desired in high-speed wireless communications.

Table 1.2: Solid-state sources compare with figures of merit desired in high-speed wireless communications (the values in the table are examples)

Technology	Compact	Tuneable	Room temperature	Power consumption	Output Power	Power efficiency	Frequecy range	Solid state	Ref
RTD	●	70 GHz @ 655 GHz	●	32 mW	40 µW	0.13% @340 GHz	0 - 2 THz	●	[1.58]
IMPATT	●	86 GHz @ 500 GHz	●	2.1 W	7.5 mW	0.35% @ 285 GHz	0 - 0.5 THz	●	[1.59]
Gunn	●	non-tuneable @ bias < 8V	●	0.92 W	85 µW	0.01% @ 479 GHz	0 - 0.5 THz	●	[1.61]
TUNNETT	●		●	0.65 W	140 µW	0.022% @ 355 GHz	0 - 0.5 THz	●	[1.135]
Frequency multipliers	16 x 12 x 3 cm^3	70 GHz @ 525 GHz	●	2.0 W	35 mW	1.75% @ 526 GHz	0 - 3 THz	●	[1.137]

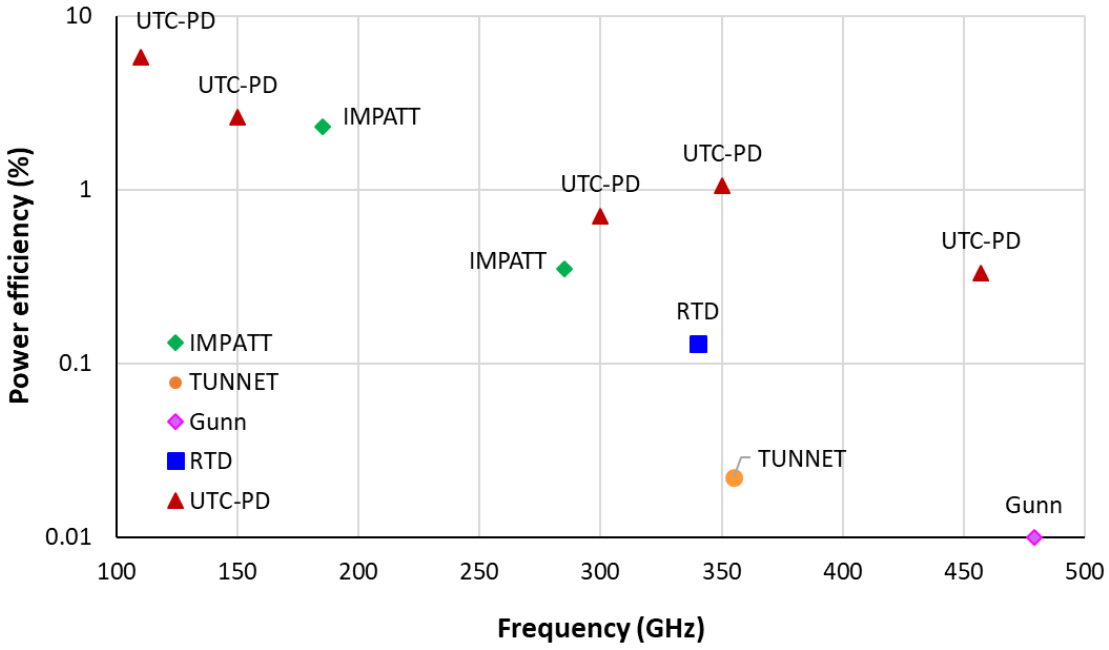

Figure 1.7: Power efficiencies of RTD, IMPATT, Gunn and TUNNETT, compared with UTC-PDs.

1.3.2 THz generation with photonic techniques

Photonic generation of THz radiations, spearheaded THz research for the past few decades, falls into two general categories: using lasers (QCL, gas lasers, p-Ge laser, etc) and using opto-electronics conversion photodiodes.

1.3.2.1 THz lasers (QCLs, Gas lasers and p-Ge lasers)

Semiconductor-based THz QCLs developed around 30 years ago and are still being refined. The THz waves are emitted by means of electron relaxation between sub-bands of quantum wells. The three main operational methods are 'bound-to-continuum' [1.64], 'interlaced' [1.65], and 'resonant phonon' [1.66]. They are different at the mechanism by which the electrons scatter after the THz-photon emission from the population inversion [1.67]. The implementation of actual devices requires compact, portable and all-solid-state THz sources, and QCLs belong to this category. The first QCL was reported by Bell Labs in 1994 with the output frequency of 75 THz (4.2 μm wavelength) and the peak power in excess of 8 mW in pulsed operation [1.68], but did not lase in CW mode. After a decade of research effort, QCL operating at 4.4 THz was demonstrated in 2002 [1.69], with an output power of more than 2 mW at low threshold current densities up to 50 K, still working in pulse mode. With continuous development efforts on multiple-quantum-well gain medium and the waveguide, THz QCLs have shown remarkable performances over the 1 - 5 THz range. In [1.70], the maximum emitted power was around 1.01 W at 10 K (420 mW at 77 K) in pulsed mode at a frequency of 3.4 THz. In [1.71], the device shows magnetic field assisted laser action at 1 THz at temperatures up to 215 K, and 3 THz lasing up to 225 K, owing to the suppression of inter-Landau-level non-radiative scattering. The maximum 1 THz power at 20.5 T was estimated to be at least 1 - 2 mW in pulse mode. However, the reported output power of THz QCL in CW mode is still relatively low and working at lower temperature, limiting its application in imaging, spectroscopy, etc. That is because for the lasers working in CW mode, the electrical power consumption of the laser is higher than working in pulse mode, increasing the laser's self-heating and resulting in the degradation of the gain. Research endeavours have been put on improving the CW output power of THz

QCLs. Based on a resonant-phonon depopulation scheme and by using a semi-insulating surface-plasmon waveguide, [1.72] reported QCLs lasering at 4.4 THz at heatsink temperatures of 10 K, with CW output power of 138 mW and pulse output power of 248 mW. In [1.73], THz QCLs with high output power up to 0.23 W (at 3.11 THz) in CW mode at 15 K were demonstrated, achieving a low threshold current density of 270 A/cm^2 and a high wall-plug efficiency of 0.64% in 2.9 mm long device. To obtain wider applications, the current research objectives are to reduce the threshold currents and lasing frequencies, increase the operational temperatures and the range of tuneable frequencies [1.67].

Optically pumped gas lasers produce high power THz radiation using the rotational transitions of heteropolar molecules in the gas phase, but with the cost of size and power consumption. The lasing frequency is determined by the filling gas, achieving the output power of 1.25 W with methanol at 2.52 THz under the CO_2 laser pump power of 125 W [1.74]. The majority of the pump radiation is converted to heat, making the lasing process is quite inefficient. Typical efficiency of converting pump radiation into THz radiation is on the order of 0.2%, and the best efficiency reported is 1% for high power operation [1.75], [1.76]. Besides, large cavities and kW power supplies are typically required [1.77].

p-type Ge laser [1.78] is another type of THz laser, which can be tuned between 1 and 4 THz. Research on Ge laser focuses on two mechanisms: the first is based on hole population inversion between the light and heavy hole Landau levels in crossed electric and magnetic fields at cryogenic temperatures (up to 80 K); the second mechanism is to lift the degeneracy in the valence band by applying a compressive force to the germanium crystal, and the laser emission frequency can be tuned by adjust the applied uniaxial stress. For the first mechanism lasers, intervalence band (IVB) lasers, they have relatively low gain (0.01 – 0.03 cm^{-1}) due to low pumping rate [1.79]. Though the gain is low in IVB Ge lasers, they can emit quite high output power. In [1.80], a 30 x 4 x 3 mm^3 Be-doped Ge laser, with a doping concentration of 1.1 x 10^{14} cm^{-3}, was reported reaching a high output power of more than 1W in the frequency range between 2.43 THz and 2.88 THz, with 4 μs voltage pulses of around 500 V applied to the laser crystal, perpendicular to a magnetic field of 1.2T. As the applied high bias current leads to the intensive heating inside the Ge crystal, pulse voltage and cooling

equipment are required to maintain the system working. Therefore, it is hard to obtain the CW operation in this mechanism. However, the CW operation can be realised in Ge lasers based on the second mechanism. In [1.81], experimental results of CW THz radiation by strained Ge were presented. The measured THz emission at the main peak frequency of around 2.5 THz was at least tens of μW, with 3.9 kbar strain applied along the [100] axis in Ge crystal. Only 2 V and 5 mA of DC bias was required to obtain lasing at 2.5 THz. Therefore, the stressed Ge laser has the feasibility of realizing a high-efficient, compact CW THz laser.

For the THz lasers discussed above (QCL, Gas lasers and p-Ge lasers), they have a big advantage than electronics THz sources when considering long distance data transmissions: compatibility with photonic components and optical fibre networks. Though all of the 3 types THz lasers are tuneable and can provide high output powers up to watt, it is very difficult for them to lase below 0.5 THz, the frequency range targeted for high-speed wireless communications. We desire room temperature operation, portability and low power supply devices for public wireless networks, however, QCLs need cooling system to maintain the continuous emission, reported cooling temperature covering the temperature range from 10 K to 255 K. Even for the QCL with compact Stirling cooler (model K535 from Ricor) [1.82], whose maximum output power was 8 mW at 3.1 THz with the corresponding input electrical power of 5.0 W, its cryocooler weighed 9.5 kg and had the dimensions of 32.1×13.9×27.4 cm^3, and consumed 220 W power to cool the QCL down to 58 K. Gas lasers can operate at room temperature, but they are not all-solid-state THz sources, containing a gas cavity. Gas THz lasers are not continuously tuneable, and typically require large cavities and at least a dozen of Watts of input power. Even the compact CO_2 laser pumped THz gas laser, reported in [1.75], is the size of a large shoe box (47x 17.1 x 17.1 cm^3) and consumed an electrical power of around 60 W, with an output power of 10-15 mW at 2.5 THz. Its corresponding power efficiency was about 0.02%, while the typical gas laser efficiencies are in the range of 0.001 - 0.1 %. For p-Ge lasers, the first mechanism radiation (IVB lasers) need cooling system and hard to realise the CW operation. The second mechanism laser (under uniaxial stress) can obtain CW radiation with low power supply, but the required stress controlling adds complexity to the laser system. Therefore, for currently interested sub-THz range

for wireless communications, all of the three THz lasers are not good candidates. Below Table 1.3 gives a quick indication to show THz lasers comparing with figures of merit desired in high-speed wireless communications.

Table 1.3: THz lasers compare with figures of merit desired in high-speed wireless communications (the values in the table are examples).

Technology	Compact	Tuneable	Room temperature	Power consumption	Output Power	Power efficiency	Frequecy range	Solid state	Ref
QCL	0.02 m^3, 12.1 kg	●	●	Laser: 5 W cooling: 220 W	8 mW	0.16% @ 3.1 THz	1 - 5 THz	●	[1.82]
Gas lasers	47x17.1x17.1 cm^3	discrete emission	●	60 W	10 - 15 mW	0.02 % @ 2.5 THz (typical < 0.1 %)	0.5 - 5 THz	●	[1.75]
p-Ge lasers	●	●	●	10 mW	tens of µW	0.1 % - 0.5 % @ 2.5 THz	2 - 10 THz	●	[1.81]

1.3.2.2 Opto-electronics conversion photodiodes

Photomixing, also known as optical heterodyne down conversion, is a technique to generate CW THz radiation with photodiodes or photoconductive switches. In THz photomixers, two coherently interfering optical modes generated by two single-mode lasers are absorbed in a photoconductive material, and time varying carrier densities (electrons and holes) are generated by exciting the electrons from valance band into conduction band. Under the applied electric field, the free carriers are accelerated and the THz wave is generated with its frequency equal to the difference of the two optical frequencies [1.83], [1.84]. The frequency of the THz signal can be tuned by adjusting the wavelengths of the two optical wavelengths. This type of THz source can continuously generate sub THz / THz radiation over a wide frequency range, from tens of GHz to several THz.

State-of-the-art photomixers are based on either GaAs or InGaAs/InP and require laser wavelengths below the semiconductor bandgap. So far, the photoconductor consisting of an interdigitated electrode capacitance on a low-temperature-grown GaAs (LT-GaAs) layer is the simplest photomixer. However, for almost twenty years, the output powers in the THz frequency ranges generated by LT-GaAs photoconductor are below tens µW. In [1.85], CW output powers of 1.2 mW at 50 GHz and 0.35 mW at 305 GHz were presented by photomixing in a low

temperature grown GaAs photoconductor, thanks to a metallic mirror-based Fabry-Perot (FP) cavity and deep submicron electrode spacing. To further increase output powers at sub-THz region, an impedance matching circuit was designed to realise 1.8 mW at 252 GHz on LT-GaAs photoconductors with the input optical power of 270 mW [1.86]. Even with the help of FP cavity, the responsivity of this type of photoconductor only reached 0.13 A/W.

The other main type of photomixer is InGaAs/InP photodiodes, which have two main types of structures: PIN-PDs and UTC-PDs. For the conventional PIN-PDs, both of electrons and holes contribute to the photocurrent response, and the low velocity of hole transport dominates the performance. Compared with surface-illuminated PIN-PDs, side-illuminated waveguide PIN-PDs improves their bandwidth, but with the sacrifice of quantum efficiency. In [1.87], experimental results at 1.55 μm wavelength showed that the multimode waveguide PIN-PDs with mushroom-mesa structure had an electrical 3 dB bandwidth of more than 75 GHz, with the external quantum efficiency is 50% or 0.63 A/W responsivity. 200 μW at frequency around 50 GHz and 1.4 μW at 1 THz were reported in [1.88], which are much lower than UTC-PDs' output power reported in [1.89], 2 mW at 60 GHz. Partially-doped absorber photodiode (PDA-PD), in which depleted and undepleted absorbers are used, operates with lower hole density than PIN-PDs and can obtain higher photocurrent. In [1.90], an 8 μm diameter backside-illuminated PDA-PD was reported having a responsivity of 0.67 A/W, with an 880 nm thick $In_{0.53}Ga_{0.47}As$ absorption region consisting of a depletion layer and graded n-type and p-type undepleted injection regions. This structure achieved a saturation current of 22 mA at the bandwidth of 45 GHz and an output power of 5 mW at 50 GHz. To increase the bandwidth and quantum efficiency, [1.91] incorporated the partially p-doped absorption layer with the evanescently edge-coupled waveguide structure in the photodiode (active areas is 150 μm^2), achieving high responsivity of 1.01 A/W, bandwidth of 50 GHz, and RF output power over 6.5 dBm with a photocurrent of 23 mA at 40 GHz operating frequency (biased at -5V). Another structure to ease the space charge limitation is dual depletion region photodiode (DDR-PD), where absorbed and non-absorbed intrinsic layers are combined. Optimizing the illumination condition to reduce the space-charge screening effect in the DDR photodiodes, a graded-index (GRIN)

lens coupling light from a SMF pigtail to a top illuminated DDR-PD was reported in [1.92]. An output power of 7.5 dBm at 10 GHz was demonstrated on 50 μm diameter photodiodes, with the photocurrent of 45 mA at -7V bias voltage. Waveguide photodiodes (WG-PD) are effective to increase the bandwidth compared with vertically illuminated photodiodes. But, they are normally designed without considering the propagation of electrical waves to the connected load, which results in the reflections in the device bring the entire junction area have an impact on the device response [1.93]. Travelling-wave photodetector (TW-PD) is a WG-PD with an electrode structure designed to support travelling electrical waves with characteristic impedance matched to that of the external circuit [1.94], whose bandwidth limitation doesn't depend on the total junction area, depending on the mismatch between optical group velocity and electrical phase velocity. The first fabricated TW-PD was reported in [1.93], with bandwidth as high as 172 GHz and bandwidth-efficiency products as large as 76 GHz, which had 50% larger bandwidth than WG-PDs or vertically illuminated photodiodes fabricated on the same wafer.

In UTC-PDs, the generated low mobility holes don't travel across the collection layer. As majority carriers in the absorption layer, they respond within the dielectric relaxation time, which for p-$In_{0.53}Ga_{0.47}As$ 1×10^{18} cm^{-3} can be as short as 33 fs [1.95]. Therefore, only photo-generated electrons cross the collection layer and contribute to the UTC response [1.96]. As electrons exhibit velocity overshoot in the carrier collection layer, their velocity (3 - 5×10^{7} cm/s) is 6 - 10 times higher than that of holes (5×10^{6} cm/s), and UTC-PDs have a larger bandwidth than conventional PIN-PDs. In addition, UTC-PDs have higher saturation current due to the reduced space charge effect in the depletion layer, which also benefits from the high electron velocity in UTC-PDs [1.96]. These properties make UTC-PDs high speed and high output power photodiodes. Through continuous optimisation in semiconductor layer structures and improvement in thermal management, UTC-PDs' output power and bandwidth have been much improved since the first devices were proposed in 1997 [1.95].

Though vertically illuminated UTC-PDs have shown improved 3dB bandwidth than PIN-PDs, their geometry requires a stringent trade-off between responsivity and bandwidth. For the normal-incidence structure, high responsivity requires a

thick absorption layer, which results in increased carrier transit time and reduced device bandwidth. Therefore, the design of vertically illuminated UTC-PDs is widely used at lower RF frequency (tens of GHz). An output power of 0.75 W (28.8 dBm) at 15 GHz from a vertically illuminated modified UTC (MUTC) was demonstrated in [1.97] for a saturation current greater than 180 mA and a reverse bias of 11 V. In waveguide UTC-PDs, the trade-off between responsivity and bandwidth can be eased significantly. As light travels perpendicular to the epitaxial layer direction in waveguide devices, it is evanescently coupled from the passive waveguide into the absorption layer. As a result, for a given device area and epitaxial structure, a waveguide coupled UTC-PD can exhibit wider bandwidth and higher output power than a vertically illuminated UTC-PD at high frequency [1.98], [1.99]. For InP membrane-based double-sided processing waveguide UTC-PDs, a responsivity of 0.7 A/W at 1.55 μm with a 3dB bandwidth beyond 67 GHz were presented in [1.100]. The record RF output power of 10 dBm at 110 GHz was achieved by this edge-coupled waveguide design, with the responsivity of 0.36 A/W at 36 mA photocurrent [1.98]. A high-power and broadband photomixer module was fabricated and evaluated in [1.101], where a short-stub is integrated with the PD chip to increase the output power at around the designed centre frequency of 350 GHz. This short stub integrated UTC-PD exhibited a 10dB bandwidth of about 300 GHz and its maximum output power of -2.7 dBm (0.53 mW) at 350 GHz. Waveguide coupled UTC-PDs are also compatible with the implementation of Travelling-Wave design [1.102] which can substantially improve the device RC limited response. In [1.103], the output power of CPW coupled Travelling-Wave UTC-PD (3 x 25 μm^2) was measured with 2.4 mW at 150 GHz and 1 mW at 200 GHz at a photocurrent of 23 mA.

To radiate sub-microwave signals from a photodiode, monolithically integrating photodiodes with planar antennas [1.04] is a promising way because it eliminates the reflection and loss in transmission lines. The antenna integrated UTC-PDs can be catalogued into two types: wideband antenna integrated UTC-PDs and narrowband antenna integrated UTC-PDs. Though the narrowband antenna sacrifices the bandwidth, the applying of a resonant matching circuit is an effective way to attain higher RF output power. In [1.105] broadband and narrowband antennas were designed to couple THz output power of Travelling-

Wave UTC-PD to free-space. Resonant antenna integrated devices resulted in two narrowband emission peaks at 457 GHz and 914 GHz, achieving high emission power of 148 μW and 24 μW respectively, at a photocurrent of 13 mA. For devices integrated with bow-tie antennas, broadband emission was obtained, with 105 μW at 255 GHz, 30 μW at 408 GHz, 16 μW at 510 GHz and 10 μW at 612 GHz with a photocurrent of 13 mA [1.105]. In [1.103], the bow tie antenna integrated Travelling-Wave UTC-PDs showed radiated RF power of 5 μW at 1.02 THz and 0.5 μW at 1.53 THz with an input optical power of less than 40 mW. In [1.106], wideband and narrowband antenna-integrated UTC-PDs were fabricated and characterized. Both of them had the absorption area of 13 μm^2, and were placed on a hyper-hemispherical Si lens. The maximum output power was 2.6 μW and 10.9 μW at 1.04 THz, with a photocurrent of 13 mA, for the log-periodic antenna-integrated UTC-PD and twin-dipole antenna- integrated UTC-PD respectively. By adjusting the twin-dipole antenna configuration, an output power of 1.2 μW was measured at 1.53 THz, at the photocurrent of 8 mA and bias voltage of -2V. An edge-illuminated double-mesa UTC-PD with a hybrid (neutral and depleted) absorber was reported in [1.107], with a 3 x 7 μm^2 junction area and integrated with a 90-degree broadband bow-tie antenna. The UTC-PD chip was packaged in a pig-tailed module with a hemispherical Si lens, and the radiated THz power was measured by Golay cell. The detected output power was 100 nW at 2 THz and 40 nW at 2.5 THz, and the module was operated at a photocurrent of 6 mA with bias voltage of -0.4V.

Comparing with electronic THz sources (Section 1.3.1) and photonic THz lasers (Section 1.3.2.1), above discussed photomixers meet all of the figures of merit desired in high-speed wireless communications (room temperature operating, solid-state, compact, tuneable, low power consumption), and compatible with optical fibre networks, a brief comparison shown in Table 1.4. The output power of above mentioned opto-electronic conversion photodiodes and their power efficiency (the ratio of RF output power to consumed electrical input power) are illustrated in Figure 1.8. It shows: 1) For the RF output power performance, PDA-PDs and DDR-PDs can effectively improve the RF output power of PIN-PDs, as the field modulation is relaxed by minimizing the space-charge effect from hole transport. But their output powers are still lower than UTC-PDs; 2) For the power

conversion efficiency, UTC-PDs performs better than other types of photodiodes; 3) For antenna integrated UTC-PDs, UTC-PDs with resonant antenna have higher output power and better power efficiency than broadband antenna integrated UTC-PDs. Overall, opto-electronics conversion photodiodes are more suitable working as transmitters of sub-THz wireless communications, compared with other THz sources (vacuum electronic devices, solid-state sources and THz lasers). Among the group of photomixing photodiodes, the UTC-PD shows the best performance and it is a promising candidate for future high-speed wireless communications. The next Section 1.4 presents the methods having been reported to improve the output power of UTC-PDs.

Table 1.4: Photodiodes compare with vacuum electronic devices, solid-state sources and THz lasers (the values in the table are examples).

Technology		Compact	Tuneable	Room temperature	Power consumption	Output Power	Power efficiency	Frequecy range	Solid state	Optical network compatible
Electronic technology	Vacuum electronic devices	Gyrotrons	1 x 3 x 1.3 m^3	●	●	3300 W	31 W	0.93% @ 394 GHz	0 - 1 THz	●	○
		BWO	200 -300 cm^3 4.5 kg	tens of GHz	●	243.6 W	1 W	0.41% @ 346 GHz	0 - 1 THz	●	○
		FEL	area: 4 x 7 m^2	0.4 - 1.2 THz	●	180 kW	CW: 580 W	0.32% @ 469 GHz	0 - 3 THz	●	○
			area: 1 x 2 m^2	0.5 - 1.5 THz	●	4 MV	pulse: 1 W (average)	NA		●	○
	Solid-state sources	RTD	●	70 GHz @ 655 GHz	●	32 mW	40 µW	0.13% @340 GHz	0 - 2 THz	●	○
		IMPATT	●	86 GHz @ 500 GHz	●	2.1 W	7.5 mW	0.35% @ 285 GHz	0 - 0.5 THz	●	○
		Gunn	●	non-tuneable @ bias < 8V	●	0.92 W	85 µW	0.01% @ 479 GHz	0 - 0.5 THz	●	○
		TUNNETT	●		●	0.65 W	140 µW	0.022% @ 355 GHz	0 - 0.5 THz	●	○
		Frequency multipliers	16 x 12 x 3 cm^3	70 GHz @ 525 GHz	●	2.0 W	35 mW	1.75% @ 526 GHz	0 - 3 THz	●	○
Photonic technology	THz lasers	QCL	0.02 m^3, 12.1 kg	●	○	Laser: 5 W cooling: 220 W	8 mW	0.16% @ 3.1 THz	1 - 5 THz	●	●
		Gas lasers	47x 17.1 x 17.1 cm^3	discrete emission	●	60 W	10 - 15 mW	0.02 % @ 2.5 THz (typical < 0.1 %)	0.5 - 5 THz	○	●
		p-Ge lasers	●	●	●	10 mW	tens of µW	0.1 % - 0.5 % @ 2.5 THz	2 - 10 THz	●	●
	Photodiodes	LT-GaAs	●	●	●	83.4 mW	1.2 mW	1.44% @ 50 GHz	0 - 2 THz	●	●
		PIN-PD	●	●	●				0 - 2 THz	●	●
		PDA-PD	●	●	●	115 mW	4.5 mW	3.91% @ 50 GHz	0 - 2 THz	●	●
		DDR-PD	●	●	●	315 mW	5.6 mW	1.78% @ 10 GHz	0 - 2 THz	●	●
		TW-PD	●	●	●				0 - 2 THz	●	●
		UTC-PD	●	●	●	1.98 W	0.75 W	37.9% @15 GHz	0 - 2 THz	●	●
						10 mW	72 mW	13.9% @ 110 GHz			

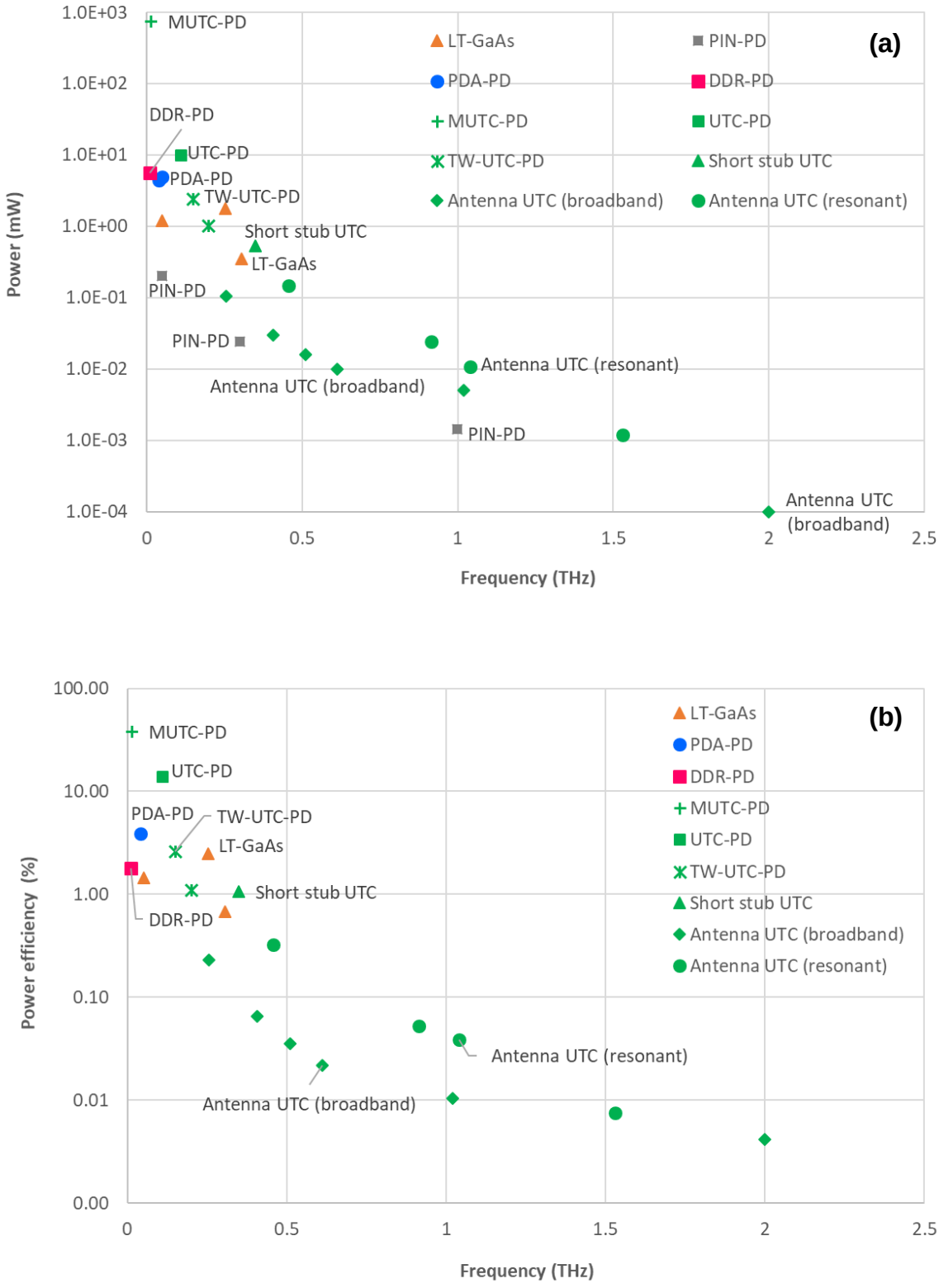

Figure 1.8: (a) the output power of electro-optics photodiodes as a function of frequency, (b) the power conversion efficiency of photodiodes at different frequencies.

1.4 High power UTC-PDs

High speed UTC-PDs with high output power (better SNR) can effectively improve the performance of THz communication systems. Wireless transmission distance will be lengthened with increasing the output power of UTC-PDs. For photodiodes, high output power requires high photocurrent. For the structure of UTC-PDs, two major factors influencing saturation photocurrent are space charge screening and thermal effects. In UTC-PDs, the space charge effect usually occurs at the junction of absorption and collection layers [1.108], [1.109], reducing the total internal electric field in the depletion region and slowing down electrons' drifting velocity. As a result, carrier drift time increases and output photocurrent saturates. Thermal limitation comes from the low thermal conductivity of materials comprising UTC-PD epitaxy layers, which prevents the Joule heat (coming from input optical light and applied electrical power) to get out of UTC-PDs, and results in high temperatures inside devices. The high temperature reduces electrons' mobility and increases their transit time, which causes the RF power saturations. Therefore, mitigating these two effects will be helpful to improve the output power of UTC-PDs. Besides optimising UTC-PD's structure, improving the input optical power coupling (between optical fibre and UTC-PDs), or improving the output RF power coupling (between UTC-PDs and antenna) can also benefit the output power of UTC-PDs. In addition to the efforts of optimizations on individual UTC-PD, combining the photocurrent or the output power from multiple devices is another option to achieve higher THz output power. In the following, five aspects are discussed regarding increasing the output power of UTC-PDs: epitaxy structure optimisation, thermal management, optical coupling, RF coupling and UTC-PDs array.

Epitaxy Structure Optimisation

In order to reduce the space charge effect, structure design optimisations have been reported to increase the output power of UTC-PDs. **a)** Modified UTC-PD (MUTC-PD): optimize the absorption and collection layers by using a partially p-doped absorption regions (0.25 μm n-doped InGaAs layer followed by a 1.25 μm p-doped InGaAs layer) and non-uniformly doped collection layer, to improve

frequency response and reduce space charge effects. High output power of 20 dBm at 10 GHz for 25 μm diameter device was reported in [1.110]. **b)** Charge-Compensated MUTC PD (CC-MUTC PD): back-illuminated photodiodes utilize a cliff layer to achieve higher output power by providing higher electric field in the undepleted InGaAs absorber region, enabling higher photocurrent before space charge effect induces saturation. The output power of 22.7 dBm has been achieved at 24 GHz for 34 μm diameter photodiode [1.111]. **c)** Novel design for the collector layer UTC-PD (N-UTC-PD): by inserting an n-type charge layer of proper thickness and doping density into the collection layer of UTC-PDs, the space charge screening is effectively suppressed without the need for an increased reverse bias voltage. Combined with the advanced flip-chip bonding structure, high power THz operation with 0.17 dBm at 280 GHz was realised by a miniaturized 3 μm diameter device [1.112]. **d)** Near-ballistic UTC-PD (NBUTC-PD): by inserting an additional p delta-doped layer in the collector of a traditional UTC-PD, near-ballistic transport can be achieved under high reverse bias voltage [1.113]. For 16 μm^2 size device, 6.12 dBm output power at 170 GHz was reported in [1.114].

In order to achieve high bandwidth and high responsivity at the same time, the breakthrough traveling wave design of UTC-PDs was brought out [1.103], [1.105]. Travelling wave structure is a structure that the optical signal travels at a velocity (phase velocity) comparable to that of the electrical signal along the waveguide electrodes. A waveguide placing immediately adjacent to the carrier collection layer enables evanescently light coupling to the active waveguide (the absorption layer). The use of travelling wave techniques allows the thickness of the absorber, which determines the electron transit time, to be reduced and thus enlarges the bandwidth further. The traveling-wave UTC-PD (TW-UTC-PD) integrated with resonant antenna achieved high THz output of 148 μW at 457 GHz and 24 μW at 914 GHz [1.105], [1.115].

Thermal Management

For dissipating the Joule heat inside UTC-PDs, the technique of flip-bonding UTC-PDs onto high thermal conductivity sub-mounts has been implemented to enhance thermal management. **a)** AlN submount: modified UTC-PD was flip-chip

bonded on AlN submount. In [1.97], the thermal modelling predicted that flip-chip bonding to AlN resulted in ~70% improvement in the thermal limit, and the maximum dissipated power density of the photodiodes was increased 65% to 90% [1.116]. The RF output power of 28.8 dBm, 25 dBm and 19 dBm at 15 GHz, 25 GHz and 30 GHz respectively were reported in [1.97], [1.116], with diameter of 40 μm, 28 μm and 20 μm MUTC-PDs flip-chip bonded on AlN sub-mount. **b)** Diamond sub-mount: InP/InGaAs MUTC-PD was flip-chip bonded on diamond sub-mount with high RF output powers of 32.7 dBm, 29.6 dBm, 28.2 dBm, and 26.2 dBm at 10 GHz, 15 GHz, 20 GHz, and 25 GHz respectively, without the external cooling system [1.117]. The failure power density on the diamond sub-mount was 300% and 50% higher than that of photodiodes without flip-chip bonding and bonded to AlN sub-mount, respectively [1.117]. **c)** Silicon sub-mount: top illuminated UTC-PD wafer was bonded to Si sub-mount using a gold intermediate layer. Its maximum dissipated power was more than 1.5 times higher than that of the same photodiode on InP substrate. The maximum output RF power was improved from 14 dBm to 16 dBm at 10 GHz (diameter = 20 μm) [1.118].

Optical Power Absorption and Coupling

In order to improve the responsivity of UTC-PDs without sacrificing the bandwidth, research has been focused on two main challenges: increasing light absorption by integrated with reflectors for vertical illuminated UTC-PDs, or improving light coupling efficiency between fibre and the absorber for waveguide UTC-PDs. For vertical illuminated UTC-PDs, the device's responsivity was improved by introducing a metallic mirror below the diode mesa through wafer bonding [1.119], producing an optical resonant cavity to enhance the optical power absorption. The responsivity was reported be improved by more than 3 times compared to the device of same epitaxial structure without metallic mirror. In [1.120], UTC-PDs were bonded to high-reflectivity distributed Bragg reflector mirrors (HR-UTC-PD) grown on S.I. GaAs substrate. The fabricated 40 μm diameter HR-UTC-PD exhibited a responsivity of 0.88 A/W at 1560 nm with -3V bias voltage, and a 3 dB bandwidth of 13.87 GHz with a saturation current of 50 mA at 1550 nm. For waveguide UTC-PDs, by integrating with spot-size converter on one chip, UTC-

PDs with the responsivity of 0.5 A/W and the RF output power of 5.1 dBm at 120 GHz (saturation current was measured to 30 mA) were reported in [1.121], where the spot-size converter was used for efficient light coupling from a single mode fibre to the waveguide of UTC-PD. In [1.122], traveling wave UTC-PD employed a mode-converting waveguide for efficient optical coupling from a lensed fiber. A DC responsivity of 0.53 A/W at 1550 nm and 3 dB bandwidth of 108 GHz were obtained with a high output power of 1 mW at 200 GHz. Besides using spot size converter and utilize mode-converting waveguide, a double cladding, high-mesa-type waveguide UTC-PD was presented in [1.123]. By changing the thickness of outer InP cladding layers, inner InGaAsP cladding layers and InGaAs core layer, the absorption ratio and mode field can be adjusted. A high responsivity of 0.6 A/W at 1550 nm was achieved with the 3dB bandwidth of 100 GHz.

RF Power Coupling

A resonating matching circuit can improve the efficiency at desired frequencies and is widely applied in monolithic microwave integrated circuits. By using the coplanar waveguide short stub matching circuit, the imaginary part of the internal impedance in the UTC-PD at the designed frequency can be compensated. In [1.124], high output powers at 100 GHz have been obtained by using matching circuits. The maximum output power of 20.8 mW (13.2 dBm) was reported with a photocurrent of 25 mA at -3V bias voltage. The device with the matching circuit showed about 50% higher efficiency at 100 GHz than the one without it.

For the antenna integrated UTC-PDs, the total power emitted by an antenna depends on the impedance match with the driving source and the radiation efficiency. The absolute level of power emitted by an antenna over the frequency range can be calculated and predicted if the UTC-PD's impedance is known and the coupling efficiency between UTC and antenna considered [1.125], [1.126]. A comprehensive study of UTC-PD output impedance and frequency photo-response was presented in [1.125]. For our antenna integrated UTC-PDs with Si lenses, the measured radiated powers at 250 GHz were 32 μW and 60 μW with photocurrent of 10 mA and 13.5 mA respectively, at a bias voltage of -2.6V [1.127]. The measured radiated powers (200 - 260 GHz) showed good agreement with the numerical results. The radiated RF power is relatively low because the bow-

tie antenna was not impedance matched with this UTC-PD, as the antenna had been designed to be impedance matched with the UTC-PDs in [1.125]. With the full-wave modelling by CST (Computer Simulation Technology) Studio Suite, the radiated power is calculated to reach 124 μW at 250 GHz with a photocurrent of 10 mA, where the bow-tie antenna is impedance matched with the UTC-PDs. This power is 5 times higher than the calculated power for non-impedance matching antenna integrated UTC-PDs.

UTC-PD Arrays

Efforts have been made in enlarging the output power of UTC-PDs by using multiple photodiodes. Two methods have been implemented and reported: combining photocurrents of multiple UTC-PDs, or using antenna arrays to increase gain of the radiated THz power. In [1.128], two identical UTC-PDs and a T-junction were monolithically integrated in a single chip and powers from the PDs were combined with the T-junction combiner, which consists of $\lambda/4$ long 50Ω coplanar waveguide (CPW) transmission line and air-bridges. The packaged WR-3 waveguide module was reported to have 1.2 mW peak power at 300 GHz and 3 dB bandwidth of 70 GHz. Back-illuminated four-element MUTC photodiode array was demonstrated in [1.129], which was flip-chip bonded to AlN sub-mounts with an integrated transmission line. The p-mesa of element MUTC photodiode have the diameter of 28 μm, and the RF output power of this 4 - photodiode array achieved 26.2 dBm at 35 GHz and 21.0 dBm at 48 GHz. Balanced PDs [1.130] have the advantage of a relatively simple layout and direct summing of the photocurrent with negligible insertion loss. In [1.131], balanced two InP/InGaAs modified UTC-PDs (back illuminated), flip-chip bonded on a diamond sub-mount (surface temperature set to -10C), was reported exhibiting high RF output power of 1.5 W under saturation current of > 320 mA at 8 GHz, with the bias voltage of -11 V. In [1.132], experimental results showed that the THz wave power from 4 × 4 two-dimensionally arrayed antennas was about 4.8 dB higher than that of the one dimensionally 4 slot antenna arrayed UTC-PD, which results in the power gain of 9.7 dB compared to the single UTC-PD power source.

The output power of above-mentioned high-power UTC-PDs are shown and compared in below graph. From Figure 1.9, we can see: 1) the most of the efforts

to increase the RF output power of UTC-PDs are focused on frequencies lower than 200 GHz, where epitaxy structure design optimisation, thermal management, optical coupling improvement and UTC-PD arrays have been applied to improve their output powers. 2) Heat dissipation by utilising high thermal conductivity substrate can further improve the RF output power after implementing the epitaxy structure optimisation. 3) For the frequencies between 200 GHz and 1 THz, the best reported emitted RF powers come from the antenna integrated TW-UTC-PDs. Also, resonant antenna integrated UTC-PDs showed higher peak output power than broadband antenna integrated UCT-PDs, but with the sacrifice of narrow bandwidth.

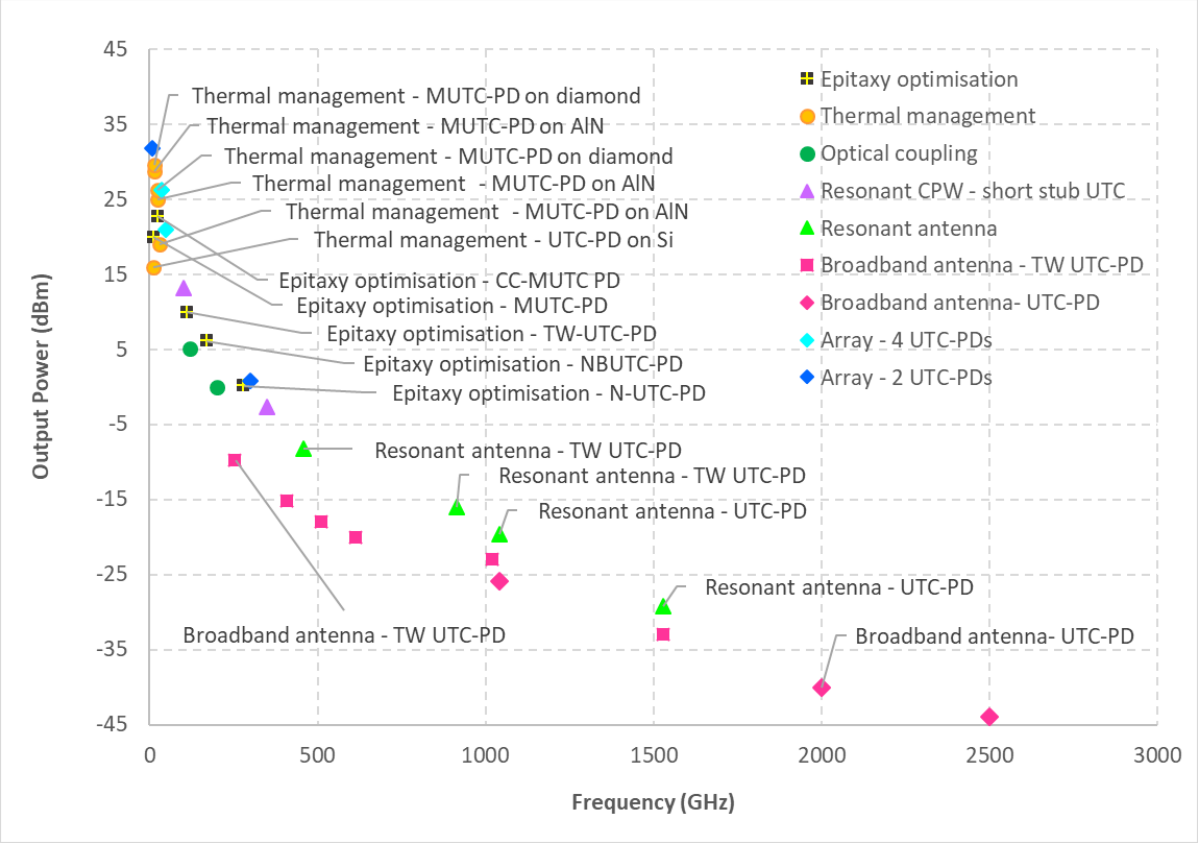

Figure 1.9: State of the art UTC-PDs output power as a function of frequency.

1.5 Conclusions

The THz band locates between microwaves and infrared in the electromagnetic spectrum (100 GHz to 10 THz), making it possess unique properties, and is

utilised in biology, security, material characterization, high-speed wireless communication and so on. THz source is essential component to realise these applications. Below Figure 1.10 summarizes the output power of various types of THz sources mentioned in this Chapter, and shows: 1) For electronic techniques, vacuum electronic devices (Gyrotron, BWO, and FEL) can generate high power signals and cover a wide THz range, from sub-THz to several THz. But the complete systems are large, heavy and need high magnetic field or high bias voltage. They are not suitable for wireless communication systems, where compact and low power consumption sub-THz sources are desirable. 2) For solid-state sources (IMPATT, TUNNETT, Gunn and RTD), another major THz generation approach of electronic techniques, though they can emit similar RF powers as UTC-PDs at the sub-THz frequency range, their power efficiencies are less than UTC-PDs' and only have limited frequency tunability. Besides, photonic based THz sources offer the convenience of integration with optical fibre networks, therefore UTC-PDs are more attractive to act as the sub-THz transmitter than solid-state sources in wireless communication systems. 3) QCLs have shown remarkable performances at frequencies above 1 THz. They can be very compact but need a cryogenic cooling system, and the challenge is to raise the temperature of operation [1.133], [1.134]. As QCLs can't work at sub-THz range and need operate at very low temperature, they are also not applicable to wireless communication networks. 4) Both of optically pumped gas lasers and p-Ge lasers (under uniaxial stress) are compact and can operate at room temperature, but it is hard for them to have emission less than 1 THz. In addition, gas lasers are not all solid-state sources and p-Ge lasers need extra stress control to work at room temperature, these make them not suitable for public wireless networks. 5) Among photomixers (photoconductor and photodiodes), benefiting from single active carriers, UTC-PDs have wider bandwidth, higher saturation power and better power efficiency than LT-GaAs photoconductors and PIN-PDs. Overall, with respect to device size, power consumption, operating temperature and compatibility with optical networks, for the interesting sub-THz band, UTC-PDs have exhibited advantages than competing structures. Therefore, for the targeted frequency range (200 - 300 GHz), UTC-PD is a promising THz source solution to achieve high-speed wireless communications.

Increasing the output power of UTC-PDs (the sub-THz source for wireless systems) can benefit the signal to noise ratio, data error rate, transmission distance, etc. Efforts have been made in optimising UTC-PD's absorption/collection layers to reduce space charge effects and utilizing waveguide/traveling wave structure to gain higher output power at higher frequencies. By optimising the heat dissipation through using high thermal conductivity sub-mounts, the output power of UTC-PDs can be further improved by around 50%. Improving the optical coupling between optical fibre and the waveguide of UTC-PDs, or RF coupling between UTC-PDs and integrated antenna, can effectively increase the radiated RF power at higher frequencies.

In order to improve the output power of our waveguide UTC-PDs at sub-THz frequency (200 - 300 GHz), my work will focus on the thermal management of antenna-integrated UTC-PDs, to reduce thermal resistance and enhance their thermal dissipation, which can improve the saturation photocurrent and the RF output power of UTC-PDs.

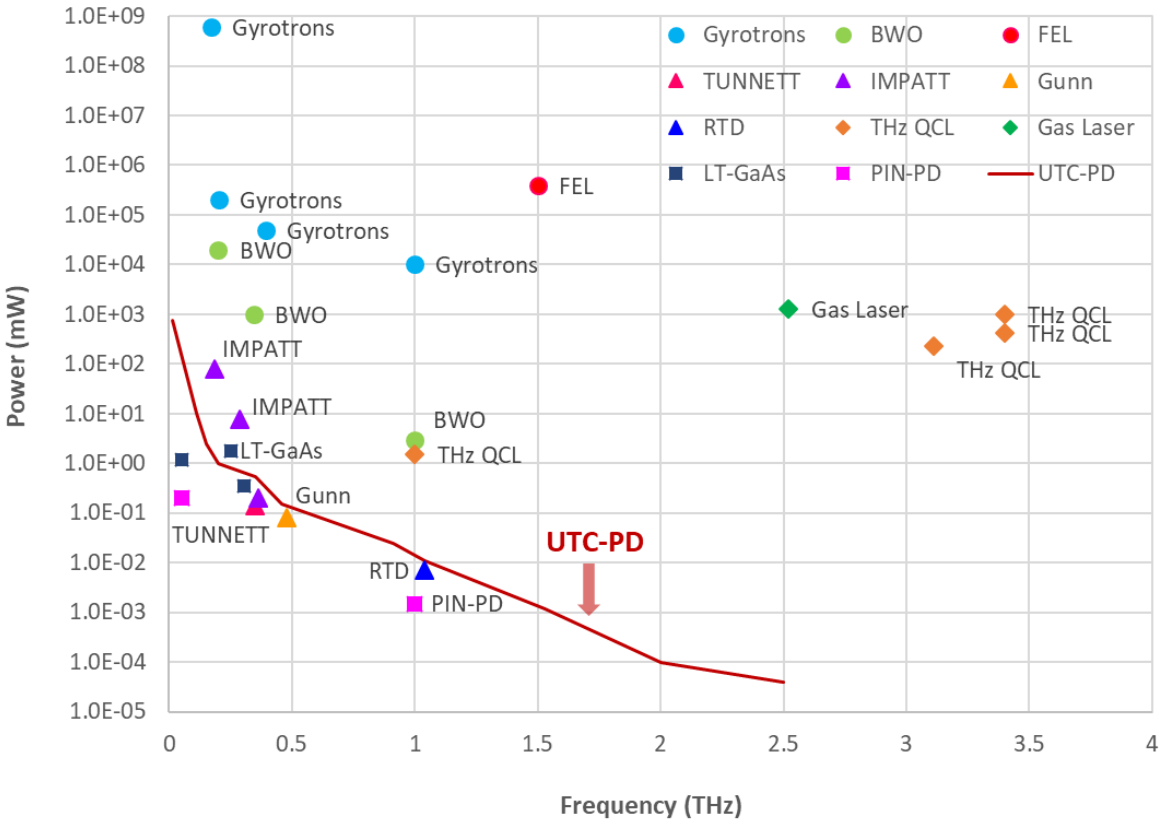

Figure 1.10: THz emission power as a function of frequency.

1.6 Organisation of the Thesis

In Chapter 2, the theory and structure of UTC-PDs are explained, and the waveguide UTC-PDs fabricated on InGaAsP-based epitaxial structures grown by Solid Source Molecular Beam Epitaxy (SS-MBE) are reported. Experiments to reduce the leakage current, and characterisation on CPW integrated UTC-PDs and antenna integrated UTC-PDs are also covered. In order to get the idea of how the RF output can be improved at the situation of less thermal effect, RF saturation powers at 100 GHz and 250 GHz were measured on CPW integrated UTC-PDs and bow-tie antenna integrated UTC-PDs respectively, under the condition of pulse optical input. Measurement arrangement and experiment results are presented in Chapter 3. To get reliable and stable measurement results, optimisations on reverse bias voltage, polarisation controller and MZ modulator are also discussed in Chapter 3. Temperature distribution inside antenna integrated UTC-PDs was modelled by COMSOL and illustrated in Chapter 4 (Section 4.2). Based on the simulated thermal distributions, the bottlenecks of heat dissipation were analysed, and three solutions to relieve the thermal block were presented as well (Section 4.3). To verify the correctness of thermal modelling, a temperature measurement experiment was conducted and recorded also in Chapter 4 (Section 4.4). Comparison between measured temperatures (at different photocurrents) and the simulated temperatures inside the absorption layer was also performed in this Chapter. In Chapter 5, saturation power measurements are done on 4x15 μm^2 antenna integrated UTC-PDs, by using Nitrocellulose and thermal conductive adhesives respectively, to compare their RF output power to see how much RF power can be improved. The work in this thesis had contributed to three publications, which are listed in Appendix E. Finally, the general summarisation, novel contributions and future work are covered in Chapter 6.

1.7 References

[1.1] M. Tonouchi, “Cutting-edge terahertz technology”, Nature Photonics, vol. 1, no. 2, pp. 97–105, (2007).

[1.2] P. H. Siegel, “Terahertz technology”, IEEE Transactions on Microwave Theory and Techniques, vol. 50, no. 3, pp. 910–928, (2002).

[1.3] https://www.eeworldonline.com/new-oscillating-material-may-tap-unused-electromagnetic-spectrum/

[1.4] Haymen Shams, Martyn Fice, Cyril Renaud, Alwyn Seeds, S Dhillon et al, “The 2017 terahertz science and technology roadmap”, J. Phys. D: Appl. Phys, vol 50, no. 4, pp. 41-43, (2017).

[1.5] Seeds A, Shams H, Fice M and Renaud C, “TeraHertz Photonics for Wireless Communications”, Journal of Lightwave Technology, vol. 33, no. 3, pp. 579–587, (2014).

[1.6] B. B. Hu and M. C. Nuss, “Imaging with terahertz waves”, Optics Letters, vol. 20, no. 16, pp.1716-1718, (1995).

[1.7] D. M. Mittleman, R. H. Jacobsen, and M. C. Nuss, “T-Ray Imaging”, IEEE Journal of Selected Topics in Quantum Electronics, vol. 2, no. 3, pp. 679-692, (1996).

[1.8] D. M. Mittleman, M. Gupta, R. Neelamani, R. G. Baraniuk, J. V. Rudd, and M. Koch, “Recent advances in terahertz imaging”, Applied Physics B: Lasers and Optics, vol. 68, no. 6, pp. 1085-1094, (1999).

[1.9] K. J. Siebert, H. Quast, R. Leonhardt, T. Loffler, M. Thomson, and S. Czasch, “Continuous-wave all-optoelectronic terahertz imaging”, Applied Physics Letters, vol. 80, no. 16, pp. 3003-3005, (2002).

[1.10] D. Woolard, R. Brown, M. Pepper, and M. Kemp, “Terahertz Frequency Sensing and Imaging: A Time of Reckoning Future Applications?”, Proceedings of the IEEE, vol. 93, no. 10, pp. 1722-1743, (2005).

[1.11] P. U. Jepsen, D. G. Cooke and M. Koch, “Terahertz spectroscopy and imaging – Modern techniques and applications”, Laser and Photonics Reviews, vol. 5, no. 1, pp. 124-166, (2011).

[1.12] Y. C. Shen, and P. Taday, “Development and Application of Terahertz Pulsed Imaging for Nondestructive Inspection of Pharmaceutical Tablet,” IEEE Journal of Selected Topics in Quantum Electronics, vol. 14, no. 2, pp. 407-415, (2008).

[1.13] E. Pickwell and V. P. Wallace, “Biomedical applications of terahertz technology,” Journal of Physics D: Applied Physics, vol. 39, no. 17, pp. R301-R310, (2006).

[1.14] W. R. Tribe, D. A. Newnham, P. F. Taday, and M. C. Kemp, “Hidden object detection: security applications of terahertz technology,” in Proceedings of SPIE, vol. 5354, pp. 168-176, (2004).

[1.15] Y. C. Shen, T. Lo, P. F. Taday, B. E. Cole, W. R. Tribe, and M. C. Kemp, “Detection and identification of explosives using terahertz pulsed spectroscopic imaging,” Applied Physics Letters, vol. 86, pp. 241116, (2005).

[1.16] J. F. Federici, B. Schulkin, F. Huang, D. Gary, R. Barat, F. Oliveira, and D. Zimdars, “THz imaging and sensing for security applications-explosives, weapons and drugs,” Semiconductor Science and Technology, vol. 20, no. 7, pp. S266-S280, (2005).

[1.17] J. Chen, Y. Chen, H. Zhao, G. J. Bastiaans, and X. Zhang, “Absorption coefficients of selected explosives and related compounds in the range of 0.1-2.8 THz,” Optics Express, vol. 15, no. 19, pp.12060-12067, (2007).

[1.18] H. B. Liu, H. Zhong, N. Karpowicz, Y. Chen, and X. C. Zhang, “Terahertz Spectroscopy and Imaging for Defense and Security Applications,” Proceedings of the IEEE, vol. 95, no. 8, pp. 1514-1527, (2007).

[1.19] A. Hirata, M. Harada, and T. Nagatsuma, “120-GHz Wireless Link Using Photonic Techniques for Generation, Modulation, and Emission of Millimeter-Wave Signals,” Journal of Lightwave Technology, vol. 21, no. 10, pp. 2145-2153, (2003).

[1.20] R. Piesiewicz, T. Kleine-Ostmann, N. Krumbholz, D. Mittleman, M. Koch, J. Schoebel, and T. Kürner, “Short-range ultra broadband terahertz communications: Concept and perspectives,” IEEE Antennas and Propagation Magazine, vol. 49, no. 6, pp. 24-39, (2007).

[1.21] C. C. Renaud, L. Ponnampalam, F. Pozzi, E. Rouvalis, D. Moodie, M. Robertson, and A. J. Seeds, “Photonically enabled communication systems beyond 100 GHz,” IEEE Topical Meeting on Microwave Photonics (MWP) 2008, pp. 55-58, (2008).

[1.22] H.-J. Song, K. Ajito, A. Wakatsuki, Y. Muramoto, N. Kukutsu, Y. Kado, and T. Nagatsuma, “Terahertz Wireless Communication Link at 300 GHz,” in IEEE Topical Meeting on Microwave Photonics (MWP) 2010, pp. 42-45, (2010).

[1.23] T. Kleine-Ostmann, T. Nagatsuma, “A Review on Terahertz Communications Research,” Journal of Infrared, Millimeter and Terahertz Waves, vol. 32, no. 2, pp. 143-171, (2011).

[1.24] Jochen Koszescha, “What Infineon Technologies is looking for in TERAFLAG”, 1st European TERAFLAG Workshop, (2018).

[1.25] Ericsson Mobility Report, June (2019).

[1.26] Fehske A, Fettweis G, Malmodin J, et al, “The global footprint of mobile communications: The ecological and economic perspective”, IEEE communications magazine, vol. 49, no. 8, pp. 55-62, (2011).

[1.27] Alwyn J. Seeds, Haymen Shams, Martyn J. Fice and Cyril C. Renaud, “TeraHertz Photonics for Wireless Communications”, Journal of Lightwave Technology, vol. 33, no. 3, pp. 579-587, (2015).

[1.28] Nagatsuma, T., Ducournau, G. & Renaud, C. “Advances in terahertz communications accelerated by photonics”, Nature Photon, 10, pp.371–379, (2016).

[1.29] A. J. Seeds, H. Shams, M. J. Fice and C. C. Renaud, "TeraHertz Photonics for Wireless Communications," Journal of Lightwave Technology, vol. 33, no. 3, pp. 579-587, (2015).

[1.30] Haymen Shams, Martyn J. Fice, Luis Gonzalez-Guerrero, Cyril C. Renaud. Frédéric van Dijk, Alwyn J. Seeds, “Sub-THz Wireless Over Fiber for Frequency Band 220–280 GHz”, Journal of Lightwave Technology, vol. 34, no. 2), pp. 4786-4793, (2016).

[1.31] X. Yu, S. Jia, H. Hu, M. Galili, T. Morioka, P. U. Jepsen, and L. K. Oxenløwe, “160 Gbit/s photonics wireless transmission in the 300-500 GHz band”, APL Photonics 1, pp. 081301, (2016).

[1.32] Zijie Lu, Shiwei Wang, Wei Li, Shi Jia, Lu Zhang, Mengyao Qiao, Xiaodan Pang, Nazar Idrees, "26.8 m 350 GHz Wireless Transmission of Beyond 100

Gbit/s Supported by THz Photonics," 2019 Asia Communications and Photonics Conference (ACP), pp. 1-3, (2019).

[1.33] Thierry Robin, Clementine Bouye, Jacques Cochard, “Terahertz applications: trends and challenges”, Proc. SPIE 8985, Terahertz, RF, Millimeter, and Submillimeter-Wave Technology and Applications VII, pp. 898512, (2014).

[1.34] Booske J H, “Plasma physics and related challenges of millimeter-wave-to-terahertz and high power microwave generation”, Physics of Plasmas, vol. 15, pp. 055502, (2008).

[1.35] Barker R J, Booske J H, Luhmann N C and Nusinovich G S, “Modern Microwave and Millimeter Wave Power Electronics”, Wiley, (2005).

[1.36] Booske J H, Dobbs R J, Joye C D, Kory C L, Neil G R, Park G-S, Park J and Temkin R J, "Vacuum Electronic High Power Terahertz Sources," IEEE Transactions on Terahertz Science and Technology, vol. 1, no. 1, pp. 54-75, (2011).

[1.37] P.C. Kalaria, K.A. Avramidis, J. Franck, et al., “Multi-frequency operation of DEMO gyrotron with realistic electron beam parameters”, 16th IEEE International Vacuum Electronics Conference, paper S23.4, (2015).

[1.38] 2014 IEEE Trans. Electron Devices (Spec. Issue Vac. Electron.) 61 special issue.

[1.39] R. Kompfner and N. Williams, “Backward-Wave Tubes,” Proc. IRE, vol. 41, no. 11, pp. 1602–1611, (1953).

[1.40] S. Krishnagopal and V. Kumar, “Free-electron lasers,” Radiat. Phys. Chem., vol. 70, no. 4–5, pp. 559–569, (2004).

[1.41] K. L. Felch, B. G. Danly, H. R. Jory, K. E. Kreischer, W. Lawson, B. Levush, and R. J. Temkin, “Characteristics and applications of fast-wave gyro devices,” Proc. IEEE, vol. 87, no. 5, pp. 752–781, (1999).

[1.42] A. Kasugai, K. Sakamoto, K. Takahashi, K. Kajiwara, and N. Kobayashi, “Steady-state operation of 170 GHz–1 MW gyrotron for ITER,” Nucl. Fusion, vol. 48, no. 5, pp. 054009 1- 054009 6, (2008).

[1.43] T. Idehara, T. Saito, I. Ogawa, and Y. Tatematsu, “High power THz technologies opened by high power radiation sources - Gyrotrons,” 2010 Int. Kharkov Symp. Phys. Eng. Microwaves, Millim. Submillim. Waves, MSMW’2010, pp. 1–6, (2010).

[1.44] T. Idehara, I. Ogawa, and H. Mori, “A THz Gyrotron FU CW III with a 20T superconducting magnet,” J. Plasma Fusion Res. Ser., vol. 8, pp. 1508–1511, (2009).

[1.45] W. He, L. Zhang, D. Bowes, H. Yin, K. Ronald, A. D. R. Phelps, and A. W. Cross, “Generation of broadband terahertz radiation using a backward wave oscillator and pseudospark-sourced electron beam”, Appl. Phys. Lett. 107, 133501, (2015).

[1.46] Wenxin Liu, Chao Zhao, Xin Guo, Zhaochuan Zhang, and Meng Wang, “The Progresses of Vacuum Electronic Terahertz Sources at IECAS”, PhotonIcs & Electromagnetics Research Symposium, pp. 550-554, (2019).

[1.47] Claudio Paoloni, Diana Gamzina, Logan Himes, Branko Popovic, Robert Barchfeld, Lingna Yue, Yuan Zheng, Xiaopin Tang, Ye Tang, Pan Pan, Hanyan Li, Rosa Letizia, Mauro Mineo, Jinjun Feng and Neville C. Luhmann, Jr., “THz Backward-Wave Oscillators for Plasma Diagnostic in Nuclear Fusion”, IEEE Transactions on Plasma Science, vol. 44, no. 4, pp. 369-376, (2016).

[1.48] N.G. Gavrilov, B.A. Knyazev, E.I. Kolobanov, V.V. Kotenkov, V.V. Kubarev, G.N. Kulipanov, A.N. Matveenko, L.E. Medvedev, S.V. Miginsky, L.A. Mironenko, A.D. Oreshkov, V.K. Ovchar, V.M. Popik, T.V. Salikova, M.A. Scheglov, S.S. Serednyakov, O.A. Shevchenko, A.N. Skrinsky, V.G. Tcheskidov, N.A. Vinokurov, “Status of the Novosibirsk high-power terahertz FEL”, Nuclear Instruments and Methods in Physics Research A 575, pp 54–57, (2007).

[1.49] Luis R. Elias, Isidoro Kimel, Delbert Larson, Dan Anderson, Mufit Tecimer and Zhong Zhefu, “A compact cw free electron laser”, Nuclear Instruments and Methods in Physics Research A304, pp. 219-223, (1991).

[1.50] Toshitaka Idehara, Jagadish C. Mudiganti, La Agusu, Tomohiro Kanemaki, Isamu Ogawa, Toshimichi Fujiwara, Yoh Matsuki, Keisuke Ueda, “Development of a Compact sub-THz Gyrotron FU CW CI for Application to High Power THz Technologies”, J Infrared Milli Terahz Waves, vol. 33, pp.v724–744, (2012).

[1.51] Ping Tan, Jiang Huang, KaiFeng Liu, YongQian Xiong and MingWu Fan, “Terahertz radiation sources based on free electron lasers and their applications”, Science China Information Sciences, vol 55, no. 1, pp. 1–15, (2012).

[1.52] M. Ino, T. Ishibashi, and M. Ohmori, “CW oscillation with p+-p-n+ silicon IMPATT diodes in 200 GHz and 300 GHz bands,” Electronics Letters, vol. 12, no. 6, pp. 148-149, (1976).

[1.53] H. Eisele, “480 GHz oscillator with an InP Gunn device,” Electronics Letters, vol. 46, no. 6, pp. 422-423, (2010).

[1.54] S. Suzuki, M. Asada, A. Teranishi, H. Sugiyama, and H. Yokoyama, “Fundamental oscillation of resonant tunneling diodes above 1 THz at room temperature,” Applied Physics Letters, vol. 97, no. 24, pp. 242102, (2010).

[1.55] Zhe Chen, Hui Wang, Byron Alderman, Peter Huggard, Bo Zhang, Yong Fan, “190 GHz high power input frequency doubler based on Schottky diodes and AlN substrate”, IEICE Electronics Express, vol 13, no. 22, (2016).

[1.56] J. V. Siles et al., “On-chip power-combining for high-power Schottky diode-based frequency multipliers,” US Patent US9143084B2, (2015).

[1.57] J. V. Siles, E. Schlecht, R. Lin, C. Lee, and I. Mehdi, “High-efficiency planar Schottky diode based frequency multipliers optimized for high power operation,” Proc. 35th Int. Conf. Infrared Millim. THz Waves, p. 1, (2015).

[1.58] Kitagawa, S., Suzuki, S., and Asada, M., “650-GHz resonant-tunneling-diode VCO with wide tuning range using varactor diode”, IEEE Electron Device Lett., vol 35, no. 12, pp. 1215–1217, (2014).

[1.59] M. Mukherjee, N. Mazumder, K. Goswami and S. Kumar Roy, "An opto-sensitive InP based IMPATT diode for application in terahertz regime," 2007 International Workshop on Physics of Semiconductor Devices, pp. 392-395, (2007).

[1.60] Jin-Tao Pan, Yue Wang, Kun-Yuan Xu, Jian-Wen Xiong, Zhi-Lie Tang, “Tunable Gunn oscillations in a top-gated planar nanodevice”, Solid State Communications, vol 271 pp. 85–88, (2018).

[1.61] H. Eisele, "480 GHz oscillator with an InP Gunn device," Electronics Letters, vol. 46, no. 6, pp. 422-423, (2010).

[1.62] J. Webber, N. Nishigami, J. Kim, M. Fujita and T. Nagatsuma, "Terahertz wireless communications using resonant tunnelling diodes with radio-over-fibre," Electronics Letters, vol. 55, no. 17, pp. 949-951, (2019).

[1.63] A. Al-Khalidi, K. Alharbi, J. Wang and E. Wasige, "THz electronics for data centre wireless links - The TERAPOD project," 2017 9th International Congress on Ultra Modern Telecommunications and Control Systems and Workshops (ICUMT), pp. 445-448, (2017).

[1.64] Vitiello, M. S. et al., “Electron-lattice coupling in bound-to-continuum THz quantum-cascade lasers”, Appl. Phys. Lett. vol. 88, 241109 (2006).

[1.65] Straub, A. et al. “Threshold reduction in quantum cascade lasers with partially undoped, dual wavelength interdigitated cascades”, Appl. Phys. Lett., vol. 80, pp. 2845–2847 (2002).

[1.66] Hu, Q. et al., “Resonant-phonon-assisted THz quantum-cascade lasers with metal–metal waveguides”, Semicond. Sci. Technol., vol. 20, S228–S236 (2005).

[1.67] Masayoshi Tonouchi, “Cutting-edge terahertz technology”, nature photonics, vol 1, pp. 97-106, (2007).

[1.68] J. Faist, F. Capasso, D. L. Sivco, and C. Sirtori, “Quantum cascade laser,” Science, vol. 264, no. 5158, pp. 553 – 556, (1994).

[1.69] R. Kohler, A. Tredicucci, F. Beltram, H. Beere, E. Linfield, G. Davies, D. Ritchie, R. Iotti, and F. Rossi, “Terahertz-semiconductor-heterostructure laser,” Nature, vol. 417, pp. 156–159, (2002).

[1.70] L. Li, L. Chen, J. Zhu, J. Freeman, P. Dean, A. Valavanis, A.G. Davies, and E. H. Linfield, “Terahertz quantum cascade lasers with >1 W output powers,” Electron. Lett., vol. 50, no. 4, pp. 309–311, (2014).

[1.71] A. Wade, G. Fedorov, D. Smirnov, S. Kumar, B. S. Williams, Q. Hu & J. L. Reno, “Magnetic-field-assisted terahertz quantum cascade laser operating up to 225 K”, Nature Photonics, vol 3, pp. 41–45, (2009).

[1.72] S. Kumar, Q. Hu and J.L. Reno, “High-power terahertz quantum-cascade lasers”, Electronics Letters, vol. 42, no. 2, pp. 89-91, (2006).

[1.73] X. Wang, C. Shen, T. Jiang, Z. Zhan, Q. Deng, W. Li, W. Wu, N. Yang, W. Chu, and S. Duan, “High-power terahertz quantum cascade lasers with ~0.23 W in continuous wave mode” AIP Adv. 6, 075210, (2016).

[1.74] J. Farhoomand and H. M. Pickett, “Stable 1.25 watts CW far infrared laser radiation at the 119 μm methanol line,” Int. J. Infrared Millimeter Waves, vol. 8, no. 5, pp. 441–447, (1987).

[1.75] E. R. Mueller, “Optically-pumped THz laser technology,” Coherent-DEOS Product Note, (2001).

[1.76] J. Farhoomand, and H. M. Pickett, “Stable 1.25 Watts cw Far Infrared Laser Radiation at the 119 um Methanol Line,” Int. J. of IR & MMW, vol.8, no.5, pp. 441, (1987).

[1.77] B. Ferguson and X.-C. Zhang, “Materials for terahertz science and technology.,” Nat. Mater., vol. 1, no. 1, pp. 26–33, (2002).

[1.78] E.Bründermann, D.R.Chamberlin, E.E.Haller, “Novel design concepts of widely tunable germanium terahertz lasers”, Infrared Physics & Technology, vol. 40, no. 3, pp. 141-151, (1999).

[1.79] Shastin, V.N, “Hot hole inter-sub-band transition p-Ge FIR laser”, Opt Quant Electron, vol. 23, pp. S111–S131, (1991).

[1.80] Bergner, A. et al, “New p-Ge THz laser spectrometer for the study of solutions: THz absorption spectroscopy of water”, Rev. Sci. Instr. vol. 76, 063110, (2005).

[1.81] Yu. P. Gousev, I. V. Altukhov, K. A. Korolev, V. P. Sinis, M. S. Kagan, E. E. Haller, M. A. Odnoblyudov, I. N. Yassievich, and K.-A. Chao, “Widely tunable continuous-wave THz laser”, Appl. Phys. Lett., vol. 75, no. 6, pp. 757-759, (1999).

[1.82] H. Richter, M. Greiner-Bär, S. G. Pavlov, A. D. Semenov, M. Wienold, L. Schrottke, M. Giehler, R. Hey, H. T. Grahn, and H.-W. Hübers, “A compact, continuous-wave terahertz source based on a quantum-cascade laser and a miniature cryocooler”, Optics Express, vol. 18, no. 10, pp. 10177-10187, (2010).

[1.83] E. R. Brown, “THz generation by potomixing in ultrafast photoconductors,” Int. J. High Speed Electr. Syst., vol. 13, no. 2, pp. 497–545, (2003).

[1.84] D. Saeedkia and S. Safavi-Naeini, “A comprehensive model for photomixing in ultrafast photoconductors,” IEEE Photon. Technol. Lett., vol. 18, no. 13, pp. 1457–1459, (2006).

[1.85] E. Peytavit, S. Lepilliet, F. Hindle, C. Coinon, T. Akalin, G. Ducournau, G. Mouret, and J.-F. Lampin, “Milliwatt-level output power in the subterahertz range generated by photomixing in a GaAs photoconductor,” Appl. Phys. Lett., vol. 99, no. 22, paper. 223508, (2011).

[1.86] E. Peytavit, P. Latzel, F. Pavanello, G. Ducournau, and J. F. Lampin, “Milliwatt output power generated in the J-Band by a GaAs photomixer,” Int. Conf. Infrared, Millimeter, Terahertz Waves, IRMMW-THz, pp. 8–10, (2013).

[1.87] K. Kato, Member, IEEE, A. Kozen, Y. Muramoto, Y. Itaya, Member, IEEE, T. Nagatsuma, Member, IEEE, and M. Yaita, “110-GHz, 50% Efficiency MushroomMesa Waveguide p-i-n Photodiode for a 1.55-pm Wavelength”, IEEE Photonics Technology Lelters, 66-67, (1994).

[1.88] S. Nellen, R. Kohlhaas, L. Liebermeister, S. Breuer, B. Globisch and M. Schell, “Continuous wave terahertz generation from photodiode-based emitters with up to 200 μW terahertz power”, IEEE 43rd International Conference on Infrared, Millimeter, and Terahertz Waves (IRMMW-THz), (2018).

[1.89] T. Umezawa, K. Akahane, A. Kanno, N. Yamamoto, K. Kashim, T. Kawanishi, “High conversion gain, low power consumption W-band photoreceiver integrated with UTC-PD and InP-PHEMT amplifier”, IEEE International Topical Meeting on Microwave Photonics (MWP), (2015).

[1.90] X. Li, N. Li, S. Demiguel, X. Zheng, J. C. Campbell, H. H. Tan, and C. Jagadish, “A partially depleted absorber photodiode with graded doping injection regions”, IEEE Photon. Technol. Lett., vol. 16, pp. 2326–2328, (2004).

[1.91] Y. S. Wu, J. W. Shi, J. Y. Wu, F. H. Huang, Y. J. Chan, Y. L. Huang, and R. Xuan, “High-performance evanescently edge coupled photodiodes with partially p-doped photoabsorption layer at 1.55-mm wavelength”, IEEE Photon. Technol. Lett., vol. 17, pp. 878–880, (2005).

[1.92] A. Joshi and D. Becker, “GRIN lens-coupled top-illuminated photodetectors for high-power applications”, Microwave Photonics, Tech. Digest, pp. 18 – 20, (2007).

[1.93] K. S. Giboney et al., "Travelling-wave photodetectors with 172-GHz bandwidth and 76-GHz bandwidth-efficiency product", IEEE Photonics Technology Letters, vol. 7, no. 4, pp. 412-414, (1995).

[1.94] K. S. Giboney, M. J. W. Rodwell, and J. E. Bowers, “Traveling wave photodetectors,” IEEE Photon. Technol. Lett., vol. 4, no. 12, pp. 1363-1365, (1992).

[1.95] Tadao Ishibashi, Satoshi Kodama, Naofumi Shimizu and Tomofumi Furuta, “High-Speed Response of Uni-Traveling-Carrier Photodiodes”, Jpn. J. Appl. Phys., vol. 36, pp. 6263-6268 (1997).

[1.96] T. Nagatsuma, H. Ito, and T. Ishibashi, “High-power RF photodiodes and their applications,” Laser Photonics Rev., vol. 3(1–2), pp. 123–137, (2009).

[1.97] Z. Li, Y. Fu, M. Piels, H. Pan, A. Beling, J. E. Bowers, and J. C. Campbell, “High-power high-linearity flip-chip bonded modified uni-traveling carrier photodiode,” Opt. Express, vol. 19, B385–B390, (2011).

[1.98] C. Renaud, D. Moodie, M. Robertson, and A. Seeds, “High output power at 110 GHz with a waveguide uni-travelling carrier photodiode,” The 20th Annual Meeting of the IEEE, pp. 782–783, (2007).

[1.99] C. Renaud, M. Robertson, D. Rogers, R. Firth, P. Cannard, R. Moore, and A. Seeds, “A high responsivity, broadband waveguide uni-travelling carrier photodiode,” Proc. SPIE, 6194(1), C1940–C1940, (2006).

[1.100] L. Shen,1, Y. Jiao,1 W. Yao, Z. Cao, J. van der Tol, G. Roelkens and M. Smit “67 GHz uni-traveling carrier photodetector on an InP-membrane-on-silicon platform”, 2016 Conference on Lasers and Electro-Optics (CLEO), pp. 1-2, (2016).

[1.101] A. Wakatsuki, T. Furuta, Y. Muramoto, T. Yoshimatsu, H. Ito, “High-power and broadband sub-terahertz wave generation using a J-band photomixer module with rectangular-waveguide output port”, 33rd International Conference on Infrared, Millimeter and Terahertz Waves, (2008).

[1.102] K. Giboney, “Traveling-wave photodetectors,” IEEE Photonics Technol. Lett., vol. 4, no. 12, pp. 1363–1365, (1992).

[1.103] E. Rouvalis, C. C. Renaud, D. G. Moodie, M. J. Robertson, and A. J. Seeds, “Continuous wave terahertz generation from ultra-fast InP-based photodiodes,” IEEE Trans. Microw. Theory Tech., vol. 60, no. 3, pp. 509–517, (2012).

[1.104] St¨ohr A, Heinzelmann R, Hagedorn K, G¨usten R, Sch¨afer F,St¨uer H, Siebe F, van der Wal P, Krozer V, Feiginov M and J¨ager D, “Integrated 460 GHz photonic transmitter module”, Electronics Letters, vol. 37, no. 22, pp. 1347 – 1348, (2001).

[1.105] E. Rouvalis, C. C. Renaud, D. G. Moodie, M. J. Robertson, and A. J. Seeds, “Traveling-wave uni-traveling carrier photodiodes for continuous wave THz generation,” Opt. Exp., vol. 18, pp. 11105–11110, (2010).

[1.106] Hiroshi Ito, Fumito Nakajima, Tomofumi Furuta and Tadao Ishibashi, “Continuous THz-wave generation using antenna-integrated uni-travelling-carrier photodiodes”, Semicond. Sci. Technol. 20, S191–S198, (2005).

[1.107] Tadao Ishibashi, Yoshifumi Muramoto, Toshihide Yoshimatsu, and Hiroshi Ito, “Continuous THz Wave Generation by Photodiodes up to 2.5 THz”, 38th International Conference on Infrared, Millimeter, and Terahertz Waves (IRMMW-THz), (2013).

[1.108] K. Kato, “Ultrawide-band/high-frequency photodetectors,” IEEE Trans. Microw. Theory Technol., vol. 47, no. 7, pp. 1265–1281, (1999).

[1.109] H. Ito, S.Kodama,Y.Muramoto, T. Furuta, T. Nagatsuma, and T. Ishibashi, “High-speed and high-output InP-InGaAs unitraveling-carrier photodiodes,” IEEE J. Sel. Topics Quantum Electron., vol. 10, no. 4, pp. 709–727, (2004).

[1.110] Mourad Chtioui, Francois Lelarge, Alain Enard, Frederic Pommereau, Daniele Carpentier, Alexandre Marceaux, Frédéric van Dijk, and Mohand Achouche, “High Responsivity and High Power UTC and MUTC GaInAs-InP Photodiodes”, IEEE Photonics Technology Letters, vol. 24, no. 4, pp. 318-320, (2012).

[1.111] Zhi Li, Huapu Pan, Hao Chen, Andreas Beling, and Joe C. Campbell, “High-Saturation-Current Modified Uni-Traveling-Carrier Photodiode With Cliff Layer”, IEEE Journal Of Quantum Electronics, vol. 46, no. 5, pp. 626-632, (2010).

[1.112] Jhih-Min Wun, Hao-Yun Liu, Yu-Lun Zeng, Shang-Da Yang, Ci-Ling Pan, Chen-Bin Huang, and Jin-Wei Shi, “Photonic High-Power Continuous Wave THz-Wave Generation by Using Flip-Chip Packaged Uni-Traveling Carrier Photodiodes and a Femtosecond Optical Pulse Generator”, Journal Of Lightwave Technology, vol. 34, no. 4, pp.v1387-1397, (2016).

[1.113] J.-W. Shi, Y.-S. Wu, C.-Y. Wu, P.-H. Chiu, and C.-C. Hong, “High-Speed, High-Responsivity, and High-Power Performance of Near-Ballistic Uni-Traveling-Carrier Photodiode at 1.55um Wavelength”, IEEE Photonics Technology Letters, vol. 17, no. 9, pp. 1929-1931, (2005).

[1.114] J.-W. Shi, F.-M. Kuo, and J. E. Bowers, “Design and analysis of ultra-high speed near-ballistic uni-traveling-carrier photodiodes under a 50 Ω load for high-power performance,” IEEE Photon. Technol. Lett., vol. 24, no. 7, pp. 533–535, (2012).

[1.115] C. C. Renaud, M. Robertson, D. Rogers, R. Firth, P. J. Cannard, R. Moore, A. J. Seeds,” A high responsivity, broadband waveguide uni-travelling carrierphotodiode”, Proc. SPIE 6194, Millimeter-Wave and Terahertz Photonics, 61940C, (2006).

[1.116] Q. Zhou, A. S. Cross, F. Yang, A. Beling, and J. C. Campbell, “High-power high-bandwidth flip-chip bonded modified unitraveling carrier photodiodes,” IEEE Photonics Conference, pp. 306–307, (2012).

[1.117] Xiaojun Xie, Qiugui Zhou, Kejia Li, Yang Shen, Qinglong Li, Zhanyu Yang, Andreas Beling, and Joe C. Campbell, “Improved power conversion efficiency in high-performance photodiodes by flip-chip bonding on diamond”, Optica, vol. 1, no. 6, pp. 429-435, (2014).

[1.118] Ning Li, Hao Chen, Ning Duan, Mingguo Liu, Stephane Demiguel, Rubin Sidhu, Archie L. Holmes, Jr., and Joe C. Campbell, “High Power Photodiode Wafer Bonded to Si Using Au with Improved Responsivity and Output Power”, IEEE Photonics Technology Letters, vol. 18, no. 23, pp. 2526-2528, (2006).

[1.119] Philipp Latzel, Fabio Pavanello, Maximilien Billet, Sara Bretin, Alexandre Beck, Mathias Vanwolleghem, Christophe Coinon, Xavier Wallart, Emilien Peytavit, Guillaume Ducournau, Mohammed Zaknoune, Jean-Francois Lampin, “Generation of mW Level in the 300-GHz Band Using Resonant-Cavity-Enhanced Unitraveling Carrier Photodiodes”, IEEE Transactions on Terahertz Science and Technology, vol. 7, no. 6, pp. 800-806, (2017).

[1.120] Qingtao Chen, Yongqing Huang, Xiupu Zhang, Xiaofeng Duan, Jiarui Fei, Xiaokai Ma, Tao Liu, Gang Wu, Kai Liu, and Xiaomin Ren, “Uni-Traveling-Carrier Photodetector with High-Reflectivity DBR Mirrors”, IEEE Photonics Technology Letters, vol. 29, no. 14, pp.1203-1206, (2017).

[1.121] Gan Zhou, Willi Ebert, Sven Mutschall, Angela Seeger, Patrick Runge, Qinglong Li and Andreas Beling, “High-Power Waveguide Integrated Modified Uni Traveling-Carrier (UTC) Photodiode with 5 dBm RF Output Power at 120 GHz”, 2016 Optical Fiber Communications Conference and Exhibition, (2016).

[1.122] Efthymios Rouvalis, Cyril C. Renaud, David G. Moodie, Michael J. Robertson, and Alwyn J. Seeds, “Continuous Wave Terahertz Generation From Ultra-Fast InP-Based Photodiodes”, IEEE Transactions On Microwave Theory and Techniques, vol. 60, no. 3, pp. 509-516, (2012).

[1.123] T. Umezawa, K. Akahane, A. Matsumoto, A. Kanno, N. Yamamoto, and T. Kawanishi, “High responsivity 100 GHz waveguide UTC photodetector”, Proc. Of SPIE vol.10128, 1012807, (2017).

[1.124] H. Ito, T. Nagatsuma, A. Hirata, T. Minotani, A. Sasaki, Y. Hirota, T. Ishibashi, “High-power photonic millimetre wave generation at 100 GHz using matching-circuit-integrated uni-travelling-carrier photodiodes”, IEEE Proceedings – Optoelectronics, vol. 150, no.2, pp. 138-142, (2003).

[1.125] M. Natrella, C.-P. Liu, C. Graham, F. van Dijk, H. Liu, C. C. Renaud, and A. J. Seeds, “Accurate equivalent circuit model for millimetre-wave UTC photodiodes,” Optics Express, vol. 24, no. 5, pp. 4698–4713, (2016).

[1.126] M. Natrella, C.-P. Liu, C. Graham, F. van Dijk, H. Liu, C. C. Renaud, and A. J. Seeds, “Modelling and measurement of the absolute level of power radiated by antenna integrated THz UTC photodiodes,” Opt. Express, vol. 24, no. 11, pp. 11793-11807, (2016).

[1.127] Xiaoli Lin, Michele Natrella, James Seddon, Chris Graham, Cyril C. Renaud, Mingchu Tang, Jiang Wu, Huiyun Liu, and Alwyn J. Seeds, “High performance waveguide uni-travelling carrier photodiode grown by solid source molecular beam epitaxy”, Optics Express, vol. 27, no. 25, pp. 37065-37086, (2019).

[1.128] Ho-Jin Song, Katsuhiro Ajito, Yoshifumi Muramoto, Atsushi Wakatsuki, Tadao Nagatsuma, and Naoya Kukutsu, “Uni-Travelling-Carrier Photodiode Module Generating 300 GHz Power Greater Than 1 mW”, IEEE Microwave and Wireless Components Letters, vol. 22, no. 7, pp. 363-365, (2012).

[1.129] Allen S. Cross,Qiugui Zhou, Andreas Beling, Yang Fu, and Joe C. Campbell, “High-power flip-chip mounted photodiode array”, Optics Express, vol. 21, no. 8, pp. 9967-9973, (2013).

[1.130] M. S. Islam, T. Jung, T. Itoh, M. C. Wu, A. Nespola, D. L. Sivco, and A. Y. Cho, B, “High power and highly linear monolithically integrated distributed balanced photodetectors”, J. Lightwave Technol., vol. 20, no. 2, pp. 285–295, (2002).

[1.131] Qiugui Zhou, Allen S. Cross,Yang Fu, Andreas Beling, Brian M. Foley, Patrick E. Hopkins and Joe C. Campbell, “Balanced InP/InGaAs Photodiodes With 1.5-W Output Power”, IEEE Photonics Journal, vol. 5, no. 3, 6800307, (2013).

[1.132] Goki Sakano, Jun Haruki, Kota Tsugami, Haruichi Kanaya, and Kazutoshi Kato, “4 × 4 Arrayed THz-wave Combiner Composed of UTC-PDs and Slot Antennas”, 2017 Conference on Lasers and Electro-Optics Pacific Rim, paper s2348, (2017).

[1.133] R. Köhler, A. Tredicucci, F. Beltram, H. E. Beere, E. H. Linfield, A. G. Davies, D. A. Ritchie, R.C. Iotti, and F.Rossi, “Terahertz semiconductor heterostructure laser,” Nature, vol. 417, pp. 156–159, (2002).

[1.134] M. A. Belkin, Q. J. Wang, C. Pflügl, A. Belyanin, S. P. Khanna, A. G. Davies, E. H. Linfield, and F. Capasso, “High-Temperature operation of terahertz quantum cascade laser sources,” IEEE J. Sel. Topics Quantum Electron 15(3), 952–967, (2009).

[1.135] H. Eisele, “355 GHz oscillator with GaAs TUNNETT diode,” Electronics Letters, vol. 41, no. 6, pp. 329-330, (2005).

[1.136] Thomas W. Crowe, William L. Bishop, David W. Porterfield, Jeffrey L. Hesler and Robert M. Weikle, “Opening the Terahertz Window with Integrated Diode Circuits”, IEEE Journal of Solid-State Circuits, vol. 40, no. 10, pp. 2104-2110, (2005).

[1.137] J. V. Siles, K. B. Cooper, C. Lee, R. H. Lin, G. Chattopadhyay and I. Mehdi, "A New Generation of Room-Temperature Frequency-Multiplied Sources With up to 10× Higher Output Power in the 160 GHz - 1.6 THz Range," IEEE Transactions on Terahertz Science and Technology, vol. 8, no. 6, pp. 596-604, (2018).

Chapter 2
Waveguide UTC-PD Grown by Solid Source MBE

Benefiting from only one travelling carrier (electrons), which possess higher diffusion and drift velocities than holes, UTC-PDs have larger bandwidth and higher output saturation current than conventional PIN-PDs. These properties make UTC-PDs high speed and high output power photodiodes, which entitle them the promising transmitter candidates for sub-THz wireless communications. Though vertically illuminated UTC-PDs have shown improved 3dB bandwidth compared with conventional PIN-PDs, their geometry requires a trade-off between responsivity and bandwidth. For waveguide UTC-PDs, this unwanted trade-off between responsivity and bandwidth can be eased significantly. By using Solid Source MBE (SS-MBE), the major issue in phosphide epitaxy growing by Metal Organic Chemical Vapour Deposition (MOCVD), associated with the unintentional diffusion of Zinc, can be overcome. This gives the benefit of superior control of the doping profile in epitaxial layers provided by MBE, without the hazards of Gas Source MBE. In this Chapter, a brief review of photodiode fundamentals is given in Section 2.1, serving as the basis for the device analysis in the rest of this thesis. In Section 2.2, fabrication and measurements on coplanar waveguide coupled UTC-PDs (CPW UTC-PDs) and antenna integrated UTC-PDs (both were grown by SS-MBE) are presented to show their characteristic performance (responsivity, dark current, bandwidth, RF power, etc.).

High power UTC-PDs can improve overall link performance of wireless communication systems including the link gain, noise figure, and dynamic range. Increasing reverse bias voltage reduces space charge effects at high photocurrents and improves nonlinearities, thus increases the RF output power of UTC-PDs. However, higher bias voltage and photocurrents cause thermal heating, which is known to lead to device failure because of dark current runaway [2.1], [2.2]. Besides, dark current plays an important role in the reliability of high-power photodiodes. Therefore, reducing dark currents can benefit the output power of UTC-PDs and their reliability. In Section 2.2.2, sources of leakage

currents were explained and experiments were done to investigate effective methods to reduce leakage currents of UTC-PDs.

2.1 Uni-Travelling Carrier Photodiodes

2.1.1 Device structures and operating principles

Photodiodes function as a device for converting optical signals to electrical signals. Electron-hole pairs are generated when photons are absorbed in PDs. In conventional PIN-PDs, the intrinsic layer is usually used as both the absorption layer and the depletion layer. Incident photons to the intrinsic region with energy equal to or higher than the bandgap energy excite electrons from the valence band to the conduction band, and leave holes in the valence band, see Figure 2.1 (a) [2.3]. The generated electrons and holes drift through this layer under an applied reverse bias voltage, and produce photocurrent. Both of generated electrons and holes contribute to the transit time limited 3 dB bandwidth of PIN-PDs. As the hole's effective mass is larger than the electron's, its velocity (5 x 10^6 cm/s) is lower than electron's (3 - 5x10^7 cm/s). Therefore, the maximum operating speed of PIN-PDs is limited by holes' velocity.

Besides, the performance of PIN-PDs is also restricted by its maximum output photocurrent. When the input optical power gets higher, the band in the undoped absorption layer of PIN-PD is bent by the space charge screening. In PIN-PDs, space charge screening arises from the spatial distribution of photo-generated carriers as they transit the photodetector's depletion region. These charge carriers create an internal electric field that opposes the external bias electric field. At sufficiently high optical power levels, the space charge induced electric field can be strong enough to collapse the external electric field. Therefore, space charge effect makes carriers' velocity reduced and results in the saturation of photocurrent.

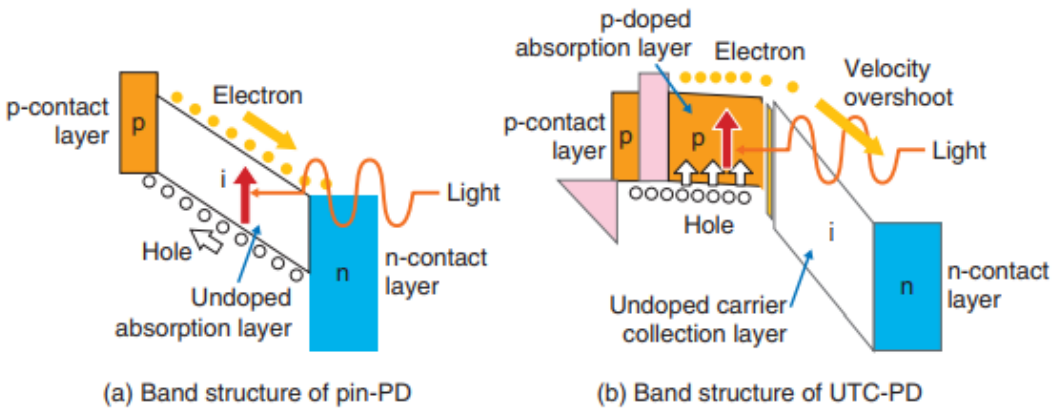

Figure 2.1: Energy band structure of PIN-PD and UTC-PD [2.3].

To mitigate the two limitations of PIN-PDs (long transit time caused by holes and saturation effect caused by space charge effect), the key solution is to increase the average carrier velocity, given by (2.1), where v_e, v_h are the electron and hole drift velocities [2.4].

$$\bar{v} = \sqrt[4]{\frac{2}{\left(\frac{1}{v_e^4} + \frac{1}{v_h^4}\right)}} \tag{2.1}$$

The UTC-PD was first developed in 1997 [2.5] to meet this requirement, which has wider bandwidth and higher photocurrent (due to higher carrier velocity) compared with the conventional PIN-PD. In the UTC-PD, the intrinsic layer of PIN-PD is divided into two parts: p-doped absorption layer (narrow band-gap) and undoped/n-doped collection layer (wider band-gap), see its band structure in Figure 2.1 (b). With the injection of light into the absorption layer of UTC-PDs, electron-hole pairs are generated in the absorption layer. For the photo generated holes, applied reverse bias voltage prevents them from diffusing into the collection layer, and holes are collected directly by the p-doped layer within the dielectric relaxation time, where holes are the majority dopant. Only electrons drift through the collection layer, therefore in UTC-PDs the maximum operating speed is determined by the velocity of electrons. That is why a UTC-PD's response is faster than conventional PIN-PDs.

At the same time, the space charge effect in UTC-PDs is much less than that in PIN-PDs because the carrier accumulation is much smaller in principle benefiting

from electron overshoot velocity (3 - 5 x 10^7 cm/s) in the depleted collection layer [2.6]. The shortened total transit time across the device reduces the space charge effect, and as a result, the saturation photocurrent of UTC-PDs is much higher than that of PIN-PDs, increased by an order of magnitude [2.8]. Considering only electrons as active carriers and the reduced space charge effect, UTC-PDs exhibit high-speed and high saturation photocurrent simultaneously.

2.1.2 Device equivalent circuit

The whole photodiode device can be considered having two parts: photodiode section and contact pad section, the equivalent circuit model shown in Figure 2.2 [2.7]. As the collection layer is depleted, we can treat it as a capacitor parallel with high resistance, which is not infinite but in the range of hundreds of kΩ. Therefore, in the photodiode section, R_p and C_p are used to represent the resistance and capacitance across the depletion region respectively. Series resistance R_s takes into account both the resistance in the homogenous regions of the diode and the resistance from the ohmic contacts (though part of series resistance coming from contact pads, we still put it into the photodiode section considering it belongs to device own structure not coming from parasitic effects). For contact pad section, external parallel C_{pad} and series inductance L_{pad} represent parasitic capacitance and parasitic inductance, deriving from capacitive coupling between P and N contact pads and coplanar waveguide contact pads, respectively. The effect of C_{pad} and L_{pad} becomes relevant at high frequencies.

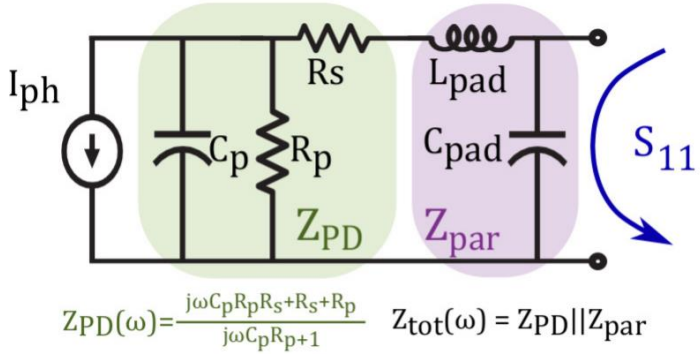

Figure 2.2: Small-circuit model of a photodiode. The intrinsic diode impedance is shown at left and the pad parasitics are on the right [2.7].

Figure 2.2 is the simplified circuit model for UTC-PDs, and the measured impedance of UTC-PDs can't be explained by employing this circuit model [2.33]. A more accurate model is proposed in [2.33] (see Figure 2.3), which shows good agreement with the experimental data. The new model uses two more RC parallel circuits (R_2C_2 and R_3C_3) to include the effects of two spacers located between absorption layer and collection layer (yellow part in Figure 2.3 (a)). The spacers with an intermediate bandgap can improve the InGaAs/InP conduction band discontinuity. The heavily p-doped absorption layer only provides a negligible resistive contribution. The parallel R_4C_4 represents the carrier collection layer, while R_1 takes into account the resistive effects of doped materials and ohmic contacts. C_p and L_p account for the parasitic capacitance and inductance respectively. By employing the new equivalent circuit, the accurate knowledge of UTC-PD's complex impedance over interested frequency range can be obtained, which is essential for designing RF antenna to realise complex conjugate impedance matching, in order to maximise the power coupling from UTC-PDs.

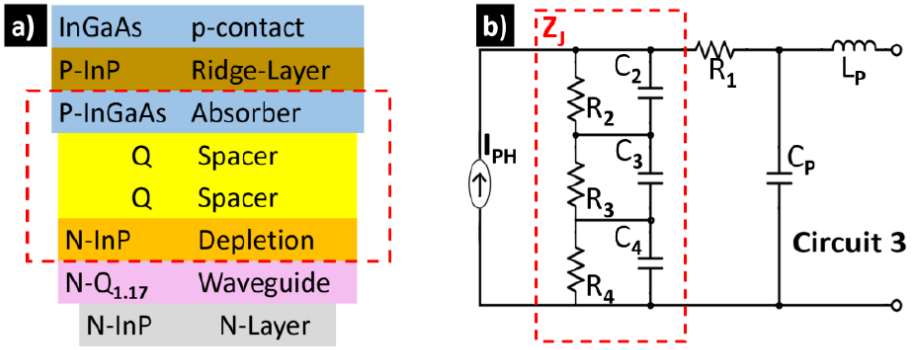

Figure 2.3: (a) The layer structure of UTC-PDs, (b) New equivalent circuit [2.33].

2.1.3 Figures of merit

Responsivity

The responsivity of a photodiode is defined as the ratio of the photon generated photocurrent I_p to the input optical power P at a given wavelength (shown in equation 2.2), where λ is the wavelength of the input light, η is quantum efficiency

depending on the material absorption coefficient, h = 6.63 x 10^{-34} J·s is the Planck constant, c = 3 x 10^{8} m/s is the speed of light and q = 1.6 x 10^{-19} C is the electron charge.

$$R = \frac{I_p}{P} = \frac{\eta q \lambda}{hc} \tag{2.2}$$

Responsivity shows how much of input optical power is converted into electrical current, and its unit is A/W. It varies with the wavelength of the incident light as well as the applied reverse bias and internal temperature. Responsivity increases slightly with applied reverse bias due to the improved charge collection efficiency in the photodiode, and also increases with the temperature due to the band gap becoming narrower at higher temperatures. In practice, there are several physical effects, such as incomplete absorption, recombination, reflection from the semiconductor surface, coupling losses, which reduce the responsivity of a photodiode.

Dark Current

Dark current of a photodiode is a key figure for low noise and high sensitivity optical detectors. It is the leakage current that flows when reverse bias voltage is applied and no optical radiation enters the detector. Dark current comes from the random generation of carriers within the depletion region of the photodiode, and approximately doubles for every 10°C increase in temperature. It is mainly dominated by diffusion current, generation-recombination current, and tunnelling current.

Series Resistance

Series resistance of the photodiode arises from the resistance of the contacts and the resistance of the un-depleted semiconductor materials. It is given by:

$$Rs = \frac{(W_s - W_d)\rho}{A} + R_c \tag{2.3}$$

where W_S is the total thickness of the photodiode, W_d is the width of the depleted region, A is the diffused area of the junction, ρ is the resistivity of the substrate

and R_C is the contact resistance. Although an ideal photodiode should have no series resistance, typical values ranging from 10 Ω to hundreds Ω are measured.

Shunt Resistance

Shunt resistance is the slope of the current-voltage curve of the photodiode at V=0. Although an ideal photodiode should have an infinite shunt resistance, actual values are in the range of hundreds of kΩ. It can be experimentally obtained by applying ±10 mV, measuring the current and calculating the resistance. For fast photodiode performance, the largest shunt resistance is desired.

Junction Capacitance

Junction capacitance is used to determine the speed of the response of the photodiode and comes from the depletion region of PN junction. The boundaries of the depletion region act as the plates of a parallel plate capacitor. The junction capacitance is proportional to the device area and inversely proportional to the width of the depletion region. Larger reverse bias makes depletion region wider and gets lower junction capacitance. In addition, higher resistivity depletion area has lower junction capacitance. The relationship between junction capacitance and reverse bias/resistivity of collection layer is given as:

$$C_j = \frac{\varepsilon_d \varepsilon_0 A}{\sqrt{2\varepsilon_d \varepsilon_0 \mu \rho (V_A + V_{bi})}} \tag{2.4}$$

where $\varepsilon_0 = 8.854 \times 10^{-14}$ F/cm, is the permittivity of free space, ε_d is the dielectric constant of depletion region, μ is the mobility of the electrons, ρ is the resistivity of the depletion area, V_{bi} is the internal built-in voltage of PN junction and V_A is the applied bias voltage.

Bandwidth

3dB bandwidth means the frequency at which the electrical output power of the photodiode falls to 50% of its peak value, and it affects the maximum data rate that can be handled by the photodiode. 3dB bandwidth is determined by three

response times of UTC-PDs: 1) τ_{dif}, the diffusion collection time of the carriers in the undepleted region (absorption layer) of the photodiode; 2) τ_{dft}, the drift collection time of the carriers in the depleted (collection layer) region of the photodiode; and 3) τ_{RC}, the RC time constant of the diode-circuit combination.

The carrier diffusion time τ_{dif} for UTC-PDs with uniform photo generation in the absorption layer is given by (2.5) [2.9], where D_e is the electron diffusion coefficient and v_{th} is the electron thermal velocity. $W^2_A/3D_e$ is the diffusion transit time and W_A/v_{th} is the correction factor associated with the finite thermal velocity.

$$\tau_{dif} = \frac{W_A^2}{3D_e} + \frac{W_A}{v_{th}} \tag{2.5}$$

The drift time τ_{dft} is determined by (2.6) [2.9], where W_c is the thickness of the depleted collection layer, and v is the velocity of the electron.

$$\tau_{dft} = \frac{W_c}{3.5\,v} \tag{2.6}$$

τ_{RC} is determined by τ_{RC} =2.2 RC, where R is the sum of the diode series resistance and the load resistance, and C is the sum of the photodiode junction capacitance and the parasitic capacitance. Since the junction capacitance is dependent on the depleted area of the photodiode and the applied reverse bias (equation 2.4), faster rise time is obtained with smaller area photodiode, and larger applied reverse bias.

Therefore, the total response time of UTC-PD is determined by (2.7), and the frequency bandwidth is roughly approximated by (2.8).

$$\tau_r = \sqrt{\tau_{dif}^2 + \tau_{dft}^2 + \tau_{RC}^2} \tag{2.7}$$

$$f_{3dB} \cong \frac{0.35}{\tau_r} \tag{2.8}$$

Non-linearity

A photodiode is considered linear if its generated photocurrent increases linearly with the incident optical power. In another words, linearity exhibits the consistency of responsivity over a range of light power. Non-linearity is the variation of the ratio of the change in photocurrent to the same change in input optical power, which means $\Delta I/\Delta P$ is not constant. With the increasing of input optical power, the photocurrent starts to increase slowly at the beginning of non-linearity, and finally stays at the saturation level, where the photocurrent remains almost constant with increasing incident optical power.

2.1.4 Output power limitations

UTC-PDs have improved the output power of PIN-PDs by mitigating the space charge effect in the collection region (benefitting from electron velocity overshoot in the depletion layer). In order to widen the application fields and lengthen the transmission distance of sub-THz wireless communications, further increasing the output power of UTC-PDs at higher frequencies is desired. Figure 2.4 shows the technical points can be looked at for the purpose of increasing the output power of UTC-PDs. For the UTC-PD device itself, the epitaxy structure can be designed to optimise the electrical field inside the absorption and collection region, with the purpose to decrease space charge effect and hence to help increase the saturation power of RF signal. Thermal management is another aspect to look at to improve the output power of UTC-PDs. With more optical energy is absorbed and higher photocurrent is generated in the absorption layer, UTC-PD's internal temperature becomes higher and electrons' mobility becomes lower, which limit its photocurrent to further increase and start to saturate. If continue increasing the input optical power, the UTC-PD will have the risk of burn out. Methods to dissipating the thermal heat can benefit the photocurrent and get higher RF output power. In addition to optimising space charge effect and thermal management, increasing the optical coupling (between optical fibre and UTC-PD) and RF coupling (between UTC-PD and antenna) are also important for increasing the output power of UTC-PDs. By integrating optical waveguide into UTC-PDs and carefully designing impedance matching between UTC-PDs and

antenna, the efficiency of optical and RF coupling can be improved and the radiated RF power will be increased.

Besides increasing the output power of individual UTD-PD, power combination using an array of photodiodes is another feasible way to get higher output RF power. There are two ways of power combining: one is to use electrical power combiner circuit to multiply the photocurrent of single UTC-PD, and then feed to antenna to emit THz wave. The other way is based on spatial THz power combination by using an array of antenna-integrated UTC-PDs. In this thesis, efforts are focused on improving heat dissipation to increase the THz output power of antenna integrated UTC-PDs. The simulations of heat distribution by COMSOL and the considerations to decrease UTC-PD's temperature will be discussed in Chapter 4.

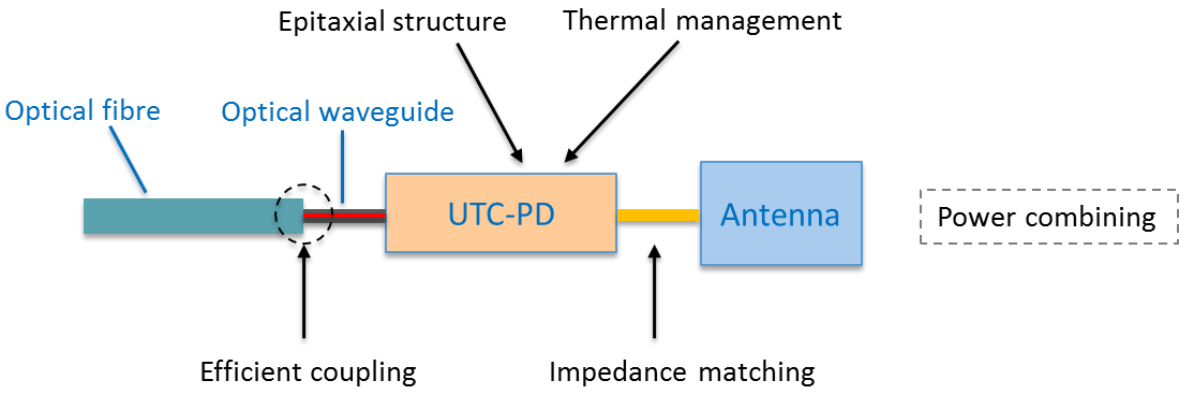

Figure 2.4: Technical points for increasing output power of UTC-PD.

2.2 Waveguide UTC-PD Grown by Solid Source MBE

Metal Organic Vapour Phase Epitaxy (MOVPE) and Gas Source Molecular Beam Epitaxy (GS-MBE) have been the predominant growth techniques for growing high quality InGaAsP material for a long time [2.10]. Until the mid-1990s, it is only possible to obtain advanced phosphide epitaxy by means of these two techniques, due to the problems associated with the high vapour pressure of white phosphorus, which is unfavourable for conventional Knudsen-type furnaces in solid-source MBE (SS-MBE) techniques [2.11]. In MOCVD and GS-MBE, arsine (AsH_3) and phosphine (PH_3) are commonly used as the source of arsenic and

phosphorus. However, AsH_3 and PH_3 are not ideal because they are toxic (needing special and expensive safety precautions) and may introduce water vapour into the reactor chamber [2.11]. Solid-source MBE enables toxic gas free growth of phosphide compound semiconductors and can realise more precise doping profiles that would be difficult to achieve by MOCVD. The first SS-MBE grown InGaAsP based UTC-PD device was demonstrated in 2012 [2.12] and showed it is possible to fabricate InGaAsP based UTC-PDs using materials grown by SS-MBE.

Though vertically illuminated UTC-PDs have shown improved 3dB bandwidth compared with conventional PIN-PDs, their geometry requires a stringent trade-off between responsivity and bandwidth. For the normal-incidence structure, high responsivity requires a thick absorption layer, which results in increased carrier transit time and reduced device bandwidth. In waveguide UTC-PDs the trade-off between responsivity and bandwidth can be eased significantly. As light travels along the epitaxial layer direction, it is evanescently coupled from the passive waveguide into the absorption layer. As a result, for a given device area and epitaxial structure (i.e. same bandwidth), a waveguide coupled UTC-PD can exhibit higher output power than a vertically illuminated UTC-PD at high frequency [2.13] [2.14]. Waveguide coupled UTC-PDs are also compatible with the implementation of a Travelling-Wave design [2.15] which can substantially improve the device RC limited response. In Section 2.2.1 and 2.2.3, the fabrication and characterisation of SS-MBE grown waveguide UTC-PDs (integrated with coplanar waveguides and antennas) are discussed respectively. Experiments to reduce leakage current are covered in Section 2.2.2.

2.2.1 Fabrication process

The UTC-PD epitaxial layer structure grown by SS-MBE is shown in Table 2.1, which was intended to achieve band gap engineering improvements (more accurately localised transitions) and more precise doping profiles. The UTC epitaxial structure was grown on an Fe-doped SI (100) InP substrate at 490°C in a Veeco Gen930 SS-MBE system [2.12], and Si and Be were used for n-type and p-type doping respectively. A 100 nm InP capping layer on top of the wafer was grown to protect the p-contact layer from oxidation. The 200 nm InGaAsP (λ_g =

1.3 μm) layer functions as a diffusion block and P-contact. The 120 nm absorption layer consists of 5 levels of $In_{0.53}Ga_{0.47}As$ with graded doping concentrations, generating the quasi-electric field which accelerates electrons to higher velocity and helps them to be swept out from the layer. Two 10 nm InGaAsP (λ_g = 1.3 μm and λ_g = 1.1 μm respectively) spacer layers, between the absorption layer and the 300 nm n-InP collection layer, are used to "smooth" the abrupt conduction band barrier at the InGaAs-InP heterojunction interface. The 300 nm InGaAsP (λ_g = 1.3 μm) waveguide layer was grown on the 600 nm n++ - InP N-contact layer.

Table 2.1: UTC-PD Layer Structure Grown By SS-MBE

Solid Source MBE UTC-PD		
Material	**Function**	**Thick (nm)**
p^{++} - $Q_{1.3}$	P contact	200
p^{+} - InGaAs	absorber	20
p^{+} - InGaAs	absorber	30
p - InGaAs	absorber	30
p - InGaAs	absorber	30
u - InGaAs	absorber	10
u - $Q_{1.3}$	spacer	10
u - $Q_{1.1}$	spacer	10
n - InP	collection	300
n^{+} - $Q_{1.3}$	waveguide	300
n^{++} - InP	N contact	600
S.I. InP	substrate	300 μm

To fabricate waveguide UTC-PDs, first need to remove the top InP capping layer with $HCl:H_3PO_4$ (1:1). Then, six mask patterns were used in sequence to fabricate the device structures. Fabrication process steps included P-contact deposition, P-contact/absorption layer etching, waveguide etching, N-contact deposition, mesa etching, passivation and via etching, illustrated in Figure 2.5. For P and N contacts, Ti / Pt / Au (75 nm / 50 nm / 400 nm) were sputtered using an SVS6000 and then processed by rapid thermal annealing (RTA) to form ohmic contacts with low contact resistivity ($\rho_c < 10^{-6}\ \Omega \cdot cm^2$). The fine device features were

achieved by dry etch processing using Reactive Ion Etching (RIE, equipment: Plasma Pro NGP80). In the four rounds of dry etching (P-contact ridge etch, waveguide etch, mesa etch and vias etch), a soft mask (S1818) was used to form the etching pattern by UV photolithography and a hard mask (SiN) was used to protect the device features during dry etching. Native oxide on the sidewall of the absorption, collection and waveguide layers (InGaAs, InP and InGaAsP respectively) contributes to surface leakage current and can increase the leakage current to several μA at -1 V reverse bias. In order to remove the unwanted oxide layer, devices were treated in 10% HCl solution for 1 min before P-contact and N-contact annealing and also before SiO_xN_y insulation layer deposition. 10% HCl solution means 10 ml HCl in 90 ml H_2O. The detail process flow and explanations for major process steps can be found in Appendix A and B respectively.

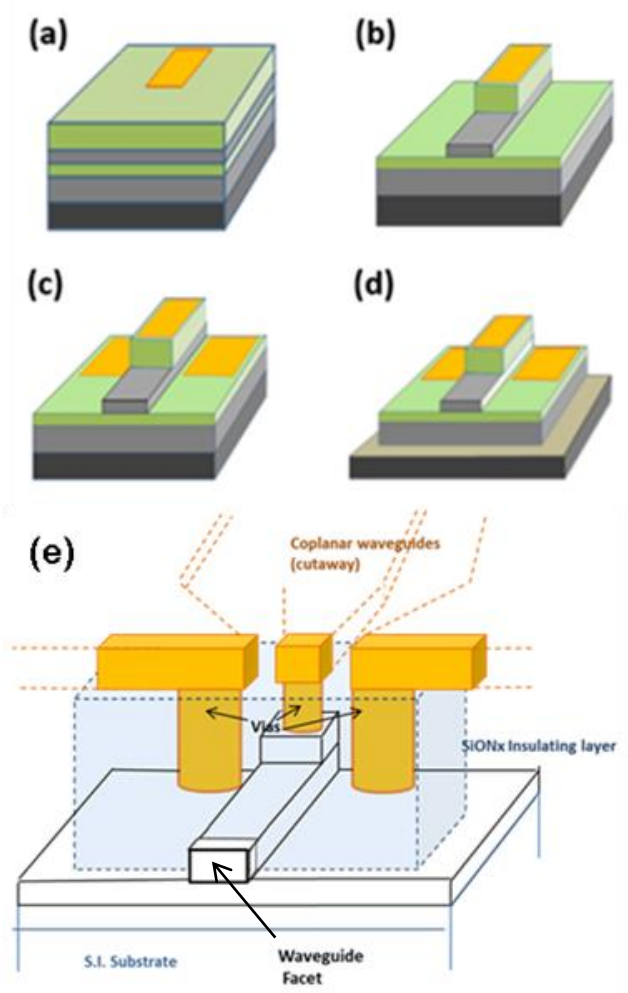

Figure 2.5: Illustration of major fabrication steps: (a) P-contact deposition, (b) P-contact ridge etching and waveguide etching, (c) N-contact deposition, (d) mesa etching and (e) passivation and via etching.

2.2.2 Leakage current optimization

2.2.2.1 Sources of leakage current in photodiodes

The reverse leakage current (I_R) of photodiodes has a bulk component (I_{RB}) flowing in the junction bulk depletion layer and a surface component (I_{RS}) flowing in the interfacial layer from the junction periphery. The I_{RS} current can have significant contribution to the total I_R current and the operational performance of devices is affected. If suitable semiconductor surface treatment is not provided, the peripheral region of the PN junction can be a path of excessive leakage reverse current even at room temperature, and the leakage current scales with the perimeter of the device. Bulk leakage mechanism consists of three main models: (i) generation and recombination (Figure 2.6 a), (ii) band-to-band tunnelling (Figure 2.6 b), and (iii) trap-assisted tunnelling (Figure 2.6 c) [2.16] [2.17].

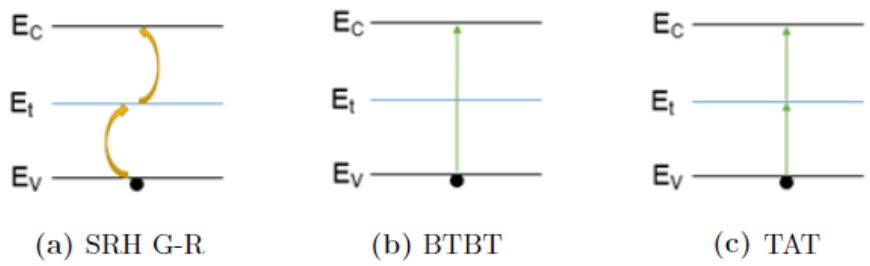

Figure 2.6: Bulk leakage current mechanisms in photodiode.

At any surface, as the solid terminates abruptly, there are unsatisfied covalent bonds (dangling bonds) that also occupy energy states in the forbidden region and lead to surface current [2.18] [2.19]. Surface passivation can tie up the dangling bonds with other atoms. Other issues like lattice damage, conductive surface oxidation also contribute to surface leakage. Lattice damage happens during drying etch process in which the acceleration potential amounts to several hundred voltages. Such high voltage causes inevitably severe lattice damage, at least deterioration of its structure which can eventually lead to a complete destruction, i.e., an amorphous surface. Reduced ion-caused lattice damage can be achieved by applying a combined dry/wet etching procedure or by etching with an inductively-coupled plasma at 13.56 MHz (e.g. helicon wave) or at 2.45 GHz

(ECRE, electron cyclotron resonance etching) [2.20]. Surface oxide comes from the oxidation during fabrication, e.g. polymer removal by O_2 plasma in etching process, or from the long time exposure in the atmosphere. For InGaAs/InP photodiode, the oxidation of As is considered as the origin of the high interface state as As-O bond provides the deep trap level in the energy band gap which accelerates the surface carrier recombination or increases the broken bonds at the interface. Diluted acid, like 10% H_2SO_4, 10% HCl, or 10% H_3PO_4, can effectively remove the native oxide without damage the photodiode structure.

2.2.2.2 Experiments and results

Waveguide UTC-PDs fabricated in December 2016 had high leakage currents. For 7x15 μm^2 devices, the average leakage current of two devices was -30.2 μA at -1V. For 4x15 μm^2 and 3x10 μm^2 devices, their leakage currents were -20 μA and -17.5 μA at -1V, respectively. As the larger size UTC-PD showed higher leakage current, we thought the surface leakage current was the major cause for the high leakage current. Three mechanisms contribute to the surface leakage current: lattice damage, dangling bond and surface oxidation. As we did the sidewall damage treatment by the buffered HF after waveguide etching and mesa etching, we thought the lattice damage was not the main cause for the high leakage current. SiO_xN_y passivation should lower the impact of dangling bonds on surface leakage currents. Therefore, the surface oxidation had the high possibility to be the main contribution to the high leakage current. Diluted acid solution can effectively clean the native oxide on the surface of photodiodes. In order to select appropriate acid solution for UTC-PDs, first we did experiments to check 3 types of diluted acid solutions' etch rate on materials of UTC-PDs. Then, we used the selected acid solutions to do experiments to compare their effectiveness on removing native oxide on UTC-PDs.

Acid Selection

The oxides of InP, InGaAs and InGaAsP are formed during the O_2 plasma etching and when UTC-PDs exposed to the atmosphere before passivation. The oxides from O_2 plasma are much thicker than from the air. For example, for InP, the O_2 plasma reaction formed oxides is ~100 Å and 5 times thicker than the oxides

formed in the air (~20 Å). The oxides of InP can be removed by soaked in 1% HCl for 2 min [2.21] and in 10% H_2SO_4 less than 1 min [2.22]. For InGaAs, its oxides can be cleaned by 10% HCl in 1 min and by 5% H_2SO_4 in 30 seconds [2.23]. Besides, 10% H_3PO_4 was reported to dissolve the oxide of InP [2.22] and clean the sidewall of UTC-PDs in 2 min [2.24]. Therefore, 10% HCl, 10% H_2SO_4 and 10% H_3PO_4 are candidates for removing the oxide layer on the sidewall of UTC-PDs. As HCl etches InP, H_2SO_4 and H_3PO_4 etch both InGaAs and InGaAsP (shown in Table 2.2), it is necessary to check whether the diluted HCl (10%) etches InP and whether 10% H_2SO_4 and 10% H_3PO_4 etches InGaAs and InGaAsP before using them to remove oxides of UTC-PDs.

Table 2.2: Wet chemical etchant selectivity on materials

	Material Selectivity											
Etchant	GaAs	InP	InGaAs	InGaAsP	GaInP	GaAsP	AlGaP	AlGaAs	AlInP	InAlAs	InGaAlAs	SiO2
HCL : H_3PO_4	S	E	S	S	E				E			
H_3PO_4 : H_2O_2 : H_2O	E	S	E		S							
H_2SO_4 : H_2O_2 : H_2O	E	S	E	E								
$C_6H_8O_7$: H_2O_2	CD	S	CD					CD		CD		
HCL : HNO_3 : H_2O	E	E					E		E			
HNO_3 : H_2SO_4 : H_2O	E					E						
HCL : H_2O_2 : H_2O	E	E				E						
HCL : H_2O	S	E	S						E	CD	CD	
BHF : H_2O								CD				E

Legend			
Etches	Selective/Stops	Composition Dependent	No Data
E	S	CD	

As the etch rate on InP < 0.1 nm/min when the concentration of HCl $\leqslant$ 2M [2.25], the native oxide can be effectively removed by 10% HCl solution (1 min) without significantly etching the InP surface. For 10% H_2SO_4 and 10% H_3PO_4, no reported evidence was found on whether such concentration etches InGaAs / InGaAsP or not, so need to do experiment to confirm it. In the etch rate experiment, S1818 was spinned as pattern mask and DektakXT was used to measure the etch depth (its vertical resolution is 0.1 nm). InGaAs and InGaAsP were soaked in 10% H_2SO_4 up to 12 min respectively, and the measurement didn't show obvious etch impact. The two materials were also soaked in 10%

H_3PO_4 up to 30 min and again the depth measurement didn't detect the etching effect. To verify our experiment method was correct, we used same mask and measurement equipment to do the etch rate measure for H_2SO_4:H_2O_2:H_2O (1:1:10). The measured etch rate for InGaAs was around 0.18 μm/min and for InGaAsP was around 0.07 μm/min, which are very close to the reported values (0.2 μm/min and 0.08 μm/min) in [2.26]. Therefore, without adding H_2O_2 into the diluted H_2SO_4 and H_3PO_4 solution, 10% H_2SO_4 and 10% H_3PO_4 have no etching effect on InGaAs and InGaAsP.

Based on above experiments, 10% HCl, 10% H_2SO_4 and 10% H_3PO_4 are safe to be used to remove the oxide layer on the sidewall of UTC-PDs. Different from HCl and H_3PO_4, H_2SO_4 etches the surface of InP, and forms a thick and fragile oxide cap that can be washed away during a subsequent water rinse step [2.21]. As no report was found whether the oxide cap layer on InGaAs/InGaAsP after H_2SO_4 treatment could be washed away by water rinse, 10% HCl and 10% H_3PO_4 solutions were chosen to be used to clean the sidewall oxide in the following experiments.

Experimental Results

As the available smallest size of probe pins is ϕ 2.4 μm, it is not easy to probe the P-contact of our UTC-PDs (3x10 μm^2, 3x15 μm^2, 4x15 $\mu m^2$and 7x15 μm^2). In order to monitor the leakage current change during the fabrication, test structure devices (5 times larger than real size devices) were used to do the dark current measurement. After the mesa etching step, two groups of test structure samples were treated in 10% HCl for 1 min and in 10% H_3PO_4 for 2 min, respectively. For each test structure sample, the leakage current was measured before and after the acid treatment. Figure 2.7 shows the leakage current changes after 10% HCl treatment, and Figure 2.8 shows the changes after 10% H_3PO_4 treatment. The plotted graphs clearly show: (i) leakage currents are decreased after both 10% HCl and 10% H_3PO_4 treatment; (ii) 10% HCl has better effect to reduce leakage current than 10% H_3PO_4, and its treatment can lower leakage currents less than 1 μA (at -1V) for 5 times bigger test structure devices. The experimental results demonstrate 10% HCl is an effective solution to reduce the sidewall leakage current of UTC-PDs.

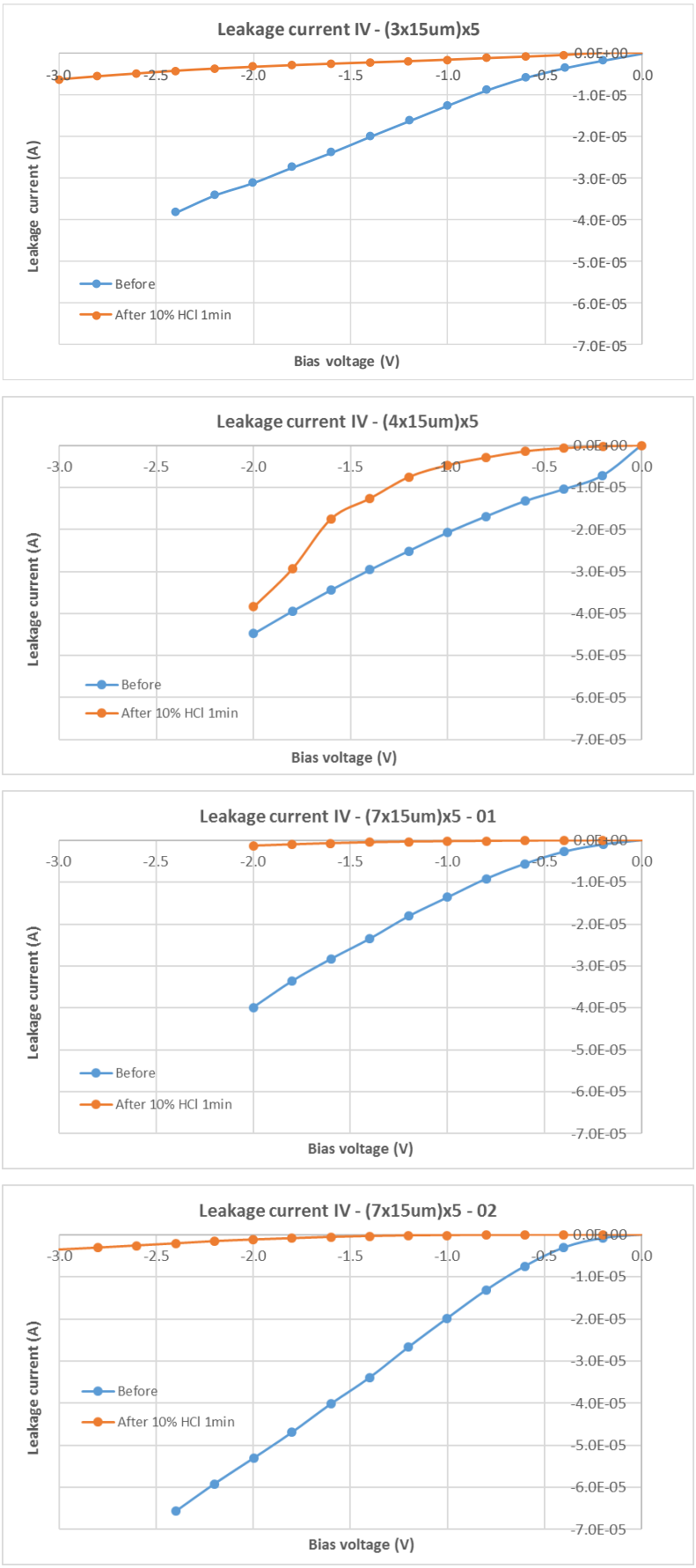

Figure 2.7: Leakage current of before and after 10% HCl treatment (1 min)

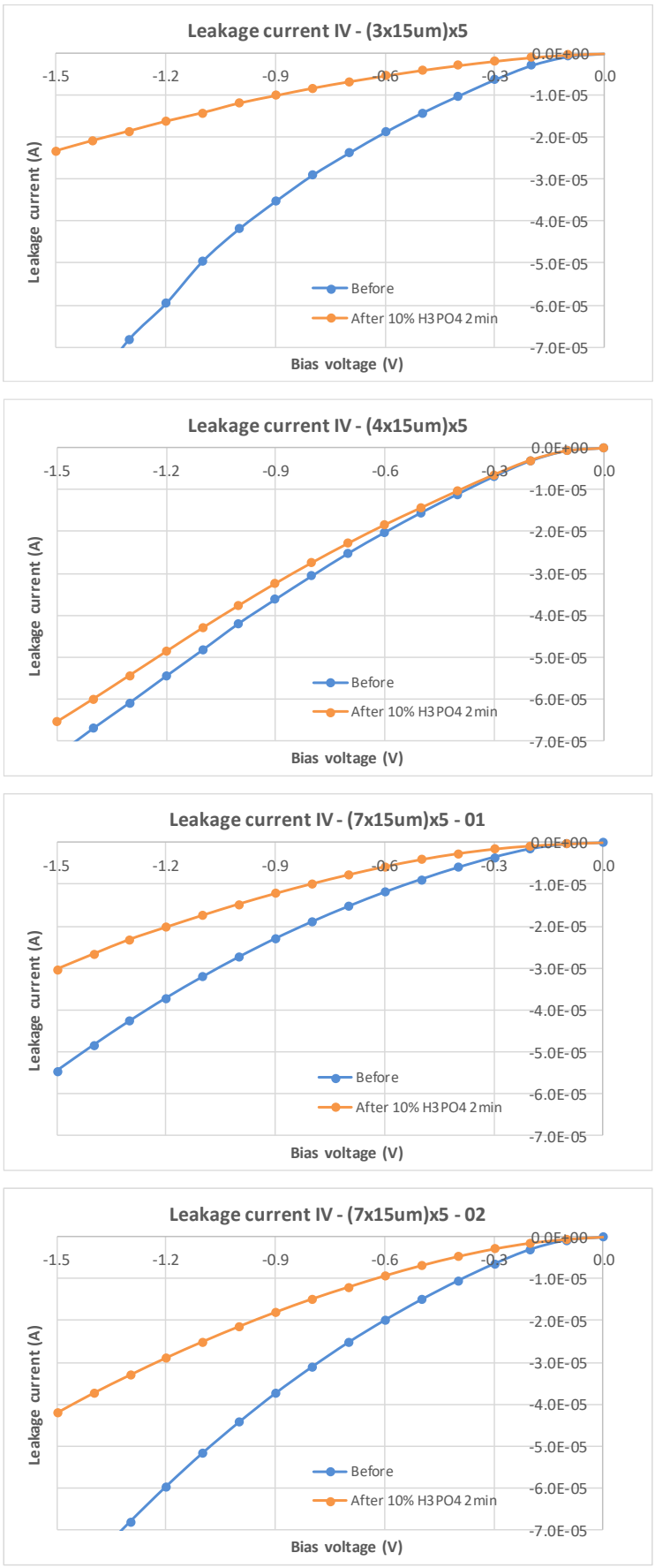

Figure 2.8: Leakage current of before and after 10% H_3PO_4 treatment (2 min)

It was also observed the leakage current increased after SiO_xN_y insulation layer deposition by PECVD (Plasma Enhanced Chemical Vapour Deposition), see Figure 2.9, which was proceeded under 300°C inside the chamber. This degradation in the leakage current is probably related to the plasma damage on the surface of UTC-PDs. As the sample surface was exposed to plasma, significant damage may occur on the surfaces during SiO_xN_y deposition [2.27]. Studies have indicated that the recombination velocity of InGaAs on the sidewall, covered with low- temperature-deposit SiN_x passivation layer formed by ICPCVD (Inductive Coupled Plasma Chemical Vapour Deposition), was much lower than that formed by PECVD [2.28]. To further reduce the leakage current of UTC-PDs, low temperature ICPCVD is an alternative way to try.

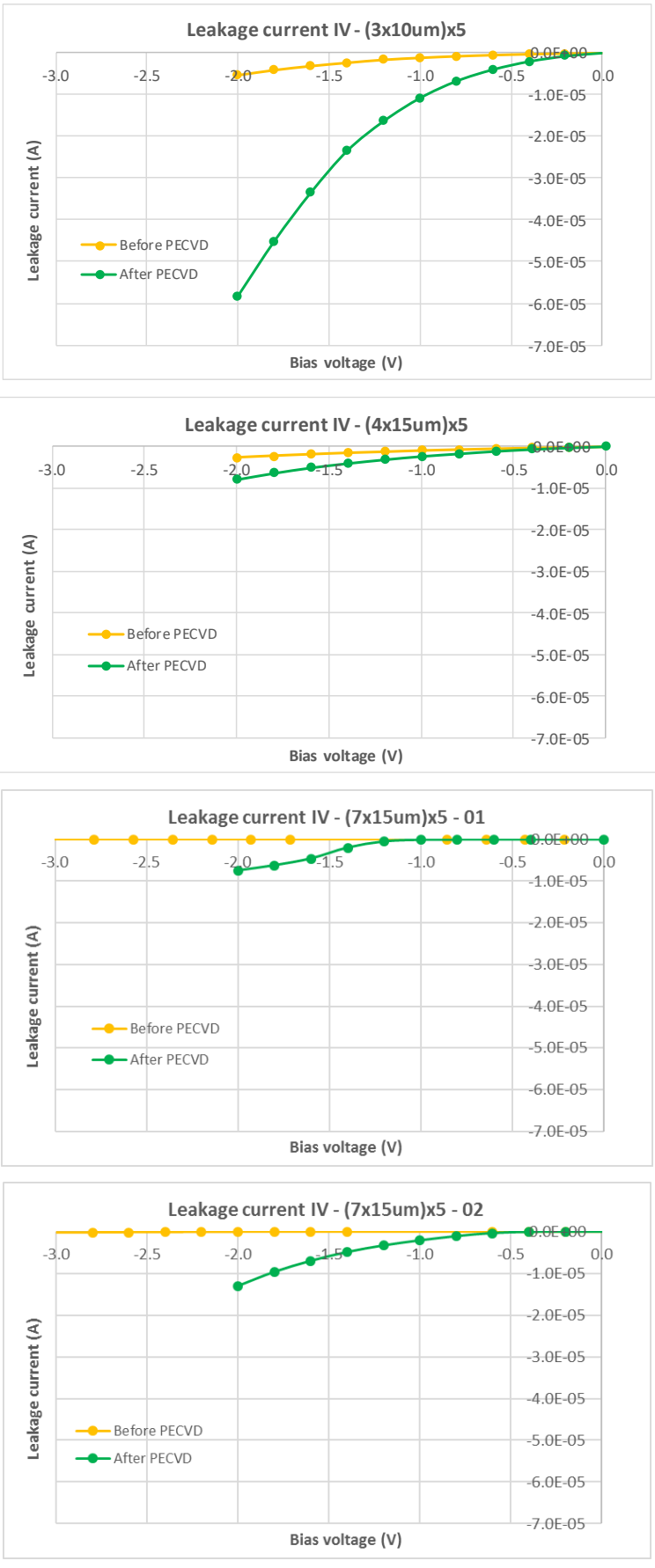

Figure 2.9: Leakage current before and after SiO_xN_y passivation by PECVD.

2.2.3 Device characterisation

2.2.3.1 Coplanar waveguide coupled UTC-PDs

After 2 μm thick SiO_xN_y was deposited to cover the whole UTC-PD as a passivation and insulation layer, Ti/Au coplanar waveguides (CPW) were sputtered on top of the device to allow RF power to be extracted and measured by means of air coplanar ground-signal-ground probes. Vias (connecting P/N contacts with CPW) were etched through SiO_xN_y down to P-contact and N-contact before CPW deposition. Figure 2.10 shows the photo of a fabricated 3 x 15 μm^2 CPW UTC-PD. The light coming from the lensed fibre is coupled into UTC-PD through the passive waveguide.

Figure 2.10: Fabricated 3x15 μm^2 CPW UTC-PD.

Typical fabricated CPW integrated UTC-PDs have exhibited dark currents of less than 100 nA at −1V reverse bias, see Figure 2.11. As shown in Figure 2.12 (a) and (b), responsivities up to 0.19 A/W and 0.22 A/W were measured for 4×15 μm^2 and 7×15 μm^2 devices respectively, at -2V bias voltage and without applying anti-reflection coating on the facet of waveguides. In waveguide UTC-PDs, the InGaAsP waveguide layer beneath the collection layer enables evanescent coupling into the absorption layer, and increases the responsivity of UTC-PDs because it increases the length over which the absorption takes place [2.29].

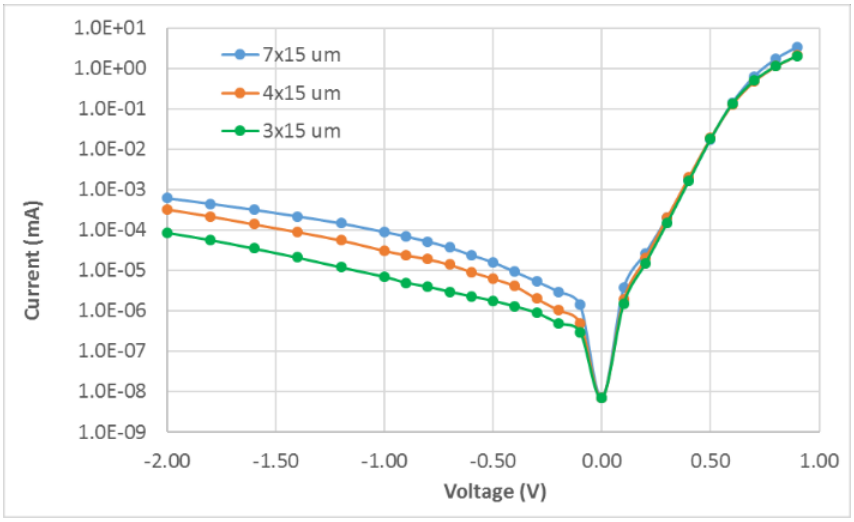

Figure 2.11: I-V curve of CPW UTC-PDs with treatment by 10% HCl (1 min). The dark current is plotted as absolute value.

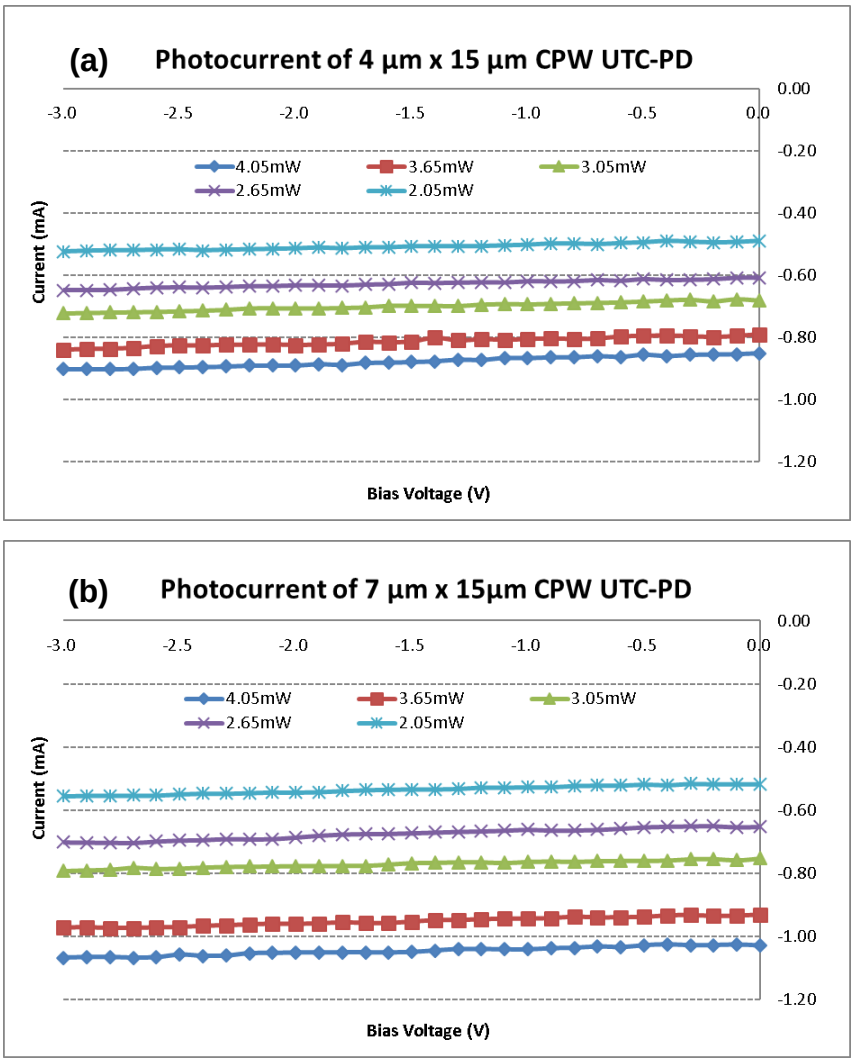

Figure 2.12: Measured photocurrent of CPW UTC-PDs with different input optical power at bias voltage 0V to -3V. Responsivities for 4×15 µm^2 and 7×15 µm^2 devices at -2V were 0.19 A/W and 0.22 A/W, respectively.

The device frequency response, measured by the Lightwave Component Analyser (calibrated to open, short and 50 Ω load), is plotted in Figure 2.13. The devices were biased with -2V voltage and the input 1550nm optical power was 5 dBm. As shown in Figure 2.13, the 7×15 μm^2 and 4×15 μm^2 devices exhibited 3 dB bandwidth of 47 GHz and 65 GHz respectively, while the 3 ×10 μm^2 device exhibited bandwidth greater than 67 GHz. The 3dB bandwidth is enhanced by the graded doping in the absorption layer. The graded doping in the p-type UTC absorption layer yields a potential gradient, and hence a quasi-field, which effectively accelerates electrons in the direction of decreasing doping levels, i.e. from the absorption towards the collection layer.

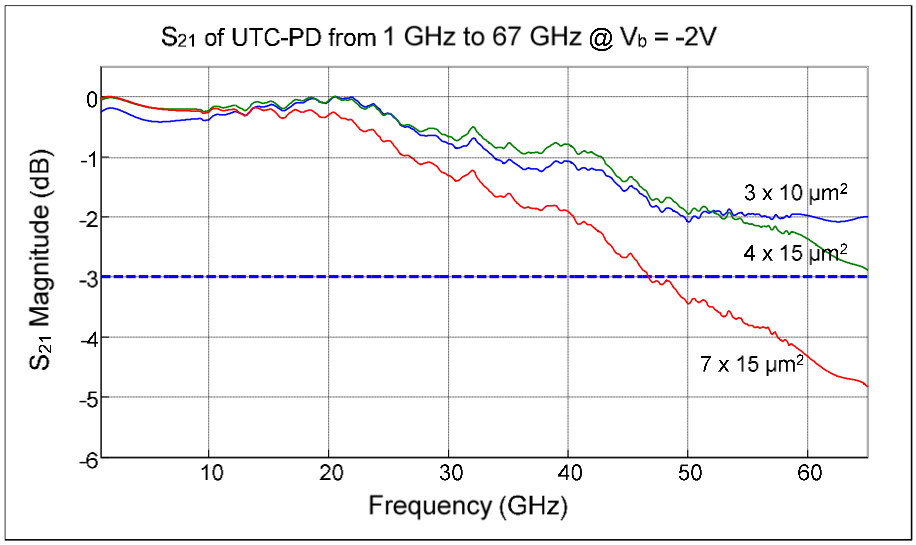

Figure 2.13: Frequency response from 1 GHz to 67 GHz of CPW coupled UTC-PDs.

The output power of CPW coupled waveguide UTC-PDs was extracted with W-band (75-110 GHz) coplanar probe coupled to an Agilent E4418B EPM series power meter via a Flann flexible W-band waveguide. The good agreement on power measurement between spectrum analyser and EPM series power meter is illustrated in [2.30]. The experimental arrangement for CPW UTC-PD power measurement is shown in Figure 2.14. The laser tones from laser 1 and laser 2 were adjusted to generate an optical heterodyne frequency of 100 GHz. Two polarization controllers were used on each laser output to set the laser

polarisations to the same state. The optical tones were then combined in a 50:50 coupler and amplified using an Erbium Doped Fibre Amplifier (EDFA). An Amplified Spontaneous Emission (ASE) filter was placed after the EDFA to reduce the contribution from ASE to the photocurrent. The optical beat signal was coupled to the UTC-PD waveguide via a lensed optical fibre with a 2.5 μm (diameter) spot size. A polarization controller was included before the lensed fibre to optimize the coupling of light to the waveguide. Reverse bias was applied to the device via the integrated bias tee in the coplanar probe. Throughout the measurements, the device was cooled using a Peltier cooler set to 20°C. In order to make reliable and precise measurements, the experiment systems need to be stable and well designed to eliminate noises/error sources. Error sources from surroundings and measurement layout are discussed in Appendix C.

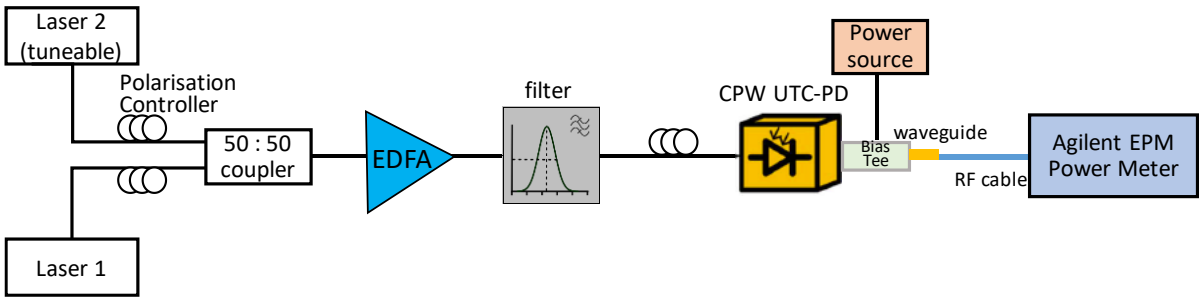

Figure 2.14: CPW coupled UTC-PD output power measurement arrangement.

The RF power dependence on average photocurrent is plotted as a function of reverse bias voltage in Figure 2.15. The maximum RF power obtained increases with reverse bias voltage. The maximum RF power recorded was 1.1 dBm with a photocurrent of 13.1 mA and reverse bias of 3V. Comparable powers were measured from our previous state-of-the-art UTC-PDs in [2.13] (0.8 dBm output power at 110 GHz at 13 mA photocurrent and -2V bias). For the device evaluated in this experiment, thermal management was impeded by a substrate thickness of 350 μm. Reduced substrate thickness enabled photocurrents up to 36 mA to be reached in [2.13], yielding a record output power of 10 dBm. High powers at 100 GHz have also been obtained using narrow-band matching circuits [2.31], or flip chip bonding [2.32] of a vertically illuminated Modified UTC-PD (MUTC-PD) with an inductive peaking circuit have been incorporated into the device design.

RF Powers of 13.2 dBm and 9 dBm for the respective devices were recorded. However, the higher emitted power comes at the expense of reduced bandwidth.

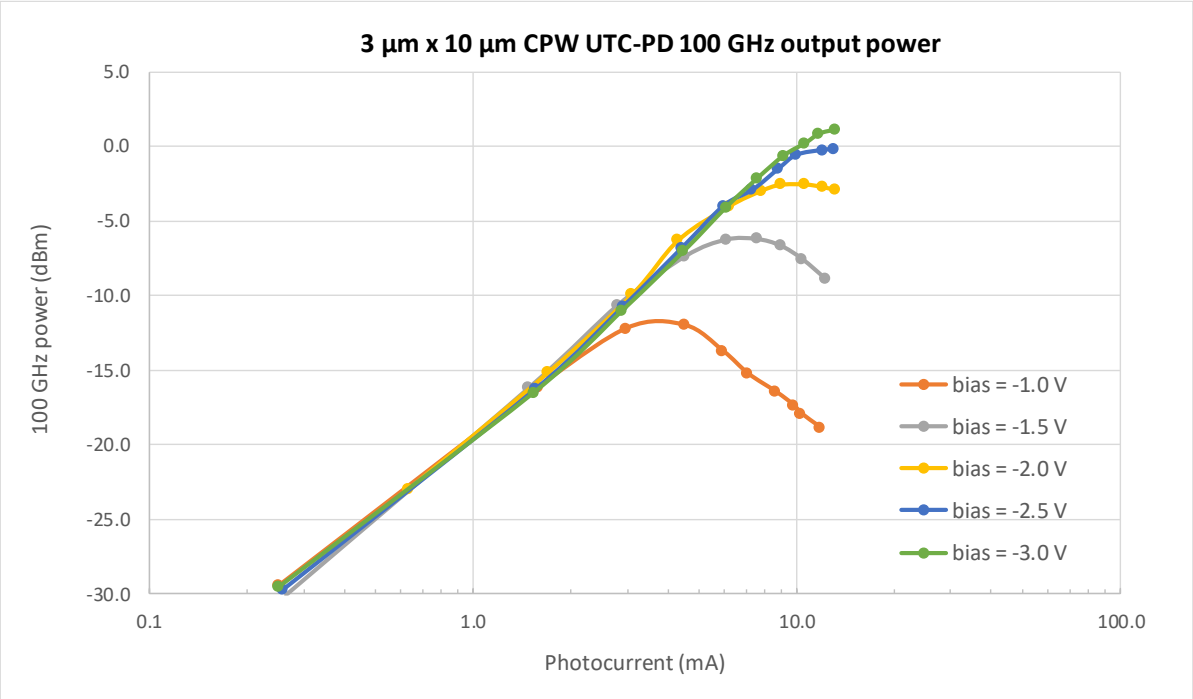

Figure 2.15: RF Output power vs photocurrent of a 3 µm × 10 µm CPW UTC-PD at 100 GHz as a function of bias.

2.2.3.2 Antenna integrated waveguide UTC-PDs

The antenna structure of Figure 2.16 (b) was deposited on the SiO_xN_y insulation layer. The deposited antenna was connected to UTC-PD's P-contact and N-contact through via holes as narrow as 2 µm. The 2 µm fine features were achieved by RIE processing. The antenna impedance had been designed to realise complex-conjugate matching to the UTC-PD in [2.33] at a frequency of 250 GHz. The total power emitted by an antenna depends on the impedance match with the driving source and the radiation efficiency. The absolute level of power emitted by an antenna over the frequency range can be calculated and predicted if the UTC impedance is known and the coupling efficiency between UTC and antenna taken into account [2.33] [2.34]. The use of a Silicon lens combined with antenna integrated UTC-PDs is an established solution to couple THz power into free space [2.35]. The design of antenna integrated UTC-PD assembled with a Si lens is shown in Figure 2.16 (a). Its far field radiation pattern

and directivity at 250 GHz, calculated with 3D full-wave modelling, is shown in Figure 2.17 [2.36].

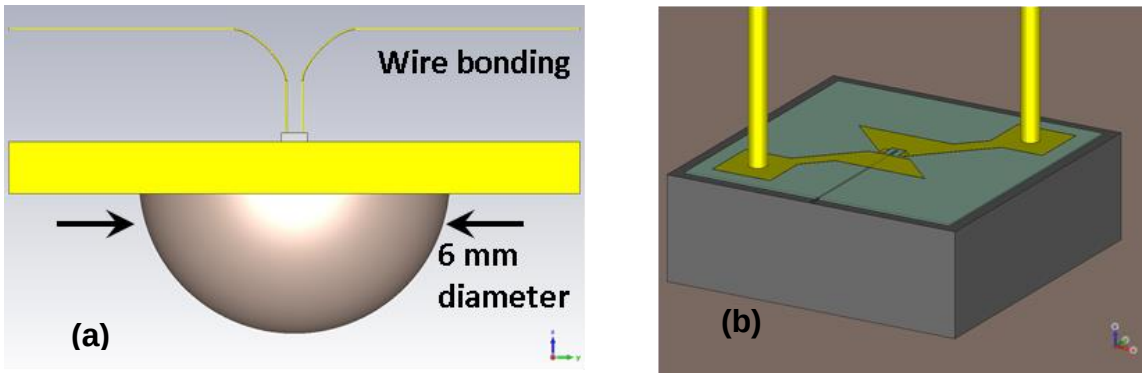

Figure 2.16: Wire-bonded antenna integrated UTC-PD on Si lens (D = 6 mm).

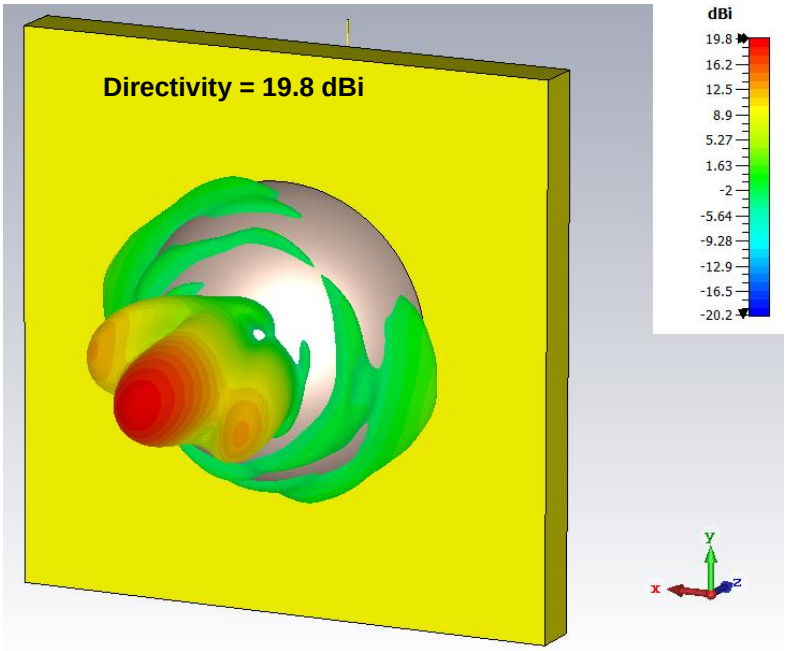

Figure 2.17: The far field radiation pattern and directivity at 250 GHz of antenna integrated UTC-PDs (4x15 μm^2) assembled with a Si lens [2.36].

By means of 3D full-wave modelling and using the knowledge of UTC impedance [2.34] [2.35], the absolute level of power emitted by antenna integrated UTCs with Si lenses can be calculated, shown in Figure 2.18, for 10 mA and 13.5 mA photocurrent. The power radiated by our fabricated antenna-integrated UTC-PD

was measured with a Thomas Keating opto-acoustic power sensor from 200 GHz to 260 GHz. The test device had a P-contact ridge size of 4×15 μm^2, and it was mounted on a 6 mm diameter Si lens and wire-bonded. The experimental arrangement is shown in Figure 2.20. The measured leakage current of UTC-PD was below 100 nA at -1V bias and the responsivity was 0.14 A/W. At -2.6 V DC bias, the measured radiated powers at 250 GHz were 32 μW and 60 μW, with photocurrent of 10 mA and 13.5 mA respectively. The measured radiated powers (200 GHz to 260 GHz) plotted in Figure 2.18 show good agreement with the numerical results. The radiated RF power is relatively low because the bow-tie antenna was not impedance matched with its UTC-PD, as the antenna had been designed to be impedance matched with the UTC-PDs in [2.33]. The radiated powers calculated for the case of the antenna driven by the impedance matched UTCs in [2.33], are plotted in Figure 2.19, for photocurrents of 10 mA and 20 mA. Figure 2.19 shows for 10 mA photocurrent the calculated RF power is 124 μW at 250 GHz, 5 times higher than the calculated power (23 μW) plotted in Figure 2.18.

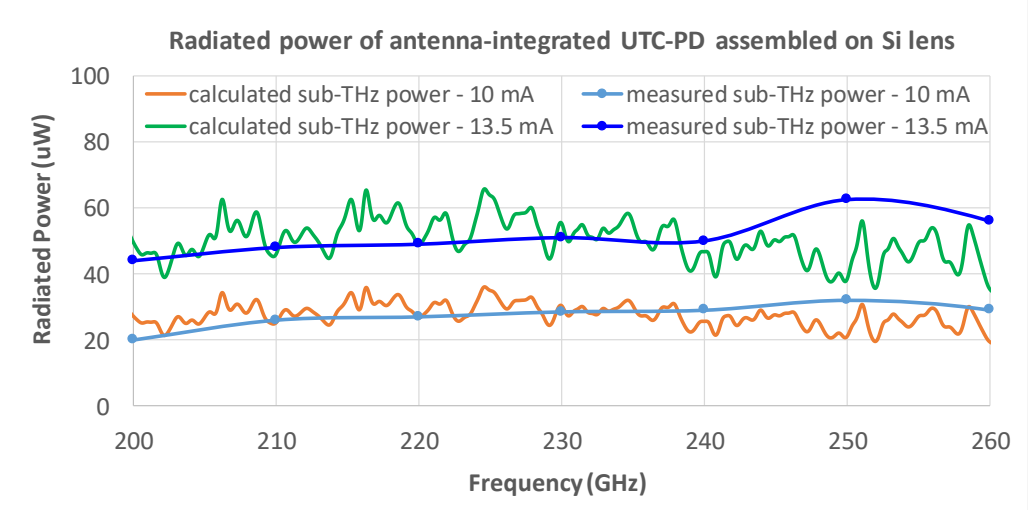

Figure 2.18: Power radiated by antenna integrated UTC-PDs (4×15 μm^2) mounted on a 6 mm diameter Si lens at the bias of -2.6 V. Here the antenna is not impedance matched with the UTC-PDs.

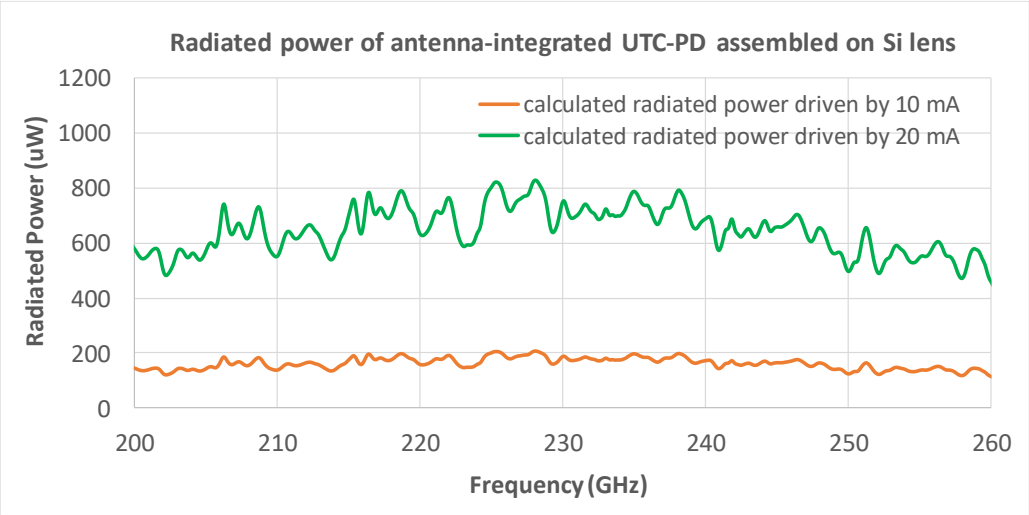

Figure 2.19: Calculated power radiated by antenna integrated UTC-PDs (4×15 μm^2) mounted on a 6 mm diameter Si lens, with antenna impedance matched with UTC-PD impedance.

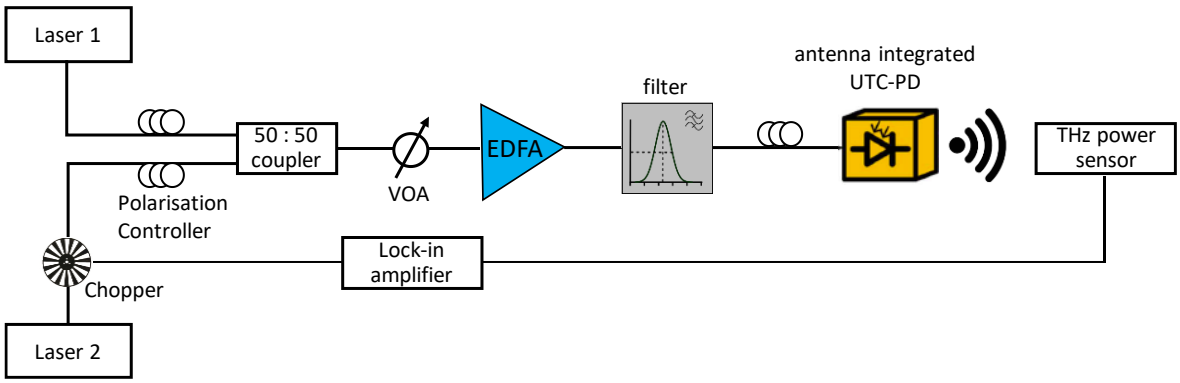

Figure 2.20: Radiated RF power measurement arrangement. VOA indicates a variable optical attenuator.

2.3 Conclusions

In this Chapter waveguide UTC-PDs fabricated on InGaAsP-based epitaxial structures grown by SS-MBE, to combine the merits of InGaAsP materials for UTC-PD performance with the advantages of SS-MBE, was reported. CPW integrated UTC-PDs and antenna integrated UTC-PDs were fabricated and

characterised. CPW integrated UTC-PDs of 4×15 μm^2 and 7×15 μm^2 ridge area, exhibited responsivities of 0.19 A/W and 0.22 A/W respectively. The 3×15 μm^2 devices achieved 3 dB bandwidths greater than 65 GHz at -2V DC bias. For CPW integrated UTC-PDs, the 100 GHz output power of > 1 dBm were obtained for an average photocurrent of 13 mA. For bow-tie antenna integrated UTC-PDs, the radiated RF power was measured from 200 GHz to 260 GHz, which was consistent with the predictions from full-wave modelling by CST Studio Suite.

To enable UTC-PDs to operate at high bias voltage, dark currents need to be controlled to low level. Native oxide on the sidewall of the absorption, collection and waveguide layers contributes to surface leakage current and can worsen the leakage current to several μA at -1V bias. Experiments were done to compare the effect of 10% HCl and 10% H_3PO_4 treatment as oxide layer remover. Measurement results show 10% HCl solution is more effective reducing leakage current than 10% H_3PO_4 solution. By soaking in 10% HCl for 1 min after the mesa etching step, typical fabricated CPW integrated UTC-PDs exhibit dark currents of 7 nA, 31 nA and 90 nA at -1V bias for 3×15 μm^2, 4×15 μm^2 and 7×15 μm^2 devices respectively.

2.4 References

[2.1] J. Paslaski, P. C. Chen, J. S. Chen, C. M. Gee, and N. Bar-Chaim, “High power microwave photodiode for improving performance of RF fiber optic links,” Proc. SPIE (Photon. Radio Freq.), vol. 2844, pp. 110-119, (1996).

[2.2] M. S. Islam, A. Nespola, M. Yeahia, M. C. Wu, D. L. Sivco, and A. Y. Cho, “Correlation between the failure mechanism and dark currents of high power photodetectors,” Proc. Lasers and Electro-Optics Society 2000 Annu. Meeting, vol. 1, pp. 82-83, (2000).

[2.3] Atsushi Wakatsuki, Yoshifumi Muramoto, and Tadao Ishibashi, “Development of Terahertz-wave Photomixer Module Using a Uni-traveling-carrier Photodiode”, NTT Technical Review, vol. 10, no. 2, (2012).

[2.4] K. Kato, “Ultrawide-band/high-frequency photodetectors,” IEEE Transactions on Microwave Theory and Techniques, vol. 47, no. 7, pp. 1265-1281, (1999).

[2.5] Ishibashi T, Shimizu N, Kodama S, et al, “Uni-traveling carrier photodiodes”, Proceedings of Ultrafast Electronics and Optoelectronics (UEO’97), pp. 166–168, (1997).

[2.6] H. Ito, S. Kodama, Y. Muramoto, T. Furuta, T. Nagatsuma, and T. Ishibashi, “High-Speed and High-Output InP-InGaAs Unitraveling-Carrier Photodiodes,” IEEE Journal of Selected Topics in Quantum Electronics, vol. 10, no. 4, pp. 709-727, (2004).

[2.7] Molly Piels, Darko Zibar, “Markov chain Monte Carlo methods for statistical analysis of RF photonic devices”, Optics Express vol. 24, no 3, pp. 2084-2097 (2016).

[2.8] T. Nagatsuma, H. Ito, and T. Ishibashi, “High-power RF photodiodes and their applications,” Laser Photonics Rev., vol. 3, no. 1–2, pp. 123–137, (2009).

[2.9] A. Beling and J. C. Campbell, “Advances in photodetectors and optical receivers,” in Optical Fiber Telecommunications Volume VIA: Components and Subsystems. Academic Press, (2013).

[2.10] C. C. Wamsley, M. W. Koch, and G. W. Wicks, “Solid source molecular beam epitaxy of InGaAsP/InP: growth mechanisms and machine operation,” J. Vac. Sci. Technol. B, vol. 14, no. 3, pp. 2322–2324, (1996).

[2.11] M. Pessa, M. Toivonen, M. Jalonen, P. Savolainen, and A. Salokatve, “All-solid-source molecular beam epitaxy for growth of III–V compound semiconductors,” Thin Solid Films, vol. 306, issue. 2, pp. 237-243, (1997).

[2.12] Michele Natrella, Efthymios Rouvalis, Chin-Pang Liu, Huiyun Liu, Cyril C. Renaud, and Alwyn J. Seeds, “InGaAsP-based uni-travelling carrier photodiode structure grown by solid source molecular beam epitaxy”, Optics Express, vol. 20, no.17, pp. 19279-19288, (2012).

[2.13] C. Renaud, D. Moodie, M. Robertson, and A. Seeds, “High output power at 110 GHz with a waveguide uni-travelling carrier photodiode,” The 20th Annual Meeting of the IEEE, pp. 782–783, (2007).

[2.14] C. Renaud, M. Robertson, D. Rogers, R. Firth, P. Cannard, R. Moore, and A. Seeds, “A high responsivity, broadband waveguide uni-travelling carrier photodiode,” Proc. SPIE, vol. 6194, 61940C, (2006).

[2.15] K. S. Giboney, M. J. W. Rodwell, and J. E. Bowers, “Traveling-Wave photodetector design and measurements,” IEEE J. Sel. TopicsQuantum Electron., vol. 2, no. 3, pp. 622-629, (1996).

[2.16] B. Chen, J. Yuan, and A. L. Holmes Jr, “Dark current modeling of InP based SWIR and MWIR InGaAs/GaAsSb type-II MQW photodiodes”, Optical and Quantum Electronics, vol. 45, no. 3, pp. 271-277, (2013).

[2.17] S. Mookerjea, D. Mohata, T. Mayer, V. Narayanan, and S. Datta, “Temperature-dependent I-V characteristics of a vertical $In_{0.53}Ga_{0.47}As$ tunnel FET”, IEEE Electron Device Letters, vol. 31, no. 6, pp. 564-566, (2010).

[2.18] W. Shockley, “On the surface states associated with a periodic potential", Phys. Rev., vol. 56, pp. 317-323, (1939).

[2.19] I. Tamm, “About a possible method of electron binding on crystal surfaces”, Journal of Physics, vol. 76, pp. 849-850, (1932).

[2.20] M. Heinbach, J. Kaindl, and G. Franz, “Lattice damage in III/V compound semiconductors caused by dry etching”, Appl. Phys. Lett. vol. 67, no. 14, pp. 2034-2036, (1995).

[2.21] O. Pluchery, Y. J. Chabal, R. L. Opila, “Wet chemical cleaning of InP surfaces investigated by in situ and ex situ infrared Spectroscopy”, Journal of Applied Physics, vol. 94, no. 4, pp. 2707-2715, (2003).

[2.22] Felix Schmitt and Nobuhiko Susa, “An Etchant for InP Native Oxide”, Jpn. J. Appl. Phys, vol. 22, no. 4, (1983).

[2.23] Yun Suna and Piero Pianetta, “Arsenic-dominated chemistry in the acid cleaning of InGaAs and InAlAs surfaces”, Applied Physcis Letters, vol. 93, 194103, (2008).

[2.24] Longfei, Shen, “Ultrafast photodetector on the InP-membrane-on-silicon platform”, PhD thesis, (2016).

[2.25] D. H. van Dorp, D. Cuypers, S. Arnauts, A. Moussa, L. Rodriguez, and S. De Gendt, “Wet Chemical Etching of InP for Cleaning Applications (II. Oxide Removal)”, ECS Journal of Solid State Science and Technology, vol. 2, no. 4, pp. 190 - 194, (2013).

[2.26] Donato Pasquariello, E. Staffan Björlin, Member, IEEE, Daniel Lasaosa, YiJen Chiu, Joachim Piprek, Senior Member, IEEE, and John E. Bowers, Fellow, IEEE, “Selective Undercut Etching of InGaAs and InGaAsP Quantum Wells for Improved Performance of Long-Wavelength Optoelectronic Devices”, Journal of Lightwave Technology, vol. 24, no. 3, pp. 1470-1477, (2006).

[2.27] M.R. Ravi, Amitava DasGupta, Nandita DasGupta, “Silicon nitride and polyimide capping layers on InGaAs/InP PIN photodetector after sulfur treatment”, Journal of Crystal Growth, vol. 268, pp. 359 - 363, (2004).

[2.28] Ying Zhou, Xiaoli Ji, Ming Shi, Hengjing Tang, Xiumei Shao, Xue Li, Haimei Gong, Xun Cao, and Feng Yan, “Impact of SiNx passivation on the surface properties of InGaAs photo-detectors”, Journal of Applied Physics, vol. 118, 034507, (2015).

[2.29] Alwyn Seeds, Cyril Renaud, Michael Robertson, “Photodetector Including Multiple Waveguides”, U.S. Patent 7851782 B2, (2010).

[2.30] E. Rouvalis, C. Renaud, D. Moodie, M. Robertson, and A. Seeds, “Continuous wave terahertz generation from ultra-fast InP-based photodiodes,” IEEE Trans. Microw. Theory Tech., vol. 60, no. 3, pp. 509 – 517, (2012).

[2.31] H. Ito, T. Nagatsuma, A. Hirata, T. Minotani, A. Sasaki, Y. Hirota, T. Ishibashi, “High-power photonic millimetre wave generation at 100 GHz using matching-circuit-integrated uni-travelling-carrier photodiodes”, IEE Proceedings – Optoelectronics, vol. 150, no. 2, pp.138-142, (2003).

[2.32] Andreas Beling, Jesse S. Morgan, Keye Sun, Qianhuan Yu, “High Power Integrated 100 GHz Photodetectors”, International Topical Meeting on Microwave Photonics (MWP), (2018).

[2.33] M. Natrella, C.-P. Liu, C. Graham, F. van Dijk, H. Liu, C. C. Renaud, and A. J. Seeds, “Accurate equivalent circuit model for millimetre-wave UTC photodiodes,” Optics Express, vol. 24, no. 5, pp. 4698 – 4713, (2016).

[2.34] Michele Natrella, Chin-Pang Liu, Chris Graham, Frederic van Dijk, Huiyun Liu, Cyril C. Renaud, and Alwyn J. Seeds, “Modelling and measurement of the absolute level of power radiated by antenna integrated THz UTC photodiodes,” Opt. Express, vol. 24, no. 11, pp. 11793-11807, (2016).

[2.35] J. Van Rudd and D. M. Mittleman, “Influence of substrate-lens design in terahertz time-domain spectroscopy,” JOSA B, vol. 19, no. 2, pp. 319 - 329, (2002).

[2.36] Xiaoli Lin, Michele Natrella, James Seddon, Chris Graham, Cyril C. Renaud, Mingchu Tang, Jiang Wu, Huiyun Liu, and Alwyn J. Seeds, "High performance waveguide uni-travelling carrier photodiode grown by solid source molecular beam epitaxy", Optics Express, vol. 27, no. 25, pp. 37065 - 37086, (2019).

Chapter 3
Waveguide UTC-PD Saturation Power Measurement

3.1 Introduction

Electrical current is generated when optical power is absorbed by photodiodes. Increasing the input optical power can get higher photocurrent. However, at high optical input power, the incident optical power and its generated RF output power do not follow the relationship at lower photocurrents. The photodiode (PD) starts to get saturated. The primary factor that limits the saturation power of a photodiode is the carrier screening of the internal electric field, which is referred to as the space-charge effect. The space charge effect reduces the internal total electric field in the depletion region and slows down the carrier drifting velocity. As a result, the carrier takes longer time to pass through the depletion region and the output photocurrent saturates. In the conventional PIN-PD, holes have a much lower drift velocity than electrons, therefore holes' transport dominates the space charge effect and saturation behaviour. For uni-traveling-carrier photodiodes (UTC-PDs), only electrons act as the active carriers which make UTC-PDs have the ability of running at higher current densities. Though UTC-PDs work faster than PIN-PDs, the power saturation still exists and occurs when the space-charge-induced electric field reduces the electrons velocity below the overshoot velocity, which in turn degrades the bandwidth.

Besides the space charge effect, the thermal effect is another factor influencing saturation current in photodiodes. Thermal limitation comes from the low thermal conductivities of materials comprising UTC-PD epitaxy layers, preventing the Joule heat (coming from the input optical power and the applied electrical power) getting out of UTC-PDs, and maintaining a high temperature inside the photodiode. With increasing input optical power, the temperature inside UTC-PD's absorption layer continues to rise. When its temperature reaches higher than 165°C, the InP photodiode will likely be damaged [3.1]. Increasing

temperature has the tendency to reduce electron's mobility. The increased temperature increases the number of phonons, which increases the probability that an electron is scattered by a phonon. Mobility μ decreases with temperature also because carriers are more energetic at higher temperature, which results in an increased number of collisions and μ decreases. Therefore, at high temperature electrons take longer time to pass across the absorption/depletion region, causing the photocurrent saturate.

To get an idea of the degree to which thermal effects impact the RF output power of WG UTC-PDs, CW optical input was replaced with optical pulses in the RF output power measurement experiments. By setting the temporal width of the optical pulses shorter than the heating time of UTC-PDs (usually it takes several μs for UTC-PDs to get temperature stabilised), the thermal effect within UTC-PDs can be mitigated and the RF saturation power in the absence of thermal effects can be measured.

At first, Section 3.2 demonstrates a quick experiment to study temperature impact on the RF output power of CPW UTC-PDs. Section 3.3 explains the saturation power measurement system arrangement and settings, with the input of pulse optical signals. In Section 3.3, first the method to determine the optical pulse duration and the repetition rate is presented. The purpose is to make sure the input optical pulses do not damage the device and keep the photodiode at a relatively low temperature. Next, how the optical pulse is amplified by EDFA is explained and why we can get higher gain by using a pulse input compared to the CW input is also demonstrated. Then, why the bias voltage oscillates around the setting value at the pulse input condition is illustrated and how this problem was solved to stabilise the bias voltage is explained. After that, the impact of laser's polarisation on the output power of waveguide UTC-PDs is discussed; and the settings of MZ modulator's bias voltage and peak-peak voltage are explained. Following that, the measurement of EDFA ASE and its interference with respect to RF power accuracy are discussed. Pulse input measurement results on CPW UTC-PDs and antenna integrated UTC-PDs are covered in Section 3.4, and compared with their CW input measurement results to show the temperature impact on saturation powers. Section 3.5 gives an analysis on CW and pulse measurement data of 3x10 μm^2, 3x15 μm^2 and 7x15 μm^2 CPW UTC-PDs in order

to find out which effect (space charge effects, or thermal effects) caused the RF output power saturation at high photocurrents.

3.2 Temperature impact on RF output power

3.2.1 RF power measurement at different boundary temperatures

To check whether and in what degree the RF output power of waveguide UTC-PDs are sensitive to temperature changes, experiments were done on waveguide UTC-PDs by measuring their RF output power at three different boundary temperatures, which were controlled by a thermoelectric cooler (TEC). Because the heat source (unit: W/m^3) and thermal resistance are related to the size of P-contact, for the same amount of dissipated heat, smaller size UTC-PDs will reach higher temperature. Therefore, two sizes of UTC-PDs (3x10 μm^2 and 4x15 μm^2) were measured for 100 GHz RF power change at three TEC temperatures (20 ºC, 30 ºC and 40 ºC), to compare the temperature impact on their RF output powers. The RF output power measurement system is same as the layout shown in Figure 2.14. The photocurrent of the UTC-PDs was changed by increasing the current of the EDFA, and the 100 GHz output power was measured by EPM series power meter with TEC temperatures set to 20 ºC, 30 ºC and 40 ºC respectively. The CPW UTC-PD test samples sat on a copper heat sink whose temperature was controlled by Peltier TEC. As the heat sink's size changes with temperatures, the position of UTC-PDs also changes with temperatures. The lensed fibre, which couples optical signal into the waveguide of the UTC-PDs, needs to be re-aligned when TEC's setting temperature is changed.

COMSOL modelling shows that the internal maximum temperature of CPW UTC-PDs is increased by 10 ºC and 20 ºC when their boundary temperature is changed from 20 ºC to 30 ºC and 40 ºC. This trend is same for both of 3x10 μm^2 and 4x15 μm^2 UTC-PDs and same for different photocurrents. Below Figure 3.1 is the modelled temperature distribution along the Z axis of 3x10 μm^2 CPW UTC-PDs with the boundary temperature set to 20 ºC, 30 ºC and 40 ºC respectively, at the photocurrent of 12 mA and biased at -3V.

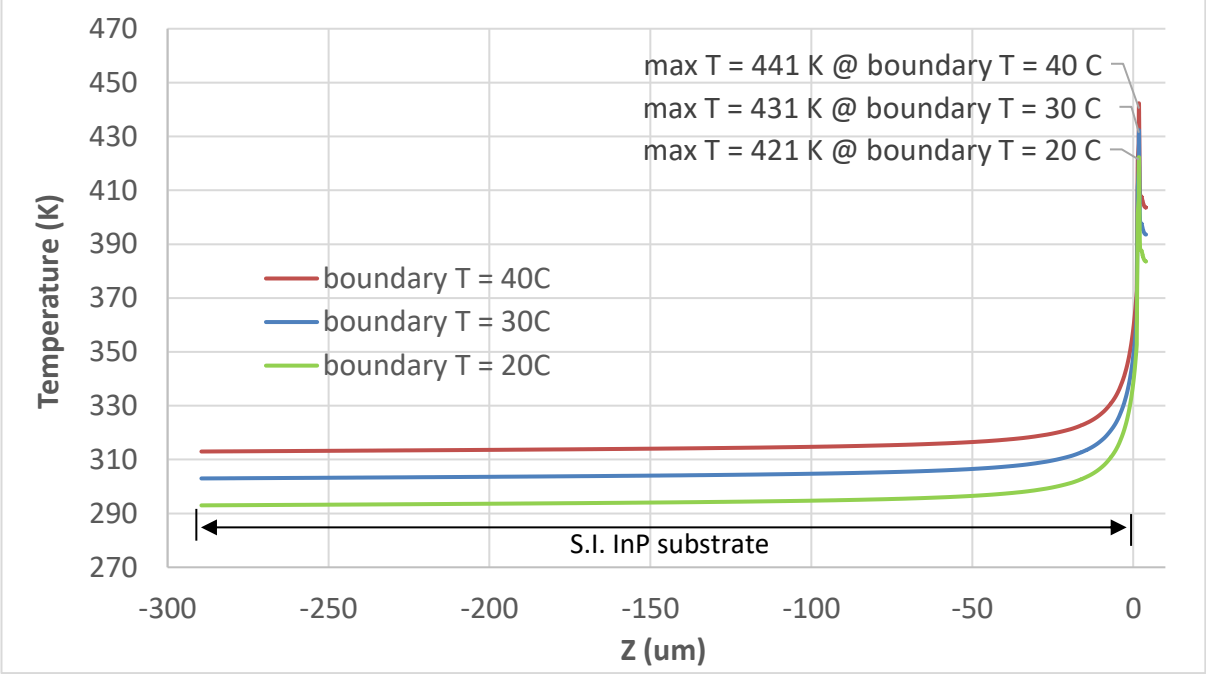

Figure 3.1: The temperature changes inside 3x10 μm^2 CPW UTC-PDs at the boundary temperature of 20 ºC, 30 ºC and 40 ºC.

At three boundary temperatures, 100 GHz output power was measured on both sizes of CPW UTC-PDs, and test samples were biased at -3V. The RF output powers changing with photocurrent at TEC temperatures of 20 ºC, 30 ºC and 40 ºC are plotted in Figure 3.2. From Figure 3.2 we can see: (1) for 4x15 μm^2 CPW UTC-PDs, there is almost no power difference for the three TEC temperatures, at the photocurrent from 2 mA to 10 mA. (2) for 3x10 μm^2 CPW UTC-PDs, at the photocurrent from 3 mA to 14.5 mA, test sample shows similar trend as 4x15 μm^2 CPW UTC-PDs. From the photocurrent of 15 mA, at the boundary temperature of 40 ºC, the RF output power starts to saturate. But for the boundary temperature of 20 ºC and 30 ºC, the RF output power doesn't show any signs of saturation. The 100 GHz power difference between 20 ºC/ 30 ºC and 40 ºC boundary temperature is around 0.6 dB at the photocurrent of 15.5 mA. The RF output power of UTC-PDs is proportional to the square of photocurrent. When UTC-PDs' photocurrents are same and lower than saturation photocurrent, the 100 GHz output powers will be same though test devices are at different temperatures.

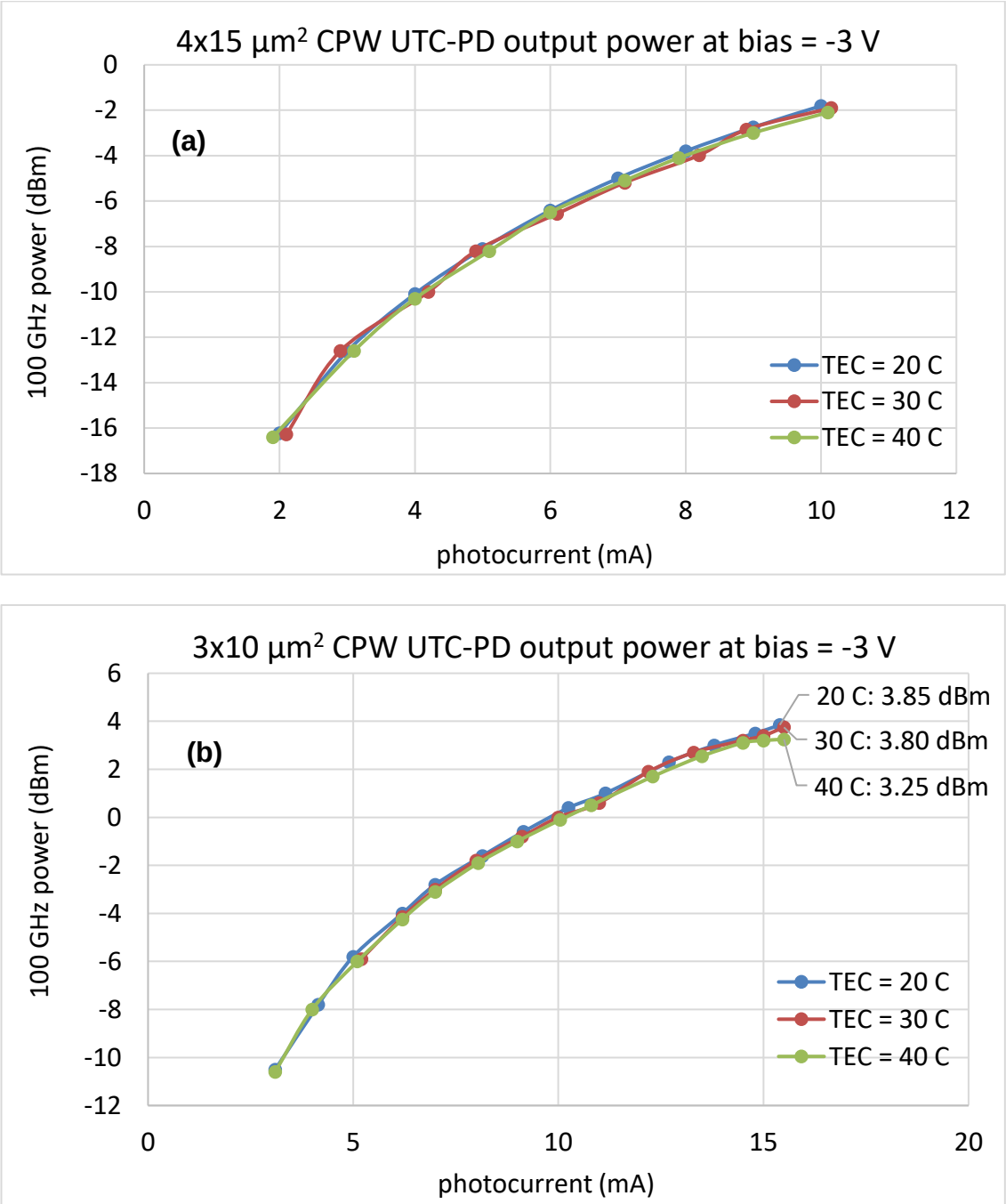

Figure 3.2: 100 GHz output power of CPW UTC-PDs vs photocurrents at TEC temperatures of 20 ºC, 30 ºC and 40 ºC. (a) 4x15 μm², (b) 3x10 μm².

Another round of experiments was carried out on 3x10 μm² CPW UTC-PDs to compare the RF output power difference at three TEC temperatures, with the same input optical powers. The 100 GHz output powers changing with input optical power at TEC temperatures of 20 ºC, 30 ºC and 40 ºC are plotted in Figure

3.3. From Figure 3.3 we can see: (1) with the same input optical power, the RF output power is higher when TEC temperature set to 40 ºC. (2) the 100 GHz output power difference between 20 ºC and 40 ºC TEC temperatures increases with input optical power increasing. The RF output power of UTC-PDs is proportional to the square of photocurrent. 100 GHz output power is higher at 40 ºC TEC temperature attributes to the higher photocurrents/responsivity at 40 ºC TEC temperature, see Table 3.1 of measured photocurrents at different TEC temperatures. The increased photocurrents come from the increased absorption coefficient. Detailed explanations are presented in the next Section 3.2.2.

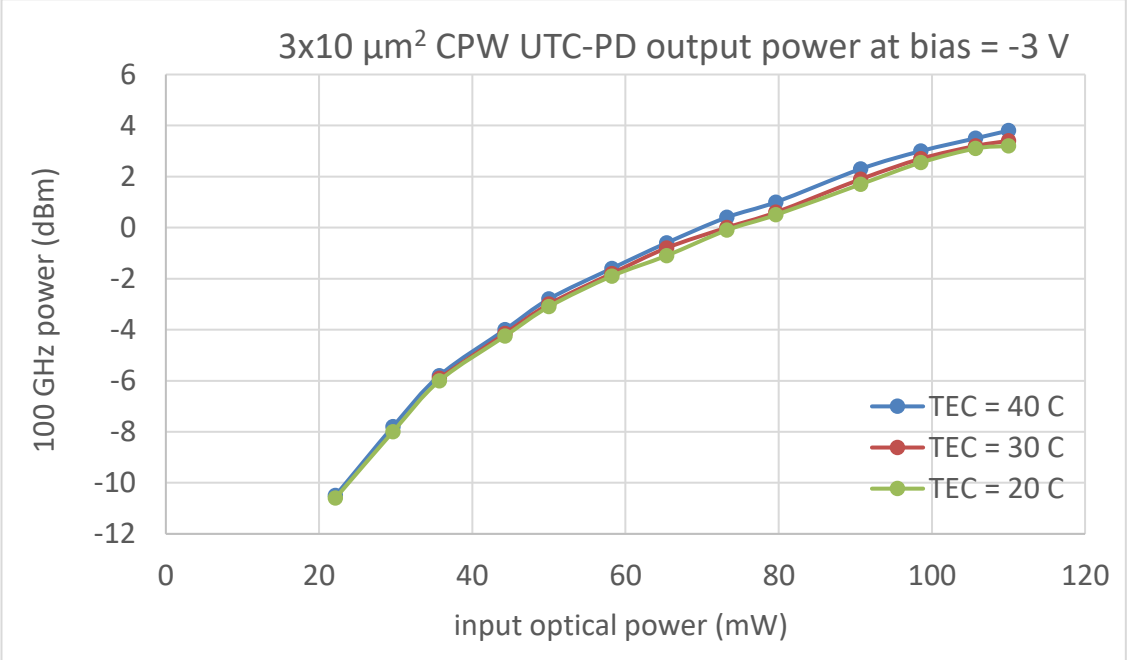

Figure 3.3: 100 GHz output power of 3x10 µm^2 CPW UTC-PDs versus input optical power at TEC temperatures of 20 ºC, 30 ºC and 40 ºC.

Table 3.1: Measured photocurrent and responsivity of 3x10 µm^2 CPW UTC-PD at the TEC temperature of 20 ºC and 40 ºC.

Input optical power (mW)	Photocurrent (mA)		Responsivity (A/W)	
	TEC = 20 ˚C	TEC = 40 ˚C	TEC = 20 ˚C	TEC = 40 ˚C
11	2.19	2.25	0.199	0.205
23	4.71	4.87	0.205	0.212
38	7.9	8.08	0.208	0.213

3.2.2 Analysis on increases of photocurrents at high temperature

When the temperature of photodiodes is increased, the bandgap of absorption layer ($In_{0.53}Ga_{0.47}As$) decreases, as shown in Figure 3.4 [3.2], which leads to the absorption coefficient of $In_{0.53}Ga_{0.47}As$ increase, see Figure 3.5 (a) [3.3]. From Figure 3.5, get the absorption coefficient of 7000 cm^{-1} for p^+-InGaAs absorber at 300 K. By using equation (3.1) and (3.2) [3.4], the absorption coefficient is calculated as 7576 cm^{-1} at 400 K. $\alpha(T)$ and $\alpha(300)$ are the absorption coefficient of the absorber at the temperature of T and 300 K respectively, ν is the frequency of incident light, and $E_g(T)$ is the energy band gap of the absorber at temperature T. Then, using equation (3.3) [3.5] (where W_{ab} is the thickness of the absorption layer, and $i(T)$ is the photocurrent at temperature T), to calculate the generated photocurrent is increased by 1.079 at 400 K, and the RF output power is increased by around 0.7 dB, which is similar as the reported measured relative power change at different junction temperatures (Figure 3.6) [3.5].

$$\alpha(T) = \alpha(300)\sqrt{\frac{h\nu - E_g(T)}{h\nu - E_g(300)}} \tag{3.1}$$

$$E_g(T) = 0.812 - 3.26\times10^{-4}T + 3.31\times10^{-7}T^2 \tag{3.2}$$

$$i(T) \propto 1 - exp\left[-\alpha(T)\cdot W_{ab}\right] \tag{3.3}$$

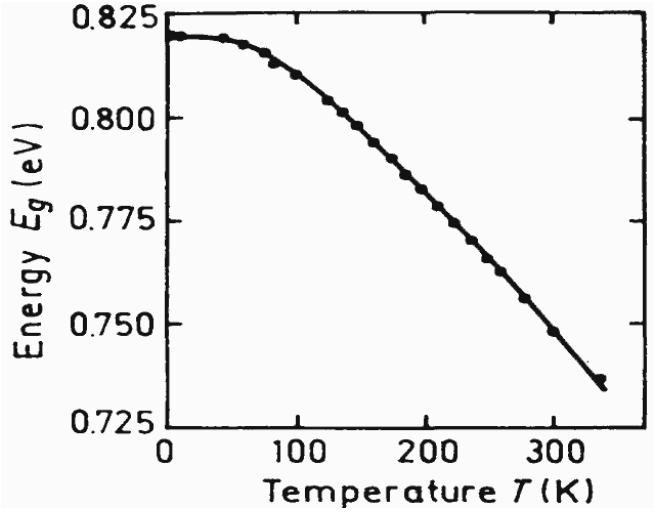

Figure 3.4: Energy band gap of $In_{0.53}Ga_{0.47}As$ vs temperature [3.2].

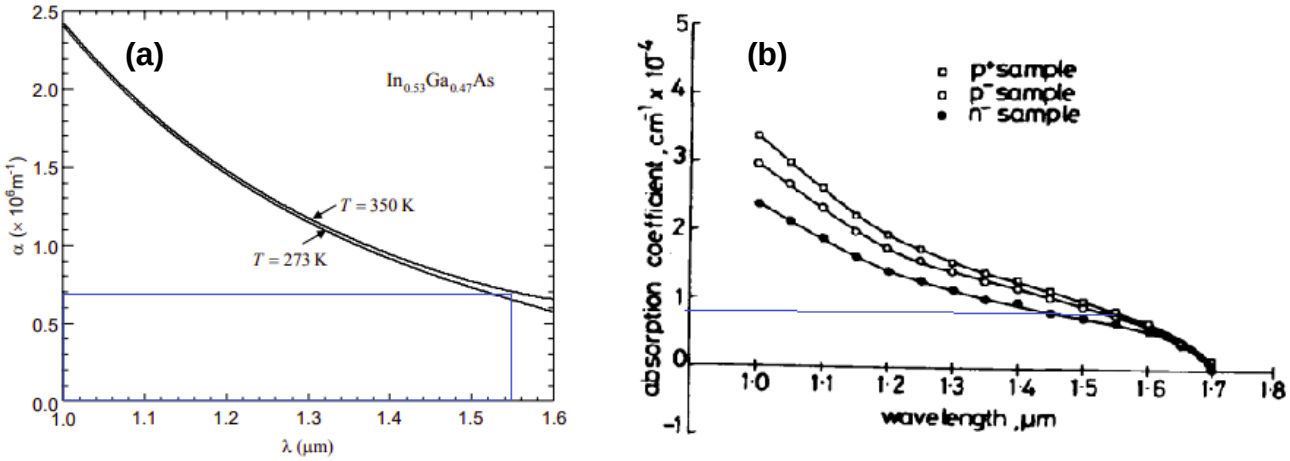

Figure 3.5: The absorption coefficient vs wavelength for $In_{0.53}Ga_{0.47}As$ (a) at 273 K & 350 K (n doped InGaAs) [3.3], and (b) with different dopings [3.6].

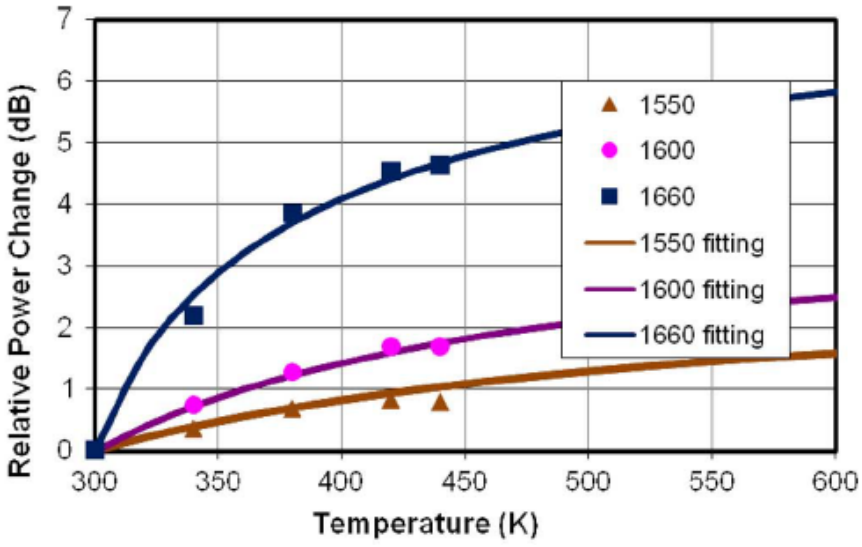

Figure 3.6: Measured and simulated relative power change as a function of junction temperature for a 44 μm diameter photodetector, biased at -6V [3.5].

Except for the InGaAs absorption layer of WG UTC-PDs, the InGaAsP ($Q_{1.3}$) waveguide layer is also related to input optical power absorption. According to below Figure 3.7 [3.7], the bandgap of InGaAsP shrinks with temperature increasing. Therefore, its absorption coefficient also increases with temperature as InGaAs. So, we need to check in what degree its increased light absorption at high temperature impacts the photocurrents of UTC-PDs. For InGaAsP $Q_{1.3}$, its absorption coefficient at 1550 nm is very low when the $h\nu$ of incident light (0.8 eV) is less than its energy band gap ($E_g = 0.9\ eV$), see Figure 3.8 [3.8]. The absorption coefficient near the band edge is taken as [3.9]:

$$\begin{aligned} \alpha(h\nu) &= A\ exp\left[\left(h\nu - E_g\right)/\sigma kT\right] \quad h\nu \leqslant E_g \\ &= A^{+}\left(h\nu - E_g\right)^{1/2} \qquad\quad h\nu > E_g \end{aligned} \tag{3.4}$$

where A, A^+, and σ (σ = 0.3) are fitting parameters, E_g is the energy band gap of waveguide layer. By using the equation (3.4), the absorption coefficient of $Q_{1.3}$ can be calculated when the 1550 nm light passes through the waveguide layer. The calculated absorption coefficient of $Q_{1.3}$ at 300 K and 400 K is 2.18 cm^{-1} and 15.144 cm^{-1}, respectively. The calculated absorption percentage of InGaAs (absorption layer) and InGaAsP $Q_{1.3}$ (waveguide layer) are listed in Table 3.2. The overall photocurrent increase of WG UTC-PDs is 1.068 at 400 K, compared to 300 K.

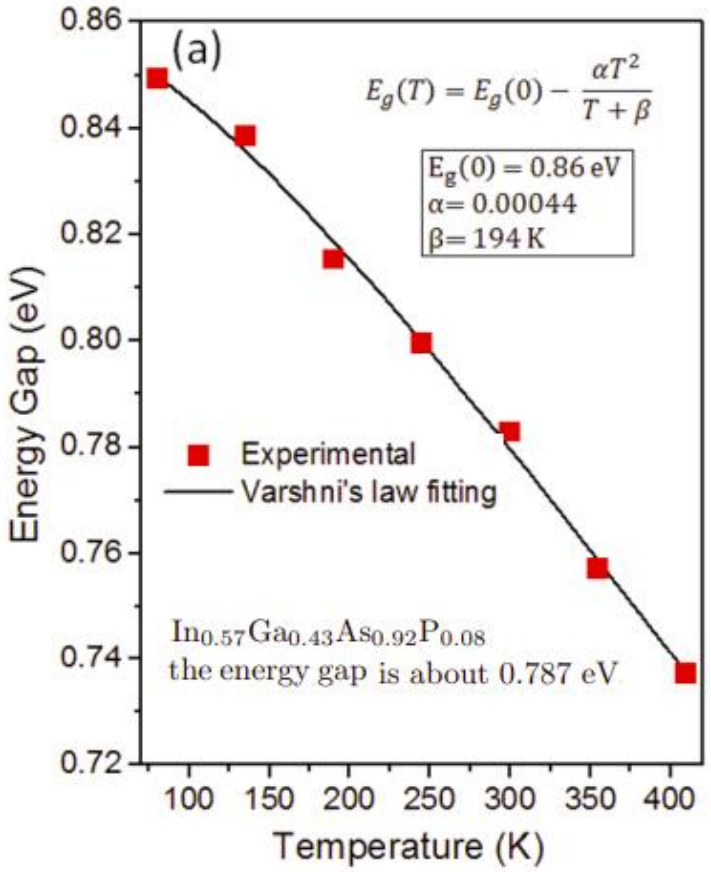

Figure 3.7: Experimentally obtained energy gap as a function of temperature (squares) and fitting curve according to Varshni's law (solid line).

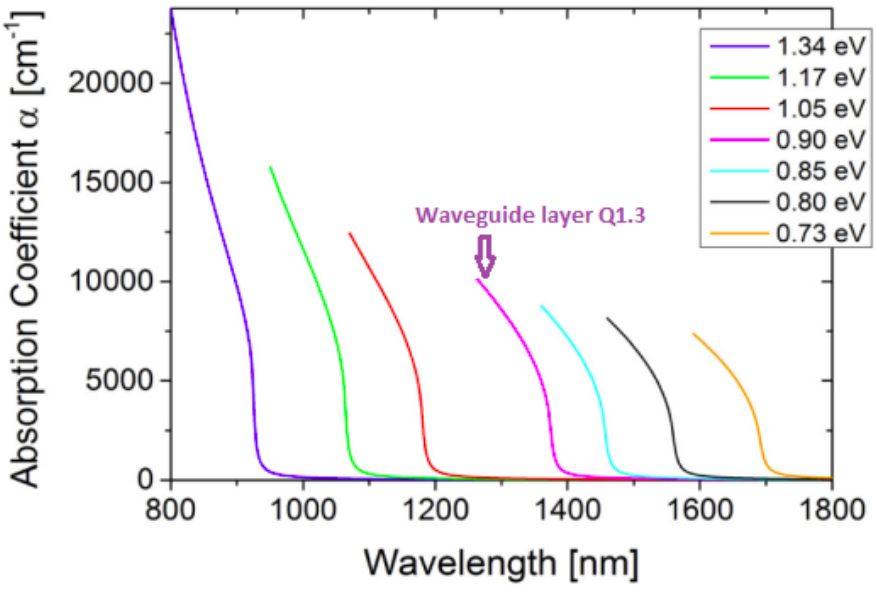

Figure 3.8: Absorption coefficient in dependence of the wavelength for different material compositions at 300 K [3.8].

Table 3.2: Calculated absorption coefficients of InGaAsP and InGaAs at the temperature of 300 K and 400 K.

	absorption coefficient (cm^{-1})		absorption percentage	
	300 K	400 K	300 K	400 K
InGaAsP $Q_{1.3}$	2.18	15.14	0.04%	0.20%
InGaAs	7000	7576	increased by 1.07	

Above experiments results and analysis show: (1) before UTC-PD's output power saturation, at different boundary temperatures, same photocurrents generate same RF output power; (2) for UTC-PDs with higher boundary temperature, its output power saturates at smaller photocurrent comparing with UTC-PDs with lower boundary temperature; (3) for the same input optical power, UTC-PDs under higher temperature gets higher photocurrents/RF output power due to the energy band gap shrinkage of absorption layer, which leads to absorption coefficient increasing.

3.3 Pulse input saturation power measurement system

In this section, we will discuss the signal settings of input optical pulses and the equipment configurations of UTC-PD's power measurement system. The thermal impact on UTC-PD's output power can be reduced by appropriately setting input optical pulses' duration and repetition rate.

3.3.1 Experimental arrangement

The experimental arrangement for UTC-PDs output power measurement with optical pulse inputs is shown in Figure 3.9. Compared with CW input power measurement system in Figure 2.14 and Figure 2.20, Mach-Zehnder (MZ) modulator is added in front of EDFA to realise optical pulses input. After being amplified by EDFA, high-power pulse signals are absorbed by the waveguide UTC-PDs. In order to monitor the optical pulses' peak power and pulse sequence waveform after amplified by EDFA, a 20dB optical coupler is added after optical

filter, to connect to digital oscilloscope through a photodiode. The purpose to use optical pulses as UTC-PD's input signals is to reduce the impact of thermal effect on power measurement. If settings of the optical pulse duration are much shorter than UTC-PD's temperature rising time, the test device will be limited to heating by the optical and electrical power.

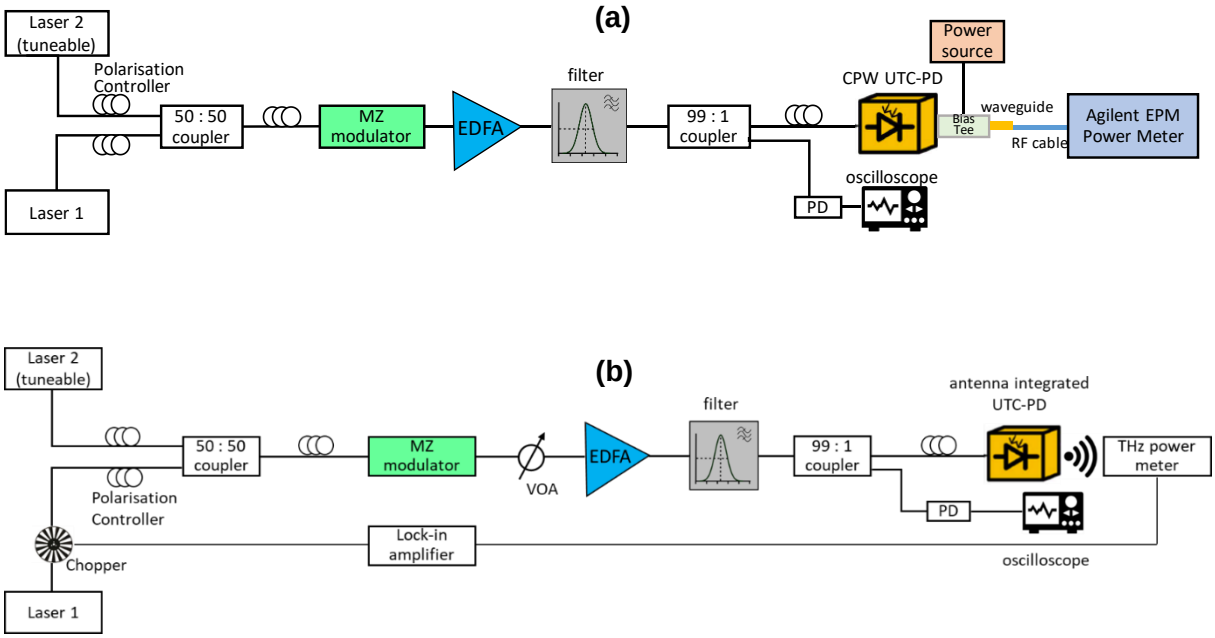

Figure 3.9: RF output power measurement system with optical pulse input on (a) CPW UTC-PDs, and (b) antenna integrated UTC-PDs.

To make sure the RF power saturation is not affected by thermal effects, the details of input pulse signals (optical pulse duration, and optical pulse repetition rate) need to be determined before conducting the saturation power measurement. The following parts in this Section give the estimation and calculation for the two parameters.

Optical Pulse Duration

For optical pulse input, we need to calculate the pulse duration to make sure the high-power optical pulse does not heat test samples to high temperature. The pulse duration was estimated based on the thermal modelling using COMSOL. Our CPW UTC-PDs have four sizes: 3 x 10 μm^2, 3 x 15 μm^2, 4 x 15 μm^2 and 7 x

15 μm^2. For the same amount of input optical power, the smallest size UTC-PD (3 x 10 μm^2) reaches the highest temperature and takes shorter time to reach the same temperature. Therefore, it is safe to use the smallest size UTC-PD to do the thermal modelling to estimate the temperature increase time. According to energy conservation, the total power delivered to the photodiode equals the sum of the output power delivered by the photodiode and power dissipated in the photodiode [3.10], expressed in (3.5), where P_{op} is the absorbed optical input power, P_{DC} is the electrical power delivered to the photodiode, P_{UTC} is the RF power generated by the UTC-PD, P_{ctc} is the joule heat on contacts, and P_{dis} is the remaining power to heat the photodiode.

$$P_{op} + P_{DC} = P_{UTC} + P_{ctc} + P_{dis} \tag{3.5}$$

Based on the experimental results, the 3 x 10 μm^2 UTC-PD generates 10 mA photocurrent and 1 mW 100 GHz power under 50 mW input optical power. The UTC-PD is biased at -2V and its series resistance is estimated about 15Ω. So, the calculated dissipated power inside UTC-PD is 40 mW. Putting this value as the heat source in COMSOL, the simulated max temperature inside 3 x 10 μm^2 UTC-PD is 109°C. With 50 mW optical power inputting to 3 x 10 μm^2 UTC-PD, it takes 7 μs for the absorption layer to increase from ambient temperature to 94°C, see Figure 3.10 (a). Figure 3.10 (b) shows the increase of temperature from 10 ns to 100 ns inside UTC-PD, and the temperature rises to 35°C at 20 ns. If setting the optical pulse duration to 20 ns, most of the thermal effect on power saturation can be eliminated.

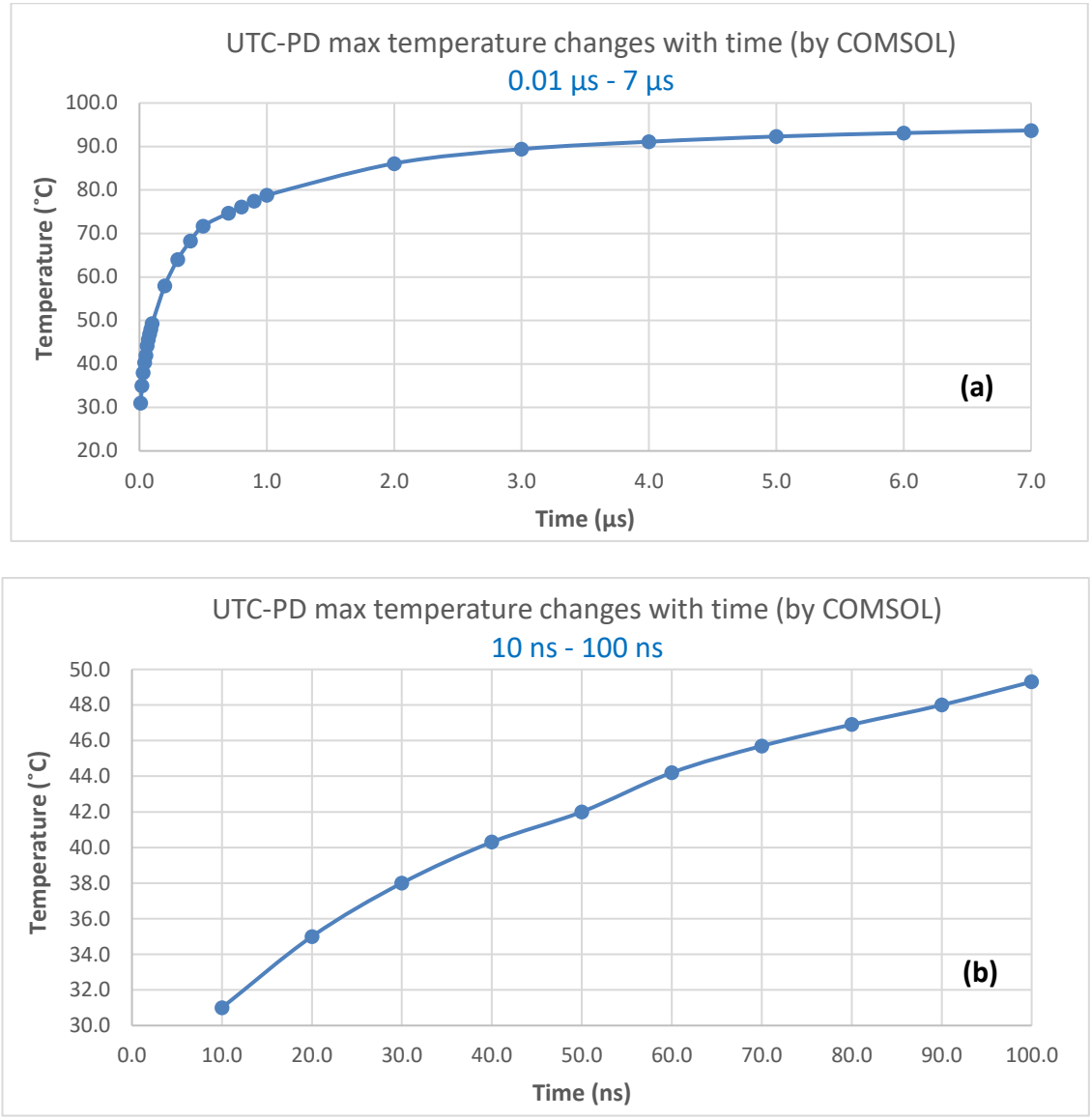

Figure 3.10: 3 x 10 µm^2 UTC-PD max temperature changes with time with 50mW optical input power, biased at -2V. (a) the change of temperature from 0.01 µs to 7 µs, (b) the change of temperature from 10 ns to 100 ns.

Optical Pulse Repetition Rate

Besides the optical pulse duration (20 ns), the time interval between each optical pulse also needs to be calculated. As 20 ns optical pulse causes the temperature of 3 x 10 µm^2 UTC-PD increase to 35°C, it is needed to allow for the photodiode to cool down to room temperature before sending the next optical pulse. COMSOL modelling shows it takes 140 ns for the temperature of 3 x 10 µm^2 UTC-

PD to decrease from 35°C to 23°C. Therefore, the interval between each 20 ns optical pulse should be at least 140 ns. In the pulse experiment, we will use 5 MHz signals with 10% duty cycle to get 20 ns optical pulse and 180 ns interval between pulses.

In the measurement system, a MZ modulator is used to get the optical pulses, which is placed in front of EDFA. Details of MZ modulator settings (bias voltage, peak-peak voltage, etc.) will be explained in Section 3.3.5. If the MZ modulator is placed after EDFA, the pulse peak power will be limited by the maximum CW output power of EDFA. In the pulse experiment, much higher optical power is needed to make UTC-PDs saturate. EDFA provides higher gain with optical pulse input, and the level of gain improvement depends on the duty cycle of input signals. Further explanations are covered in the next Section 3.3.2.

3.3.2 Optical pulse amplification by EDFA

First, a quick explanation is given on why choosing EDFA to amplifiy the optical pulse, not Semiconductor Optical Amplifier (SOA). EDFA is typically better suited than SOA for amplifying laser pulses. The two types of optical amplifier differ in their saturation energies, gain saturation dynamics, and carrier lifetimes. In semiconductor amplifiers, the saturation energy is relatively low, on the order of a few picojoules. This limits the amplified pulse energy that can be achieved by semiconductor amplifiers. In fiber amplifiers, the saturation energy can exceed microjoule levels. Therefore, an EDFA is less prone to experience gain saturation compared to an SOA. Additionally, the gain recovery time in SOA is governed by the carrier lifetime, which is in the 10 ps to 100 ps timescale. EDFA's operation is based on the stimulated emission of optically pumped Er^{+3} ions in silica. When electrons are excited to the upper state of Erbium ions by 980 nm pumping light, they rapidly decay non-radiatively to the meta-stable state ($^4I_{13/2}$ state). The lifetime of the meta-stable state is typically in the 1 ms to 10 ms timescale, as shown in Figure 3.11 [3.11]. As the EDFA's lifetime is much longer than the pulse repetition period in our experiment, EDFA can be regarded as responding to the pulses' average power, as opposed to its peak power. Therefore, through amplification by an EDFA, higher pulse peak power can be achieved.

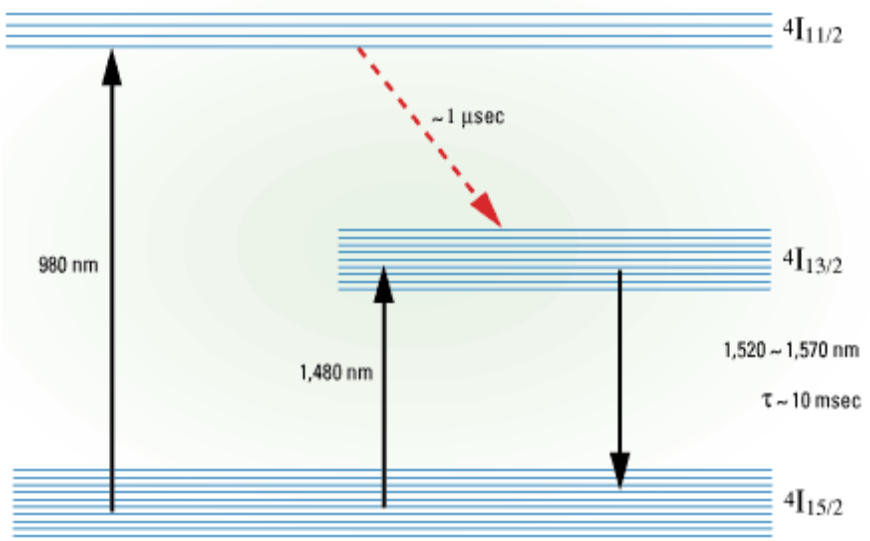

Figure 3.11: Energy level diagram of Erbium ion [3.11].

Before the EDFA is used to amplify 20 ns optical pulses to get higher optical power input into UTC-PDs, we need to understand what is the gain of our EDFA for 20 ns optical pulses, and how high the pulse peak power can get at the maximum EDFA pump current of 1000 mA. As the EDFA can be considered as responding to the pulses' average power, the peak power of optical pulses, after amplified by an EDFA, will be much higher than the amplified power of CW signals. The EDFA we used to amplify the optical pulse is Thorlabs EDFA100S. From Thorlabs website [3.12], we can see the temporal profile of the amplified femtosecond (fs) pulse at two output pulse energies, shown in Figure 3.12. Femtosecond laser pulses centred at 1550 nm were emitted by an erbium fibre oscillator, and its pulse width was measured by an intensity autocorrelator as 430 fs FWHM (Full Width at Half Maximum). The average output power of the fibre oscillator was 1.1 mW. Since the repetition rate of the fibre oscillator was 50 MHz, the measured pulse energy was 22 pJ. These 430 fs FWHM, 22 pJ pulses were propagated into EDFA100P amplifier. The total output power was adjusted by changing the fibre amplifier's pump current (see Figure 3.13).

Based on the information on fs pulse amplification provided by EDFA's supplier, we can calculate out the average output power of EDFA at 1.1 nJ output pulse energy is 1.1 nJ x 50 MHz = 55 mW, corresponding to the pump current of 600

mA. As the maximum average output power of EDFA100S is 200 mW (at 1000mA pump current), the max output pulse energy for 5 MHz pulse repetition is 200 mW/5 MHz = 40 nJ. Then, we can work out the max peak power of 20 ns pulse after EDFA is about 40 nJ / 20 ns = 2.0 watt. Therefore, we can use EDFA100S to amplify 20 ns optical pulse (10% duty cycle) to get output optical pulse up to 2.0 watt. For example, for 300 mW (24.7 dBm) pulse peak power, its pulse energy is 6.0 nJ and average output power is 30 mW. Figure 3.13 shows we can get 30 mW (14.7 dBm) CW output power at pump current of 400 mA with 0 dBm input power, therefore the corresponding amplification gain for 20 ns optical pulse (10% duty cycle) is 24.7 dB, 10 dB higher than the gain for CW input signals.

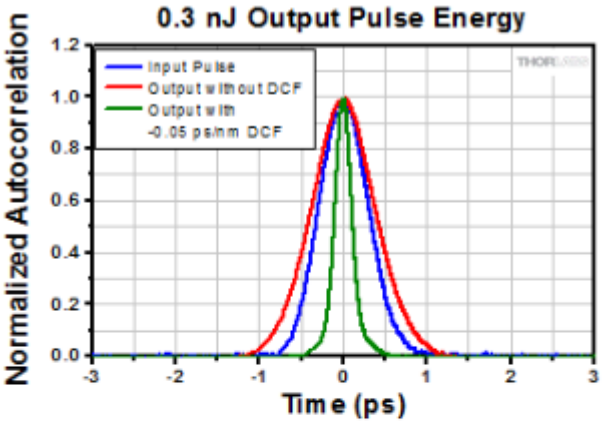

Click to Enlarge

When the amplifier was set to 0.3 nJ output pulse energy, we observed minimal distortion to the temporal profile of the output pulse. The use of a dispersion-compensating fiber (DCF) compressed the output pulse to 150 fs.

0.3 nJ Test	Measured Pulse Width (FWHM)	Calculated Peak Power
Input Pulse	430 fs	45 W
Output Pulse (No DCF Precompensation)	570 fs	0.46 kW
Output Pulse (-0.05 ps/nm DCF Precompensation)	150 fs	1.76 kW

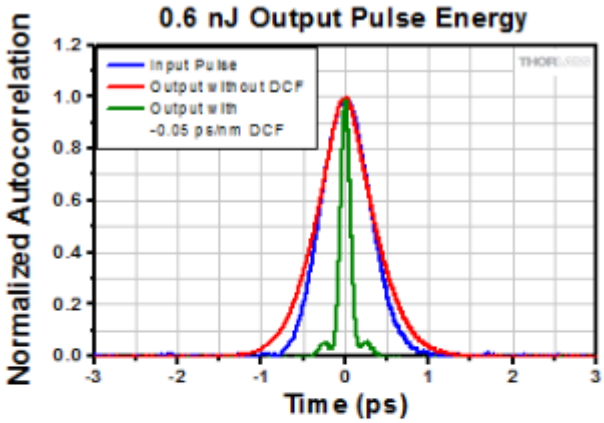

Click to Enlarge

When the amplifier output pulse energy was doubled to 0.6 nJ, there was still minimal distortion to the non-precompensated output pulse. By applying precompensation, the output pulse was compressed to 88 fs, but pedestals associated with nonlinearities appeared on the sides. The peak output power in the precompensated case was 6 kW.

0.6 nJ Test	Measured Pulse Width (FWHM)	Calculated Peak Power
Input Pulse	430 fs	45 W
Output Pulse (No DCF Precompensation)	480 fs	1.1 kW
Output Pulse (-0.05 ps/nm DCF Precompensation)	88 fs	6 kW

Figure 3.12: Femtosecond (fs) laser pulse amplification at three output pulse energies (0.3 nJ and 0.6 nJ,) [3.12].

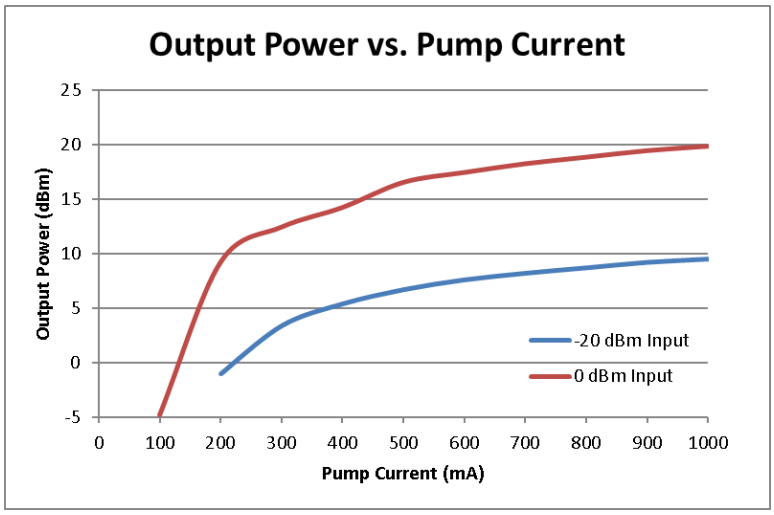

Figure 3.13: Relationship between pump current and output power at -20 dBm and 0 dBm input optical power [3.12].

To verify we can get higher output power when the EDFA's input is a pulse signal, we connected the output of the EDFA to oscilloscope (through a 20dB coupler) to show the output power differences between CW input and pulse input (a photodiode was placed in front of oscilloscope to convert optical signals to electrical signals), see Figure 3.14. The blue line represents the EDFA output power level at CW input condition, and the yellow line represents the EDFA output power level at pulse input condition (10% duty cycle). Both of them were amplified at the same current of the EDFA. From Figure 3.14 we can clearly see the pulse output power is much higher than CW output power.

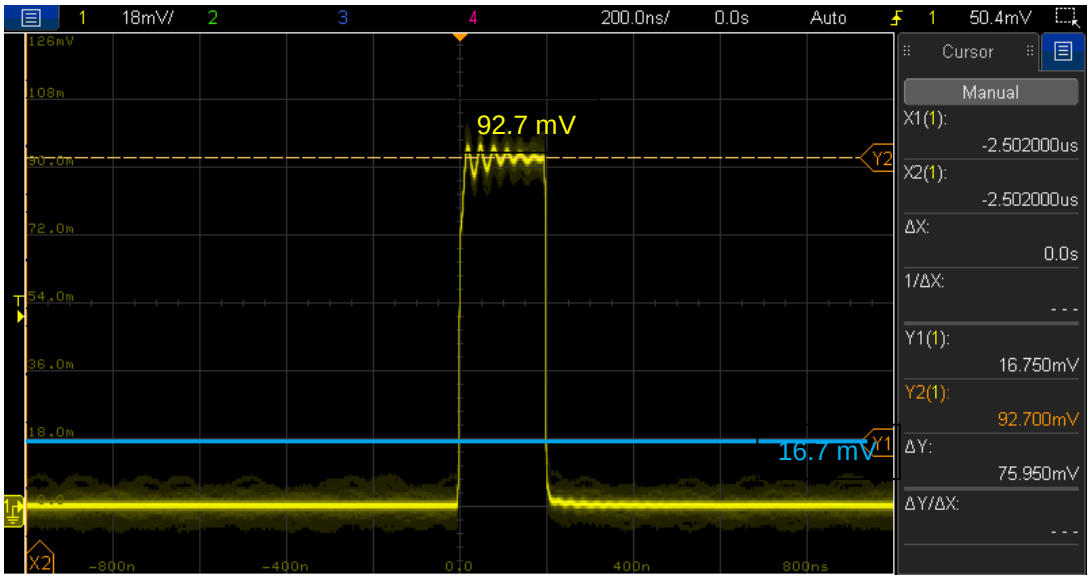

Figure 3.14: CW and pulse input signals are amplified by the EDFA at the same pump current.

3.3.3 UTC-PD bias voltage stabilisation

Under the 10% duty cycle pulse input condition, the measured average 100 GHz power was not stable when changing the optical pulse width (keep the optical pulse power at the same level). Below Table 3.3 lists the average 100 GHz power readings at different pulse widths, which shows average 100 GHz power (read from Agilent E4418B EPM series Power Meter) was increased when setting the pulse duration longer (keeping 10% duty cycle). A bias tee integrated waveguide probe was used to provide bias voltage to CPW UTC-PDs and to pass the RF signals to the EPM series power meter. Optical pulses generate photocurrent pulses in UTC-PDs, which makes the capacitor in the bias tee charged/discharged (producing a potential difference) and causes the applied bias voltage unstable. Figure 3.15 shows the bias voltage of UTC-PD (the orange line) to be unstable with input optical pulses (the blue line). The optical pulse's duty cycle was set to 20%, and the pulse duration was 200 ns. The test device was biased at 0 V. Figure 3.15 shows the bias voltage changed from -0.22V to 0.35V, which indicates the unstable bias voltage is the cause for 100 GHz power instability when changing the pulse durations.

Table 3.3: 100 GHz average power readings at different pulse widths

pulse width (10 % duty cycle)	20 ns	50 ns	100 ns	200 ns	500 ns
avg photocurrent (mA)	0.79	0.8	0.8	0.81	0.81
avg 100 GHz (dBm)	-15.7	-15.2	-15.2	-14.6	-14.4

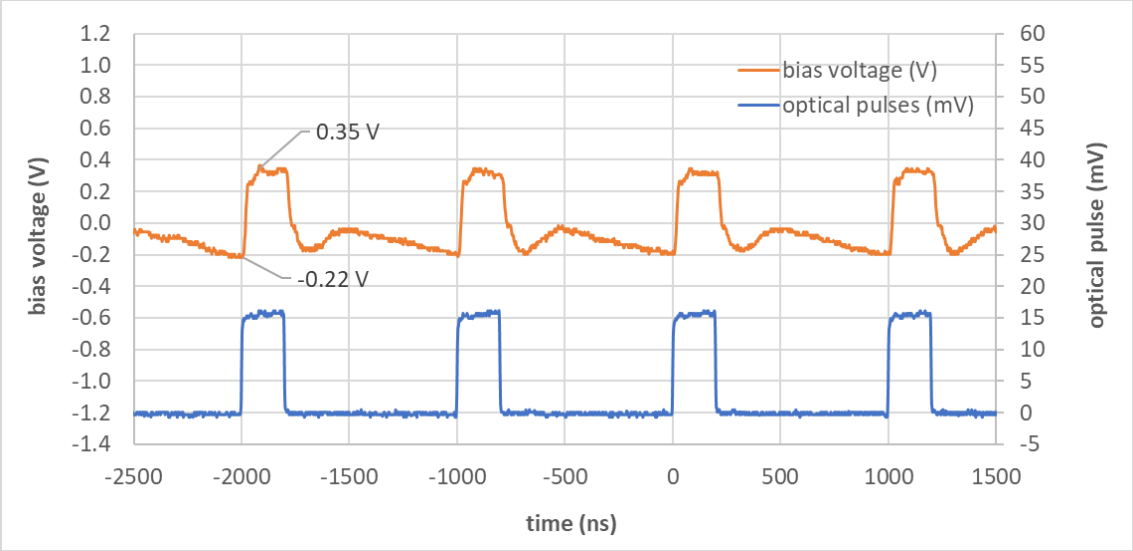

Figure 3.15: The UTC-PD's input optical pulse waveform (the blue line, connected to oscilloscope through a photodiode) and the bias voltage variation (the orange line).

Two more experiments were done to further investigate the optical pulse's impact on UTC-PD's bias voltage. Both of the experiments used 20% duty cycle signals as UTC-PD's input optical pulses, and reverse bias was set to -2 V. In the first experiment, the pulse frequency was set to 20 MHz (pulse width = 10 ns). The optical pulse's peak power was set to three different values to see its impact on the bias voltage. The experimental results are plotted in Figure 3.16, from which we can see higher optical pulse power (also higher photocurrent) causes bigger bias voltage change. For photocurrent = 1.5 mA, the bias voltage oscillated from -2.13 V to -1.82 V (ΔV = 0.31 V); for photocurrent = 4.0 mA, the bias voltage

oscillated from -2.35 V to -1.56 V (ΔV = 0.79 V). In the second experiment, the UTC-PD's average photocurrent was tuned to 2.0 mA. The optical pulse frequency was changed to compare its impact on the bias voltage stability, see Figure 3.17. It shows lower optical pulse frequency causes bigger bias voltage change. For pulse frequency = 2 MHz, the bias voltage changes from -2.4 V to -1.1 V (ΔV = 1.3 V); for pulse frequency = 10 MHz, the bias voltage changes from -2.3 V to -1.5V (ΔV = 0.8 V). The two experiments show the higher the photocurrent and the lower the optical pulse frequency cause bigger bias voltage changes, when UTC-PD's input signals are optical pulses.

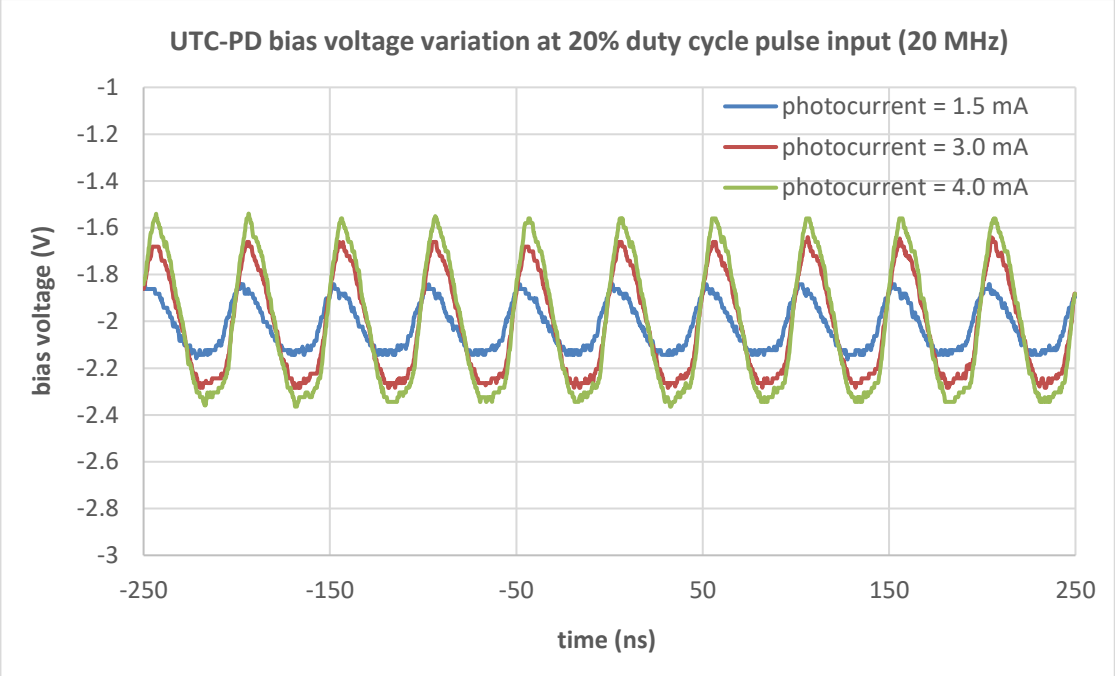

Figure 3.16: The bias voltage of UC-PD changes at different photocurrents. The UTC-PD is biased at -2 V, and input optical signals are 20% duty cycle pulses.

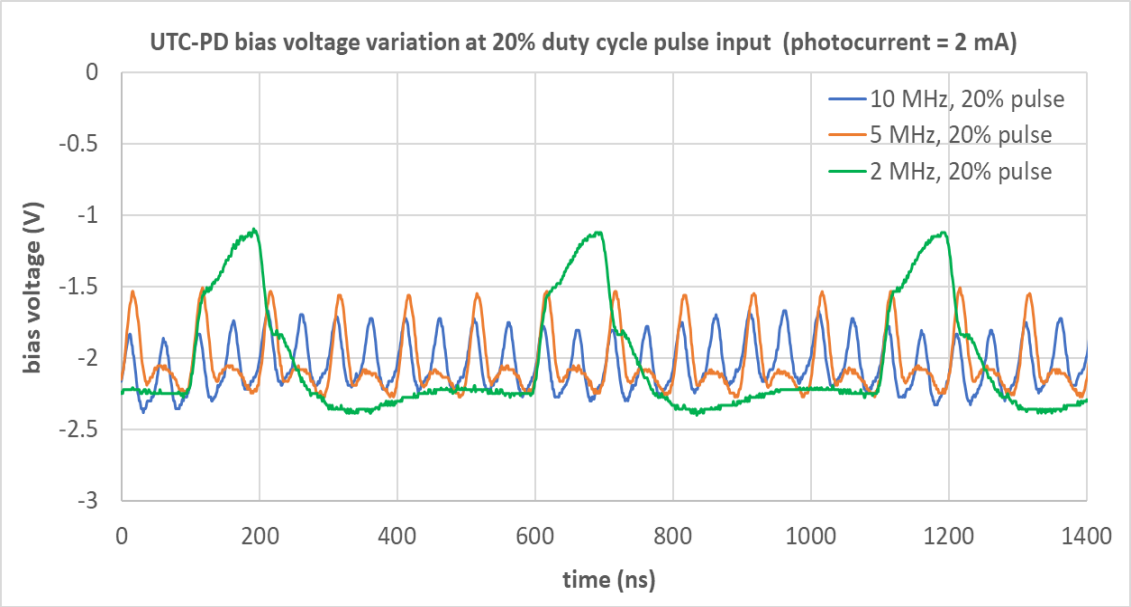

Figure 3.17: The bias voltage of UC-PD changes at different optical pulse frequencies. The UTC-PD is biased at -2 V, and has an average photocurrent of 2 mA.

According to $Q = I \times \Delta t = C \times V$, for the same photocurrent pulses, if increase the capacitance of the capacitor, the voltage change caused by photocurrent pulse will be reduced. A 1 µF capacitor was added in parallel to the UTC-PD's voltage supply, and the bias voltage change was measured again to check the effectiveness (shown in Figure 3.18). Except for adding a 1 µF capacitor, all other conditions are same as the experiment in Figure 3.17. We can see the bias voltage is much more stable and only has 0.07 V variance at 1 MHz and 5 MHz optical pulse inputs. 100 GHz power was also measured at the two frequencies, and their average RF power readings were very close: -18.4 dBm (photocurrent = 1.01 mA) and -18.6 dBm (photocurrent = 0.99 mA) for 1 MHz and 5 MHz pulse frequency respectively. Therefore, CPW UTC-PD's bias voltage can be stabilised by adding capacitor parallel to the bias supply.

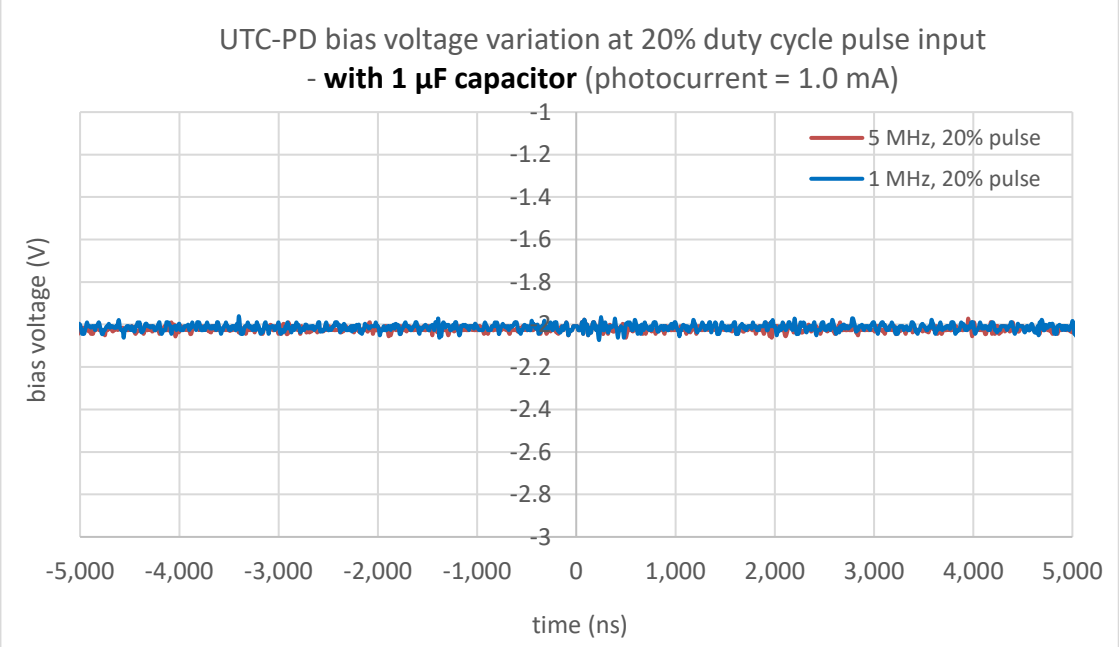

Figure 3.18: The bias voltage of UC-PD changes at different optical pulse frequencies, with 1 µF capacitor in parallel with UTC-PD's voltage supply. UTC-PD is biased at -2 V.

3.3.4 Polarisation optimisation

The absorption layer of our waveguide UTC-PDs is only 120 nm thick. Since the absorber is very thin, the TM modes have a poor optical coupling in the absorber resulting in strong polarisation dependence. In order to optimise the coupling efficiency between the lensed fibre and waveguide UTC-PDs, a polarisation controller is employed between EDFA and waveguide UTC-PDs. To maximise the heterodyning signals and get better responsivity, a polarisation controller is added after each laser to align the polarisation of the two lasers. Compared to CW input saturation power measurement (Figure 2.14), one more polarisation controller is needed in front of MZ modulator in the pulse input saturation measurement (Figure 3.9 (a)).

It has been shown that the fringe visibility is a function of the angle between the state of polarisation (SOP)'s orientation of the interfering vibrations, like the MZ interferometer. This dependency leads to the fact that a slight instability of the input SOPs can generate any interferometer phase noise [3.13], [3.14]. The MZ

intensity modulator (Thorlabs LN82S-FC) used in pulse measurement has a polarisation maintenance (PM) input optical fibre, which makes sure the SOP in the two arms of MZ modulator is same. By adjusting the polarisation controller before the MZ modulator, two lasers' polarisations can be aligned to the PM input fibre of the MZ modulator.

3.3.5 MZ modulator

MZ intensity modulator was used to generate optical pulse signals in the saturation power measurement. To work out its DC bias and RF modulation peak-peak voltage, MZ modulator's transmission function need to be measured. Figure 3.19 shows the relationship between MZ modulator's DC bias and its output optical power. According to Figure 3.19, for pulse generation, the MZ modulator was biased at -0.6 V with the RF modulation range of 5.8 V, so the bias changed between -3.5 V and 2.3 V. The oscilloscope in Figure 3.9(a) was used for monitoring the optical pulses' waveform, to make sure optical pulses have the highest extinction ratio and the lowest optical power when the pulse was off. When MZ modulator was bias at -3.5 V, corresponding to the state of no pulses, the measured 100 GHz power was -41 dBm. The "off" state power should be subtracted from the RF power readings from EPM series power meter when calculating the peak power of output RF pulses.

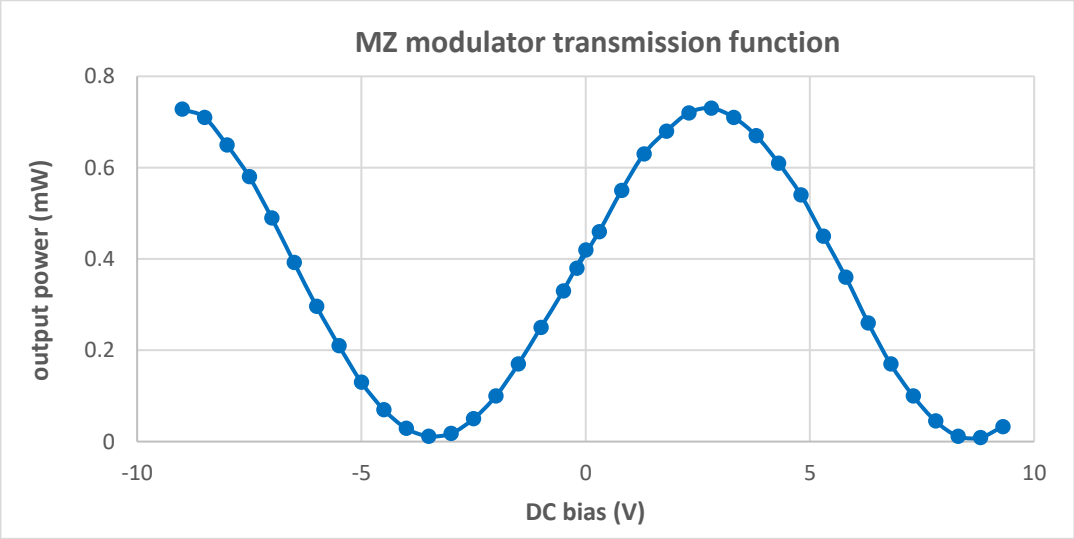

Figure 3.19: The relationship between the DC bias and the output optical power of MZ modulator.

3.3.6 EDFA ASE measurement

As shown in Figure 3.11, the stimulated electrons have a finite excited state lifetime, and some of the electrons return spontaneously to the ground state and emit a photon. This photon has no coherence characteristics with respect to the incoming light signal, as opposed to a photon generated by stimulated emission. The collection of such spontaneously generated photons, being multiplied by the fibre amplifier, forms a background noise of the EDFA. This background noise is known as amplified spontaneous emission (ASE) [3.15], [3.16].

In the CW and pulse input saturation power measurement systems (Figure 2.14 and Figure 3.9 (a)), narrow band pass optical filter (at the output of the EDFA) is used to reduce the noises from the EDFA. The pump shot noise is filtered in this filter. However, the pump power affects transmission performance from its contribution to ASE, which can't be filtered out. In the pulse measurement, we do not want ASE affect the accuracy of our measurement. As ASE can't be totally filtered out by narrow band filter, we need to know how much ASE is absorbed by UTC-PD and whether it impacts the measurement accuracy.

A polarization extinction method was used to measure the power level of ASE. This method uses the fact that the signal from EDFA's stimulated emissions is polarized and the ASE in the EDFA is not polarized. By placing a polarizer in front of the optical spectrum analyser and adjusting the polarization to null out the signal, the stimulated emission can be extinguished from the measurement, leaving ASE/2 received at the optical spectrum analyser. Based on this method, the ASE power of EDFA was measured when it was pumped at the highest current, 1000 mA. The measured ASE power is 50.6 μW. As the polarizer's extinction ratio is 28 dB, the EDFA's stimulated output can't be completely blocked by the polarizer. Therefore, the actual ASE power should be lower than this value, and it can be ignored for our measurement.

3.4 Pulse input saturation power measurement

3.4.1 CPW UTC-PDs measurement results

The 100 GHz saturation power measurements with pulse input was done on 3x10 μm^2, 3x15 μm^2, and 7x15 μm^2 CPW UTC-PDs. All UTC-PDs under test were biased at -3.0 V and placed on thermoelectric cooler (TEC) driven by a temperature controller (set to 20 ºC). Optical input pulses were generated by MZ modulator and amplified through an EDFA. The amplified optical pulses were aligned into CPW UTC-PD's waveguide through lens fibre pigtail (spot size = 2.5 μm). For each size of CPW UTC-PDs, CW measurement was done first, then 50% pulse measurement and following with 10% pulse measurement. For the 50% pulse measurements, the pulse width was set to 50 ns and 20 ns respectively, and the repetition frequency was set to 10 MHz and 25 MHz respectively. For the 10% pulse measurements, the pulse width was set to 20 ns and the repetition frequency was set to 5 MHz. As the optical input are pulse signals, the readings of photocurrent and 100 GHz output power are average values. To calculate the values of pulse photocurrent and RF pulse power, it is needed to establish the relationship between meter readings (the average values) and the pulse values. For rectangle pulses with a constant duty cycle, the power of pulsed RF signal is determined by the average power of pulses divided by the pulse duty cycle, see Figure 3.20. For example, for 10% duty cycle pulses, the pulse power (in dBm) is the measured average power (in dBm) plus 10dB.

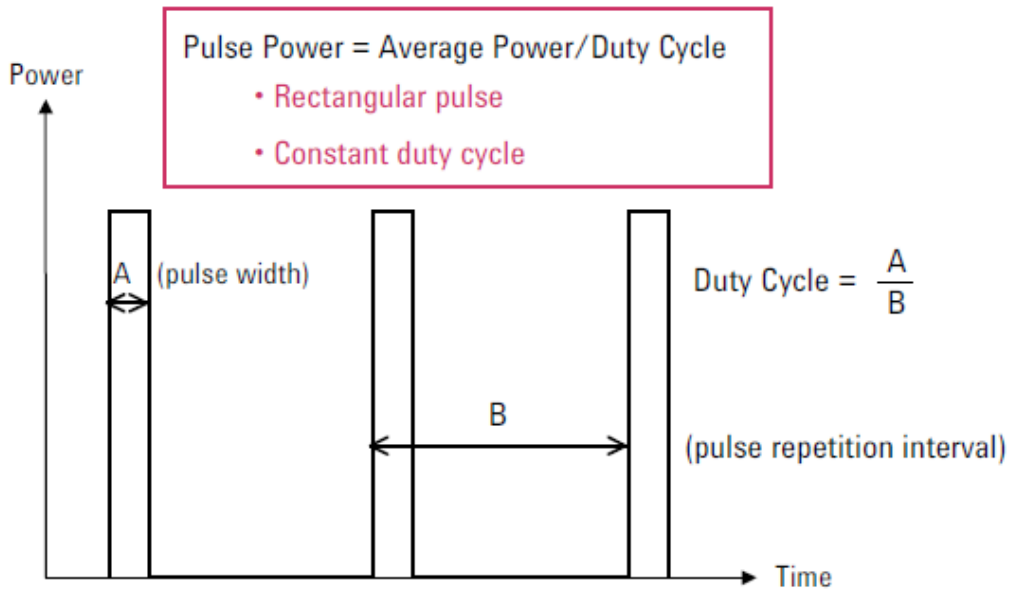

Figure 3.20: Relationship between the pulse average power and the pulse power.

The relationship between photocurrent and 100 GHz output power for 3 sizes of CPW UTC-PDs are plotted in Figure 3.21 to Figure 3.23. From these pulse measurement plots, we can see: (1) the RF output power saturates at higher photocurrents at pulse input conditions. 10% pulse input gets higher saturation power than 50% pulse input. For the same duty cycle input (50 %), pulses with shorter pulse duration enables UTC-PDs radiated higher RF output power. (2) For CPW UTC-PDs with bigger size of P-ridge, their saturation power improvement at 10% pulse input is less than those with smaller size of P-ridge. For the 3x15 μm^2 CPW UTC-PD, its saturation power of 10% pulse input is 3.8 dB higher than that of CW input condition, less than this value of 3x10 μm^2 CPW UTC-PD, which is 4.7 dB. (3) with 10% pulse input, the output power of bigger size UTC-PDs saturates at higher photocurrent than smaller size UTC-PDs. For 7x15 μm^2 CPW UTC-PD, its 100 GHz output power saturates at the photocurrent of 36 mA. For 3x10 μm^2 and 3x15 μm^2 CPW UTC-PDs, their output power saturates at 23 mA and 25 mA respectively.

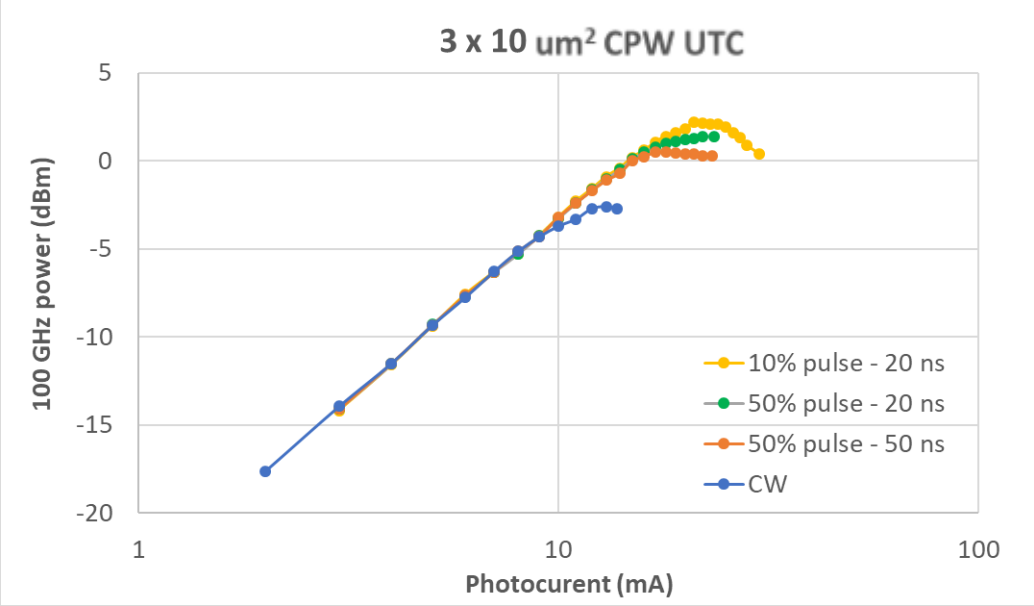

Figure 3.21: 100 GHz output power measurement with CW, 50% and 10% pulse input on 3 x 10 μm^2 CPW UTC-PDs, biased at -3V.

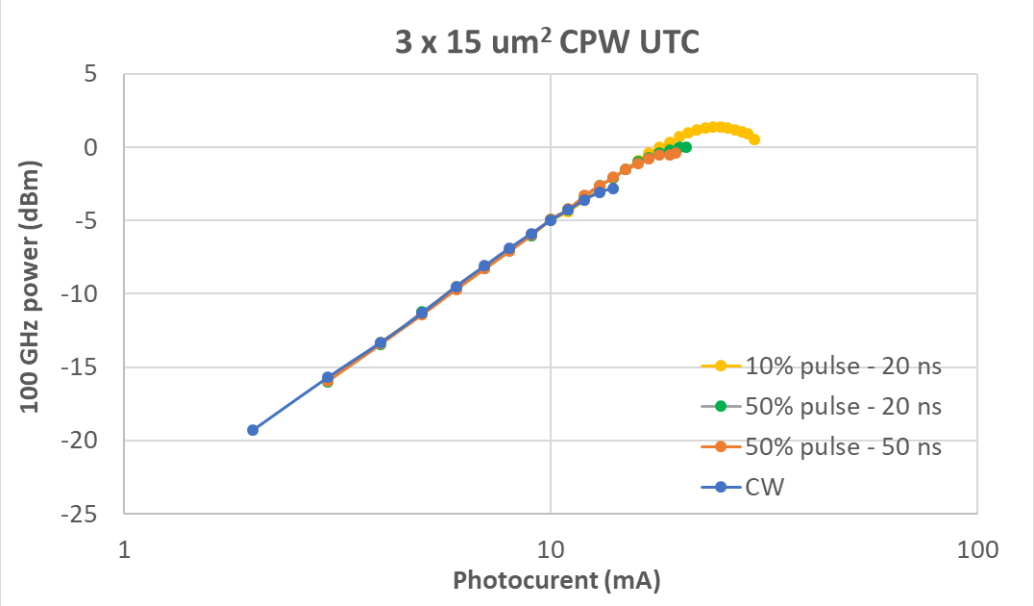

Figure 3.22: 100 GHz power measurement with CW, 50% and 10% pulse input on 3 x 15 μm^2 CPW UTC-PDs, biased at -3V.

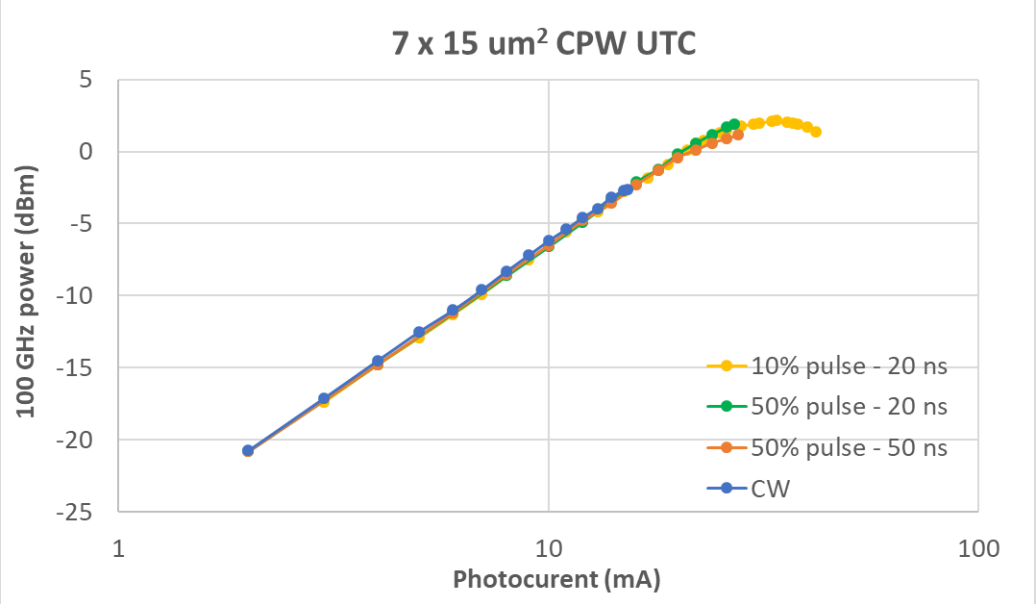

Figure 3.23: 100 GHz output power measurement with CW, 50% and 10% pulse input on 7 x 15 μm^2 CPW UTC-PDs, biased at -3V.

3.4.2 Antenna integrated UTC-PDs measurement results

The 250 GHz saturation power measurements with optical pulse input was done on 4x15 μm^2 bow-tie antenna integrated UTC-PDs, whose schematic diagram is shown in Figure 2.16. The device was biased at -2.0 V voltage and mounted on a 6 mm hyper-hemispherical Si lens. Same as the pulse measurement on CW devices, input optical pulses were generated by MZ modulator and amplified through EDFA. CW measurement was done first and followed with 50%, 20% and 10% pulse measurement. The pulse width was set to 25 ns and repetition frequencies were set to 20 MHz, 8 MHz and 4 MHz respectively. Optical input signals were set to rectangular pulses, and the measured photocurrents and 250 GHz power were average values. For 50%, 20%, and 10% pulse measurement, the pulse photocurrent and pulse output power were calculated by multiplying their average readings by 2, 5 and 10 respectively.

CW and pulse measurement results on one 4x15 μm^2 bow-tie antenna integrated UTC-PD are shown in Figure 3.24. For the CW input conditions, the max output power is measured as 56 μW (-12.5 dBm) at 13.2 mA. For 50 % pulse input, the

output power is improved to 88 μW (-10.6 dBm) at 15 mA, and for 20 % pulse input, the output power is further improved to 125 μW (-9.0 dBm) at the photocurrent of 18 mA. For 20% and 10% optical pulse input, the max RF output power was improved by 3.5 dB and 3.8 dB respectively, compared to CW input measurement. Pulse measurement results indicate the 250 GHz output power of bow-tie antenna integrated UTC-PDs can be increased by more than 3 dB with lower junction temperature.

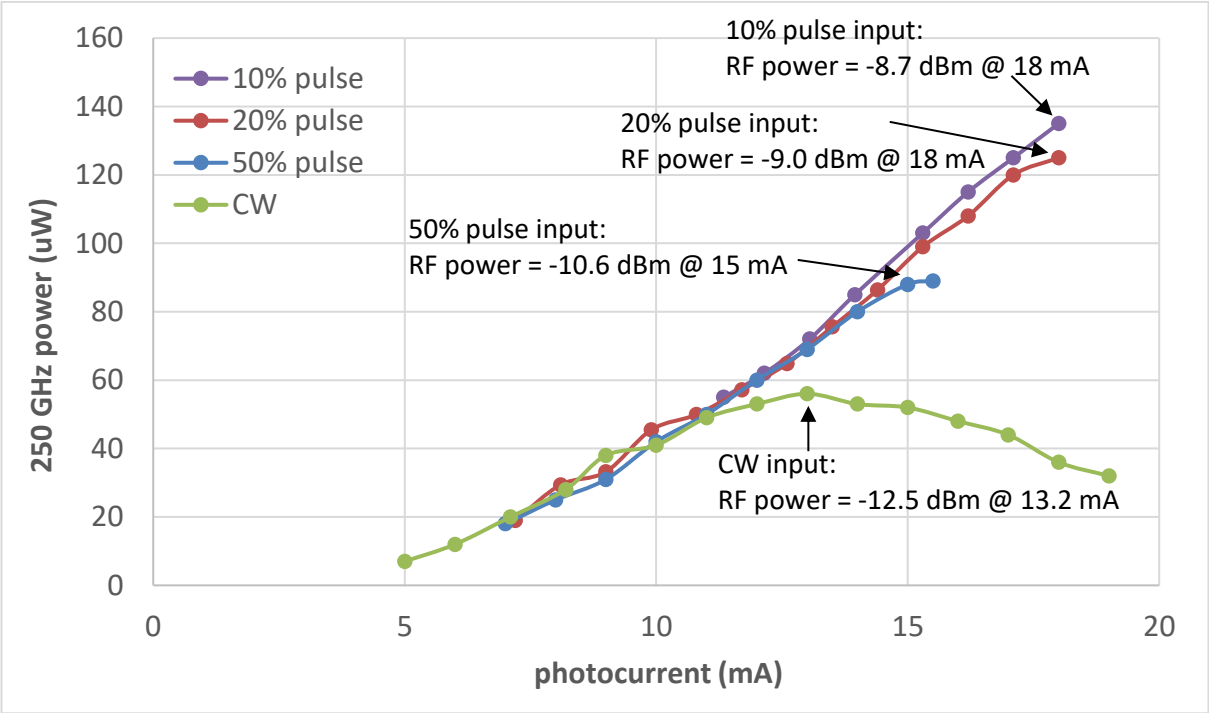

Figure 3.24: 250 GHz radiated power of 4x15 μm^2 bow-tie antenna UTC-PDs on Si lens, with CW & pulse optical input (25 ns pulse width), biased at -2V.

3.5 Pulse measurement results analysis

Optical pulse input measurement results of different sizes CPW UTC-PDs and antenna integrated UTC-PDs in Section 3.4 have similar performance trend: the RF output power saturates at higher photocurrents at pulse input conditions than CW input conditions, and 10% pulse input gets higher saturation power than 50% pulse input. In this Section, detail analysis was done on CW and pulse measurement data of 3x10 μm^2 CPW UTC-PDs (Figure 3.25) in order to find out

which effect (space charge effects, or thermal effects) caused the RF output power saturation at high photocurrents. Also, the electric field at the absorption/collection layer interface was calculated on 3x15 μm^2 and 7x15 μm^2 CPW UTC-PDs, at their saturation photocurrents of 10% duty cycle pulse input.

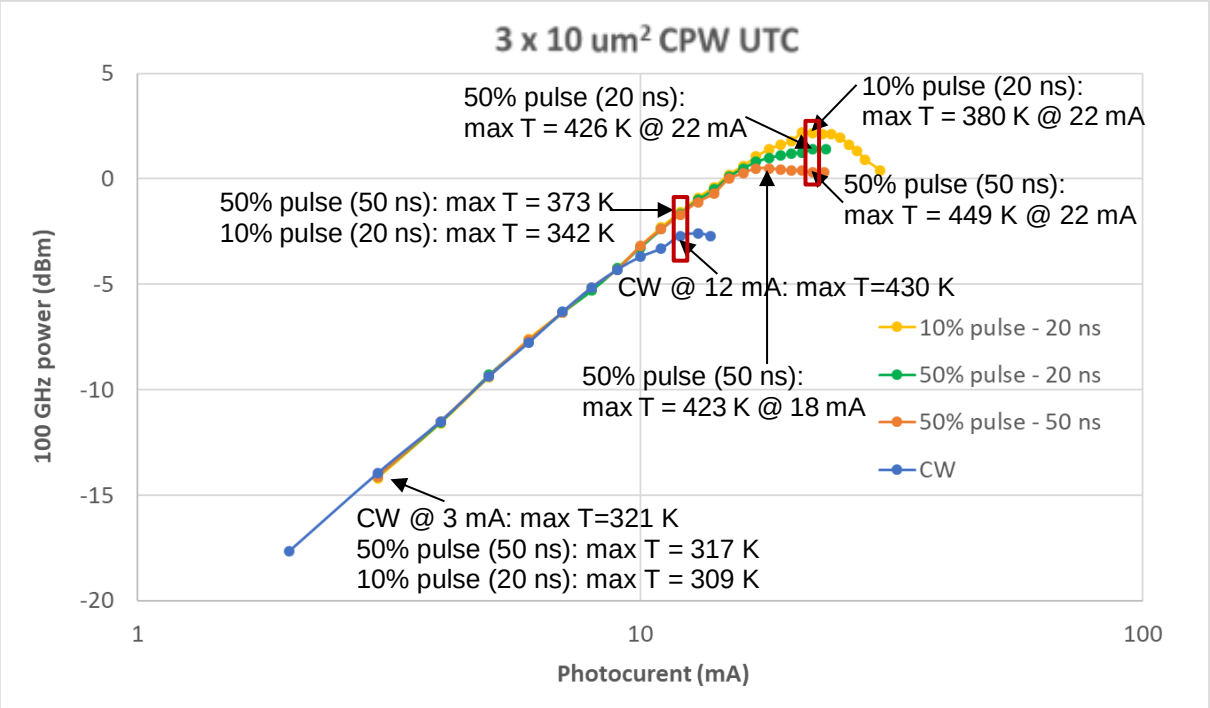

Figure 3.25: 100 GHz output power of 3x10 μm^2 CPW UTC-PDs, with CW optical input and pulse optical input.

In Figure 3.25, for the photocurrent from 2 mA to 9 mA, the 100 GHz output power of the CW optical input and pulse optical input overlaps, which means the RF output power is determined by photocurrents, not by the temperature inside active region of UTC-PDs. At the photocurrent of 3 mA, 5 mA and 7 mA, their simulated max internal temperatures under CW and pulse inputs are plotted in Figure 3.26, from which we can clearly see their temperature differences. 10% pulse input has lowest temperature and CW input has highest temperature in the absorption layer when at the same photocurrent.

From the photocurrent of 10 mA, the 100 GHz output power under CW input starts to saturate, and is saturated at the photocurrent of 12 mA. The corresponding max temperature is modelled as 430 K. But for 10% and 50% pulse input

conditions, their RF output power still keeps the same increasing slope until the photocurrent of 15 mA. At 12 mA photocurrent (CW input saturation photocurrent), the max temperatures of 10% and 50% pulse input are modelled as 342 K and 373 K respectively, much lower than the max temperature of CW optical input (430 K). This indicates the output power saturation of CW input is caused by thermal effects, not by space charge effects. To double check this conclusion, the electric field inside UTC-PDs needs to be calculated and compared with the critical field ($E_c \approx$ 10 kV/cm). When the electric field at the absorption/collection layer interface (E_{int}) is smaller than the critical field E_c, the electron velocity overshoot (due to the non-equilibrium transport of electrons) will not take place [3.17] and the electron drift velocity (v_e) will decrease to the saturation velocity (see Figure 3.28). At this point, the power saturation of photodiodes will be caused by space charge effects. For the photocurrent of 12 mA, we need to check E_{int} to see whether it is higher or lower than E_c to confirm whether the output power saturation of CW input is caused by space charge effects or thermal effects. The calculated electric field at 12 mA photocurrents is around 50.6 kV/cm at the interface of absorption and collection layer, much higher than E_c. This further confirms the output power saturation of CW input is caused by thermal effects, not by space charge effects. The details of how the electric field is calculated are shown in Appendix D.

For 50% duty cycle input with 50 ns pulse duration (the orange line), the 100 GHz power saturated at the photocurrent of 18 mA, and the max temperature is modelled as 423 K. The max temperature changing with time is shown in Figure 3.27 (a). For 50% duty cycle input with 20 ns pulse duration (the green line), 100 GHz output power saturated at the photocurrent of 22 mA, and its max temperature is 426 K. The max temperature changing with time is shown in Figure 3.27 (b). For 10% duty cycle input, the output power saturated at 23 mA / 24 mA, and its corresponding max temperature is 384 K / 390 K, see Figure 3.27 (c). For photocurrent = 23 mA (the 10% pulse input saturation photocurrent), the calculated electric field E_{int} at the interface of absorption and collection layer is 25.2 kV/cm, still higher than E_c. Therefore, for my understanding, it is also the thermal effects causing power saturation for 10% optical pulse input.

For 3x15 μm^2 and 7x15 μm^2 CPW UTC-PDs, their 100 GHz output power saturates at the photocurrent of 25 mA and 36 mA respectively, when their input optical signals are 10% duty cycle pulses, see Figure 3.22 and Figure 3.23. The electric field at the absorption/collection layer interface was calculated in order to check whether the power saturation was caused by space charge effects. For 3x15 μm^2 and 7x15 μm^2 CPW UTC-PDs, the calculated interface electric fields E_{int} are 38.6 kV/cm and 42.7 kV/cm, respectively. Both of these fields are higher than E_c, which suggests that RF power saturation at 10% pulse input is caused by thermal effects.

In summary, for 3x10 μm^2, 3x15 μm^2 and 7x15 μm^2 CPW UTC-PDs, their RF output power saturations were caused by thermal effects both in CW and 10% pulse measurements, and their 100 GHz output power saturated at 23 mA, 25 mA and 36 mA respectively under 10% pulse input conditions. Pulse measurement results indicate thermal effects cause RF output power saturation before space charge effects in small size UTC-PDs, and the RF output power can be improved by reducing the temperature in the junction area.

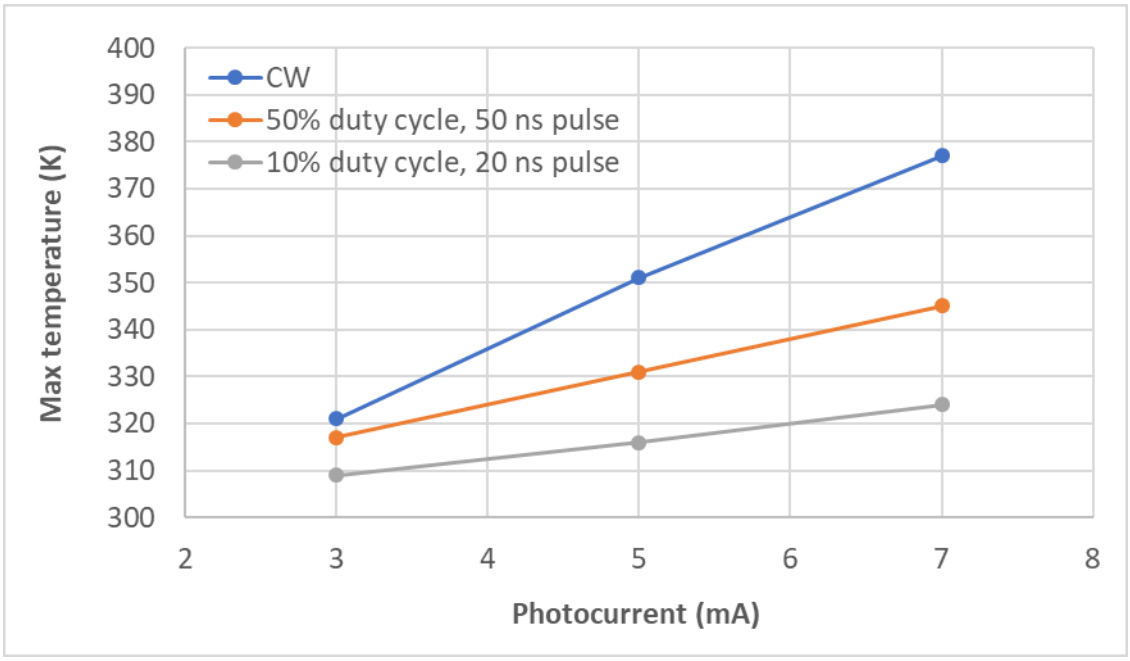

Figure 3.26: the simulated max temperature in active region of 3x10 μm^2 CPW UTC-PDs at the photocurrent of 3 mA, 5 mA and 7 mA, biased at -3 V.

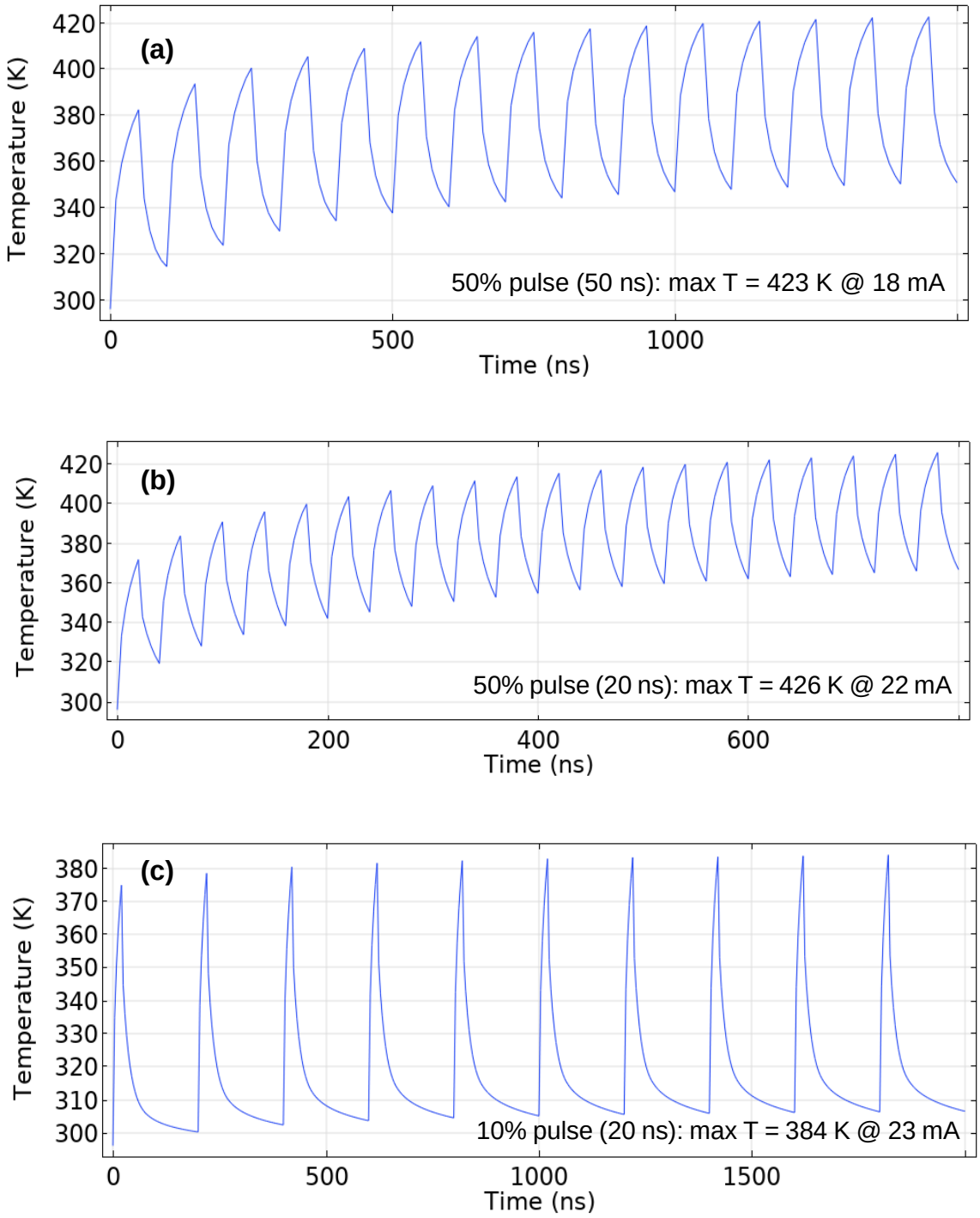

Figure 3.27: the max temperature in 3x10 μm^2 CPW UTC-PDs changes with time under pulse input conditions. (a) 50% optical pulse input (pulse duration = 50 ns) at 18 mA photocurrent, (b) 50% optical pulse input (pulse duration = 20 ns) at 22 mA photocurrent, (c) 10% optical pulse input (pulse duration = 20 ns) at 23 mA photocurrent.

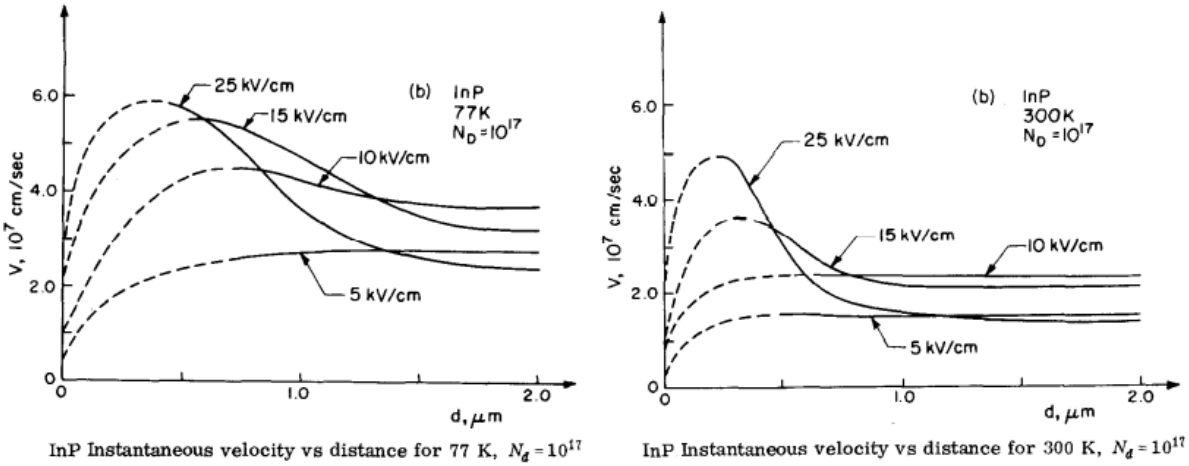

Figure 3.28: InP drift velocity at distance less than 2 μm. (a) Instantaneous drift velocity changes with distance for 77 K, (b) Instantaneous drift velocity changes with distance for 300 K [3.18].

3.6 Conclusions

The RF output power of UTC-PDs saturates at high photocurrents due to space charge effects or thermal effects. By using optical pulses as input signals, the max temperature of UTC-PDs can be reduced. Pulse measurements were done on CPW UTC-PDs and antenna integrated UTC-PDs, to see how much the output power can be increased by reducing their thermal effects. A MZ modulator was utilized to generate short duration optical pulses, which was then amplified by an EDFA and coupled into waveguide UTC-PDs through 2.5 μm spot-size lens fibre in the saturation power measurement. Pulse measurement results indicate: (1) the RF output power saturates at higher photocurrents under pulse input conditions. (2) For UTC-PDs with bigger size of P-ridge, their saturation power improvement at pulsed input is less than devices with smaller size of P-ridge. (3) the RF output power of CPW UTC-PDs and antenna integrated UTC-PDs can be increased by more than 3 dB at 10% pulse input conditions (pulse width is 20 ns / 25 ns).

In order to analyse which effects (space charge effects or thermal effects) caused the RF output power saturation in CW and pulse measurements, electric fields at the interface of absorption and collection layer were calculated and compared

with the critical field ($E_c \approx 10$ kV/cm) on 3x10 μm^2, 3x15 μm^2 and 7x15 μm^2 CPW UTC-PDs. Calculations show their RF output power saturations were caused by thermal effects both in CW and 10% pulse measurements. Therefore, the RF output power of CPW and antenna integrated UTC-PDs can be increased by improving their thermal management. In the next Chapter, possible ways are discussed to lower UTC-PD's junction temperature and use COMSOL modelling to show and compare their effectiveness.

3.7 References

[3.1] Xiaojun Xie, Qiugui Zhou, Kejia Li, Yang Shen, Qinglong Li, Zhanyu Yang, Andreas Beling, And Joe C. Campbell, "Improved power conversion efficiency in high-performance photodiodes by flip-chip bonding on diamond", Optica, vol. 1, no. 6, pp. 429-435, (2014).

[3.2] E. Zielinski, H. Schweizer, and K. Streubel, "Excitonic transitions and exciton damping processes in InGaAs/InP", Journal of Applied Physics, vol. 59, no. 6, pp. 2196-2204, (1986).

[3.3] J. M. Torres Pereira, "Frequency response analysis of photodiodes for optical communications", Optoelectronics and Advanced Materials - Rapid Communications, vol. 4, no. 7, pp. 916-921, (2010).

[3.4] Pereira, J. T. "The effect of temperature on the frequency response of p-i-n photodiodes for optical communications", Proceedings of conference on telecommunications - ConfTele, vol. 1, pp. 141-144.

[3.5] Hao Chen, Andreas Beling, Huapu Pan, and Joe C. Campbell, "A Method to Estimate the Junction Temperature of Photodetectors Operating at High Photocurrent", IEEE Journal of Quantum Electronics, vol. 45, no. 12, pp. 1537 – 1541, (2009).

[3.6] Humphreys, D. A., R. J. King, D. Jenkins, and A. J. Moseley, "Measurement of absorption coefficients of Ga 0.47In 0.53As over the wavelength range 1.0-1.7 μm", Electronics Letters, vol. 21, no. 25, pp. 1187-1189, (1985).

[3.7] Lee, HR., Lee, SY., Jeong, TY. et al, “Temperature-dependent optical constant of an InGaAsP layer as determined from the reflectance spectrum,” Journal of the Korean Physical Society, vol. 70, no. 12, pp. 1064–1069, (2017).

[3.8] Sten Seifert and Patrick Runge, "Revised refractive index and absorption of In1-xGaxAsyP1-y lattice-matched to InP in transparent and absorption IR-region," Optical Materials Express, vol. 6, no. 2, pp. 629-639, (2016).

[3.9] Temkin, H., V. G. Keramidas, M. A. Pollack, and W. R. Wagner. "Temperature dependence of photoluminescence of n-InGaAsP." Journal of applied Physic, vol. 52, no. 3, pp. 1574-1578, (1981).

[3.10] Yang Shen, John Gaskins, Xiaojun Xie, Brian M. Foley, Ramez Cheaito, Patrick E. Hopkins, and Joe C. Campbell, “Thermal Analysis of High-Power Flip-Chip-Bonded Photodiodes”, Journal of Lightwave Technology, vol. 35, no. 19, pp. 4242-4246, (2017).

[3.11] https://www.fiberoptics4sale.com/blogs/archive-posts/95051142-edfa-fundamentals-explained-in-details

[3.12] https://www.thorlabs.com/newgrouppage9.cfm?objectgroup_id=10680&pn=EDFA100S

[3.13] A. D. Kersey, M. J. Marrone, and A. Dandridge, ‘‘Observation of input-polarization-induced phase noise in interferometric fiber-optic sensors,’’ Opt. Lett. vol. 13, no. 10, pp. 847-849, (1988).

[3.14] A. D. Kersey, M. J. Marrone, and A. Dandridge, ‘‘Analysis of input-polarization-induced phase noise in interferometric sensors and its reduction using polarization scrambling,’’ J. Lightwave Technol., vol. 8, no. 6, pp. 838–845, (1990).

[3.15] E. Desurvire, Erbium-Doped Fiber Amplifiers: Principles and Applications, Wiley, NY, (1994).

[3.16] Akram Abu-aisheh, Saeid Moslehpour, “Pre-amp EDFA ASE noise minimization for optical receiver transmission performance optimization”, Optics Communications vol. 283, no. 12, pp. 2603-2606, (2010).

[3.17] N. Shimizu, Y. Miyamoto, A. Hirano, K. Sato and T. Ishibashi, “RF saturation mechanism of InP/InGaAs uni travelling-carrier photodiode”, Electronics Letters, vol. 36, no. 8, pp. 750-751, (2000).

[3.18] T. J. Maloney and Jeffrey Frey, "Transient and steady‐state electron transport properties of GaAs and InP", Journal of Applied Physics, vol. 48, no. 2, pp. 781-787, (1977).

Chapter 4
Waveguide UTC-PD Thermal Modelling

4.1 Introduction

In our waveguide UTC-PDs, the optical power is coupled through the waveguide facet from the lens fibre, and then evanescently absorbed in the absorption layer and generates electron-hole pairs, where only electrons contribute to the photocurrents. Except for the output RF power and joule heat, the remaining energy generates thermal heat, which makes the temperature of UTC-PD increase. When UTC-PDs operate at high input optical power and high bias voltage, the remaining thermal heat will be large, and it is difficult to transfer this large amount of heat to the outside of photodiodes as the thermal conductivities of UTC-PD's layers are relatively low (see Table 4.1). If there is no effective thermal management to dissipate these remaining energies, it will increase the temperature of photodiodes. All characteristics of photodiodes are impacted by temperature changes, including shunt resistance, dark current, breakdown voltage, responsivity, saturation power and etc. High temperature degrades the performance of photodiodes and shortens their lifetime, and some photodiodes face burn out before their power saturation due to thermal effects.

Table 4.1: Thermal properties of materials composing UTC-PDs.

UTC-PD Layer	Material		Thermal Conductivity W / (m·K)	Heat Capacity J / (kg·K)
P-contact	p^{++}-InGaAsP		7.2	337
Absorption	p-InGaAs		5	300
Collection	n-InP		68	310
Waveguide	n-InGaAsP		7.2	337
N-contact	n^{++}-InP		68	300
S.I. InP	InP		68	300
Insulation	SiO_xN_y	SiO_2	1.4	680
		Si_3N_4	30	673

According to the pulse measurement results in Chapter 3, the saturation power of UTC-PDs can be improved by reducing their max temperature at high optical inputs and high photocurrents. Sitting UTC-PDs on the thermoelectric cooler (TEC) can help to reduce the internal temperature of devices, but the cooling effect is limited as the heat source (in the junction of UTC-PDs [4.1]) is located close to P-contact on the top but relatively far from the bottom of UTC-PDs. Flip-chip bonding the P-contact of UTC-PDs onto high thermal conductivity sub-mounts (like AlN, diamond) was reported helping dissipate the thermal heat out of UTC-PDs [4.2] – [4.4]. In order to work at the frequency range (200 – 300 GHz) for high-speed wireless communications, the P-contact size of our UTC-PDs (3x10 μm^2, 3x15 μm^2, 4x15 μm^2) is much smaller than that of reported UTC-PDs flip-chip bonded to high thermal conductivity sub-mounts for thermal management. The diameter of gold bumps (usually 10 - 20 μm) is much larger than the P-contact size of our UTC-PDs, therefore the flip-chip technique can't be used to reduce our devices' internal temperature. Besides, as our UTC-PDs target is to work as the source of wireless communication networks, they are integrated with broadband antennas and attached to a Si substrate integrated lens (diameter = 6 mm), which helps increasing the directivity of the antenna and mitigating substrate modes, see an example of antenna integrated UTC-PDs in Figure 4.1. Therefore, in the new design for reducing thermal effects, its impact on the impedance of UTC-PDs should also be considered, to minimise the influence on impedance mismatch which decides the RF power coupling between the UTC-PD and antenna [4.5], [4.6]. Also, the fabrication of new design should be feasible and reproducible.

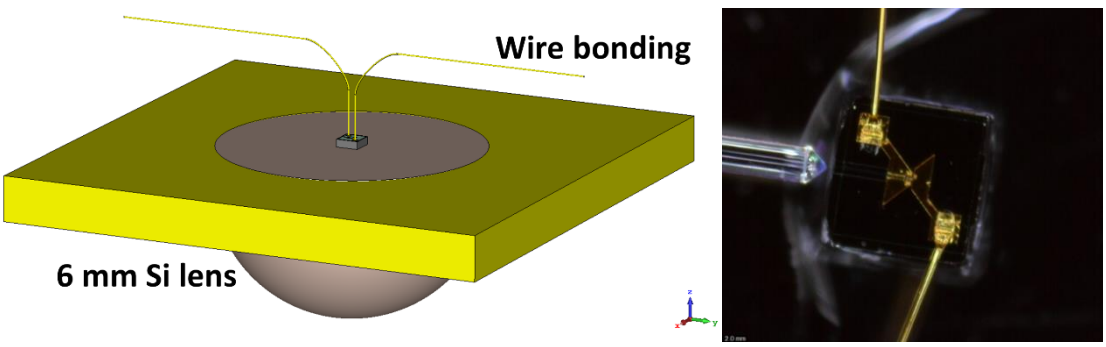

Figure 4.1: Wire-bonded antenna UTC-PD on Si lens (D = 6 mm).

In this Chapter, possible ways are to be discussed to reduce the thermal effect of antenna integrated waveguide UTC-PDs, in order to increase their radiated RF power. In Section 4.2, thermal modelling is performed on the current design of our antenna integrated UTC-PDs. Based on the simulated thermal distribution and the device structure, analysis is done to figure out the reasons preventing thermal energy dissipating. According to these simulations and analyses, three solutions are developed to help dissipate heat from the UTC-PDs in Section 4.3. Good solutions should consider heat transfer efficiency, impact on UTC-PDs' performance (like impedance, mechanical stress, etc.) and process feasibility. But it is not easy to cover all of them in one solution. For solution 1 (utilize thicker antenna, details in 4.3.1), fabrication process is achievable and not complicated, but the heat dissipation effect is limited. For solution 2 (deposit AlN layer on the top of antenna, details in 4.3.2), the heat dissipation effect is much better than solution 1, but need intense work on process development to obtain high thermal conductivity and low intrinsic (growth) stress AlN films. For solution 3 (using thermal conductive adhesive replacing current bonding layer, details in 4.3.3), this approach is achievable and also can provide good effect on heat dissipation. In Section 4.4, the method to measure the temperature in the active region of waveguide UTC-PDs is presented and compares with the thermal simulations by COMSOL, in order to verify the thermal modelling.

COMSOL Multiphysics was used to do the thermal modelling in this Chapter. COMSOL Multiphysics is a cross-platform finite element analysis, solver and multiphysics simulation software. It allows conventional physics-based user interfaces and coupled systems of partial differential equations (PDEs). COMSOL provides an integrated development environment (IDE) and unified workflow for electrical, mechanical, fluid, acoustics and chemical applications. The heat transfer module was used to simulate thermal distributions, which is a powerful tool to study the three types of heat transfer (conduction, convection, and radiation).

4.2 Thermal analysis on current UTC-PD design

4.2.1 Thermal modelling

In order to reduce our UTC-PD's temperature at high photocurrents, the first step is to get the temperature distribution of current structure. The device structure used for thermal modelling is shown in Figure 4.1. The antenna integrated WG UTC-PD is attached to the hyper-hemispherical Si lens by a layer of Nitrocellulose (15 μm thickness), and the Si lens is inserted into a brass holder (20 x 12 x 0.6 mm), which helps to hold the whole assembly in front of the lensed fibre. Elementary antennas on planar dielectric substrates suffer power loss due to substrate modes. This substrate mode problem can be solved if the dielectric substrate the antenna is deposited on is semi-infinite. By using dielectric lens which has the similar dielectric constant as the substrate, the substrate modes can be eliminated [4.7]. The dielectric constant of Si is 11.7, which is very close to the dielectric constant of InP (12.5). That is why Si lens is chosen as the substrate lens placed beneath our antenna integrated InP UTC-PDs.

According to energy conservation, the total power delivered to the photodiode must equal to the sum of the output power delivered by the photodiode and the power dissipated in the photodiode [4.8], expressed in (4.1). $P_{optical}$ is the absorbed input optical power, P_{DC} is the electrical power delivered to the photodiode, P_{UTC} is the radiated RF power by UTC-PD, $P_{contact}$ is the joule heat on contacts, and $P_{dissipated}$ is the remaining power to heat the device.

$$P_{optical} + P_{DC} = P_{UTC} + P_{contact} + P_{dissipated} \quad (4.1)$$

Based on the experiment results of 3x15 μm^2 antenna integrated UTC-PD, the UTC-PD generates 13.5 mA photocurrent and 60 μW RF power with 64 mW input optical power and -2V bias voltage. The optical power coupling ratio is about 45% between the waveguide of UTC-PD and the lensed fibre (spot size = 2.5 μm). The series resistance of same size CPW UTC-PD was measured as 15 Ω. Based on (4.1), the calculated dissipated power inside UTC-PD is 52.5 mW, which was set as the heat source in the thermal modelling.

Besides conduction, convection is another type of heat transfer for UTC-PDs. Convection is the transfer of heat by the movement of a fluid (liquid or gas) between areas of different temperatures. The heat transferred by convection is proportional to three parameters: heat transfer area of the object, convective heat transfer coefficient and temperature difference between the object's surface and the fluid. The surface of heated UTC-PDs has higher temperature than room temperature (the lab's temperature is controlled to 20 ºC by an air conditioner), therefore the convective heat flux between air and the device surface should be included though the heat convection effect is very limited because the surface area of UTC-PDs is very small. Convective heat transfer can be through natural convection or forced convection. Natural convection is caused by buoyancy forces due to density differences from temperature variations in the fluid. Where the fluid displaced is accelerated by wind or artificial means the process is called forced convection. Convective heat transfer coefficients (h_c) depends on the type of media and flow properties, such as velocity, viscosity and other flow and temperature dependent properties. Typical convective heat transfer coefficients for free air convection is in the range of 0.5 - 100 W/(m^2K), and for forced air convection the value is in the range of 10 - 1000 W/(m^2K). In my COMSOL modelling, the air convective coefficient is set to 5.0 W/(m^2·K) refer to [4.9]. Different values of air convective coefficient were applied in the modelling to see the influence on the temperature distribution (1, 10, and 20 W/(m^2·K)). The impact on the highest temperature inside UTC-PDs is very limited, less than 1 ºC.

The materials' properties also need to be set in COMSOL and the properties needed for thermal simulation are thermal conductivity, density, and heat capacity. Table 4.1 lists the thermal properties of materials composing our UTC-PDs. A material's thermal conductivity is dependent on temperature, pressure and doping level. We can estimate these properties for each material based on published values in papers. Papers [4.10] and [4.11] show that the doping level has an influence on the heat generation mechanism of semiconductors. The thermal conductivity/diffusivity value of doped InP is less than that for undoped samples. In Table 4.1, for collection layer and n-contact layers (n-InP and n^{++}-InP respectively), I use the reported thermal conductivity of n-type InP (doping = $2x10^{16}$ cm^{-3}) [4.12] at normal temperature and pressure (NTP). For absorption,

p-contact and waveguide layers (p-InGaAs, p^{++}-InGaAsP and n-InGaAsP), I use the reported value for undoped InGaAs and InGaAsP [4.13] at NTP.

The simulated temperature distribution inside 3 x 15 μm^2 bow-tie antenna integrated UTC-PD is shown in Figure 4.2. The max temperature inside device is 454 K (181 ºC), located in the absorption layer. From Figure 4.2, we can see: 1) There is 50.5 ºC temperature difference between UTC-PD's substrate and Si lens. 2) On the top surface of antenna UTC-PD, the most of heat concentrates at the P-contact area, and the gold antenna doesn't help for heat dissipation. 3) The cross-section temperature distribution indicates heat energy trapped inside the P-ridge and only a small part of heat dissipated through InP substrate.

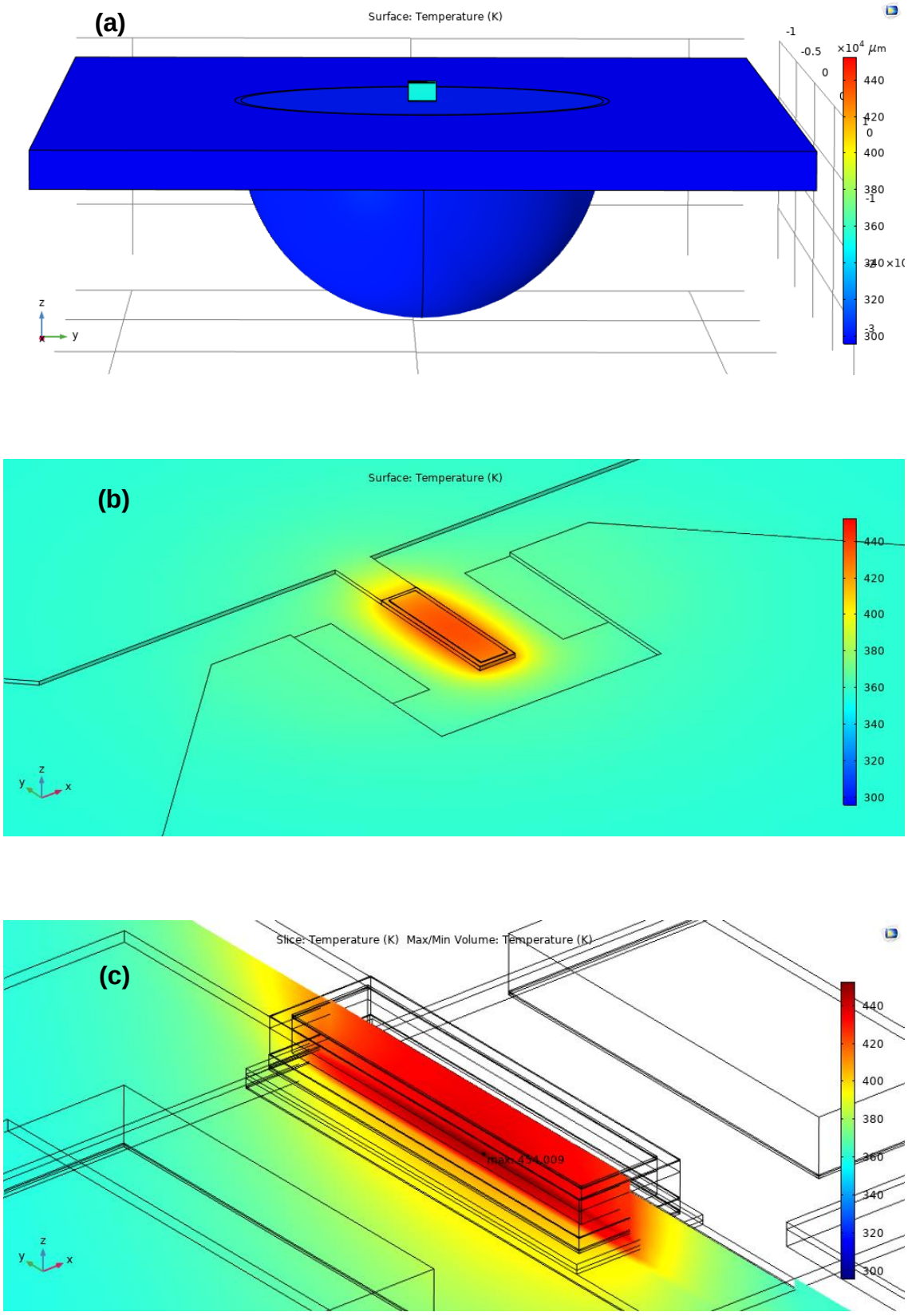

Figure 4.2: (a) Temperature distribution of bow-tie antenna integrated UTC-PD (3x15 μm^2) on Si lens, (b) Temperature distribution on the top surface, (c) Temperature distribution of P ridge cross section.

4.2.2 Modelling results analysis

Thermal resistance is the reciprocal of thermal conductance. Just as an electrical resistance is associated with the conduction of electricity, thermal resistance is associated with the conduction of heat. Thermal resistance determines the heat insulation property of a material, and can be calculated by $R_t = L / (K \cdot A)$, where K is the material's thermal conductivity, L is the material's thickness and A is the area of heat passing-through. Figure 4.3 (a) shows the change of temperature along the z-axis in the centre of P-contact, from the top of device to the Si lens. Figure 4.3 (b) is the magnified view of Figure 4.3 (a) which shows the change of temperature along the z-axis from the top of device to the 50 μm below the interface between n-contact layer and S.I. InP substrate. Below Table 4.2 summarises the temperature changes in each material layer, giving the whole picture of the temperature distribution. In the temperature change column, the values are calculated by using the temperature at the top of the layer subtract the temperature at the bottom of the layer. Positive values mean the temperature is dropped after this layer, and negative values mean the temperature is increased after this layer.

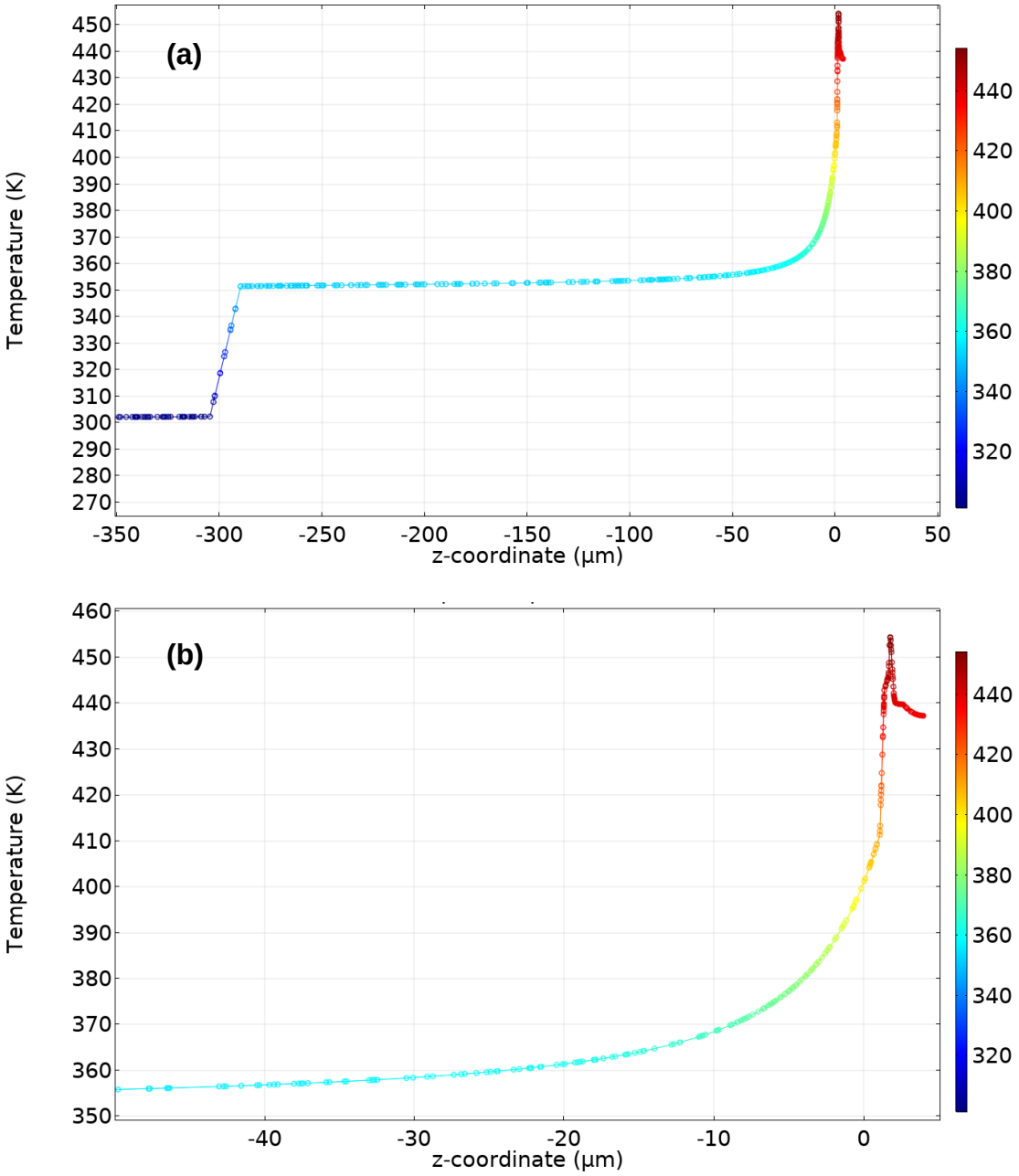

Figure 4.3: (a) The change of temperature along the z-axis in the centre of P-contact, from the top of device to the Si lens, (b) the change of temperature along the z-axis from the top of device to the 50 µm below the interface between n-contact layer and S.I. InP substrate.

Table 4.2: The temperature changes in each material layer, from the top of antenna UTC-PD P-contact to Si lens.

Device Layer	Material	Thickness	Thermal Conductivity W / (m·K)	Temperature Change (ºC)
P electrode	Ti/Pt/Au	75nm/50nm/400nm	17 / 72 / 314	-1.9
P-contact	p^{++}-InGaAsP	200 nm	7.2	-11
Absorption	p-InGaAs	120 nm	5	6.2
Collection	n-InP	300 nm	68	3.5
Waveguide	n-InGaAsP	300 nm	7.2	31.4
N-contact	n^{++}-InP	600 nm	68	6.1
S.I. InP	InP	290 µm	68	53.7
Bonding layer	Nitrocellulose	15 µm	0.142	50.5
Substrate lens	Si	r = 3.0 mm	142	0.87

The material used to bond UTC-PD to Si lens is Nitrocellulose. Its thermal conductivity is very low, only 0.142 W/(m·K). The chip size of the UTC-PD is 460 x 460 μm^2, and the thickness of Nitrocellulose is about 15 µm. The calculated thermal resistance for this bonding layer is 499.2 K/W. This layer's thermal resistance can be reduced if using higher thermal conductivity material or increase the size of UTC-PD chip. The temperature change through the S.I. InP substrate is 53.7 ºC, but 70% of the temperature change happens within the 10 µm depth, which has a high thermal resistance of 3268 K/W. That is why the heat can't be effectively dissipated through the InP substrate. If the InP substrate can be etched to less than 10 µm, it will be helpful for heat dissipation. But, even though we can realise the thin InP membrane, it has a high risk to damage the fabricated devices when cleaving to get a flat waveguide facet. Figure 4.2 (b) shows most of the heat is blocked in the P-ridge and the temperature is as high as 440 K at the top of the P-contact, just 14 K lower than the highest temperature (454 K). Though the gold antenna is sputtered on the high temperature P-contact, it doesn't contribute to reduce the temperature because there is limited heat transferred from the P-ridge to the antenna. Gold is a very good thermal conductor and has a high thermal conductivity of 314 W/(m·K). But why the gold antenna doesn't conduct the heat out of P-ridge? The answer is high thermal resistance. After the Ti/Pt/Au P-contact is sputtered on the top of UTC-PD's P-

ridge, SiO_xN_y is deposited to cover UTC-PDs to passivate and protect the etched surfaces. Then vias are etched down to the P-contact and N-contact. Finally, the bow-tie antenna is sputtered on the top of SiO_xN_y and connected to the P-contact and N-contact through the etched vias. Figure 4.4 gives the idea of the via structure and how it connects to electrodes (this photo is for CPW UTC-PDs). The vias are hollow holes and their inner surfaces are covered with a layer of Ti/Au (35 nm/400 nm). That means for 3x15 μm^2 UTC-PDs, the cross-section area between the antenna and the P-contact is only 3 µm x 435 nm, through which the heat conduction passes. Therefore, the corresponding thermal resistance between the P-contact and gold antenna reaches 14642 K/W. Such a high thermal resistance blocks the heat path and confines the heat inside the P-ridge.

In summary, the optical power is absorbed and the photocurrent is generated in the absorption layer of UTC-PDs, where the heat source locates. Due to the high thermal resistance between P-contact and gold antenna, the heat can't be easily extracted out from the P-ridge. Besides, the high thermal resistances between UTC-PD and InP substrate, and between InP substrate and Si lens, result in poor heat dissipation through the UTC-PD's substrate. In the next Section, solutions are explored and discussed to reduce these high thermal resistances, in order to improve the heat dissipation and reduce the high temperature of antenna integrated UTC-PDs.

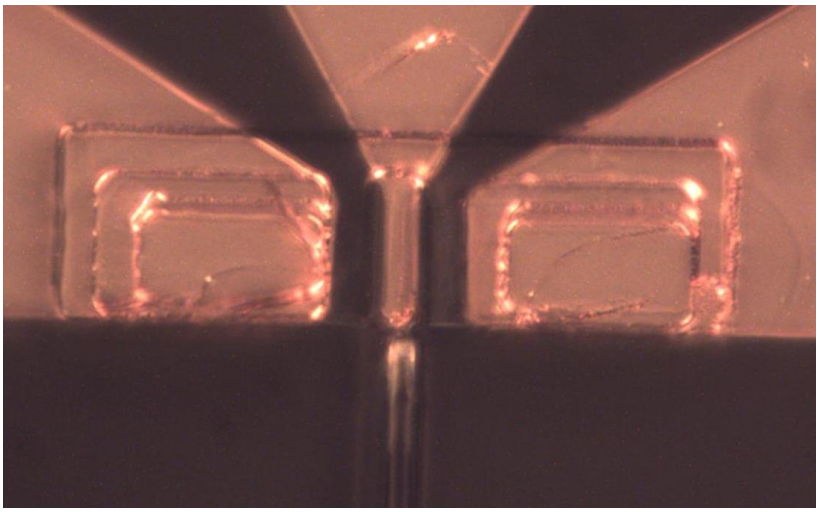

Figure 4.4: The via structure and connections to the electrodes.

4.3 Thermal management improvement solutions

Based on the analysis in Section 4.2.2, the high temperature inside antenna integrated UTC-PDs can be lowered by bringing down their high thermal resistances. According to the formula of thermal resistance $R_t = L/(K \cdot A)$, thermal resistance is proportional to material's thickness L, and inversely proportional to material's thermal conductivity K and area A. Therefore, decrease L or increase K and A will reduce thermal resistance. For the thermal resistance between UTC-PD's InP substrate and Si lens, if the chip size is increased from 460 µm x 460 µm to 800 µm x 800 µm, the thermal resistance will be decreased from 499.2 K/W to 165.1 K/W and the maximum temperature will be reduced from 454 K to 417 K (37 ºC lower), see Figure 4.5. Though increasing the chip size of UTC-PDs could help to dissipate thermal heat, it decreases the device amount in the same size wafer and increases the cost. Therefore, it is not a practical solution for mass production.

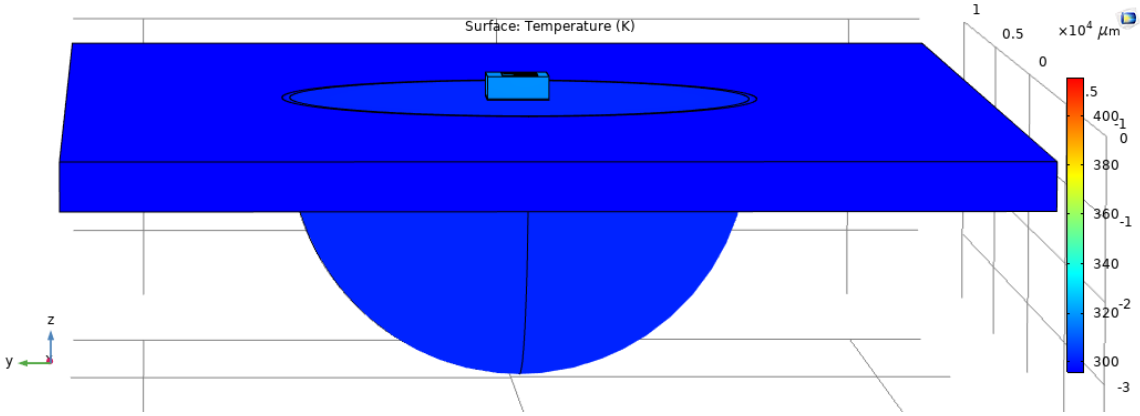

Figure 4.5: Temperature distribution of antenna integrated UTC-PD (3x15 µm^2) on Si lens. UTC-PD chip size is 800 µm x 800 µm.

Considering the thin InP membrane solution is not suitable for our waveguide UTC-PDs, I will focus on reducing the thermal resistances at two positions in this Section: between P-contact and gold antenna, and between InP substrate and Si lens. On the top of the P electrode, the temperature reaches 440 K, just 14 K below the maximum temperature. The temperature is close to the max temperature inside UTC-PDs due to thin absorption layer (120 nm) and P-contact

layer (200 nm) though their thermal conductivities are low. As the thermal resistance between P electrode and antenna is very high, 14642 K/W, the bow-tie antenna can't act as heat spreader despite of their high thermal conductivity. The thermal conductivity of bonding layer between InP substrate and Si lens is only 0.142 W/(m·K), preventing heat spread into Si lens, which is a good heat dissipation material. Besides this high thermal resistance, another factor that hinders the heat dissipation is the SiO_xN_y passivation layer, whose thermal conductivity is relatively lower (SiO_2: 1.4 W/(m·K), Si_3N_4: 30 W/(m·K)). Also, it only covers a narrow strip of side surface of P-ridge (see Figure 4.6), which results in a high thermal resistance between P-ridge and SiO_xN_y. In Sections 4.3.1 to 4.3.3, three solutions are presented to solve the problem of high thermal resistances respectively.

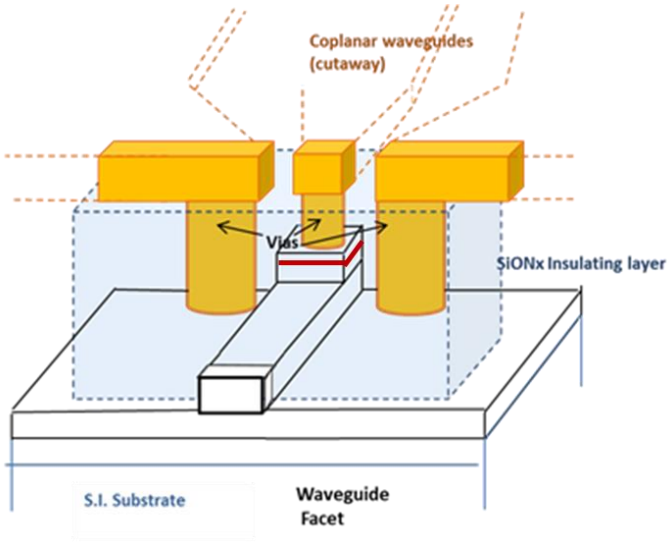

Figure 4.6: The passivation/insulation layer of SiO_xN_y covers the P-ridge and waveguide. Red lines indicate the absorption layer.

4.3.1 Solution 1 – solid P via

The reason for such high thermal resistance R_{th_a} between P electrode (sputtered directly on the top of P-contact layer and has the same size of P-contact) and bow-tie antenna is only 435 nm thick of gold connecting them at the edge of the etched P via. If not change the P-ridge size and the bow-tie antenna structure, the remaining way to lower the high thermal resistance is to widen the width of

the heat path, therefore make the cross-section area of heat dissipation path larger. This can be realised by 1) filling the hollow P-via with gold, and 2) make the bow-tie antenna (connected to the P electrode) thicker. Below Figure 4.7 shows the corresponding maximum temperature of antenna integrated UTC-PDs on Si lens at different thickness of bow-tie antenna at the condition of solid P-via. We can see: 1) With solid via and thicker bow-tie antenna, the max temperature can be reduced, 2) the temperature change starts to slow down when the thickness of antenna is larger than 5 µm. Also, too thick gold will increase process time and the device cost. Therefore, 5 µm is chosen as the thickness of the bow-tie antenna and the maximum temperature is decreased by 22 ºC. At this thickness, the calculated thermal resistance R_{th_a} is about 1274 K/W, 11.5 times smaller than the thermal resistance with hollow P-via.

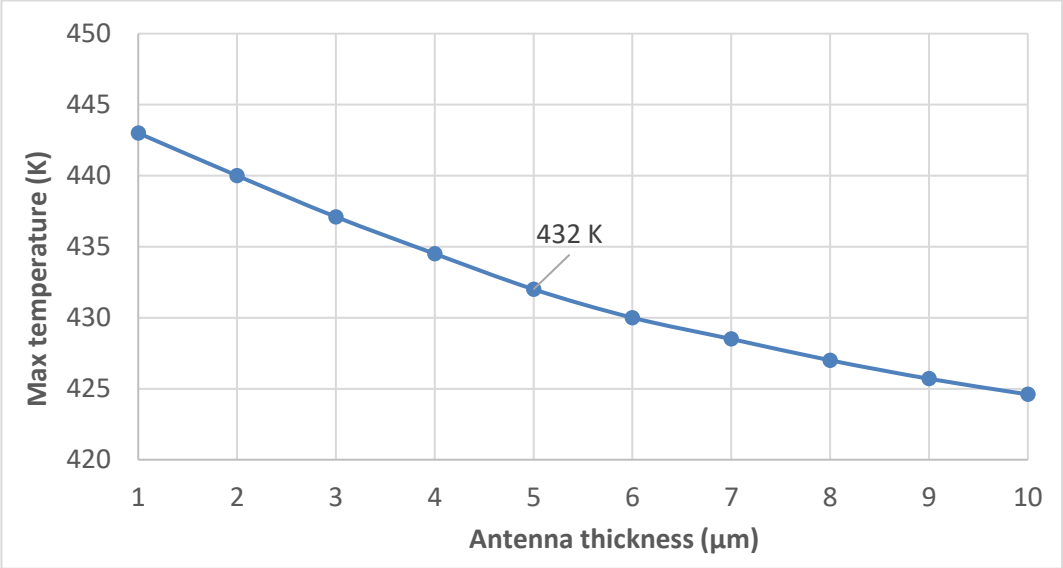

Figure 4.7: The max temperature of antenna integrated UTC-PDs at different thickness of bow-tie antenna.

Figure 4.8 illustrates that more heat can be extracted out through the solid P-via and thicker bow-tie antenna (see the part in the blue circle), but the heat dissipation effect is not ideal. By analysing the structure of UTC-PDs, the SiO_xN_y passivation layer beneath the bow-tie antenna is restricting the heat dissipating effect of the thicker antenna. As SiO_xN_y has a lower thermal conductivity and covers the hot P-ridge, the heat has difficulty to escaping from this passivation

layer, resulting in the high temperature at the top of SiO_xN_y, from 350 K to 396 K. The temperature is higher where it is close to P-ridge and lower at the edge of the device. The gold bow-tie antenna is deposited on the top of SiO_xN_y, therefore the antenna's temperature is influenced by the temperature of SiO_xN_y, except for the P-ridge area. In order to further reduce the high temperature inside UTC-PDs, need to find out ways to dissipate the heat in SiO_xN_y. Next Section 4.3.2 will work to solve this problem.

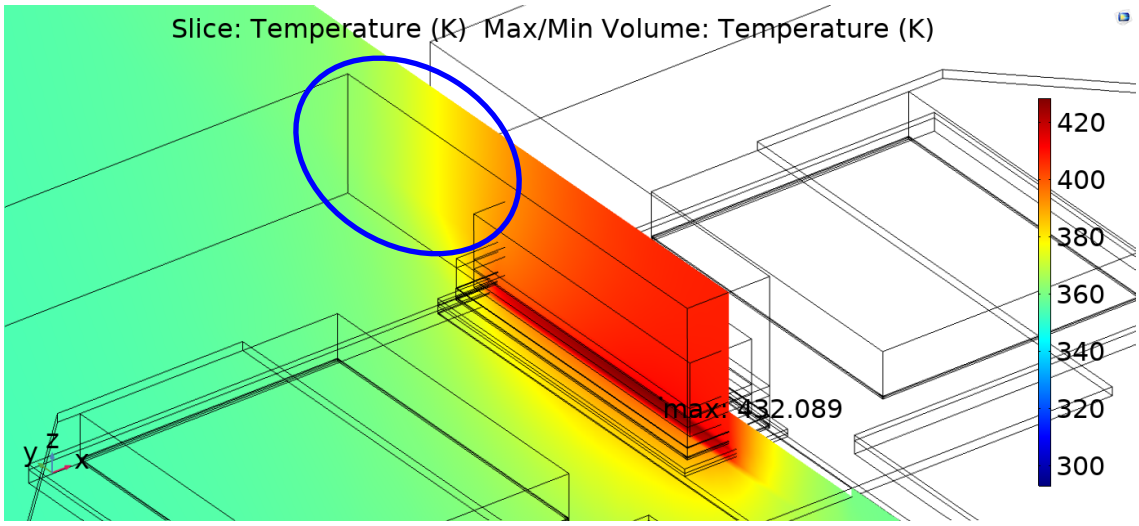

Figure 4.8: Temperature distribution of P ridge cross section with solid P-via and 5 µm thick bow-tie antenna.

4.3.2 Solution 2 – AlN heat spread layer

In order to reduce the impact of low thermal conductivity SiO_xN_y layer, solutions need to be worked out to dissipate the heat inside the P-ridge of UTC-PDs. The target is to find a high thermal conductivity material, utilizing the big surface area of P-contact (3x15 μm^2) and at the same time not impact the RF radiation of the antenna. AlN is a good candidate, which has high thermal conductivity (285 W/m·K), excellent electrical insulation, low dielectric constant and low thermal expansion coefficient. Placing a thin layer of AlN on the top of antenna is a possible way to help heat dissipation. As the P-ridge size of our UTC-PDs is very small, the flip-chip bonding technique is not suitable. In addition, our UTC-PDs are waveguide coupled photodiodes, flip-chip bonding to a submount will

influence the optical coupling from lensed fibres. If AlN can be deposited on the top of antenna, these problems associated with flip-chip bonding will be solved. Various techniques such as metal organic chemical vapor deposition (MOCVD) [4.14], molecular beam epitaxy (MBE) [4.15], and pulsed laser ablation [4.16] have been used to deposit AlN films. However, most of these techniques require a high substrate temperature (in the range of 600 ºC - 1200 ºC), and the use of expensive and corrosive gas mixtures. Direct current (DC) and radio frequency (RF) sputtering have the advantages of low temperature and low-cost. High-power impulse magnetron sputtering (HiPIMS) has proved to be a very promising route to tailor thin film microstructures and residual stress [4.17], [4.18]. HiPIMS deposition provides a significant amount of metal ions (up to 40% - 80%) [4.19], within a plasma density greater than 10^{-13} cm^{-3} [4.20]. Therefore, films deposited by HiPIMS are usually dense and smooth [4.21], while their stoichiometry and structural quality can be easily controlled at lower deposition temperatures compared with other techniques [4.22], [4.23].

The crystal structure of AlN plays a major role in determining the thermal conductivity. To obtain a high thermal conductivity, four requirements need to be met: low atomic mass, strong bonding, simple crystal structure, and a low inharmonic behaviour [4.24] These are influenced by the sputtering process parameters and by the choice of substrate material [4.25]. In [4.25] the influence of the RF power and sputtering pressure on the deposition of AlN films on Au layers was investigated. It was found that the AlN films, prepared by using the higher RF power of 400 W and sputtering pressure of 7 mTorr, have stronger c-axis orientation and exhibit smoother morphologies. In [4.22], AlN films were deposited by HiPIMS with different thicknesses. The samples' thermal conductivities rapidly increased when the AlN film thickness was up to 3300 nm and then showed a tendency to remain constant. A thermal conductivity as high as 250 W/K·m at room temperature was obtained. Based on these reported results, high thermal conductivity AlN deposited on Au/SiO_xN_y is achievable by using HiPIMS technique [4.22], [4.23] through adjusting RF power, sputtering pressure and the thickness of AlN deposition. This is a challenging task as it is the first time we try depositing AlN on Au and SiO_xN_y. In order to get the crystallographic structure AlN with high thermal conductivity, we need time to

investigate the impact of sputtering parameters on the morphology of AlN film. Due to the time limitation, this process research will be covered in the future work.

Figure 4.9 shows how the max temperature inside WG UTC-PDs changes with the different thicknesses of AlN layer (the blue line). The P-ridge size is 3x15 μm^2 and the photocurrent is 13.5 mA. Figure 4.9 indicates: 1) Depositing AlN on the top of P-electrode can effectively dissipate heat, and thicker AlN has better temperature reduction effect; 2) With the thickness of AlN layer increasing, the temperature reduction effect gets weaker; 3) The AlN layer has better heat dissipation effect than solution 1 (solid via with a thicker antenna). As the thermal conductivity of AlN film increases with the thickness, and also considering the intrinsic stress (from the deposition process) gets higher at the thicker AlN, 3-5 µm thick AlN is a good start to investigate the deposition process. Below Figure 4.10 shows the temperature distribution of P-ridge cross section with the 4 µm thick of AlN on the top of P-electrode (solid P-via, 0.4 um thick antenna). The max temperature is 406.5 K, 47.5 ºC lower than our current design (454 K). If combined with the larger InP substrate size (800 µm x 800 µm), the highest temperature will be further reduced 37 K. The max temperature will be 369.5 K and the overall temperature decrease will be 84.5 ºC.

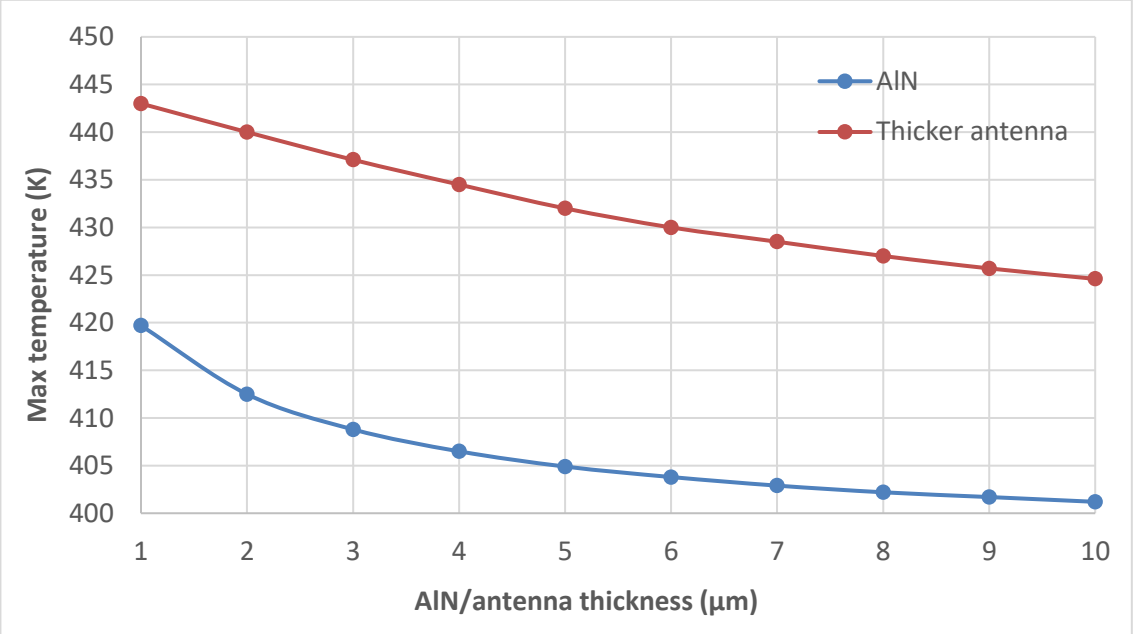

Figure 4.9: The max temperature of antenna integrated WG UTC-PDs at different thickness of AlN layer. The P-ridge size is 3x15 μm^2 and the photocurrent is 13.5 mA.

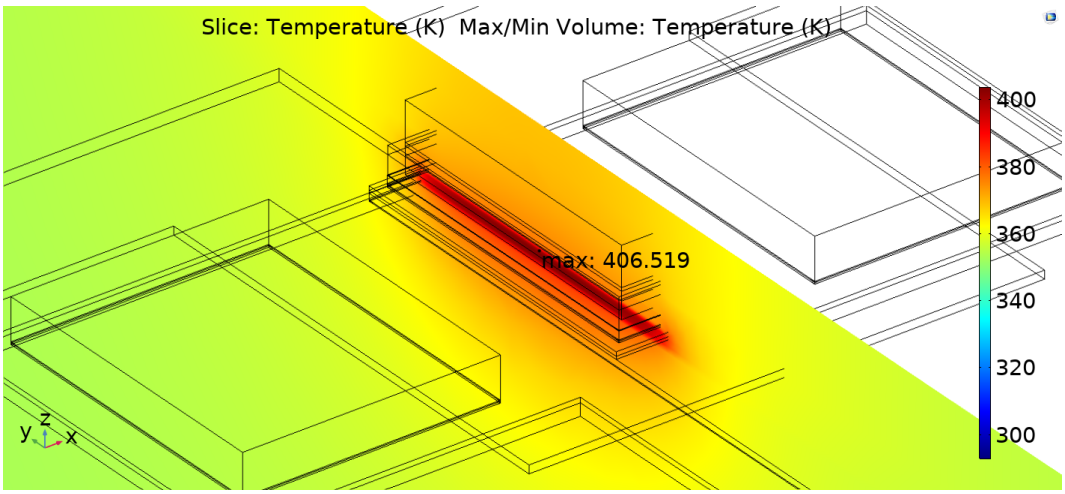

Figure 4.10: the temperature distribution of P-ridge cross section with the 4 μm thick of AlN on the top of P-electrode.

Stress generation is a result of the subsequent atomic rearrangement within the film that is constrained by its attachment to the substrate. As to the stress originated from the extra AlN layer, two parts are included: intrinsic (growth) stress and thermal stress. Sources of intrinsic stress are related to any strained regions due to structural modifications taking place: (1) within the film bulk (defect, voids, recrystallization, etc.), (2) at the film and substrate interface (lattice-mismatch, intermixing, etc.), and (3) at the growing film surface (adsorption, surface diffusion, etc.) [4.26]. The intrinsic stress in deposited films is a process sensitive property. In [4.27], the intrinsic stress in ion beam sputtered AIN films was investigated as a function of deposition temperatures. With increasing the deposition temperature, the stress initially decreases gradually followed by a rapid drop for $T_d > T_m/3$. T_d is the deposition temperature, and T_m is the absolute melting point. The relationship between residual stress and substrate bias voltage/pressure was studied in [4.28]. The residual stress changed from compressive values at high substrate voltage (25-30 V) to much less compressive (or even tensile) values at low substrate voltage (5-10 V). For the same value of substrate voltage, smaller values of stress were obtained as pressure was increased. The deposition technique also impacts the intrinsic stress. [4.29] compares the characteristics of AlN films deposited by pulsed laser deposition and reactive magnetron sputtering. The experiments showed that the films deposited by pulsed laser deposition at 600 °C were subjected to a high compressive stress of 30 GPa while the films deposited by reactive magnetron

sputtering at the same substrate temperature were under a residual compressive stress of 5 GPa. Also, the intrinsic stress of films will further rise during venting due to the sorption of water vapor [4.30]. Therefore, to precise control of the intrinsic stress during thin film deposition, we need a simultaneous manipulation of multiple processing parameters.

Besides the consideration of thermal conductivity and residual stress from the deposition process, the impact on radiated RF power from the extra AlN layer also need to be checked to make sure it doesn't deteriorate the device's performance. Figure 4.11 plots the calculated RF output power of antenna integrated UTC-PDs without and with AlN layer on the top of bow-tie antenna at 200 - 300 GHz frequency range, which shows: 1) the radiated RF power at 250 GHz keeps a similar value by adding AlN on top of antenna, 2) the frequency of peak power shifts to lower frequency side.

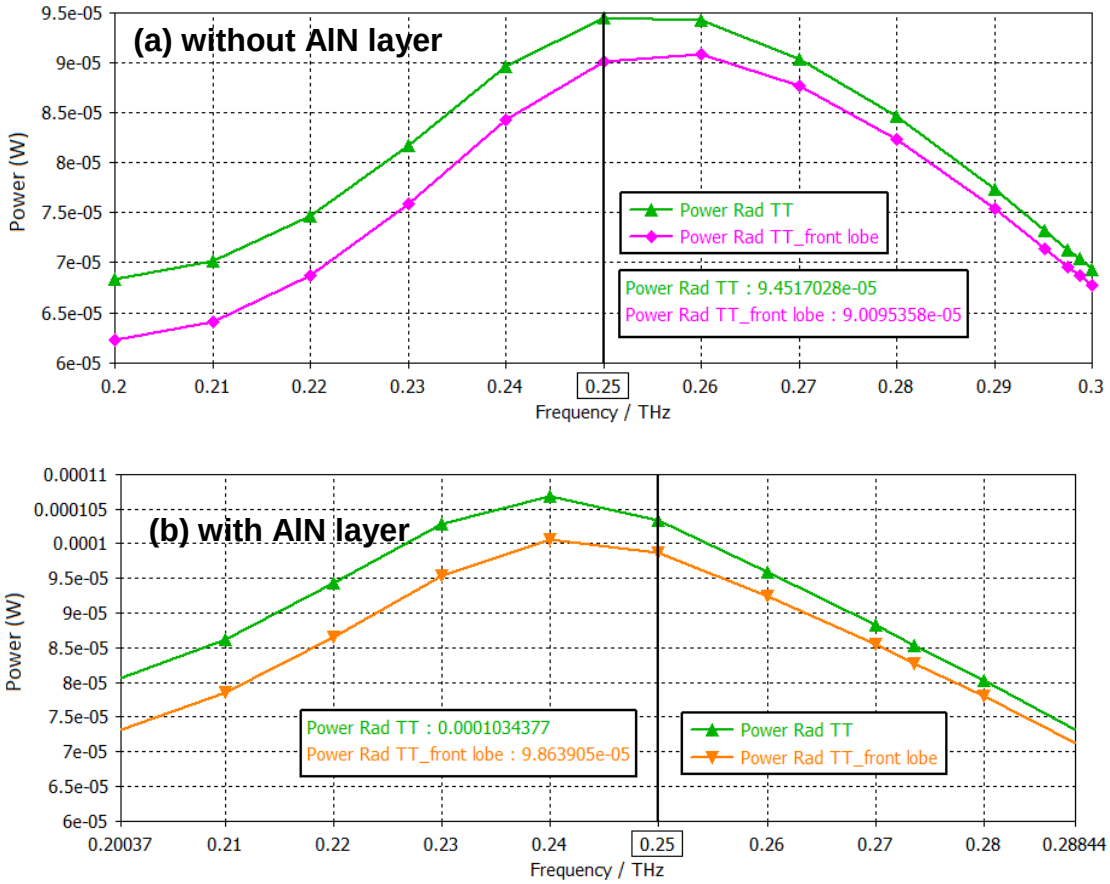

Figure 4.11: the radiated RF power of antenna integrated UTC-PD: (a) without AlN layer, (b) with 4 μm AlN layer. Power Rad TT means the total radiated RF power, and Power Rad TT_front lobe means the radiated RF power through Si lens.

4.3.3 Solution 3 – thermal conductive adhesive

Currently, the antenna integrated UTC-PDs chip is bonded to a hyper-hemispherical Si lens through a layer of Nitrocellulose (around 15 μm thickness). The thermal conductivity of Nitrocellulose is very low, just 0.142 W/m·K, and the temperature increasing across this layer is as high as 50 K. To increase the heat exchange between UTC-PDs and Si lens, thermal conductive adhesives can be used to replace this Nitrocellulose layer. As a Si substrate lens is used to couple THz radiation into free space and with high resistivity ($1x10^{14}$ Ω·cm), the replacement thermal conductive adhesives also need to have high volume resistivities. Besides high thermal conductivity and high volume resistivity, the new adhesive needs to have a low dielectric dissipation at sub-THz range and dielectric constant close to Si (or InP). Through careful selection and comparison, the thermal conductive adhesive in below Table 4.3 is chosen to replace the current bonding layer (Nitrocellulose).

Table 4.3: Properties of cured thermal conductive adhesive (multicomp: MC002964).

Volume resistivity	Thermal conductivity	Density	Specific heat	Dielectric constant @ 1 kHz	Dielectric dissipation @ 1 kHz	Thermo-conductive component
$2x10^{13}$ Ω· cm	1.44 W/m·K	2.30 g/mL	0.907 J/g·K	5.43	0.025	ceramic powders

Using the thermal properties of this new adhesive to do the thermal modelling, the temperature increase across the bonding layer is decreased from 50 K to 7 K and the highest temperature inside UTC-PD is reduced by 43 K, see Figure 4.12. To make sure the new adhesive layer not absorb (or dissipate) much RF power, its impact on the radiated RF power need to be checked. The comparison of RF power between Nitrocellulose layer and the new bonding layer at room temperature is plotted in Figure 4.13, which shows there is almost no power difference between the two adhesives. Therefore, the new thermal adhesive can be used to increase the heat dissipation without influencing the RF power coupling between antenna integrated UTC-PDs and Si lens.

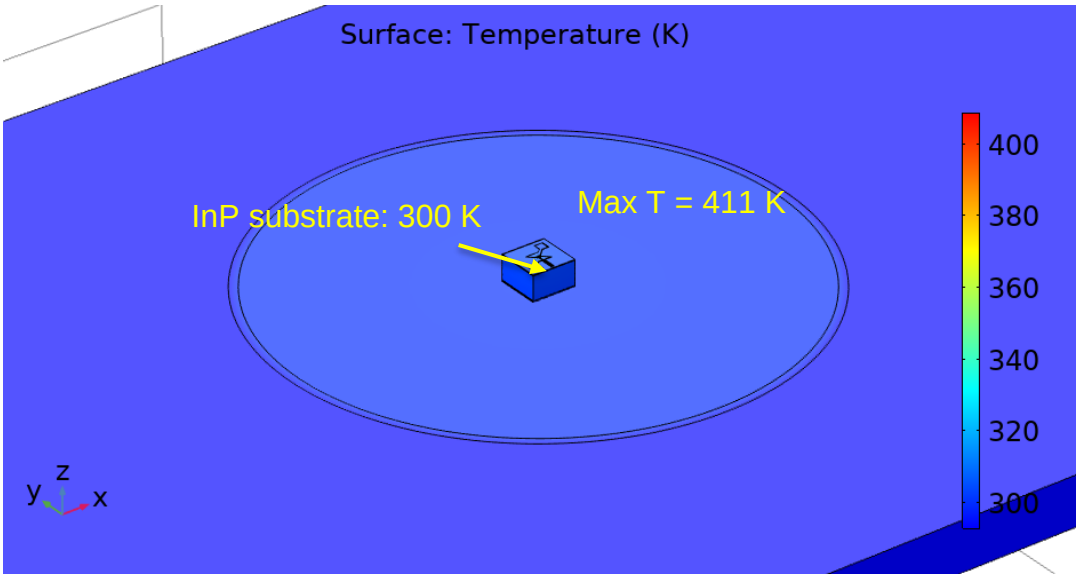

Figure 4.12: Thermal modelling of 3x15 μm^2 antenna integrated UTC-PD on Si lens. The bonding layer beneath UTC-PD is thermal conductive adhesive. The max temperature inside UTC-PDs is 411 K at the condition of 13.5 mA photocurrents, biased at -2 V.

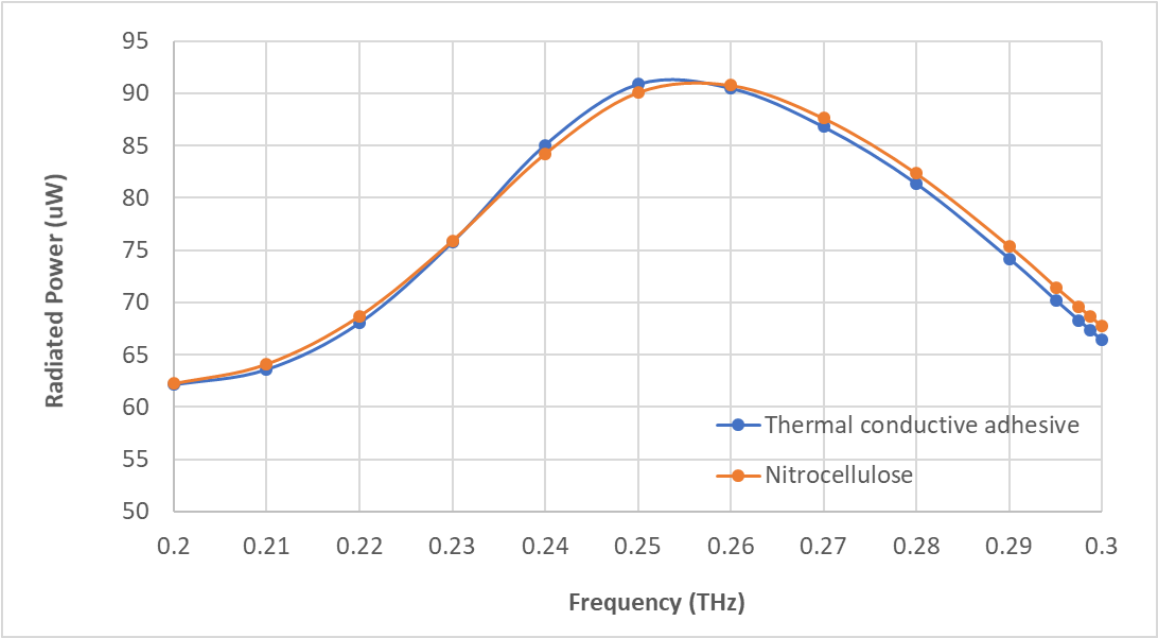

Figure 4.13: The comparison of RF power radiated through Si lens (radius = 3 mm): with thermal adhesive and without thermal adhesive (Nitrocellulose). The size of antenna integrated UTC-PD chip is 520 µm x 520 µm. The P-contact size of UTC-PD is 3x15 μm^2, and the photocurrent is 10 mA.

4.4 Thermal modelling verification

To verify the correctness of the thermal modelling, it is better to measure the internal temperature of waveguide UTC-PD at different photocurrents, and compare them with the simulated temperatures by thermal modelling. As our UTC-PD's ridge size is only 3x15 μm^2, high-quality thermal camera is needed to get sufficient temperature distribution. However, the cost for such thermal camera is quite high. Like FLIR's advanced A655sc infrared camera, which has a high thermal resolution of 640 x 480 pixels producing over 300,000 temperature measurement points per image, its price is more than £20,000. Besides the high price, the thermal camera can only measure the temperature distribution on the surface of UTC-PDs, and can't detect the DUT's internal temperatures. Therefore, even equipped with such high-level camera, we still can't get the information of the max temperature inside UTC-PDs.

Techniques have been developed to measure the junction temperature of semiconductor photodiodes. There are mainly two groups: optical properties based technique and electrical characteristics based technique. Optical technique is based on changes in the optical characteristics with temperature. For example, the output power and wavelength of an LED is sensitive to the junction temperature [4.31]. The electrical technique monitors the electrical characteristic' changes with temperature, such as voltage drop across the p-n junction in the forward biased devices [4.32] and dark current in the reverse biased devices [4.33]. In this section, the method to measure the temperature in the active region of waveguide UTC-PDs is presented, and also the measured temperatures are compared with those simulated by COMSOL. In Section 4.4.1, the output RF power changes of waveguide UTC-PDs were measured at different temperatures (without changing the input optical power). Based on this measurement, the temperature of UTC-PDs at different photocurrent was estimated. Section 4.4.2 shows the comparison of UTC-PD temperatures between estimation and thermal modelling at different photocurrents, and a good agreement is achieved.

4.4.1 Waveguide UTC-PD junction temperature estimation

In order to measure the junction temperature of waveguide UTC-PDs at different photocurrents, two rounds of experiment were performed. First, the relative output power changes of the UTC-PDs were measured at different temperatures. UTC-PD's temperature was controlled by Peltier thermoelectric heater. For this experiment, it is referred as calibration measurement. In the calibration measurement, the relationship between RF power change and UTC-PD temperature was established. Details are explained in Section 4.4.1.1. Then, the UTC-PD was heated by an extra laser (3rd laser) through increasing the photocurrent, which didn't contribute to RF output power. In this experiment, the relationship between the relative RF power changes of UTC-PDs and the photocurrents was established. Combined with the experiment results in the calibration measurement, the UTC-PD's junction temperature at different photocurrents can be worked out. Details are presented in Section 4.4.1.2.

4.4.1.1 Calibration measurement

A 3x15 μm^2 waveguide UTC-PD was measured in this experiment, with a responsivity of 0.16 A/W and a dark current of 0.53 µA at -1V bias voltage at room temperature. Reverse bias voltage was applied to the device via the integrated bias tee in the W-band (75-110 GHz) coplanar probe, and the 100 GHz output power of CPW coupled waveguide UTC-PDs was extracted through the coplanar probe, which coupled to an Agilent E4418B EPM series power meter via a Flann flexible W-band waveguide. The device was placed on Peltier thermoelectric heater, which was used to control DUT's temperature. The experiment layout is shown in Figure 4.14, which is same as the optical pulse measurement set-up in Section 3.3.1. The purpose of using optical pulse as input signal is to eliminate the heating effect coming from optical and electrical powers. Thus, the device's junction temperature is controlled by the setting temperature of Peltier heater.

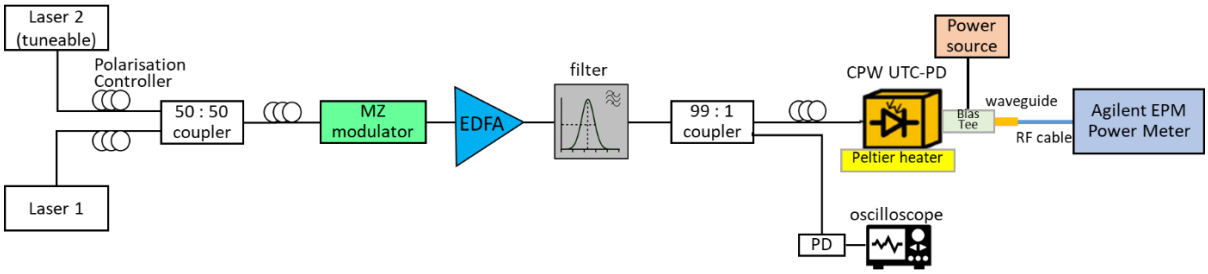

Figure 4.14: Experiment layout for measuring the relative RF output power changes at different temperatures, controlled by Peltier heater UTC-PD seated on.

The wavelengths from Laser 1 and Laser 2 were tuned to generate an optical heterodyne frequency of 100 GHz at 1550 nm wavelength range. Optical signals were modulated by MZ modulator to produce 50% duty cycle pulse signals with the pulse width of 20 ns. 3x15 μm^2 CPW UTC-PD was biased at -3 V and EDFA's pump current was adjusted to get 0.25 mA average photocurrent at room temperature (23 ºC). 100 GHz output power's changes were recorded down at different heat sink's temperatures. Due to the limitation of the Peltier module, the heat sink's temperature can only be increased to 95 ºC. The calibration measurement was done twice on the same device, and measurement results are shown in Figure 4.15. From 20 ºC (293 K) to 90 ºC (363 K), the RF output power increases around 0.1 dB with every 10 ºC temperature increase. This measurement trend is very close to the reported results in [4.34], where the relative responsivity change is measured at temperature range from 300 K to 440 K on InGaAs-InP MUTC photodiodes at 1550 nm. Fig. 3(a) in [4.34] shows the MUTC-PD's relative power change tends to be flatter when its temperature is higher than 380 K (107 ºC). The RF output power increasing with temperature comes from the absorption coefficient of InGaAs increases at higher temperature. When a photodiode's temperature increasing, the bandgap of absorption layer decreases as shown in (4.2) [4.31].

$$E_g(T) \approx E_{g0} - \frac{\alpha_0 T^2}{\beta_0 + T} \tag{4.2}$$

where E_{g0} is the bandgap of InGaAs at $T = 0\,K$, and α_0, β_0 are fitting parameters. For InGaAs, E_{g0} is $0.81\,eV$, α_0 is $4.91 \times 10^{-4}\,eV/K$ and β_0 is

$301\ K$ [4.35]. The absorption coefficient of a direct bandgap material near the band edge is

$$\alpha(T) = A \cdot \left(hv - E_g(T)\right)^{1/2} \tag{4.3}$$

The parameter A is related to the transition probability, depending on the effective mass, the refractive index, and the bandgap [4.35]. Combining (4.2) and (4.3), we can see the absorption coefficient of InGaAs increases with increasing temperature. As the generated photocurrent is linked to the absorption coefficient as in equation (4.4) [4.34], the temperature increase causes the rise of photocurrent.

$$i(T) \propto 1 - \exp[-\alpha(T) \cdot W_{ab}] \tag{4.4}$$

where W_{ab} is the thickness of absorption layer. The output RF power is proportional to the square of the photocurrents, therefore the output power of the UTC-PD is increased with increasing temperature. Fig. 3(a) in [4.34] shows the RF output power of MUTC-PD increases by around 1dB when its temperature reaches 450 K, comparing with the output power at room temperature (300 K). This phenomenon of photodiode's responsivity increase due to bandgap shrinkage is not conflicted with the fact that UTC-PD's output power is saturated at high temperature. The high input optical power generates high volume of electrons and causes the temperature of the UTC-PDs to increase. The increased responsivity at high temperature contributes extra electrons. High temperature reduces the mobility of electrons and limit UTC-PD's output power further increase. Therefore, at high temperature the output power of UTC-PDs can't further increase even though it has a higher responsivity.

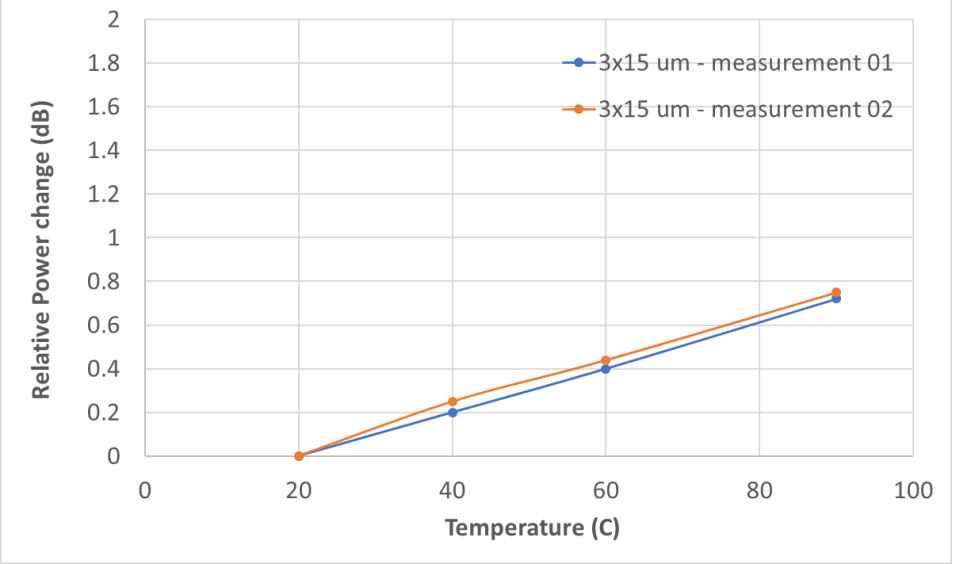

Figure 4.15: Measured relative power changes as a function of temperature for 3x15 μm^2 CPW UTC-PD biased at -3 V.

4.4.1.2 UTC-PD temperature estimation

After the calibration measurement, another round of measurements were taken to establish the relationship between the relative RF power change of UTC-PDs and the photocurrent. The same device used in 4.4.1.1 was measured in this experiment. The experiment layout is shown in Figure 4.16. A 3rd laser was introduced as the heating source for a 3x15 μm^2 UTC-PD (biased at -3V), see the red part in Figure 4.16. The laser 3's wavelength was set to 1580 nm, and its output power was coupled into the device through 50:50 optical fibre couple after amplified by another EDFA. The junction temperature of UTC-PD was changed by increasing the photocurrent generated from the amplified output power of laser 3. The relative changes of 100 GHz output power at different photocurrents are recorded and shown in Figure 4.17. In order to avoid space charge effects impact the output power change, the highest photocurrent used to heat device was controlled up to 5 mA, which is much lower than the saturation current of 3x15 μm^2 CPW UTC-PDs.

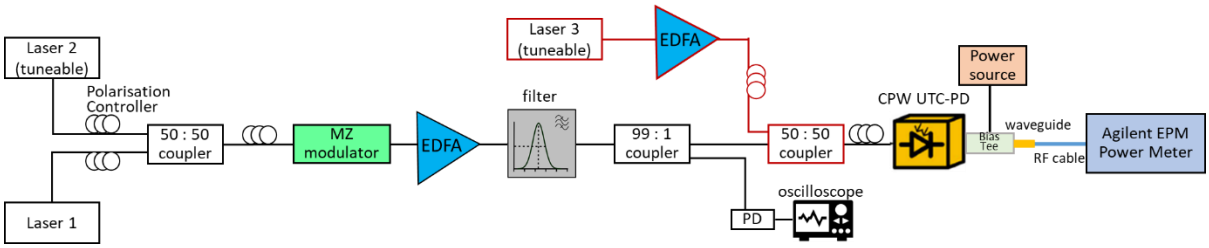

Figure 4.16: Experiment layout for measuring the relative power change of RF output power by using CW signal (Laser 3) to generate self-heating.

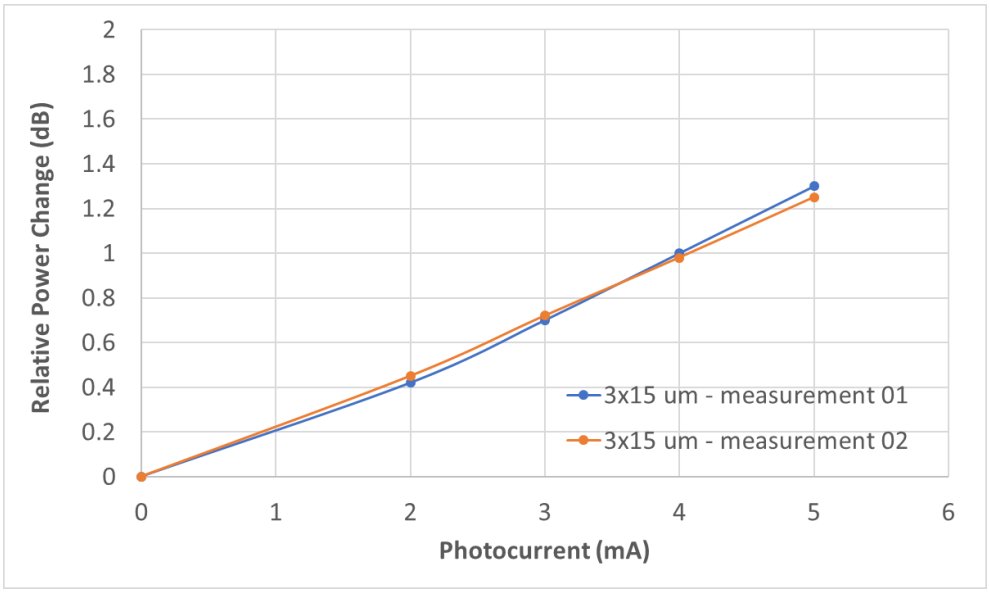

Figure 4.17: Measured relative RF output power change vs. heating photocurrent. CPW UTC-PD is biased at -3V.

Combining Figure 4.15 and Figure 4.17, the relationship between UTC-PD photocurrents and its junction temperature can be worked out, see Figure 4.18. It shows that for a 3x15 μm^2 UTC-PD, at 1 mA and 3 mA photocurrents, the highest temperature is around 40 ºC (313 K) and 90 ºC (363 K), respectively. According to thermal modelling and reported results in [4.34], smaller size UTC-PDs will have higher junction temperature at same optical power input, because of higher heat source power density and higher thermal resistivity.

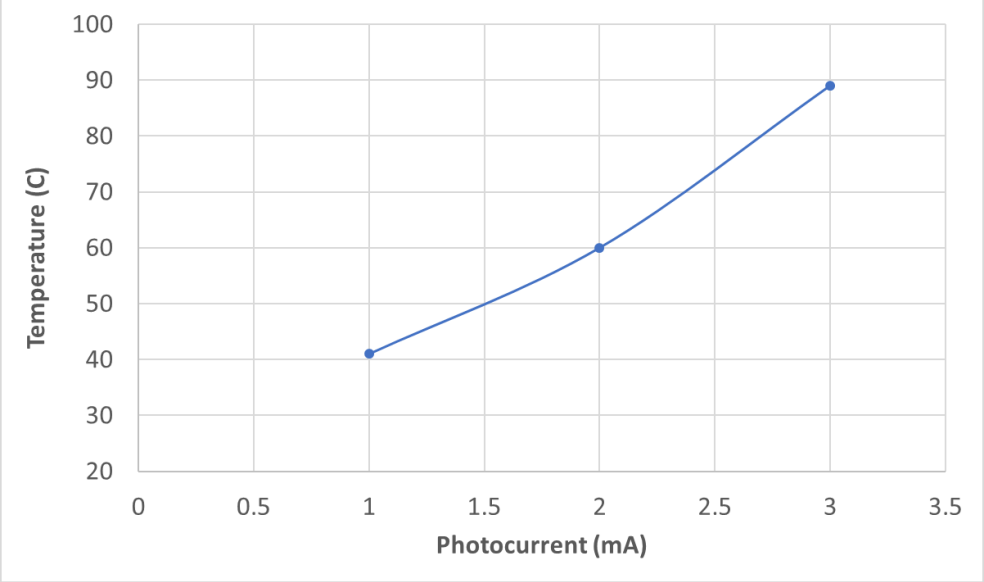

Figure 4.18: The estimated junction temperature of 3x15 μm^2 CPW UTC-PD at different photocurrents (biased at -3V).

4.4.2 Thermal modelling verification

In the previous Section 4.4.1, the temperature in absorption layer of 3x15 μm^2 UTC-PD is measured at 1 mA - 3 mA photocurrents when biased at -3V. To verify the correctness of COMSOL thermal modelling (details explained in Section 4.2), the simulated junction temperatures of a 3x15 μm^2 UTC-PD at photocurrents of 1 mA - 3mA are compared with the measured junction temperatures to see whether they agree with each other. The dissipated power inside the absorption layer needs to be calculated and input into the COMSOL thermal modelling to calculate the temperature distribution inside the CPW UTC-PDs. According to (4.1), the dissipated powers inside the UTC-PDs at a photocurrent of 1mA, 2mA and 3mA are calculated as 5.8 mW, 11.56 mW and 17.8 mW respectively, with the input optical power of 6.2 mW, 12.5 mW and 19.1 mW and the reverse bias voltage of 3V. By applying the calculated heat source densities into the thermal modelling, the max temperatures inside the UTC-PDs are calculated as 42.8 ºC, 62.6 ºC and 86.3 ºC, corresponding to 1 mA, 2 mA and 3mA photocurrents, shown in Figure 4.19 and comparing with the measurement results in Figure 4.20.

The simulated junction temperatures agree well with the experimentally measured temperatures, indicating the thermal modelling presented in Section 4.2 can properly reflect the thermal performance inside UTC-PDs.

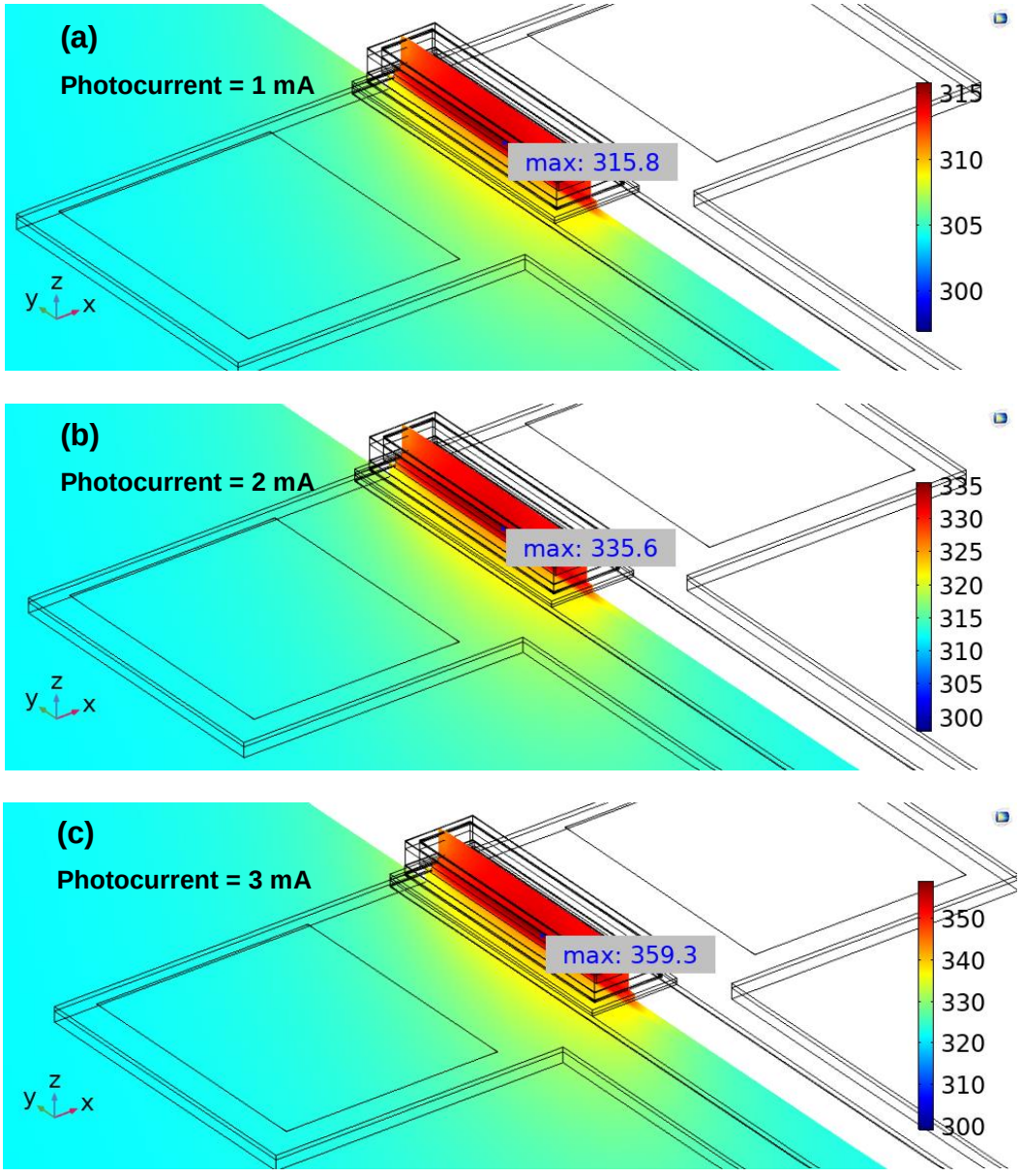

Figure 4.19: Simulated ridge temperature distributions of 3x15 μm^2 UTC-PD at photocurrents of (a) 1 mA, (b) 2mA and (c) 3mA.

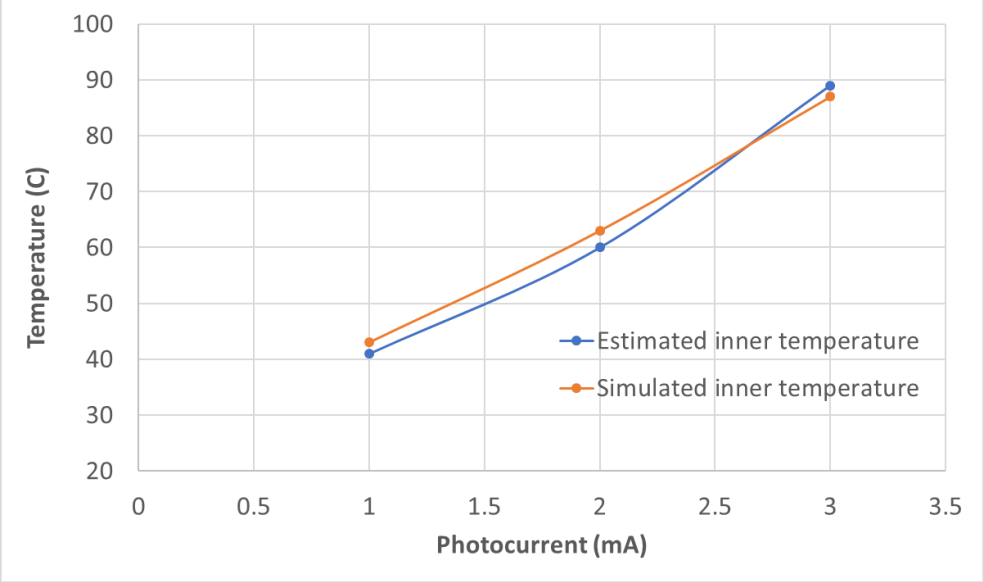

Figure 4.20: 3x15 μm^2 CPW UTC-PD junction temperature vs. photocurrent (biased at -3V), comparing between experiment results and thermal modelling simulations. The blue line is plotted based on measurement results shown in Section 4.4.1.2, and the orange line is plotted based on COMSOL simulations.

4.5 Conclusions

Thermal modelling on antenna integrated UTC-PDs illustrates the places where heat dissipations are blocked. There are three locations: the bonding layer between UTC-PD devices and the Si lens, S.I. InP substrate and the connection between P-contact and deposited antenna. These places have high thermal resistances, which are caused by their small cross-section area along the heat conducting path, or low thermal conductivity. Enlarging heat passing areas or increasing the material's thermal conductivity can effectively improve the heat dissipation and reduce the high temperature inside antenna integrated UTC-PDs.

Three possible solutions are discussed to assist the heat dissipation inside antenna integrated UTC-PDs: solid P via with thicker bow-tie antenna (solution 1), a layer of AlN deposited on the top of P-electrode (solution 2), and thermal conductive adhesives replacing low thermal conductivity bonding layer (solution 3). For solution 1, the device's max temperature can be reduced by 22 ºC with 5

μm thick antenna. For solution 2, the device's max temperature can be decreased by 47.5 ºC with 4 μm thick AlN layer. And for solution 3, the max temperature can be lowered by 43 ºC by using thermal adhesives with the thermal conductivity of 1.44 W/m·K. Solution 2 is more challenging as the AlN deposition process needs intense efforts to optimize the deposition process parameters (substrate voltage, pressure, temperature, deposition thickness/rate, etc.) to obtain suitable AlN layer for our antenna integrated UTC-PDs, high thermal conductivity and low intrinsic (growth) stress.

In order to verify the correctness of thermal modelling, experiments were done to measure the junction temperature of 3x15 μm^2 CPW UTC-PDs. The measured temperatures are 41 ºC, 60 ºC and 89 ºC at the photocurrent of 1 mA, 2 mA and 3 mA respectively. Comparing with the simulated temperatures by COMSOL, their differences are within 3 ºC. Good agreement between experimental results and simulations is achieved.

4.6 References

[4.1] Yang Shen, John Gaskins, Xiaojun Xie, Brian M. Foley, Ramez Cheaito, Patrick E. Hopkins, and Joe C. Campbell, "Thermal Analysis of High-Power Flip-Chip-Bonded Photodiodes", Journal of Lightwave Technology, vol. 35, no. 19, pp. 4242-4246, (2017).

[4.2] Z. Li, Y. Fu, M. Piels, H. Pan, A. Beling, J. E. Bowers, and J. C. Campbell, "High-power high-linearity flip-chip bonded modified uni-traveling carrier photodiode," Opt. Express, vol. 19, no. 26, pp. B385–B390, (2011).

[4.3] Q. Zhou, A. S. Cross, F. Yang, A. Beling, and J. C. Campbell, "High-power high-bandwidth flip-chip bonded modified unitraveling carrier photodiodes," IEEE Photonics Conference, pp. 306–307, (2012).

[4.4] Xiaojun Xie, Qiugui Zhou, Kejia Li, Yang Shen, Qinglong Li, Zhanyu Yang, Andreas Beling, and Joe C. Campbell, "Improved power conversion efficiency in high-performance photodiodes by flip-chip bonding on diamond", Optica, vol. 1, no. 6, pp. 429-435, (2014).

[4.5] M. Natrella, C.-P. Liu, C. Graham, F. van Dijk, H. Liu, C. C. Renaud, and A. J. Seeds, “Accurate equivalent circuit model for millimetre-wave UTC photodiodes,” Optics Express, vol. 24, no. 5, pp. 4698-4713, (2016).

[4.6] Michele Natrella, Chin-Pang Liu, Chris Graham, Frederic van Dijk, Huiyun Liu, Cyril C. Renaud, and Alwyn J. Seeds, “Modelling and measurement of the absolute level of power radiated by antenna integrated THz UTC photodiodes,” Opt. Express, vol. 24, no. 11, pp. 11793-11807, (2016).

[4.7] D. P. Neikirk, D. B. Rutledge, D. B. Rutledge, M. S. Muha, H. Park, and C.-X. Yu, “Far-infrared imaging antenna arrays,” Appl. Phys. Lett., vol. 40, no. 3, pp. 203-205, (1982).

[4.8] U. Gliese, K. Colladay, A. S. Hastings, D. A. Tulchinsky, V. J. Urick, and K. J. Williams, “53.5% photodiode RF power conversion efficiency,” in Proc. Nat. Fiber Opt. Eng. Conf., paper PDPA7, (2010).

[4.9] Hao Chen, Andreas Beling, Huapu Pan, and Joe C. Campbell, “A Method to Estimate the Junction Temperature of Photodetectors Operating at High Photocurrent”, IEEE Journal of Quantum Electronics, vol. 45, no. 12, pp. 1537-1541, (2009).

[4.10] Sajan D. George, Achamma Kurian, Martin Lase, V. P. N. Nampoori, C. P. G. Vallabhan, “Thermal characterization of doped InP using photoacoustic technique”, Photonic Systems and Applications, Proceedings, vol 4595, pp. 183-191, (2001).

[4.11] Juliana Jaramillo-Fernandez, Emigdio Chavez-Angel, Reza Sanatinia, Himanshu Kataria, Srinivasan Anand. “Thermal conductivity of epitaxially grown InP: experiment and simulation”, CrystEngComm, vol.19, pp. 1879-1887, (2017).

[4.12] Aliev, S. A., A. Ya. Nashelskii, and S. S. Shalyt, Sov, Phys. Solid State, vol. 7, 1287, (1965).

[4.13] S.Adachi, Physical Properties of III-V Semiconductor Compounds, Chapter 4, John Wiley and Sons, (1992).

[4.14] Tai-Chang Chen, Mike Johnson, Kunakorn Poochinda, Thomas GStoebe, N Lawrence Ricker, “A systematic study on group III-nitride thin films with low

temperature deposited via MOCVD", Optical Materials, vol 26, no. 4, pp. 417-420, (2004).

[4.15] Ž. Gačević, A. Das, J. Teubert, Y. Kotsar, P. K. Kandaswamy, Th. Kehagias, T. Koukoula, Ph. Komninou, and E. Monroy, "Internal quantum efficiency of III-nitride quantum dot superlattices grown by plasma assisted molecular-beam epitaxy", J. Appl. Phys., vol. 109, pp. 103501, (2011).

[4.16] A. Jacquot, B. Lenoir, A. Dauscher, P. Verardi, F. Craciun, M. Stölzer, M. Gartner, and M. Dinescu, "Optical and thermal characterization of AlN thin films deposited by pulsed laser deposition," Appl. Surf. Sci., vol. 186, no. 1–4, pp. 507–512, (2002).

[4.17] G. Greczynski, J. Lu, J. Jensen, S. Bolz, W. Kölker, Ch. Schiffers, O. Lemmer, J.E. Greene, L. Hultman, "A review of metal-ion-flux-controlled growth of metastable TiAlN by HIPIMS/DCMS co-sputtering," Surface and Coatings Technology, vol. 257, pp. 15-25, (2014).

[4.18] G. Greczynski, S. Mraz, H. Ruess, M. Hans, J. Lu, L. Hultman, and J. M. Schneider, "Extended metastable Al solubility in cubic VAlN by metal-ion bombardment during pulsed magnetron sputtering: film stress vs subplantation", Journal of Applied Physics, vol. 122, 025304, (2017).

[4.19] Erik Lewin, Daniel Loch, Alex Montagne, Arutiun P. Ehiasarian, Jörg Patscheider, "Comparison of Al-Si-N nanocomposite coatings deposited by HIPIMS and DC magnetron sputtering", Surface and Coatings Technology, vol. 232, pp 680-689, (2013).

[4.20] J. T. Gudmundsson, N. Brenning, D. Lundin, and U. Helmersson, "High power impulse magnetron sputtering discharge", Journal of Vacuum Science & Technology A,v 30, no. 3, 030801, (2012).

[4.21] Jing F J, Yin T L, Yukimura K, Sun H, Leng Y X and Huang N, "Titanium film deposition by high-power impulse magnetron sputtering: Influence of pulse duration", Vacuum, vol. 86, no. 12, pp. 2114-2119, (2012).

[4.22] K Ait Aissa, N Semmar, A Achour, Q Simon, A Petit, J Camus, C Boulmer-Leborgne and M A Djouadi, "Achieving high thermal conductivity from AlN films

deposited by high-power impulse magnetron sputtering", J. Phys. D: Appl. Phys., vol. 47, 355303, (2014).

[4.23] Kok-Wan Tay, Cheng-Liang Huang, Long Wu, "Highly c-axis oriented thin AlN films deposited on gold seed layer for FBAR devices", J. Vac. Sci. Technol. B, vol. 23, no. 4, pp. 1474-1479, (2005).

[4.24] G.A.Slack, "Nonmetallic crystals with high thermal conductivity", Journal of Physics and Chemistry of Solids, vol 34, no 2, pp. 321-335, (1973).

[4.25] V. Moraes, H. Riedl, R. Rachbauer, S. Kolozsvári, M. Ikeda, L. Prochaska, S. Paschen, and P. H. Mayrhofer, "Thermal conductivity and mechanical properties of AlN-based thin films", J. Appl. Phys., vol. 119, 225304, (2016).

[4.26] Grégory Abadias, Eric Chason, Jozef Keckes, Marco Sebastiani, Gregory B. Thompson, Etienne Barthel, Gary L. Doll, Conal E. Murray, Chris H. Stoessel, and Ludvik Martinu, "Review Article: Stress in thin films and coatings: Current status, challenges, and prospects", Journal of Vacuum Science & Technology A, vol. 36, 020801, (2018).

[4.27] H. Windischmann, "Temperature dependence of intrinsic stress in Fe, Si, and AlN prepared by ion beam sputtering", Journal of Vacuum Science & Technology A, vol. 7, 2247, (1989).

[4.28] E. Iborra, J. Olivares, M. Clement, L. Vergara, A. Sanz-Hervás, J. Sangrador, "Piezoelectric properties and residual stress of sputtered AlN thin films for MEMS applications", Sensors and Actuators A, vol. 115, pp. 501–507, (2004).

[4.29] K. Jagannadham, A. K. Sharma, Q. Wei, R. Kalyanraman, and J. Naraya, "Structural characteristics of AlN films deposited by pulsed laser deposition and reactive magnetron sputtering: A comparative study", Journal of Vacuum Science & Technology A, vol. 16, pp. 2804-2815, (1998).

[4.30] K. Scherer, L. Nouvelot, P. Lacan, and R. Bosmans, "Optical and mechanical characterization of evaporated SiO2 layers. Long-term evolution," Appl. Opt., vol. 35, pp. 5067-5072, (1996).

[4.31] B. Siegal, "Practical Considerations in High Power LED Junction Temperature Measurements," 2006 31st IEEE/CPMT International Electronics Manufacturing Technology Symposium, pp. 62-66, (2006).

[4.32] W.Nakwaski, “Thermal properties of P-side-down ridge-wavegllide lasers”, Optica Applicata, vol. xx, no. 2, pp. 143-163, (1990).

[4.33] Pin Jern Ker, Andrew R. J. Marshall, Andrey B. Krysa, John P. R. David, and Chee Hing Tan, “Temperature Dependence of Leakage Current in InAs Avalanche Photodiodes”, IEEE Journal of Quantum Electronics, vol. 47, no. 8, pp. 1123-1128, (2011).

[4.34] Hao Chen, Andreas Beling, Huapu Pan, and Joe C. Campbell, “A Method to Estimate the Junction Temperature of Photodetectors Operating at High Photocurrent”, IEEE Journal of Quantum Electronics, vol. 45, no. 12, pp. 1537-1541, (2009).

[4.35] E. Zielinski, H. Schweizer, K. Streubel, H. Eisele, and G. Weimann, “Exciton transitions and exciton damping processes in InGaAs / InP”, J. Appl. Phys., vol. 59, no. 6, pp. 2196–2204, (1986).

Chapter 5

RF Output Power Improvement by Using Thermal Conductive Adhesives

By using thermal conductive adhesives (thermal conductivity = 1.44 W/m·K) replacing the Nitrocellulose bonding layer (thermal conductivity = 0.142 W/m·K), for 4x15 μm^2 antenna integrated UTC-PDs with a dissipated power of 60 mW, the temperature increasing across the bonding layer can be decreased from 50 K to 5 K and the highest temperature inside UTC-PD can be reduced by 45 K, see Figure 5.1. With lower temperature, antenna integrated UTC-PDs will saturate at higher photocurrent and radiate more RF power. In order to verify the feasibility of increasing the RF output power of antenna integrated UTC-PDs by using thermal conductive adhesives, test samples were prepared with Nitrocellulose and thermal conductive adhesives respectively, and their RF output powers were measured to compare performance differences. In Section 5.1, the radiated RF power of 4x15 μm^2 bow-tie antenna integrated UTC-PDs (using thermal conductive adhesives) is estimated by CST modelling at different photocurrents. Section 5.2 explains the details of experiments measuring the output power of 4x15 μm^2 bow-tie antenna integrated UTC-PDs, which used thermal conductive adhesives to bond on Si lens (diameter = 6 mm).

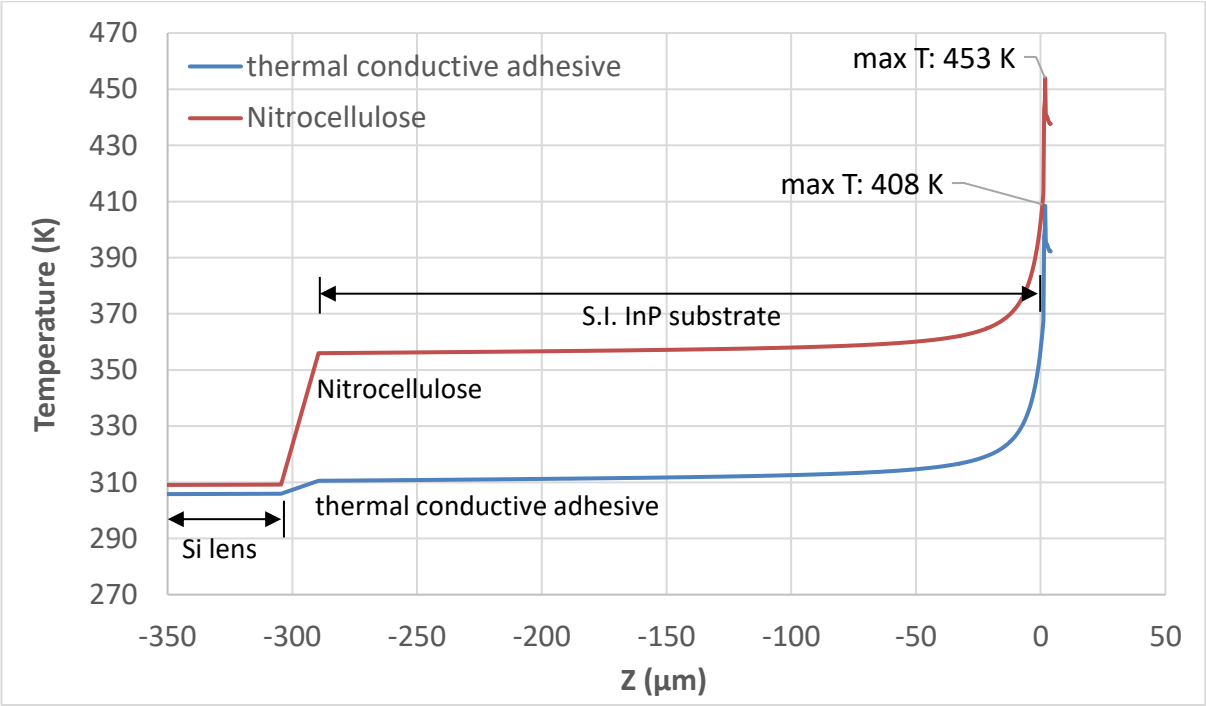

Figure 5.1: Temperature distribution comparison on 4x15 µm^2 bow-tie antenna integrated UTC-PDs (bonding layer using Nitrocellulose vs thermal conductive adhesive), with the dissipated power of 60 mW.

5.1 RF output power estimation by CST modelling

By using thermal conductive adhesives to bond antenna UTC-PDs to Si lens, the heat dissipation will be improved, and antenna UTC-PDs have the chance to saturate at higher photocurrents and radiate higher RF power. To have an idea of how much the radiated RF power can be expected by applying thermal conductive adhesives between antenna UTC-PDs and Si lens, CST modelling was used to estimate the radiated power at different photocurrents at the frequency range from 200 GHz to 300 GHz.

In the CST modelling for 4x15 µm^2 antenna integrated UTC-PDs using thermal conductive adhesives, the current source (photocurrent) is set to 13 mA to 18 mA, the calculated RF output powers in the frequency range 200 GHz - 300 GHz are plotted in Figure 5.2, which shows by increasing the saturation photocurrent (the photocurrent at which the RF output power saturates), the RF output power can be increased. The RF output power is increased by 10-15 µW when the saturation

photocurrent is increased by 1 mA. In the next Section 5.2, RF power measurement will be taken on devices with the two kinds of adhesives to compare their radiation performances.

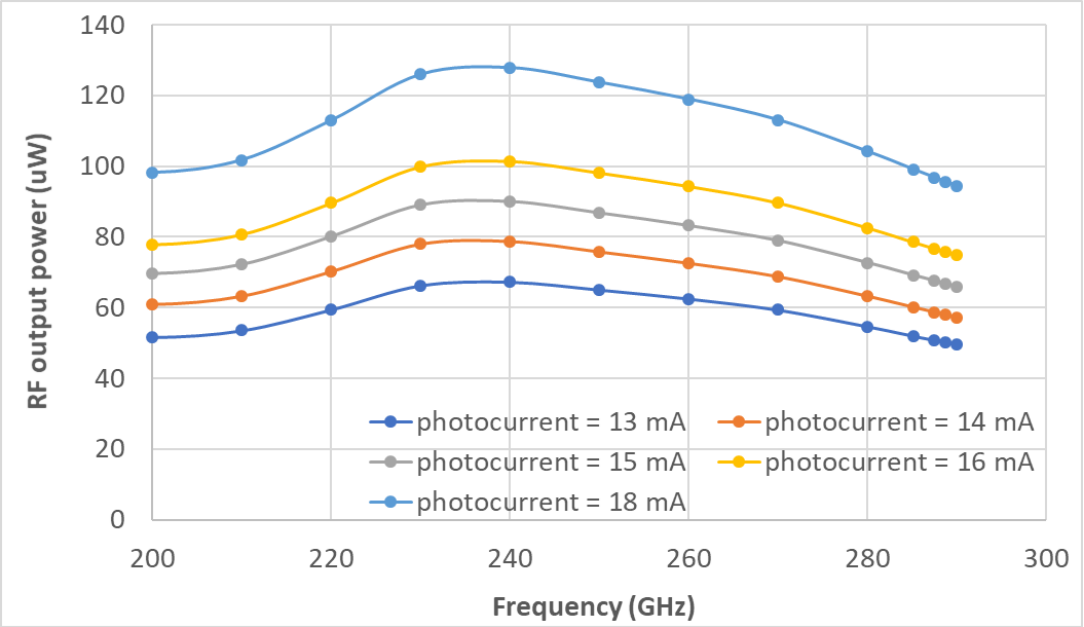

Figure 5.2: Calculated RF output powers of 4x15 μm^2 bow-tie antenna integrated UTC-PDs at the frequency range of 200 GHz - 300 GHz.

5.2 Output power measurement and comparison

Experiment was done to check whether the RF output power can be improved by using thermal conductive adhesives to bond antenna UTC-PDs on Si lens. Two groups of test samples were prepared for the output power comparison measurement. Each group had two devices of 4x15 μm^2 bow-tie antenna integrated UTC-PDs. Samples in one group used Nitrocellulose, and the other group used thermal conductive adhesives. The RF output power of the four DUTs were measured by using the lay-out in Figure 5.3. Two laser tones were adjusted to generate an optical heterodyne frequency of around 250 GHz. One of the laser tones was chopped using a 20 Hz optical chopping frequency. Polarization controllers were used after each laser to align two lasers' polarisations to the same state. Two optical inputs were then combined in a 50:50 coupler and amplified by EDFA. A 5 nm passband ASE filter was placed after the EDFA to

reduce the contribution from ASE to the photocurrent. The optical beat signal was coupled to the waveguide of antenna integrated UTC-PD via a lensed optical fibre (2.5 µm spot size). A 3rd polarization controller was placed before the lensed fibre to optimize the light coupling into the waveguide. The RF output power was measured using the Thomas Keating (TK) power meter. TPX lenses were used to collimate and focus the THz radiation onto the power meter.

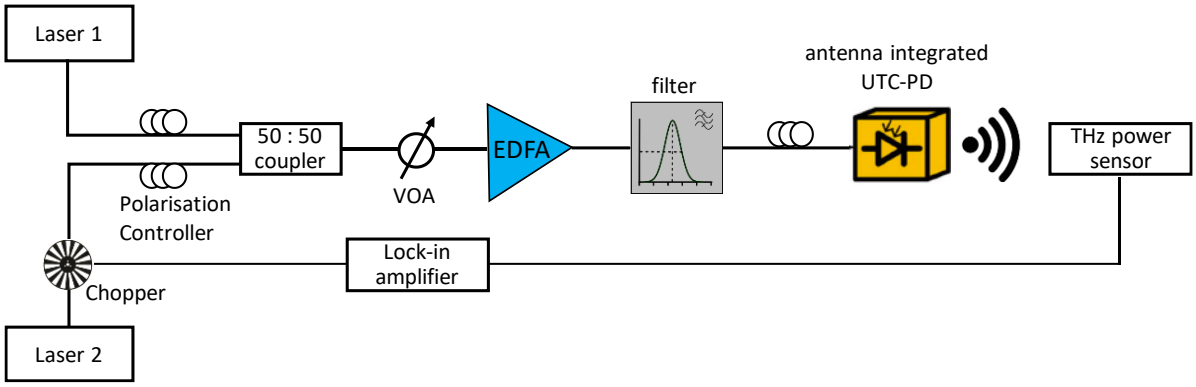

Figure 5.3: RF output power measurement arrangement for antenna integrated UTC-PDs.

To find the optimum operation condition, the bias voltage was scanned from -1.4 V to -2.6 V and the beat signal of two lasers were scanned from 200 GHz to 300 GHz. Their relationship with the radiated RF output power were plotted in Figure 5.4 and Figure 5.5, for antenna integrated UTC-PDs with Nitrocellulose and thermal conductive adhesives respectively. Figure 5.4 shows for UTC-PDs using Nitrocellulose, the optimum bias voltage is -1.8 V and the peak RF output power occurs at the frequency of 250 GHz. Figure 5.5 shows for UTC-PDs using thermal conductive adhesives, the optimum bias voltage is also -1.8 V and the peak RF output power occurs at the frequency of 239 GHz. Using thermal adhesives made the peak power frequency shift 11 GHz towards the lower frequency end, which has the same trend as the prediction from the modelling. The frequency shift maybe is caused by the lower dielectric constant of thermal conductive adhesives (ε = 6.6).

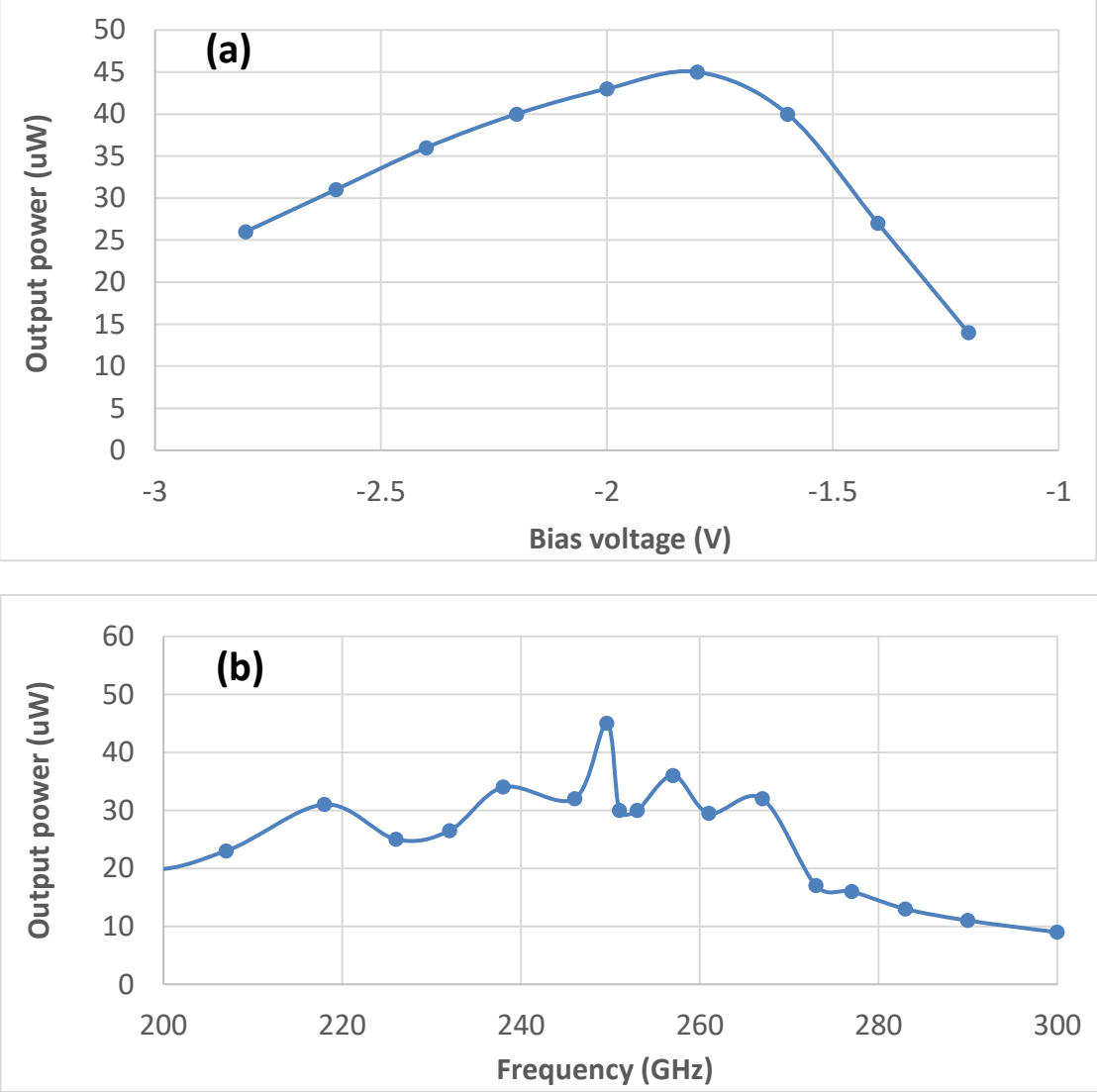

Figure 5.4: For 4x15 μm^2 bow-tie antenna integrated UTC-PDs with Nitrocellulose: (a) 250 GHz power changes with bias voltage. The range of photocurrent is from 10.2 mA to 10.5 mA; (b) RF power at the frequency range of 200 GHz - 300 GHz with the bias voltage of -1.8 V and photocurrent of 10.2 mA.

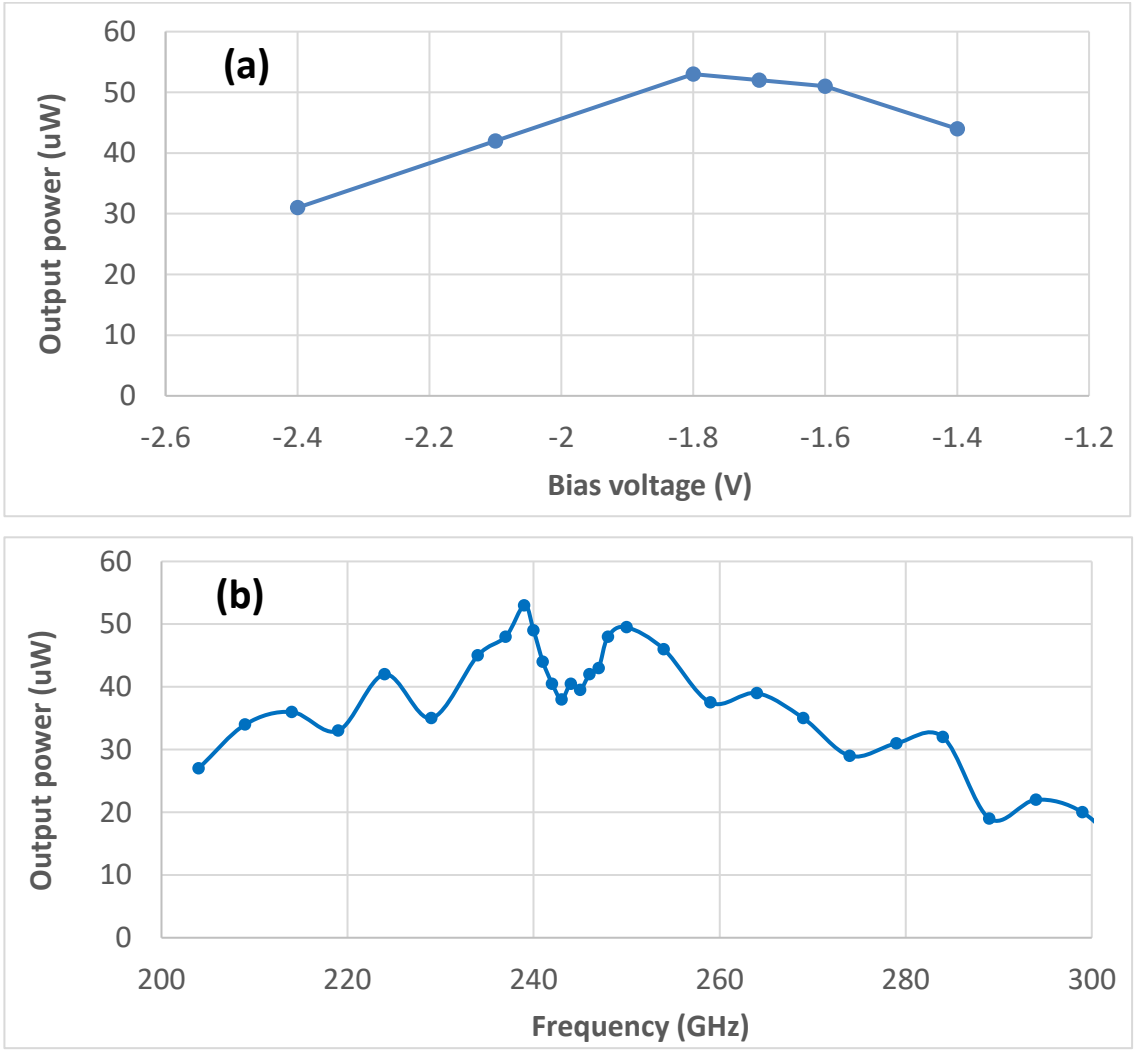

Figure 5.5: For 4x15 μm^2 bow-tie antenna integrated UTC-PDs with thermal conductive adhesives: (a) 239 GHz power changes with bias voltage. Photocurrents range from 10.0 mA to 10.25 mA, (b) RF power at the frequency range of 200 GHz - 300 GHz with the bias voltage of -1.8 V and photocurrent of 10.1 mA.

Applied with the optimum operation conditions (bias voltage and peak power frequency), the output power of two group test samples were measured and plotted in below Figure 5.6. The photocurrents of DUTs were continuously increased until the radiated RF power were saturated by increasing the input optical powers through EDFA. Figure 5.6 shows: (1) Two DUTs in each test group performed similar. The output power of antenna integrated UTC-PDs with thermal conductive adhesives saturated at a higher photocurrent (15.5 mA), which was

2.3 mA bigger than antenna integrated UTC-PDs with Nitrocellulose (13.2 mA). (2) antenna integrated UTC-PDs with thermal conductive adhesives had larger RF output power (74 μW) than devices with Nitrocellulose (56 μW), 1.2 dB (18 μW) improvement. The measured power improvement (18 μW) is close to the value calculated by CST modelling, which is 26 μW power increase for the photocurrent increasing from 13.2 mA to 15.5 mA. Measurements results indicate that using thermal conductive adhesives (solution 3) helps to reduce antenna integrated UTC-PDs' temperature and has the chance to get higher RF output power. If combining with solution 1 or solution 2, the max temperature of antenna integrated UTC-PDs will be further reduced and a higher output RF power can be achieved.

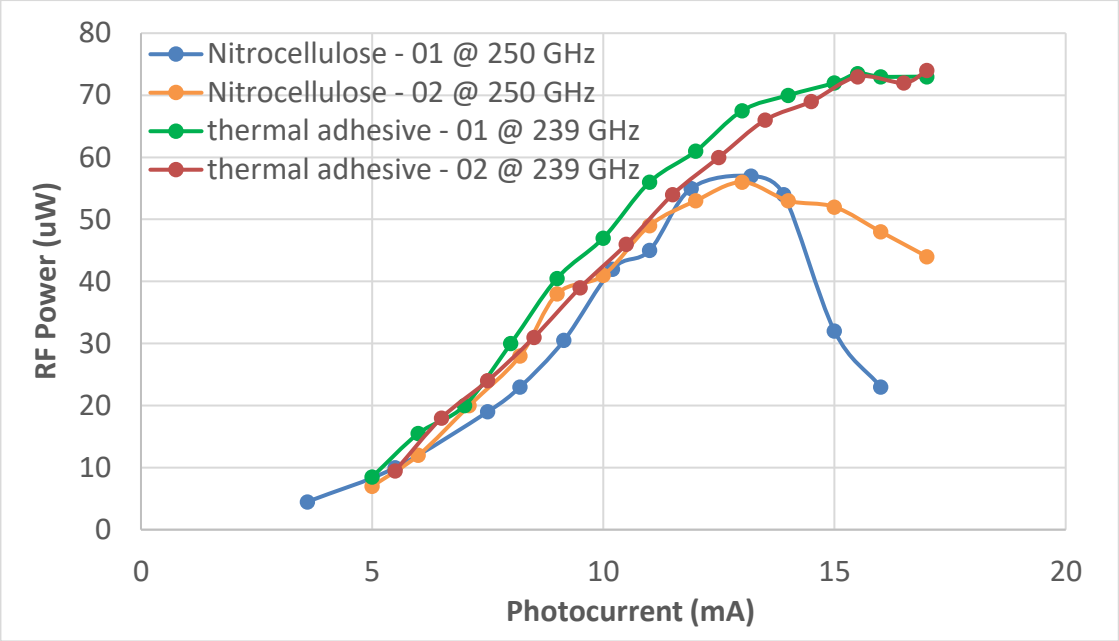

Figure 5.6: The output power of 4x15 μm^2 antenna integrated UTC-PDs on Si lens with Nitrocellulose and thermal conductive adhesives.

5.3 Conclusions

Three solutions are worked out to reduce the max temperature of antenna integrated UTC-PDs in Chapter 4. To verify the validity of solution 3 (details in Section 4.3.3) and check how much the RF output power can be improved, test samples (4x15 μm^2 antenna integrated UTC-PDs) were prepared by using

Nitrocellulose (nail polish) and thermal conductive adhesives respectively. Their output powers were measured and compared, and measurement results show that devices applied with thermal conductive adhesives saturate at a higher photocurrent, and have 1.2 dB higher output power than devices using Nitrocellulose. Therefore, the RF output power measurement in this Chapter verifies the effectiveness of solution 3 (using thermal conductive adhesives replacing Nitrocellulose), and proves the RF output power of antenna integrated UTC-PDs can be increased by improving their thermal management.

Chapter 6
Conclusions and Future Work

6.1 Summary of the thesis

The THz band, located between microwaves and infrared in the electromagnetic spectrum (100 GHz to 10 THz), has higher frequencies, larger available bandwidth than microwave band, making it superior in high speed wireless communications. For the interested wireless communication frequencies (200 GHz - 300 GHz), UTC-PDs have exhibited higher output power and larger bandwidth than competing structures, and are a promising THz source solution to achieve high-speed wireless communications, benefiting from only photogenerated electrons passing cross the collection layer and contributing to the photocurrent response. Vertically illuminated UTC-PDs have shown improved 3 dB bandwidth, but their structure requires a trade-off between responsivity and bandwidth, which is eased significantly by applying waveguide structures in UTC-PDs.

By using SS-MBE, the major issue in phosphide epitaxy growing by MOCVD, associated with the unintentional diffusion of Zinc, can be overcome. This gives the benefit of superior control of the doping profile in epitaxial layers provided by MBE, without the hazards of GS-MBE. In Chapter 2, the fabrication and characterisation of the first SS-MBE grown waveguide coupled UTC-PDs (CPW integrated UTC-PDs and antenna integrated UTC-PDs) are presented. 1.1 dBm output power was obtained at 100 GHz for an average photocurrent of 13 mA for 3x10 μm^2 device, biased at -3V bias. By using narrow-band matching circuits [6.1] or flip chip bonding [6.2] with an inductive peaking circuit, higher output RF power can be achieved. Measurement results in Section 3.4 showed the saturated 100 GHz output power can be improved by around 4.7 dB for 3x10 μm^2 device if the thermal heating effect can be eliminated.

To achieve better SNR and longer transmission distance in wireless communication networks, high output RF power from UTC-PDs are desired. Increasing reverse bias voltage can reduce space charge effects and increase

the RF output power of UTC-PDs. But higher bias voltage and photocurrents worsen thermal heating, and lead to device failure due to dark current runaway. To reduce this risk, study on reducing leakage currents was conducted. Native oxide on the sidewall of the absorption, collection and waveguide layers contributes to surface leakage current and can worsen the leakage current to several μA at -1V bias. Experiments were done to compare the effect of removing oxide layer between 10% HCl and 10% H_3PO_4 treatment. Measurement results showed 10% HCl solution has better effect to reduce leakage current than 10% H_3PO_4 solution. By soaked in 10% HCL for 1 min after the mesa etching step, typical fabricated CPW integrated UTC-PDs exhibit the dark currents of 7 nA, 31 nA and 90 nA at -1V bias for 3x15 μm^2, 4x15 μm^2 and 7x15 μm^2 devices respectively.

For photodiodes, high output power requires high photocurrent. Space charge screenings and thermal effects are the two major factors influencing saturation photocurrent in UTC-PDs. In this thesis, efforts are focused on thermal effects study on waveguide UTC-PDs and heat dissipation solutions to reduce their temperatures, in order to realise the purpose of increasing saturation photocurrents and RF output power. When UTC-PDs are illuminated with high optical power and biased at high reverse voltage, the temperature inside UTC-PD's absorption layer increases accordingly. The increased temperature generates more phonons and reduces the mobility of electrons, which lead to photocurrent saturate. Optical pulse signals can effectively reduce the temperature inside UTC-PDs, thus decrease the impact of thermal effects on power saturation. In Chapter 3, CW and pulse measurements were done to compare the output power performance of CPW UTC-PDs and antenna integrated UTC-PDs, respectively. In the pulse measurement arrangement, MZ modulator was utilized to generate optical pulses and then amplified by EDFA. The bias voltage of UTC-PDs was stabilised by adding 1 μF capacitor parallel to the bias supply. CW and pulses measurements were done on 3 sizes of CPW UTC-PDs (3x10 μm^2, 3x15 μm^2 and 7x15 μm^2) and 4x15 μm^2 antenna integrated UTC-PDs. Pulse measurement results show: 1) optical pulses with narrower width and small duty cycle make UTC-PDs saturate at higher output power. 2) the max output power can be increased by more than 3 dB under the condition

of 20 ns pulse input (10% duty cycle), comparing with CW measurement results. As shown in Figure 3.27, shorter pulses have less heating effect and can reduce the temperature inside UTC-PDs. Pulse measurement results verify the idea that reducing the temperature of UTC-PDs can make photodiodes saturate at higher photocurrent and get larger RF output power.

As UTC-PDs target to work as the sub-THz (200 GHz - 300 GHz) source of high-speed wireless communications, they are integrated with broadband bow-tie antennas and bonded to 6 mm Si substrate lens. In Chapter 4, the temperature distribution of antenna integrated UTC-PDs is modelled by COMSOL, and the highest temperature inside 3x15 μm^2 device is 454 K (181 ºC), located in the InGaAs absorption layer, with the input optical power of 64 mW, the photocurrent of 13.5 mA, and the bias voltage of -2V. Thermal distribution simulation shows there is limited heat transfer through the layers beneath the absorption layer, because of the low thermal conductivity of these materials and the thick layer of S.I. InP substrate (300 µm). Replacing the low thermal conductivity bonding layer (between InP substrate and Si lens, thermal conductivity = 0.142 W/m·K) with thermal conductive adhesives (thermal conductivity = 1.44 W/m·K), the max temperature can be reduced by 45 K (solution 3). To verify the effectiveness of solution 3 and check how much the RF output power can be improved, experiments were done to measure the output power of 4x15 μm^2 antenna integrated UTC-PDs, whose bonding layers are Nitrocellulose and thermal conductive adhesives respectively (Section 4.3.3). Measurement results show that devices with thermal conductive adhesives have 1.2 dB higher output power than devices using Nitrocellulose, which proves that the output power of UTC-PDs can be increased by improving their thermal management.

On the top of UTC-PDs, the bow-tie antenna is deposited and connected to P-contact just through the side walls of the etched via. The cross-section area of this gold connection path is only 3 µm x 435 nm, and its corresponding thermal resistance reaches as high as 14642 W/(m·K), which blocks the heat dissipating through the gold antenna and confines the heat inside the junction of UTC-PDs. As the max temperature position is close to the top of P-contact, it is better to find ways to dissipate the thermal heat from the top of antenna integrated UTC-PDs. Besides solution 3, two more possible solutions are brought out to assist the heat

dissipation inside UTC-PDs: solid P via with thicker bow-tie antenna (solution 1), and a layer of AlN deposited on the top of integrated antennas (solution 2). COMSOL simulations show: for solution 1, the device's max temperature can be reduced by 22 ºC with 5 μm thick antenna; and for solution 2, the device's max temperature can be reduced by 47.5 ºC with 4 μm thick AlN layer.

In order to verify the correctness of thermal modelling, two rounds of experiments were done to measure the junction temperature of 3x15 μm^2 CPW UTC-PDs, and then compared with the COMSOL simulated temperatures, details are covered in Section 4.4. First, in the calibration measurement, the relationship between RF power change and UTC-PD temperature was established. In the 2nd experiment, the relationship between the relative RF power change of UTC-PDs and the photocurrents was established. Combining the measurement results from the two experiments, the relationship between the UTC-PD junction temperature and its photocurrent can be established. Comparing the simulated junction temperatures of 3x15 μm^2 CPW UTC-PD with experiment measured temperatures, a good agreement was achieved (the temperature differences are within 3ºC).

6.2 Novel contributions

- The first waveguide coupled phosphide-based UTC-PDs grown by SS-MBE are reported. CPW integrated UTC-PDs of 4x15 μm^2 and 7x15 μm^2 ridge area exhibited responsivities of 0.19 A/W and 0.22 A/W respectively. The 3×15 μm^2 CPW devices achieved 3 dB bandwidths greater than 65 GHz at -2V bias.

- A process to reduce the leakage current of waveguide UTC-PDs was developed. The leakage current of 7x15 μm^2 waveguide UTC-PDs was decreased from several μA to less than 100 nA by treated in 10% HCL for 1 min after the mesa etching step.

- Pulse measurement techniques for CPW integrated UTC-PDs and antenna integrated UTC-PDs were developed. To get reliable experimental data, the importance of stabilising bias voltage, configuring MZ modulator and optimising polarisation controller were demonstrated.

- In pulse measurement, the method to calculate peak powers from average values was worked out, which made corrections to the calculation equation reported in [6.3].
- Pulse measurement experiments on CPW integrated UTC-PDs and antenna integrated UTC-PDs demonstrated the RF output power of UTC-PDs can be improved by 3-4 dB through reducing their thermal effects.
- Thermal modelling on antenna integrated UTC-PDs identified three places blocking heat dissipation inside small size UTC-PDs: (1) high thermal resistance between P-contact and antenna, (2) high thermal resistance between P-ridge and SiO_xN_y passivation layer, and (3) high thermal resistance between InP substrate and Si lens.
- Three solutions to reducing high thermal resistance and improving thermal management were proposed: (1) solid P via with thicker bow-tie antenna, (2) AlN heat spreading layer deposited on the top of antenna, and (3) thermally conductive adhesive (thermal conductivity = 1.44 W/m·K) replaces the Nitrocellulose bonding layer (thermal conductivity = 0.142 W/m·K).

Above contributions had leaded to three publications, which are listed in Appendix E.

6.3 Future work

The thesis has reported the impact of thermal effects on waveguide UTC-PDs' RF output power, and proposed solutions to improve the heat dissipation inside antenna integrated UTC-PDs to increase the radiated RF power. In order to realise reliable high-power antenna integrated UTC-PDs for high-speed wireless communications, further optimisations and developments are needed. In this section, a list of suggestions for future research work is summarized and categorised into 3 areas: design and modelling, process and fabrication, and performance improvements.

1) **Thermal modelling optimization:** currently only the heat transfer module was used to build the thermal distribution modelling for UTC-PDs in COMSOL Multiphysics. The dissipated power was calculated by (4.1) and input as heat source in the thermal modelling. In order to make the modelling more accurately reflect the physics inside UTC-PDs, it is better to involve wave optics module and semiconductor module into the modelling, to deal with optical power transmission/absorption and photocurrents generation in UTC-PDs. Besides, to get more precise thermal modelling results, the material properties of each component layer should closely reflect the real values. Such as the thermal conductivity of InP, it is not a fix value and changes with temperatures [6.4] and doping densities [6.5], [6.6], which should be implemented to optimise the thermal modelling.

2) **Thermal stress modelling:** as explained in Section 4.3.2, in order to further reduce the temperature inside UTC-PDs, one solution is to deposit a layer of AlN on top of antenna integrated UTC-PDs. But extra stress will be introduced by the additional AlN layer: intrinsic (growth) stress and thermal stress. Intrinsic stress is related to any strained regions due to structural modifications taking place during fabrication, which will be covered in AlN deposition process study in the future work. Thermal stress is related to temperature change. During cooling or heating, the tensile or compressive thermal stresses will develop and can be estimated from the difference in CTE (coefficient of thermal expansion) between the film and the substrate. According to the solution 2 explained in Section 4.3.2, the deposited AlN layer will have contact with the passivation layer SiO_xN_y and the integrated bow-tie antenna. With the Solid Mechanics module added into current COMSOL thermal simulation, the mechanical stress coming from thermal heating can be simulated in the modelling, based on the mechanical properties of materials, see Table 6.1. By comparing the stress level between with and without AlN layer, we can know whether the additional AlN layer will bring harm to antenna integrated UTC-PDs or not.

Table 6.1: Mechanical properties of the materials in UTC-PDs.

Material		Thermal Conductivity W / (m·K)	CTE (1/K)	Young's Modulus (GPa)	Compressive Yield Stress (MPa)	Tensile Yield Stress (MPa)
SiO_xN_y	SiO_2	1.4	0.65	73	1380	110
	Si_3N_4	30	3.3	317	2800	400
AlN		285	4.5	310	2100	197
InGaAsP		7.2	5.66	67.7	533	200
InGaAs		5	5.66	67.7	533	200
InP		68	4.6	61	533	200
Au		320	14.2	78		

3) **Fabrication and characterisation of antenna integrated UTC-PD devices with solid P-via and thicker antenna:** the thermal modelling in Section 4.3.1 showed the max temperature of antenna integrated UTC-PDs can be decreased by 22 ºC with the P-via being filled with gold and increasing the thickness of antenna to 5 µm. By enlarging the size of device chip from 460 x 460 μm^2 to 800 x 800 μm^2, the thermal resistance can be decreased by 67% and the max temperature can be reduced by 37 ºC. Combining the two changes will reduce the max temperature by 59 ºC. To verify this design's feasibility, need fabricate devices and measure its junction temperature. Currently, the gold coating of via's inside wall and the antenna deposition are sputtered at the same time. Considering the via's depth is only about 1.5 - 2 µm, it is better to fill the P-via by sputtering first, then plating 5 µm thick antenna on the top of UTC-PDs. As the width of P-via is only 2 µm, it is a challenging to align the antenna mask with the P-via. Need process study to make sure fabricated devices meet the design expectations.

4) **Study the AlN deposition process to get high thermal conductivity and low growth stress:** the heat dissipation effect of solid P-via and thicker antenna is limited. To further reduce the max temperature inside UTC-PDs, depositing a layer of AlN on top of antenna integrated UTC-PDs is another way worth to try. This AlN layer need to have high thermal conductivity and low residual stress. High-power impulse magnetron sputtering (HiPIMS) has

proved to be a promising method to tailor thin film microstructures and residual stresses [6.7], [6.8]. To get suitable AlN layer, intense efforts and experiments need to be done to work out the proper AlN deposition thickness and sputtering process parameters, such as substrate voltage / temperature, chamber pressure, deposition thickness / rate, and etc.

5) **Further reduce the leakage current of UTC-PDs:** Experiments in Section 2.2.2 have shown the sidewall leakage current can be effectively reduced by soaking UTC-PDs in 10% HCl 1 min after mesa etching. But, the leakage current was observed increased after SiO_xN_y layer deposition by PECVD, which was caused by damages on the sidewall of P-ridge from exposure to plasma in high temperature chamber (300 ºC) [6.9]. ICPCVD is a low temperature plasms technology which can deposit high density SiN_x films at temperature lower than 150 ºC. ICPCVD deposited SiN_x film can effectively slow traps and reduce the densities of the interface states, contributing to less surface recombination velocity and low surface current, which attributes to the disorder suppression on the interface due to the high density of SiN_x film and less processing energy in ICPCVD. Studies have indicated that the recombination velocity of InGaAs on the sidewall, covered with SiN_x passivation layer formed by ICPCVD, is much lower than that formed by PECVD [6.10]. To further reduce the leakage current of UTC-PDs, low temperature ICPCVD is a replacement worth to try.

6) **InP epitaxy wafer grown on Si substrate:** Emerging Silicon (Si) photonics is a cost-effective platform and benefits from compatibility with the established Si complementary metal-oxide semiconductor (CMOS) technology. Waveguide photodiodes are critical basic elements in Si photonics. Efforts have been devoted to develop high power and high frequency waveguide photodiodes on Si platform. UTC structures have been integrated on silicon-on-insulator (SOI) waveguides using wafer-bonding technology. In [6.11], InP-based modified UTC-PD on SOI, exhibited internal responsivity of 0.64 A/W, bandwidth of 48 GHz, and RF output power of 12 dBm at 40 GHz. By reducing the size of MUTC-PD to 30 μm^2, their bandwidth was increased to 65 GHz and delivered -2 dBm at 70 GHz [6.12]. By integrating waveguide UTC-PDs

on an InP-membrane-on-silicon platform, 3 dB bandwidth of beyond 67 GHz and responsivity of 0.7 A/W at 1550 nm were reported in [6.13]. Germanium based waveguide PIN-PDs can be directly grown on SOI substrates; 67 GHz bandwidth with 0.74 A/W responsivity (4 nA dark current at -1V) and 32 GHz bandwidth with 1.1 A/W responsivity (1.3 μA dark current at -4V) were demonstrated in [6.14] and [6.15] respectively. A summary on the performance of different PD technologies is given in Table 6.2. The problems of wafer-bonding are the low manufacturing yield and the lack of reproducibility. Direct epitaxial growth of the III-V semiconductors on the Si substrates is considered to be the most desirable approach for the III-V/Si integration [6.16], more suitable for large-scale, low-cost and streamlined manufacture. However, semiconductor lattice mismatch and thermal expansion coefficients difference between III-V semiconductors and Si have been the bottle neck for the monolithic growing III-V compounds on Si substrates. This long existing technology barrier was broken through by direct growth of CW InAs/GaAs quantum dot laser on Si substrates [6.17] by SS-MBE, which had a low threshold current density of 62.5 $A \cdot cm^{-2}$, an output power of more than 105 mW and can operate up to 120 ºC. This shows a potential of growing UTC-PDs on Si substrates, through a layer of III-V compound to ease the lattice mismatch between InP and Si substrate. As Si has a much higher thermal conductivity (130 W/m·K) than InP (68 W/m·K), epitaxially growing UTC-PDs on Si substrates will give help on heat dissipation.

Table 6.2: Performance comparison between Si based WG PD and SS-MBE grown InP WG UTC-PDs.

WG Photodiode Technology	Bias (V)	Responsivity (A/W)	Dark Current (μA)	Bandwidth (GHz)	Output power (dBm)	Photocurrent (mA)	Frequency (GHz)	Size (μm²)
SS-MBE InP UTC-PD	-3	0.19	0.007 (@ -1V)	> 67	1.1	13	100	3x10
InP UTC-PD on SOI [6.11]	-7.5	0.64 (internal)	0.01 (@ -5V)	48	12	40	40	10x21
InP UTC-PD on SOI [6.12]	-3	0.13	0.001	65	-2	20	70	30
InP membrane UTC on Si [6.13]	-4	0.7	0.153	> 67	NA	NA	NA	3x10
Ge PIN-PD on Si [6.14]	-1	0.74	0.004	67	NA	NA	NA	0.5x14.2
Ge PIN-PD on Si [6.15]	-1	1.1	1.3	32	NA	NA	NA	0.8x10

6.4 General conclusions

Benefiting from the reduced space charge effects in the depletion layer, UTC-PDs provide high bandwidth and high RF output power, which entitles them the promising transmitter candidates for sub-THz wireless communications. By reducing the thermal effects inside UTC-PDs, their saturation output power can be effectively improved, which was verified by conducting pulse input measurements on CPW integrated UTC-PDs and antenna integrated UTC-PDs. Thermal modelling shows the max temperature inside 3x15 μm^2 antenna integrated UTC-PDs is 454 K (at the photocurrent of 13.5 mA and the bias voltage of -2V), and the thermal modelling at low photocurrent conditions is verified by temperature measurement experiment. Three solutions to improving the heat dissipation are proposed, which give the possibility to reduce the max temperature by around 84 K. In the future work, efforts will be put on fabricating antenna integrated UTC-PD devices according to the solutions explained in Section 4.3.1 and Section 4.3.2, to check their feasibility on improving the output power of UTC-PDs.

6.5 References

[6.1] H. Ito, T. Nagatsuma, A. Hirata, T. Minotani, A. Sasaki, Y. Hirota, T. Ishibashi, “High-power photonic millimetre wave generation at 100 GHz using matching-circuit-integrated uni-travelling-carrier photodiodes”, IEE Proceedings – Optoelectronics, vol. 150, no.2, pp. 138-142, (2003).

[6.2] Andreas Beling, Jesse S. Morgan, Keye Sun, Qianhuan Yu, “High Power Integrated 100 GHz Photodetectors”, International Topical Meeting on Microwave Photonics (MWP), pp. 1-4, (2018).

[6.3] Andreas Beling, Xiaojun Xie, and Joe C. Campbell, “High-power, high-linearity photodiodes”, Optica, vol. 3, no. 3, pp. 328-338, (2016).

[6.4] S.Jordan, “Some thermal and mechanical properties of InP essential to crystal growth modelling”, Journal of Crystal Growth, vol 71, no. 3, pp. 559-565, (1985).

[6.5] Sajan D. George, Achamma Kurian, Martin Lase, V. P. N. Nampoori, C. P. G. Vallabhan, “Thermal characterization of doped InP using photoacoustic technique”, Photonic Systems and Applications, vol. 4595, pp. 183-191, (2001).

[6.6] Juliana Jaramillo-Fernandez, Emigdio Chavez-Angel, Reza Sanatinia, Himanshu Kataria, Srinivasan Anand. “Thermal conductivity of epitaxially grown InP: experiment and simulation”, CrystEngComm, vol. 19, pp. 1879-1887, (2017).

[6.7] Greczynski, Grzegorz, Jun Lu, Jens Jensen, S. Bolz, W. Kölker, Ch Schiffers, O. Lemmer, Joseph E. Greene, and Lars Hultman, "A review of metal-ion-flux-controlled growth of metastable TiAlN by HIPIMS/DCMS co-sputtering." Surface and Coatings Technology, vol. 257 pp. 15-25, (2014).

[6.8] Greczynski, Grzegorz, S. Mráz, H. Ruess, M. Hans, Jun Lu, Lars Hultman, and J. M. Schneider. "Extended metastable Al solubility in cubic VAlN by metal-ion bombardment during pulsed magnetron sputtering: film stress vs subplantation," Journal of Applied Physics, vol. 122, no. 2, 025304, (2017).

[6.9] M.R. Ravi, Amitava DasGupta, Nandita DasGupta, “Silicon nitride and polyimide capping layers on InGaAs/InP PIN photodetector after sulfur treatment”, Journal of Crystal Growth, vol. 268, pp. 359-363, (2004).

[6.10] Ying Zhou, Xiaoli Ji, Ming Shi, Hengjing Tang, Xiumei Shao, Xue Li, Haimei Gong, Xun Cao, and Feng Yan, “Impact of SiNx passivation on the surface properties of InGaAs photo-detectors”, Journal of Applied Physics, vol. 118, 034507, (2015).

[6.11] Xie, Xiaojun, Qiugui Zhou, Erik Norberg, Matt Jacob-Mitos, Yaojia Chen, Anand Ramaswamy, Gregory Fish, John E. Bowers, Joe Campbell, and Andreas Beling. "Heterogeneously integrated waveguide-coupled photodiodes on SOI with 12 dBm output power at 40 GHz." Optical Fiber Communication Conference, pp. Th5B-7, (2015).

[6.12] Ye Wang, Ze Wang, Qianhuan Yu, Xiaojun Xie, Taylor Posavitz, Matt Jacob-Mitos, Anand Ramaswamy, Erik J. Norberg, Gregory A. Fish and Andreas Beling, “High-Power Photodiodes With 65 GHz Bandwidth Heterogeneously Integrated onto Silicon-on-Insulator Nano-Waveguides”, IEEE Journal of Selected Topics in Quantum Electronics, vol. 24, no. 2, 6000206, (2018).

[6.13] L. Shen, Y. Jiao, W. Yao, Z. Cao, J. P. van Engelen, G. Roelkens, M. K. Smit, and J. J. G. M. van der Tol, “High-bandwidth uni-traveling carrier waveguide photodetector on an InP-membrane-on-silicon platform”, Optics Express, vol. 24, no. 8, pp. 8290-8301, (2016).

[6.14] H. Chen, P. Verheyen, P. De Heyn, G. Lepage, J. De Coster, S. Balakrishnan, P. Absil, W. Yao, L. Shen, G. Roelkens, and J. Van Campenhout, “-1 V bias 67 GHz bandwidth Si-contacted germanium waveguide p-i-n photodetector for optical links at 56 Gbps and beyond”, Optics Express, vol. 24, no. 5, pp. 4622-4631, (2016).

[6.15] Dazeng Feng, Shirong Liao, Po Dong, Ning-Ning Feng, Hong Liang, Dawei Zheng, Cheng-Chih Kung, Joan Fong, Roshanak Shafiiha, Jack Cunningham, Ashok V. Krishnamoorthy, and Mehdi Asghari, “High-speed Ge photodetector monolithically integrated with large cross-section silicon-on-insulator waveguide”, Applied Physics Letters, vol. 95, pp. 261105, (2009).

[6.16] Tanabe, Katsuaki, Katsuyuki Watanabe, and Yasuhiko Arakawa. "III-V/Si hybrid photonic devices by direct fusion bonding." Scientific reports, vol. 2, no. 1 pp. 1-6, (2012).

[6.17] S. Chen, W. Li, J. Wu, Q. Jiang, M. Tang, S. Shutts, S. N. Elliott, A. Sobiesierski, A. J. Seeds, I. Ross, P. M. Smowton, and H. Liu, "Electrically pumped continuous wave III–V quantum dot lasers on silicon," Nature Photonics, vol. 10, no. 5, pp. 307-311, (2016).

Appendix A

Fabrication Process Flow of Waveguide UTC-PDs

1. Remove capping layer

capping layer: p++ - InP

HCL/H_3PO_4 (1:1) 15-20 seconds

2. Sputter P contact

LOR-10B resist spin 30s at 3000 rpm, and soft bake 10 min @ 205°C

S1818 photoresist spin 30s at 3000 rpm, and soft bake 2.5 min @ 115°C

Align to 'P contact mask' by MJB3 mask aligner and UV exposure for 3.7s

Develop: soak in MF-319 for 25-30s

P contact sputtering: first 2min milling, then deposit Ti / Pt / Au with the thickness of 75 nm / 50 nm / 400 nm

Lift-off: soak in 1165 overnight

3. P layer etch

Deposit 300nm of SiN by PECVD (deposition rate: ~40 nm/min, around 7 min)

Coated with S1818: spin 30s at 4000 rpm, and soft bake 2.5min @ 115C

Align to 'P layer etch' mask to pattern on SiN, then UV exposure for 3.7s

Develop: soak in MF-319 for 30s, and check the alignment by microscope

Dry etch SiN hard mask in Oxford RIE:

- Recipe: JH Nitride etch (CHF_3 & O_2)
- Etch rate: 60 nm/min, need 5-6 min to etch away SiN on top of P layer

Remove photoresist by O_2 plasma

- Recipe: JH resist strip, 5 min

P contact/absorption layer etching: to remove P contact/absorber ~340 nm

- Recipe: 'Etch for InP INGaAs GaAs' for 5min and 'O_2 plasma' for 5min to remove polymer on device surface; then 'Etch for InP INGaAs GaAs' 3 min and 'O_2 plasma' 3 min

Remove SiN mask on the top of gold P contact by JH Nitride etch (5 min)

Check the P-ridge height after SiN etching

4. Waveguide etch

Deposit 300nm of SiN by PECVD (deposition rate: ~40 nm/min, around 7 min)

Coated with S1818: spin 30s at 4000 rpm, and soft bake 2.5min @ 115°C

Align to 'waveguide etch mask' to pattern on SiN, then UV exposure for 3.7s

Develop in MF-319 for 30s, and check the alignment by microscope

Etch SiN hard mask in Oxford RIE:

- Recipe: JH Nitride etch (CHF_3 & O_2)
- Etch rate: 60 nm/min, need 5-6 min to etch away SiN on top of collection layer

Remove photoresist by O_2 plasma

- Recipe: JH resist strip, 5 min

Collection layer & sallow waveguide layer etch: to remove all collection layer (300 nm) and 50 nm waveguide layer

- Recipe: 'Etch for InP INGaAs GaAs' for 5 min and 'O_2 plasma' for 5 min to remove polymer on device surface; 3 rounds

Remove SiN mask on the top of P-ridge and waveguide by JH Nitride etch (5 min)

Check the waveguide height after SiN etching

Oxide removing: soak in 10% HCl, 1min, then HF cleaning (30s in HF/NH_4)

5. Sputter N contact

Use ‘N contact’ mask

Process is same as Step 3: Sputter P contact

6. Mesa etch

Deposit 600 nm of SiN by PECVD

Coated with S1818: spin 30s at 4000 rpm, and soft bake 2.5 min @ 115°C

Align to ‘Mesa etch mask’ to pattern on SiN, then UV exposure for 3.7s

Develop in MF-319 for 30s, and check the alignment by microscope

Etch SiN hard mask in Oxford RIE:

- Recipe: JH Nitride etch (CHF_3 & O_2)
- Etch rate: 60 nm/min, need 10 min to etch away SiN

Remove photoresist by O_2 plasma:

- Recipe: JH resist strip, 5min

Dry etch at least 900 nm to get down to SI InP layer:

- Recipe: ‘Etch for InP INGaAs GaAs’ for 5 min and ‘O_2 plasma’ for 5 min to remove polymer on device surface; 6 rounds

Remove SiN mask on the top of mesa by JH Nitride etch (10 min)

Check the mesa’s height after SiN etching

Oxide removing: soak in 10% HCl, 1min, then HF cleaning (30s in HF/NH_4)

7. Annealing P & N contacts

425°C 1min (only N_2 gas inside RTA chamber)

8. SiO_xN_y deposition

Deposit SiO_xN_y by PECVD (1.5-3 μm is accepted)

- Recipe: 'LFSiON', power 60W, 27 min (about 1.8 um thickness)

9. Via etch

Coated with S1818: spin 30s at 4000 rpm, and soft bake 2.5 min @ 115°C

Align to 'Via etch mask', then UV exposure for 3.7s

Develop in MF-319 for 30s, and check the alignment by microscope

Dry etch SiO_xN_y in Oxford RIE:

- Recipe: 'JH Nitride etch', run 25 min

Remove photoresist by O_2 plasma, then clean with 1165

10. CPW deposition

LOR-10B resist spin 30s at 3000 rpm, and soft bake 10 min @ 205°C

S1818 photoresist spin 30s at 3000 rpm, and soft bake 2.5 min @ 115°C

Align CPW mask by MJB3 mask aligner and UV exposure for 3.7s

Develop in MF-319 for 25-30s

Surface cleaning by Asher Diener (10 min)

CPW contact sputtering: deposit Ti / Au with the thickness of 35 nm / 400 nm

Lift-off: soak in 1165 overnight

Appendix B
Major Process Steps

Major fabrication steps of waveguide UTC-PDs are P-contact deposition, P-contact/absorption layer etching, waveguide etching, N-contact deposition, mesa etching, passivation, vias etching and CPW deposition. Below gives detail explanation for etching, passivation and contact deposition.

Etching

Etch processes can be divided into wet and dry etching while there is a further separation into isotropic and anisotropic processes, and also a separation in chemical and physical etch characteristics. In an isotropic etch process, the etching occurs in lateral and vertical directions. Thereby layers are removed not only in thickness but also in their circumference. In anisotropic process, the layer is only removed in vertical direction. Because the wet etching generally has isotropic etch profile, it is used very rare for structuring. In the dry etching, also known as plasma etching process, plasma or etchant gases are used to remove the substrate material. There are three types of dry etching: physical removal, chemical reactions, and a combination of chemical reactions and physical removal. In physical dry etching, high energy kinetic energy beams (ion, electron, or photon) to etch off the substrate atoms. When the high energy particles knock out the atoms from the substrate surface, the material evaporates after leaving the substrate. There is no chemical reaction taking place and therefore only the material that is unmasked will be removed, see Figure B.1 (a) [B.1]. In chemical dry etching (also called vapour phase etching), chemical reactions are involved between etchant gases to attack the substrate surface. The substrate surface atoms are removed by forming the bond between the reactive ion and the substrate atom. Due to the directional nature of dry etching, undercutting can be avoided. Figure B.1 (b) shows the reaction that takes place in chemical dry etching [B.1]. Reactive ion etching (RIE) uses both physical and chemical mechanisms and therefore the process is much faster. The high energy collision from the ionization helps to dissociate the etchant molecules into more reactive species. Cations are produced from reactive gases which are accelerated with

high energy to the substrate and chemically react with the substrate. As seen in Figure B.1 (c), both physical and chemical reactions are taking place in RIE process.

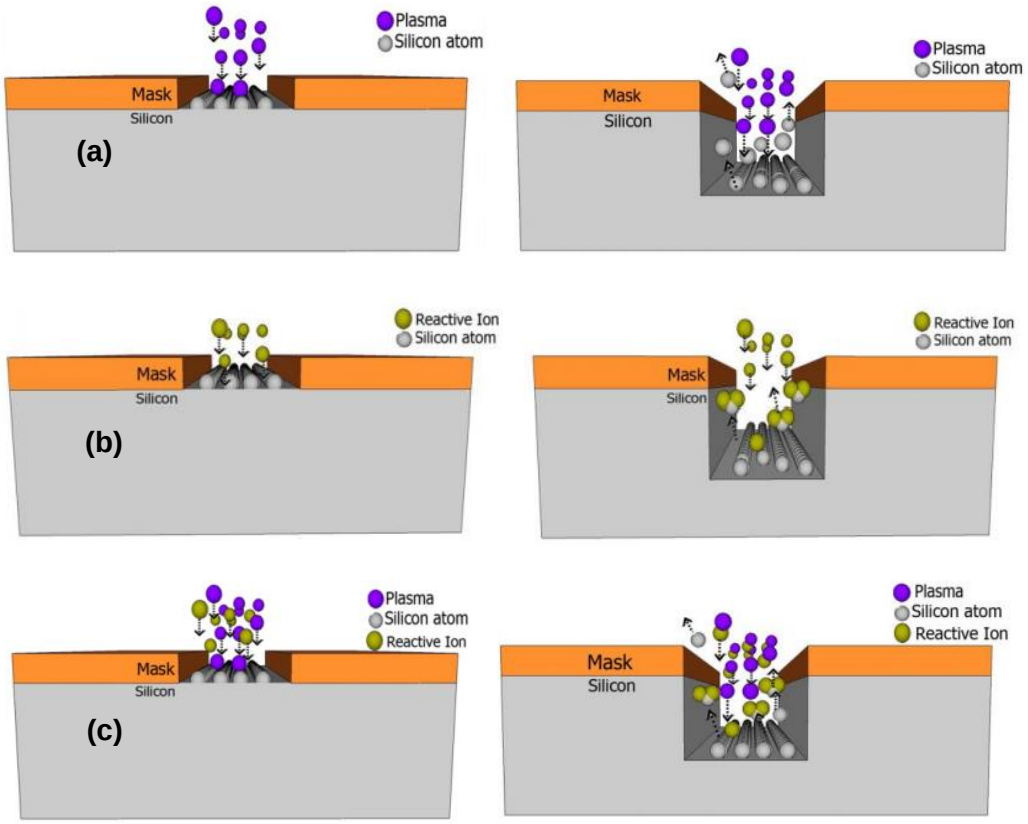

Figure B.1: (a) The plasma atoms hitting the surface and the substrate atoms being evaporated off from the surface, (b) The interaction between the reactive ion and the substrate atom and chemically remove the bond from the surface, (c) RIE process involves both physical and chemical reactions to etch off the substrate atoms [B.1].

For indium containing III-V semiconductors, CH_4/H_2 plasmas produce smooth anisotropic etching at relatively low rates. In applications requiring etch rates near 1um/min, $CH_4/H_2/Cl_2$ electron cyclotron resonance discharges have proved effective. The CH_4 removes group III elements, probably as metalorganic-type species, whereas the H_2 removes the group V elements as hydrides. A major drawback is that the etch rate is not consistent until the chamber is properly seasoned by depositing a polymer around the reactor walls [B.2], [B.3]. CH_4/H_2 discharges do not chemically etch any common masking material, but rather

deposit a polymer on any non-etching surface. The polymer can be removed by a short oxygen plasma clean-up, which removes the polymer both from the chamber and off the mask. The ratio CH_4:H_2 must be kept between 1:2 and 1:6 or else polymer deposition becomes prohibitive at the former ratio and preferential loss of the group V species becomes dominant at the latter values. Because there is little spontaneous chemical etching with CH_4/H_2 mixtures, the etching is usually very anisotropic. Too much methane or hydrogen in the discharge will lead to rough surfaces, and there is essentially no selectivity for one indium-based material over another (e.g. InP/InGaAs). Factors such as applied coil or electrode power, reactant gas flow rates, duty cycles, and chamber pressures can affect the etching rate and performance, and the smoothness of etching surface will influence the effect of passivation.

In our process to fabricate TW-UTC-PD, four rounds of RIE dry etching (the mixture gas of CH_4 and H_2) are used to form P-contact ridge, optical coupling waveguide, isolation mesa and vias for connecting CPW contact, see photos in Figure B.2. For our dry etching process, we use gas rate 14sccm/50sccm for CH_4/H_2 with 150W power under the pressure of 35mTorr. The measured average etching rate for P-contact ridge (InGaAsP [200nm]/InGaAs [140nm]) is about 40nm/min, and the etching rate for Mesa etch (InGaAsP[250nm]/InP[800nm]) is about 25nm/min. After the CH_4/H_2 etching, O_2 plasma is applied to remove the polymer.

Figure B.2: From left to right: P-contact ridge etch, waveguide etch, mesa etch and vias etch.

Passivation

At the surface of III-V compound semiconductors, the continuity of the bulk is broken with introduction of dangling bonds, surface reconstruction, defects, native surface oxides, contaminants, etc., which introduce energy levels in the energy bandgap. Dielectric deposition needs to be carried out to preserve as much of the surface as possible. The passivation process involves suitable treatment and coating of the PN junction peripheral edge with dielectric material layer, with the idea of modifying the surface so that least possible surface states or best possible electronic properties (low leakage current, high voltage) can be preserved and be stable over the life of the device. Surface state density must be reduced below $10^{12}/cm^2 \cdot eV$ level for good device performance and lift time [B.4]. Such lower values can be achieved and retained through the life of the device by using dielectric surface passivation. Dielectric layers are commonly deposited by Plasma Enhanced Chemical Vapour Deposition (PECVD), and the surface of the semiconductor is exposed to plasma before the deposition starts. Energetic ions, chemical radicals, UV light, etc. all causes surface damage. To maintain high-quality dielectric without introducing excessive damage, plasma system's bias voltage, RF power, deposition temperature and deposition rate need to be carefully designed and optimized. For our UTC-PD device, SiO_xN_y is used as the passivation layer to protect the P-contact/absorber ridge, deposited by PECVD with RF power of 60W and deposition chamber temperature of 300°C.

Contact Deposition

An ohmic contact is defined as a metal-semiconductor contact that has a negligible contact resistance relative to the bulk or series resistance of the semiconductor. When metal combining with semiconductor, the ideal ohmic contact is one where no barriers to the carrier flow are encountered in either the positive and negative current direction. This situation only occurs when the work functions of the metal and the semiconductor are the same and there are no interface states which tend to pin the Fermi Level. It is obviously impossible as the work function of semiconductor differs with elements, structure and doping concentration. When a metal is placed in contact with a III-V semiconductor, the resulting potential barrier depends on the work function of the metal, φ_m, the work

function of the semiconductor, φ_s, and the electron affinity, χ, see Figure B.3. The potential barrier height φ_b to electron flow from the metal is $\varphi_b = \varphi_m - \chi$, and it is called Schottky barrier. Ohmic contacts is dependent on this Schottky barrier height, which sets the threshold for the excess energy an electron requires to pass from the semiconductor to the metal [B.5]. Electrons may traverse this potential barrier (φ_b) by having enough thermal energy (thermionic emission) or by quantum mechanical tunnelling (field emission) if the barrier is sufficiently narrow. The tunnelling emission makes ohmic contact possible. The most common approach to fabricating ohmic contacts on III-V semiconductor is to apply an appropriate metallization to the wafer, and then alloy the metal into the semiconductor. During the alloy and cooling period, a component of the metal enters into the semiconductor and highly dopes the surface layer to form the ohmic contact [B.6].

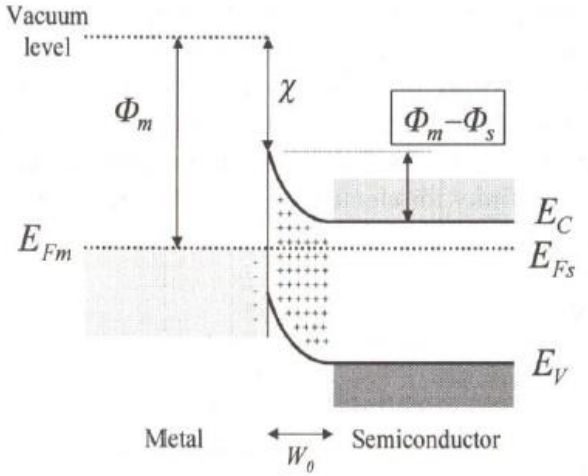

Figure B.3: Band bending at metal-semiconductor junction [B.7].

P and N contact patterns are defined by aligning sample with contacts mask after being coated by two layers of photoresist (LOR 10B & S1818), then exposed to UV light to form the pattern. Photolithography is the technique to transferring geometric pattern of a designed mask to the target wafer surface. The process steps include photoresist coating, hot plate baking, contact mask alignment, UV exposure and developing. The purpose of baking is solvent volatilization and

resist solidification; and the UV exposure is to weaken the resist, the parts not covered by the pattern mask and can be easily removed in the developer step. Then Ti/Pt/Au are deposited by sputtering with the thickness of 75nm/50nm/400nm. After the sputtering, the sample was soaked in the lift-off solvent 1165 for overnight to remove the parts covered with photoresist. To form ohmic contact between the deposited metal alloys and semiconductors, post-deposition annealing is performed to promote the inter-diffusion between metal elements and its beneath semiconductor, which narrowing the barrier height and making electron tunnelling emission possible. Below Figure B.4 shows the finished 3x15 um UTC-PD with CPW contacts.

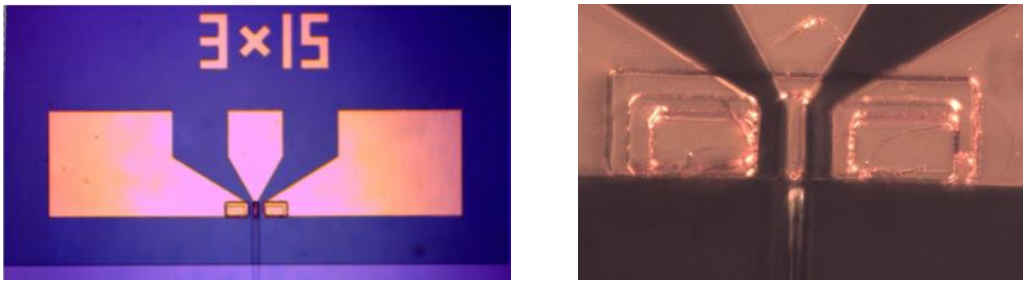

Figure B.4: 3x15um^2 UTC-PD with CPW contacts.

References

[B.1] Avinash P. Nayak, Logeeswaran VJ, M. Saif Islam, “Wet and Dry Etching”, http://web.ece.ucdavis.edu/~anayakpr/Papers/Wet%20and%20Dry%20Etching_submitted.pdf

[B.2] Sadeghi, Nader, Toshiki Nakano, Dennis J. Trevor, and Richard A. Gottscho. "Erratum: Ion transport in an electron cyclotron resonance plasma,” Journal of Applied Physics, vol. 71, no. 7, pp. 3648-3648, (1992).

[B.3] T.R. Hayes, in "InP and Related Compounds", edited by A. Katz (Artech House, Boston, MA) Ch. 8, (1990).

[B.4] Tiku, Shiban, and Dhrubes Biswas, eds, “III-V integrated circuit fabrication technology: Fabrication, Integration and Applications,” CRC Press, pp. 453, (2016).

[B.5] From Wikipedia, https://en.wikipedia.org/wiki/Ohmic_contact

[B.6] Shao-Qiu Xiao, Ming-Tuo Zhou. “Millimeter Wave Technology in Wireless PAN, LAN, and MAN”. CRC Press, (2008).

[B.7] Manijeh Razeghi. “Fundamentals of Solid State Engineering”, Kluer Academic Publishers, (2002).

Appendix C

Error Sources in sub-THz Measurements

The RF output power of UTC-PDs at sub-THz range (like the interested frequencies 100GHz and 250 GHz in this thesis) are relatively low at small photocurrents. For example, the 100 GHz output power of 3x15 μm^2 UTC-PDs at 2 mA photocurrent is around 11 μW, and 250 GHz output power of 4x15 μm^2 UTC-PDs at 5 mA photocurrent is around 7 μW. In order to make reliable and precise measurements, the experiment systems need to be stable and well designed to eliminate noises/error sources. In this Appendix, the error sources from surroundings and measurement layout and the calibration on power measurement equipment are discussed.

The repeatability of RF power readings is also important for reliable measurements. For each UTC-PD under test, its power measurement was taken at least 5 times by different operators during system debugging and optimisation process. Once stable and repeatable measurement results were achieved, the test system was regarded as acceptable and RF power readings were recoded.

Error Sources

Several sources of random and systematic errors exist throughout the measurement process. They cause the variances and deviations and eventually contribute to the uncertainty in the RF output power measurement. The sources of random error include laser intensity fluctuation, optical and electronic noise, vibration, etc. whereas the sources of systematic error include mechanical drift, reflections, sample alignment, etc. Regarding the natural difference between two types of error in RF output power measurement, a random error occurs in a relatively short time scale; in contrast to a systematic error that can be observed when the measurement time span is long enough [C.1]. Taking measurements over a short time is helpful to avoid the systematic drift, but can not avoid random errors, while recording over a long period can average out random errors but bringing the problem of drift.

For 100 GHz output power measurements on CPW UTC-PDs, measurement uncertainty comes from laser amplitude fluctuation, laser frequency shift, optical bench vibration, experiment layout thermal deformation, EDFA ASE, fibre alignment, etc. For laser frequency shift (due to temperature) and experiment layout thermal deformation, we use air conditioner to manage lab temperature and wait for experiment system stabilisation to reduce their impacts. For laser amplitude fluctuation and optical bench vibration, air compressor is employed to minimise the vibration and averaging several measurements to decrease the fluctuation noises. For EDFA ASE, optical filter (5 nm pass band) is added after EDFA to reduce its contribution to RF output power. The lensed fibre is shift away from its optimised position with time, it is better to re-do the fibre alignment before taking each measurement. By applying the above methods, random errors and systematic errors can be controlled in an accepted level.

For 250 GHz output power measurements on antenna integrated UTC-PDs, as their output power is measured in free space by Thomas Keating (TK) opto-acoustic power sensor (shown in Figure 2.20), its measurement system has more error sources than 100 GHz output power measurement system. The extra error sources are TPX lenses alignment (used to collimate and focus the THz radiation onto the Thomas Keating power sensor), UTC-PD devices sitting position on 6 mm Si lens, sound/vibration/light from surroundings (like doors open/close, loud sound from street, lamplight, etc.). For TPX lenses alignment, it is not easy to find the optimum position to focus the THz radiation, it needs time and patience to slowly adjust each TPX lens to collimate 250 GHz power onto the centre of TK power sensor. We usually use the infrared sensor card to locate where the highest RF power position is. For the background sound/vibration/light, we do calibration every 4 hours to offset their impact on power readings.

Calibrations

The goal of calibration is to minimise any measurement uncertainty by ensuring the accuracy of test equipment. Calibration quantifies and controls errors or uncertainties within measurement processes to an acceptable level. We do equipment self-calibration on Agilent E4418B EPM series power meter (used for 100 GHz power measurement) and TK opto-acoustic power sensor (used for 250 GHz power measurement) every 4 hours before using them take measurements.

For 100 GHz output power measurements on CPW UTC-PDs, the RF power is extracted from devices with an air coplanar probe and measured using an Agilent E4418B EPM series power meter. A flexible W band waveguide is used in between the probe and the power meter head to reduce mechanical strain. The loss of the waveguide is measured as 3.2 dB at 100 GHz by using a network analyser, and the loss of the air coplanar probe is listed as 1.2 dB in its datasheet. The measured output powers are corrected for the losses in both the probe and the waveguide.

References

[C.1] Withawat Withayachumnankul, Bernd M. Fischer, Hungyen Lin, and Derek Abbott, "Uncertainty in terahertz time-domain spectroscopy measurement," J. Opt. Soc. Am. B, vol. 25, no. 6, pp.1059-1072, (2008).

Appendix D

Electric Field Calculation for UTC-PDs

For UTC-PDs, RF output power saturation is caused by space charge effects or thermal effects. Space charge effects: at high photocurrents, electrons are accumulated in the collection layer, the negative charge in the collection layer bends the potential profile shown by the broken lines in Figure D.1 [D.1], and the electric field at the absorption/collection layer interface (E_{int}) decreases. When E_{int} is smaller than the critical field ($E_c \approx 10$ kV/cm), the electron velocity overshoot (due to the non-equilibrium transport of electrons) will not take place and the electron drift velocity (v_e) will be the saturation velocity [D.1].

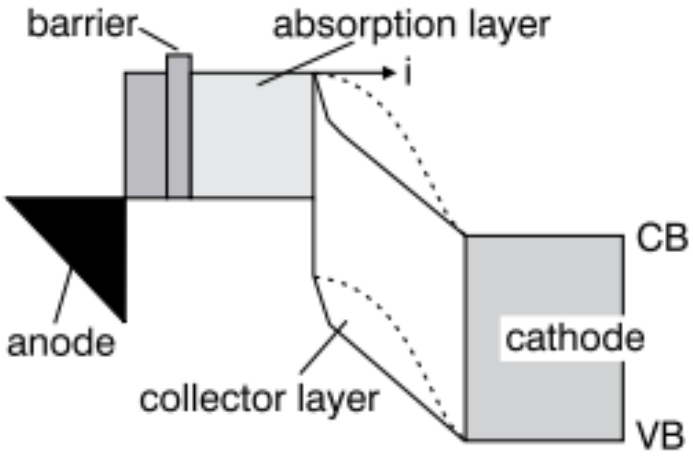

Figure D.1: Schematic diagram of potential profile of UTC-PD [D.1].

Thermal effects: when temperature increases, the lattice vibration increases which impacts electrons moving direction and decrease electron drift velocity, see Figure D.2 (for the steady-state drift velocity). For the instantaneous drift velocity, temperature impacts the peak value of electron overshoot velocity and the critical field (E_c), see Figure 3.28. Comparing Figure 3.28 (a) with (b), for temperature higher than 300 K, the E_c will be higher than 10 kV/cm and the overshoot velocity will be decreased.

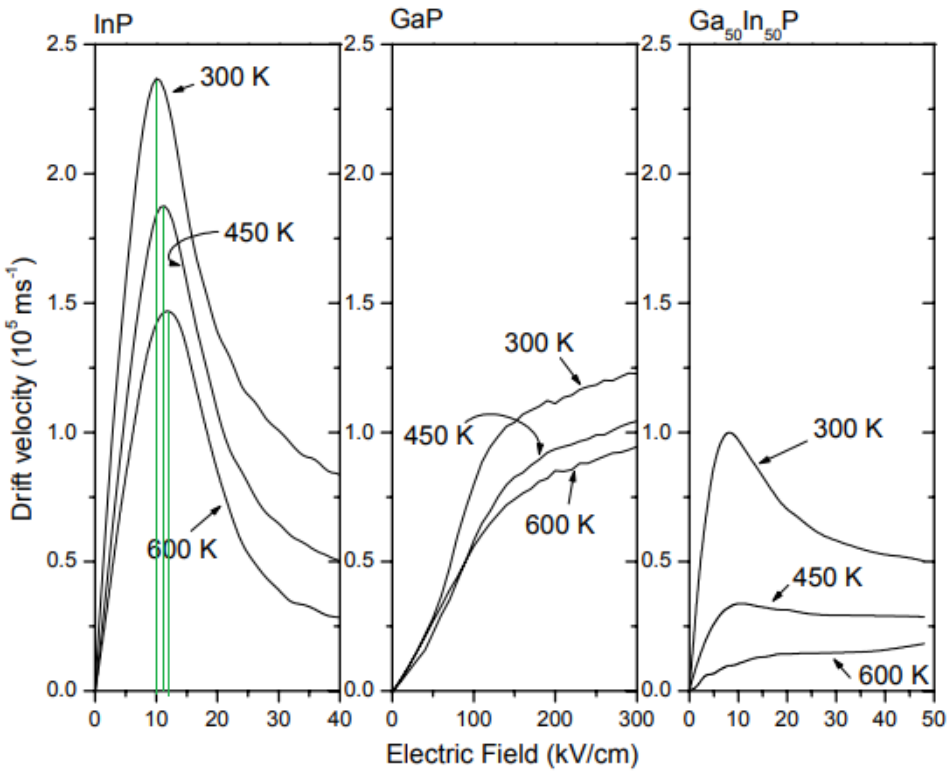

Figure D.2: Calculated electron steady-state drift velocity in bulk InP, GaP and $Ga_{0.5}In_{0.5}P$ as a function of applied electric field at various lattice temperatures and assuming a donor concentration of 10^{16} cm^{-3}. The peak drift velocity decreases while the threshold field increases by the same percent as the lattice temperature increases from 300 K to 600 K [D.2].

By calculating the electric field at the interface of absorption and collection layer of UTC-PDs, we can judge whether their RF output power saturation is caused by space charge effects (higher than E_c) or not (lower than E_c). The negative charge density in the collector layer (Q-) and the voltage across UTC-PDs (V_{UTC}) are expressed as (D.1) and (D.2).

$$Q_- = \frac{j}{v_e} - qN_d \qquad (D.1)$$

$$V_{UTC} = V_{DC\_bias} - I_{ph} \cdot R_s \qquad (D.2)$$

where Q- is negative charge density in the collector layer, j is photocurrent density, ν_e is electron drift velocity (use 4×10^7 cm/s), N_d is donor density in the collection layer (10^{16} 1/cm^3), V_{DC_bias} is the applied bias voltage, V_{UTC} is voltage applied across UTC-PDs, I_{ph} is photocurrent and R_s is series resistance of UTC-PDs.

From Poisson equation (D.3), electrical potential Φ is derived as (D.4). By applying boundary conditions (D.5) & (D.6), C1 and C2 can be calculated out. Then, the electric field E at the interface of absorption layer and collection layer can be worked out by using equation (D.7).

$$\frac{d^2\,\Phi}{d\,x^2} = -\frac{Q_-}{\varepsilon} \qquad (D.3)$$

$$\Phi = \frac{-Q_-\,x^2}{2\varepsilon} + C1\,x + C2 \qquad (D.4)$$

x_1 = 0 nm, $\Phi 1 = 0\ V$ (D.5)

x_2 = 300 nm, $\Phi 2 = V_{DC\_bias} - I_{ph} \cdot R_s$ (D.6)

$$E = -\frac{d\,\Phi}{d\,x} \qquad (D.7)$$

where Φ is electrical potential, ε is the permittivity of collection layer, x is the position in collection layer ($x_2 - x_1$ is the thickness of collection layer), and E is electric field.

For photocurrent = -12 mA (the CW power saturation photocurrent of 3x10 μm^2 CPW UTC-PDs), the calculated electric field E_{int} at the interface of absorption and collection layer is 50.6 kV/cm. For photocurrent = -23 mA (the 10% pulse input saturation photocurrent of 3x10 μm^2 CPW UTC-PDs), the calculated electric field E_{int} at the interface of absorption and collection layer is 25.2 kV/cm. Both of the values are higher than Ec, therefore we think for 3x10 μm^2 CPW UTC-PDs, the RF output power saturations were caused by thermal effects in CW and 10% pulse measurements.

References

[D.1] N. Shimizu, Y. Miyamoto, A. Hirano, K. Sato and T. Ishibashi, “RF saturation mechanism of InP/InGaAs unitravelling-carrier photodiode”, Electronics Letters, vol. 36, no. 8, pp. 750-751, (2000).

[D.2] A. Mokhles Gerami, H. Rahimpour Soleimani, H. Arabshahi and M.R. Khalvati, “Temperature and Doping Dependencies of Hot Electron Transport Properties in Bulk GaP, InP and Ga0.5In0.5P”, Adv. In Nat. Appl. Sci., vol. 3, no.3, pp. 357-362, (2009).

Appendix E
List of Publications

[1] **Xiaoli Lin**, Michele Natrella, James Seddon, Chris Graham, Cyril C. Renaud, Mingchu Tang, Jiang Wu, Huiyun Liu, and Alwyn J. Seeds, "High performance waveguide uni-travelling carrier photodiode grown by solid source molecular beam epitaxy", Optics Express, vol. 27, no. 25, pp. 37065-37086, (2019).

[2] James P. Seddon, Michele Natrella, **Xiaoli Lin**, Chris Graham, Cyril C. Renaud, Alwyn J. Seeds, "Photodiodes for Terahertz Applications", IEEE Journal of Selected Topics in Quantum Electronics, vol. 28, no. 2, pp. 1-12, (2022).

[3] James P. Seddon, Katarzyna Balakier, **Xiaoli Lin**, Chris Graham, Alwyn J. Seeds and Cyril C. Renaud, "A Photonics Enabled Millimetre Wave Frequency Domain Spectrometer for Glucose Concentration Sensing," 2018 43rd International Conference on Infrared, Millimeter, and Terahertz Waves (IRMMW-THz), pp. 1-2, (2018).